Colliding Plasmas in Air

Submitted by:

Stephen J. Davitt

B. Sc. Hons.

A thesis submitted for the Award of:

DOCTOR OF PHILOSOPHY

Presented to:

The School of Physical Sciences

Dublin City University

Research Supervisor

Prof. John T Costello

Co-Supervisor

Dr. Mossy Kelly

(University of Hull)

October 2018

Declaration

I hereby certify that this material, which I now submit for assessment on the programme of study leading to the award of Doctor of Philosophy is entirely my own work, that I have exercised reasonable care to ensure that the work is original, and does not to the best of my knowledge breach any law of copyright, and has not been taken from the work of others save and to the extent that such work has been cited and acknowledged within the text of my work.

Signed: ______________________

ID No.: 59448853

Date: _____________

Dedicated to my father John, for always fostering my curiosity since a young age and encouraging my pursuit of knowledge.

Acknowledgements

Firstly, I would like to thank my supervisor Prof. John Costello for giving me the opportunity to undertake this research. Thank you for all of your guidance and help over the years. I would also like to thank my co-supervisor Dr. Mossy Kelly along with Dr. Paddy Hayden for their continued support and advice throughout the Ph.D. Thanks to all of the members of the group – Nicky, Colm, Ben, Will, Get, Hu, Pramod, Sadaf, Ares, Tejaswi, Columb and Muhammad, it was a pleasure working with you and I wish you all the best.

I would like to express my thanks to all of the members of the physics department and NCPST, in particular I wish to acknowledge the support from - Henry, Lisa, Des, Alan, Pat, Enda, Sheila, Michael and Justin you were all always happy to help with any problems or issues that arose.

I would like to thank Dr. Eilish McLoughlin for indoctrinating me into the world of science communication, it has truly been a passion of mine throughout the course of the Ph.D. and it has benefitted both my personal and academic life greatly. On that topic, I would like to thank my science communication partner in crime, Dr. Claire O’Connell, you were always ready to jump at the next opportunity with me, including having to drive a campervan across Europe that time.

A special thanks to my family - my mother Sharon, my father John, and my siblings Lisa and Karl, for their continued support and keeping me going when times got tough. I cannot forget my other brother, gym buddy and friend, Piers O’Brien, I could always count on you when I needed cheering up or just to hang out with some games. Sarahjane I would like to thank you for your support and putting up with me during the end stages, it wasn’t always easy, but you were always there.

Finally to all of the many other friends I have made within the department and beyond – Ronan, Cleo, Deirdre, Aggie, Paul, Brian, Huw, Aoife, David, Adam, Louis, Conor, Dave, Tom and Éanna. I would like to thank you all for making the past few years some of my best with many fond memories.

Table of Contents

Declaration ii

Acknowledgements iv

List of Figures viii

List of Tables xix

List of Abbreviations xx

Abstract xxii

1 Introduction 1

1.1 Laser Produced Plasmas & LIBS 1

1.2 Colliding Plasmas and Stagnation Layers 2

1.3 Colliding Plasmas in Ambient Air 3

1.4 Fourier transform spectrometer for LIBS 6

1.5 Thesis Outline 6

References 8

2 Theoretical Background 12

2.1 Plasma Definition 12

2.2 Atomic Processes in Laser Plasmas 15

2.3 Laser Plasma Formation 23

2.4 Plasma Equilibrium 33

2.5 Colliding Plasma Plumes 37

2.6 Optical Emission from Laser Produced Plasmas 39

2.7 Summary 51

References 52

3 Experimental Systems xxii

3.1 Spectron Laser System 55

3.2 Fast Imaging and Intensified CCD (ICCD) Cameras 58

3.3 Kymera Spectrometer 62

3.4 Target Geometries 65

3.5 Optical Delivery System 66

3.6 Fast Imaging Setup 67

3.7 Optical Emission Spectroscopy (OES) Setup 71

3.8 Synchronisation and Timings 73

3.9 Summary 75

References 76

4 Imaging Colliding and Confined Plasmas 77

4.1 Colliding Plasmas 77

4.2 Broadband Fast Imaging 79

4.3 Spectrally Resolved Fast Imaging 100

4.4 Summary 108

References 110

5 Optical Emission Spectroscopy (OES) of Colliding Plasmas in Air 113

5.1 Broad Spectral Band Time Resolved Optical Emission Spectroscopy 115

5.2 Spatial Distributions of Al^+ 358.7 nm and Al^0 396.15 nm Line Emission 119

5.3 Spatio-Temporal Electron Temperatures & Densities 124

5.4 Comparison of Line Emission for Different Targets 137

5.5 Summary 144

References 146

6 Development of a Wollaston Prism Fourier Transform Spectrometer for LIBS Applications 147

6.1 Fourier Transform Spectroscopy 147

6.2 The Wollaston Prism 149

6.3 WPFT Spectrometer 152

6.4 Stellarnet® EPP2000 162

6.5 Comparison between the WPFT and Stellarnet® EPP2000 Spectrometers 162
6.6 LIBS Experiment: Mn in Steel 167
6.7 WPFT Spectrometer: Conclusions and Future Work 171
References 173
7 Conclusions 175
7.1 Summary and Conclusions 175
7.2 Future Work 177
References 181
Appendices 173
A. Courses, Conferences, & Publications 183
B. Supplementary Fast Imaging Data 186
C. Supplementary Optical Emission Spectroscopy Data 210

List of Figures

Fig. 1.1 Taken from [36]. A) 2D relative refractive index profile at $1600\,ns$. Below graph shows a lineout of the refractive index at $1.45\,mm$. B) Refractive index at $0.57\,mm$ for various time delays. Reflected shocks and plasmas hill can be seen. 5

Fig. 2.1 Schematic of the atomic processes impact excitation (left) and impact de-excitation (right). $E1$ and $E2$ are the lower and upper energy levels and e is a free electron with energies $(\varepsilon 1)$ and $(\varepsilon 2)$ where $\varepsilon 2 < (\varepsilon 1) \geq E2 - E1$. 17

Fig. 2.2 Schematic of the atomic processes photoabsorption (left) and spontaneous emission (right) [5]. $E1$ and $E2$ are the lower and upper energy levels and γ is a photon of energy $hv = E2 - E1$. These absorption processes may also occur with multiple photons however for simplicity only the single photon case is shown here. 18

Fig. 2.3 Schematic of the atomic processes impact ionisation (left) and three-body recombination (right). $E1$ and $E2$ are bound energy levels, $E\infty$ the continuum, e' is the captured/liberated free electron with energy$(\varepsilon 3)$ and e is a second free electron with energies $(\varepsilon 1)$ and $(\varepsilon 2)$. 19

Fig. 2.4 Schematic of the atomic processes photoionisation (left) and radiative recombination (right) [5]. $E1$ and $E2$ are finite energy levels, $E\infty$ the continuum, and γ represents a photon. 20

Fig. 2.5 Schematic of the atomic processes bremsstrahlung (left) and inverse bremsstrahlung (right) [5]. $E\infty$ is the continuum, and γ is a photon of energy hv. 22

Fig. 2.6 Schematic of the atomic processes multi-photon photoionisation (left) and Multi-photon absorption (right). $E1$ and $E2$ are finite energy levels, $E\infty$ the continuum, and γ is a photon of energy hv. 23

Fig. 2.7 Schematic of laser produced plasma formation. A) An incident laser pulse of duration τL is incident on a solid target. B) As the leading edge of the pulse interacts with the target surface, material is ablated, and a dilute plasma is formed. C) The remaining pulse energy excites the plasma and it expands isothermally. D) After the laser pulse has

terminated the plasma will continue to expand adiabatically into the surrounding medium. Adapted from [4]. 24
Fig. 2.8 Schematic diagrams of A) The development of a laser plasma from a solid surface. The absorption zone, plasma volume and shock front are all labelled. B) A laser-supported detonation (LSD) wave, the shock wave preceding the absorption zone and plasma front and the three zones are separated. Figures recreated from [4]. 31
Fig. 2.9 Criteria for applicability of different thermodynamic equilibrium models for laser plasmas. Adapted from [18] 34
Fig. 2.10 Examples of two expanding plasma plumes exhibiting A) Interpenetration and B) Stagnation. In interpenetration the plasma constituents will pass through one another with the main interactions being binary collisions. At the other extreme the plasma plumes decelerate rapidly at the collision front and stagnate. The remaining material from the plumes accumulate at the collision plane and so the density starts to rise even further. For the case of two expanding plasmas, interpenetration or stagnation may occur depending on the collisionality parameter ζ. 38
Fig. 2.11 Gaussian and Lorentzian profiles with equal full-width half max values. The Voigt profile is the result of the convolution of the Gaussian and Lorentzian functions. Recreated from [4]. 44
Fig. 2.12 Simulated solution to equation (2.53) from the ratio of the Al^+358.7 nm and Al 396.1 nm transitions for a range of electron densities. 49
Fig. 2.13 Flow chart of the numerical method used to solve for the electron temperature in equation (2.53). The electron temperature is varied until the calculated intensity ratio is within a tolerance of the recorded value.. 49
Fig. 3.1 Schematic of the Spectron™ SL803 laser system. The SL803 is a Q-Switched Nd:YAG laser with an oscillator and an amplifier. [2] .. 56
Fig. 3.2 Spectron SL803 (average) pulse energy vs. ½-waveplate angle. Experimentally measured using a Coherent PowerMax PM30 power meter. 57

Fig. 3.3 Basic schematic of the ½-Wave plate polariser attenuator pairs. Stacking two of these systems allows fine control of the laser pulse energy without changing the beam profile. 57
Fig. 3.4 Schematic of the optical signal intensity vs. elapsed time after the pulse from the laser. It can be seen that during the first ~10 ns the optical signal intensity rises sharply before relaxing over time as the plasma evolves. Also shown are the laser pulse duration and detector gate width tg, which is delayed by some time td with respect to the laser pulse. Recreated from [4]. 59
Fig. 3.5 Schematic of the Andor™ image intensifier. An incoming photon strikes the photocathode which emits an electron. The electron is accelerated down one of the MCP channels, colliding with the sidewalls, creating secondary electrons, as it does so. Thus a weak optical image, focused onto the photocathode, results in a bright electron replica at the output of the MCP. The electron image strikes the phosphor to form a corresponding bright optical image which is focused onto the camera CCD sensor. The number of secondary electrons emitted can be varied by controlling the applied voltage on the MCP allowing control of the gain. Image recreated from [3]. 60
Fig. 3.6 Schematic view of an MCP Single Channel amplification process. As an incoming electron $e-$ cascades down the channel it produces a series of secondary electrons via impact ionisation. Recreated from [3]. 60
Fig. 3.7 Gain calibration curves for A) Andor™ DH5H7 ICCD and B) Andor™ iStar sCMOS cameras of recorded HeNe 632.8 nm over a range of gain settings. 61
Fig. 3.8 Schematic of the Andor Technologies™ Kymera 328i spectrograph. The Kymera 328i uses a Czerny-Turner layout and has a focal length of 328 mm and a numerical aperture of f/4.1. 63
Fig. 3.9 Comparison of Ocean Optics™ Deuterium-Halogen lamp calibration file with experimental data recorded with Grating 2 (300 lines/mm) for relative intensity correction. 64
Fig. 3.10 A) Schematic of the target design, 30°, 60°, and 90° V-channels and a 180° flat target. B) Schematic of incident laser impinging on the two walls of a V-channel. C) Design for the actual target wheel used in

the experiments shown in this work. D) Plasma observation direction with relation to target wheel...65

Fig. 3.11 Schematic of the optical delivery system used in the imaging and spectroscopy experiments for colliding laser plasmas in air 66

Fig. 3.12 Schematic of the fast-imaging experimental setup along with corresponding photographs from the laboratory. The filter wheel shown in the dashed box was removed when undertaking broadband imaging. 68

Fig. 3.13 A) Schematic of the lens relay system. The object is placed at a distance equal to the focal length of lens 1 ($f1$) and the image will be formed at a distance equal to the focal length of lens 2 ($f2$). The magnification of the system will be approximately in the ratio $f2/f1$. B) Backlit sample image of a pin in the 60° V-channel. C) Backlit sample image of a clear ruler and pin. 68

Fig. 3.14 A) Binned data of millimetre ruler spacings from backlit image. B) Plots of the pixel number vs. line spacings to extract number of pixels per millimetre for spatial calibration. 69

Fig. 3.15 Transmission curves for narrow bandpass filters used in the filtered imaging of A) Al 394.4 nm & 396.15 nm lines, B) A^{l+} 466.3 nm line, and C) Al^{2+} 569.6 nm line. 70

Fig. 3.16 Schematic of the optical emission spectroscopy experimental setup along with corresponding photographs from the laboratory. The dove prism shown in the dashed box was added/removed as needed. 72

Fig. 3.17 Function of the dove prism. With the dove prism present the image of the plasma is rotated 90° so that the plasma expansion is directed along the entrance slit of the spectrograph. 72

Fig. 3.18 A) Timing and synchronisation system for the laser plasma experiments undertaken B) Corresponding timing diagram. Δt, the time delay between the triggering of the laser Q-Switch and the ICCD is swept throughout the experiment to obtain time resolved plasma images. 74

Fig. 4.1 Schematic diagram of the two methods investigated for colliding laser plasmas in air, along with two sample images recorded $500\,ns$ after the incident laser showing the expansion of the plasma at that time. The gatewidth was $10\,ns$. A) Typical method used in previous work in vacuo for splitting the incoming laser to form two discrete seed plasmas on the V-channel walls. B) Method investigated here which uses a soft focus of the incoming laser to encompass the two walls of the V-channel, forming two seed plasmas with close to zero separation. 78

Fig. 4.2 Crater images of A) Flat, B) 30° V-channel, C) 60° V-channel, and D) 90° V-channels viewed under a microscope with a magnification of 42.39×. The spot sizes were measured to be on the order of 200 μm along with some melting visible around the craters. E) Indication of crater position in targets 79

Fig. 4.3 ICCD images of the initial plasma with the plasma front and primary plasma components indicated. Images are from the flat Al target at A) 40 ns and B) 100 ns... 82

Fig. 4.4 Sample images of the evolution of a laser plasma created on the Flat target. The broadband images have been normalised at each time-step across all targets for ease of comparison. The ICCD gatewidth was 10 ns. 83

Fig. 4.5 The luminous plume expansion of a laser plasma in air from a flat target. 84

Fig. 4.6 The luminous plume expansion of a laser plasma in air from the A) 90° B) 60° C) 30° V-channel targets. 85

Fig. 4.7 Sample images of the evolution of a laser plasma created on the V-channel targets at $60\,ns$ and $100\,ns$. The broadband images have been normalised at each time-step across all targets for ease of comparison. The ICCD gatewidth was 10 ns. 87

Fig. 4.8 Sample images of the evolution of a laser plasma created on the V-channel targets at $160\,ns$ and $250\,ns$. The broadband images have been normalised at each time-step across all targets for ease of comparison. The ICCD gatewidth was 10 ns. 88

Fig. 4.9 Sample images of the evolution of a laser plasma created on the V-channel targets at $500\,ns$ and $1000\,ns$. The broadband images have been normalised at each time-step across all targets for ease of comparison. The ICCD gatewidth was 10 ns. 89

Fig. 4.10 ICCD images of the plasma with the lobe plasma and stationary plasma components indicated. Images are from the 90° V-channel Al target at A) 250 ns and B) 1000 ns. 90

Fig. 4.11 Fits to the luminous expansion data for the A)90° and B) 30° V-channel targets. Point explosion models were fitted to the plasma front (PE Front) and primary plasma (PE Primary) for the early delay times while the drag force model (DF) was fitted at later time delays. 92

Fig. 4.12 Fits to the luminous expansion data for the A)Flat and B) 60° V-channel targets. Point explosion models were fitted to the plasma front (PE Front) and primary plasma (PE Primary) for the early delay times while the drag force model (DF) was fitted at later time delays. The circled data point in the flat target data is determined to be an outlier and hence was omitted from the corresponding fits. 93

Fig. 4.13 Broadband images of the expanding plasma 60 ns after the arrival of the laser pulse on target for the four different targets. Image intensities are normalised with correction factors show bottom left where required. 94

Fig. 4.14 Broadband images of the expanding plasma 160 ns after the laser pulse arrived at the target for the four different targets. Image intensities are normalised with correction factors show bottom left where required. 96

Fig. 4.15 Broadband images of the expanding plasma 1000 ns after the laser pulse arrived at the target for the four different targets. Image intensities are normalised with correction factors show bottom left where required. 98

Fig. 4.16 Broadband images of the expanding plasma 2000 ns after the laser pulse began for the four different targets. Image intensities are normalised with correction factors show bottom left where required. 99

Fig. 4.17 Spectrally filtered images of the flat target showing the different distributions of the Al, Al^+, and Al^{2+} species as the plasma evolves. 101

Fig. 4.18 Spectrally filtered images of the 90° V-channel target showing the different distributions of the Al, Al^+, and Al^{2+} species as the plasma evolves. 103

Fig. 4.19 Spectrally filtered images of the 60^{O} V-channel target showing the different distributions of the Al, Al+, and Al2+ species as the plasma evolves. 104
Fig. 4.20 Spectrally filtered images of the 30^{O} V-channel target showing the different distributions of the Al, Al^{+}, and Al^{2+} species as the plasma evolves. 105
Fig. 4.21 Sample images showing the presence of the bright spots from forced recombination in A) Broadband fast imaging and B) Filtered Al Neutral fast imaging 107
Fig. 5.1 Slit positions for spectroscopic measurements on plasmas formed on the different targets along the X- and Y-directions. 114
Fig. 5.2 Time resolved optical emission spectra of the 90^{o} V-channel target in the wavelength range 320 nm – 480 nm with slit positioned in Y-direction. Lines have been tagged with their corresponding elements for reference. 116
Fig. 5.3 Sample spectra from X-direction of $Al0\ 394.4\,nm$ and $396.15\,nm$ doublet for the A) 60^{o} V-channel and C) Flat targets at a time delay of $500\,ns$. B) and D) show corresponding $Al0$ filtered images, while E) and F) the spatial profiles of the emission lines within the spectra to aid comparison. 118
Fig. 5.4 Time resolved spatial distributions of the $Al0\ 396.15\,nm$ and $Al+\ 358.7\,nm$ line emission along the Y-direction for the Flat and 90^{o} V-channel targets. 120
Fig. 5.5 Time resolved spatial distributions of the $Al0\ 396.15\,nm$ and $Al+\ 358.7\,nm$ line emission along the Y-direction for the 60^{o} and 30^{o} V-channel targets. 123
Fig. 5.6 Bin positions along the Y-direction where each bin corresponds to a height of 0.5 mm to provide reasonable space resolution. Sample spectra in the figure are for the 90^{o}V-channel target at 250 ns. 125
Fig. 5.7 Aluminium doublet spectrum with corresponding Voigt peak fits using Origin. From the fit parameters integrated line intensities and Stark broadened FWHM values could be obtained........................ 126
Fig. 5.8 Comparison of the measured spatio-temporal electron densities for the different targets along the Y-direction. 128

Fig. 5.9 Electron densities of the different targets along the Y-direction at time delays of A) $1000\,ns$ and B) $2000\,ns$ 129
Fig. 5.10 Comparison of the measured spatio-temporal electron densities for the different targets along the X-direction. 130
Fig. 5.11 Measured spatio-temporal electron temperatures for the different targets along the Y-direction. 132
Fig. 5.12 Time position maps along the Y-direction for $Al0$ collisional ionisation rates ($Al0 \rightarrow Al+$) for the various targets. Rates are shown as $\log_{10}$ values to preserve contrast. 134
Fig. 5.13 Time position maps along the Y-direction for $Al+$ radiative recombination rates ($Al+ \rightarrow Al0$) for the various targets. Rates are shown as $\log_{10}$ values to preserve contrast. 134
Fig. 5.14 Comparison of the various ionisation and recombination rates ($Al0 \leftrightarrow Al+$) as a function of time for the different targets. Data points obtained by integrating over the range $0.0 - 0.5\,mm$ along the Y-direction. 135
Fig. 5.15 Time position maps along the Y-direction for $Al+$ three-body recombination rates ($Al+ \rightarrow Al0$) for the various target. Rates are shown as $\log_{10}$ values to preserve contrast. 135
Fig. 5.16 Comparison of spatially integrated line intensity as a ratio of the V-channel target values to the flat target emission intensity for A) $Al+\ 358.7\,nm$ and B) $Al\,396.15\,nm$ lines as a function of time delay. . 138
Fig. 5.17 Integrated intensities of A) Al^+ 358 nm line and B) Al 396 nm line. Intensities are integrated via the trapezoidal method over 100 – 2000 ns to give a more accurate depiction of the total emission..... 140
Fig. 5.18 Integrated line intensities for the various targets showing comparisons with the flat target. The percentage difference for the V-channel targets with respect to the flat target are included for ease of comparison. 141
Fig. 5.19 Comparison of signal to background ratios of the V-channel targets with the flat target as a function of time for the A) $Al+\ 358.7\,nm$ and B) $Al\,396.15\,nm$ lines. 143
Fig. 6.1 Interferograms and their corresponding Fourier transforms. a) A single wavelength source and sharp peak spectrum. b) A dual wavelength source resulting in a spectrum with two sharp peaks. c) A

broadband source with it’s corresponding continuum or band spectrum. Recreated from [9] 148
Fig. 6.2 Schematic diagram of a Wollaston prism I. Unpolarised light enters the Wollaston prism and splits into two orthogonal polarisation components. Each of the components experiences two instances of refraction, one at the interface of the two wedges and the second when exiting the prism into the air 150
Fig. 6.3 Schematic diagram of a Wollaston prism II. In the centre of the Wollaston prism the optical path lengths within each prism are equal and there is no net phase shift between the ordinary and extraordinary rays. However, if you move a finite distance D away from the centre the optical path length of one prism becomes larger (d2>d1) and an optical path difference (and hence phase shift) between the prisms will be introduced. 151
Fig. 6.4 Photo and corresponding schematic of the prototype WPFT spectrometer in the linear achromat based configuration. The system is housed in a Thorlabs™ 30 mm cage system with one-inch optics making the system compact and rugged. 153
Fig. 6.5 A) Sample section taken from a Sodium (Na) discharge lamp interferogram recorded using the prototype WPFT spectrometer and the Point Grey FLEA®3 FL3-U3-88S2C-C machine vision camera. B) Sample section of the corresponding 1-D intensity plot. 154
Fig. 6.6 A) A raw Mercury (Hg) interferogram, with corresponding baseline calculated using a moving average. B) The baseline corrected Mercury interferogram which is now flat and centred about zero. ... 155
Fig. 6.7 Sample Sodium (Na) discharge lamp spectrum. As the two Na-D lines are separated by only a fraction of 1 nm, they are not resolved here, nor indeed are they by grating based compact spectrometers with similar spectral coverage and size. 156
Fig. 6.8 The JAI™ CM-140GE-UV Machine vision camera. This camera is equipped with a UV sensitive Sony ICX407BLA sensor with 4.65μm square pixels and a horizontal by vertical pixel count of 1340(H) × 1040(V). B) The JAI™ CM-140GE-UV Relative Sensitivity vs. Wavelength graph is ßtaken from [6]. 158

Fig. 6.9 A) The α-BBO Wollaston prism; the Wollaston prism was manufactured by United Crystals with a wedge angle of 4.3 degrees. It has dimensions of 15 mm × 15 mm and is housed in a one-inch optical mount. B) Theoretical number of fringe pairs created vs. wavelength for an α -BBO 15 mm × 15 mm prism. The region formed between the two lines is determined by the desired resolution and the limitations of the camera resolution. It determined a Wedge angle of ~4.3 degrees was the optimal wedge angle for the system. 160

Fig. 6.10 Transmission vs. Wavelength & Contrast Ratio vs. Wavelength data for the Edmund Optics broadband polarisers, Part#89-602 Taken from [8] 161

Fig. 6.11 Spectrum of a Mercury gas (Hg) bulb with its corresponding interferogram inset. The mercury spectrum is dominated by the $546.1\ nm$ emission line. This line also dominates the interferogram, and the remaining emission lines contribute to the beating observed in the interferogram 163

Fig. 6.12 Resolution test data; various interferograms were created using sets of sine waves while the number of fringe pairs was varied from 200-1000. For each interferogram the sampling frequency was varied from 4 to 8 pixels per fringe pair 164

Fig. 6.13 Set up of the signal to noise comparison; a Na gas discharge bulb is placed $1.1\ m$ from an attenuator and spectrometer the attenuator is used to lower the source intensity and the signal is recorded for comparison 165

Fig. 6.14 Sample stand-off spectra of a Na discharge bulb $\sim 1.1\ m$ from A) the prototype spectrometer and B) the Stellarnet® EPP2000. The prototype was seen to exhibit a far greater SNR. 166

Fig. 6.15 SNR vs. Attenuator Transmission graph. The graph shows the linear response of the two spectrometers as the signal was attenuated. The prototype spectrometer averaged a five times improvement in SNR over the Stellarnet®. 166

Fig. 6.16 Schematic of the experimental system used for the LIBS experiments along with images of the experimental set up from the lab. 168

Fig. 6.17 Sample spectra of laser produced plasmas of A) Aluminium, B) Copper, C) 1.2% Manganese in Steel. Spectra were all recorded in air at atmospheric pressure. 169
Fig. 6.18 Region of interest form the Manganese in Steel spectra part of the LIBS experiment for the A) prototype spectrometer and B) Stellarnet® EPP2000. Spectra were normalised to the $Fe\ 495.8\ nm$ line. 170
Fig. 7.1 Example spectrum from a stagnation layer formed from dissimilar targets. By colliding plasma formed form dissimilar targets spectroscopy can be used to verify that the different species indeed stop at the collision plane of the stagnation layer 178

List of Tables

Table 2.1 Summary of the main atomic processes in laser produced plasmas 16
Table 3.1 Specification of the Spectron™ SL803 Laser System 55
Table 3.2 Grating specifications for the Andor Technologies™ Kymera 328i spectrometer. Window size and FWHM linewidths were obtained experimentally using Cd & Hg gas discharge lamps. 63
Table 4.1 Fitting parameters obtained by fits to the point explosion model for the plasma front. R^2 is the corresponding correlation coefficient from the fit. 91
Table 4.2 Comparison of average velocities for the initial expansion $0-60\,ns$ of the different target geometries. 93
Table 4.3 Fitting parameters obtained by fits to the point explosion model for the primary plasma. *Indicates that the value was forced to this value by the boundaries set in the fitting. R^2 is the corresponding correlation coefficient from the fit. 94
Table 4.4 Comparison plasma widths at 160 ns of the different target geometries. 95
Table 4.5 Parameters obtained by fits to the drag force model for times $\geq 600\,ns$. R^2 is the corresponding correlation coefficient from the fit. .. 97
Table 5.1 Electron impact parameter w values for the spectral lines of interest 127
Table 5.2 Transition probability constants for the spectral lines of interest. 127
Table 5.3 Time delays at which the emission of the V-channel targets fall below the flat target emission for the $Al+\ 358.7\,nm$ ($tAl+$), and $Al0\ 396.15\,nm$ ($tAl0$) lines 139

List of Abbreviations

α-BBO	Alpha Barium Borate (birefringent crystal material)
CE	Coronal Equilibrium
CMOS	Complimentary Metal-Oxide Semiconductor
CRE	Collisional Radiative Equilibrium
CTE	Complete state of Thermodynamic Equilibrium
DF	Drag Force (model)
EUV	Extreme Ultraviolet (wavelength range)
FFT	Fast Fourier Transform
FT	Fourier Transform
FWHM	Full Width at Half Maximum
ICCD	Intensified Charged Coupled Device
LA-ICP-MS	Laser Ablated Inductively Coupled Plasma Mass Spectroscopy
LIBS	Laser Induced Breakdown Spectroscopy
LIF	Laser Induced Fluorescence
LOD	Limit of Detection
LSC	Laser Supported Combustion
LSD	Laser Supported Detonation
LSR	Laser Supported Radiation
LTE	Local Thermodynamic Equilibrium
MCP	Micro-Channel Plates
MFP	Mean Free Path
Nd:YAG	Yttrium Aluminium Garnet doped with Neodymium
NIST	National Institute of Standards and Technology
OA	Optic Axis
OES	Optical Emission Spectroscopy
OPD	Optical Path Difference
PE	Point Explosion (model)
PLD	Pulsed Laser Deposition

SBR	Signal to Background Ratio
SNR	Signal to Noise Ratio
TTL	Time-To-Live
UV-VIS	Ultraviolet to Visible (wavelength range)
WPFT	Wollaston Prism Fourier Transform (spectrometer)

Abstract

Stephen J. Davitt

Colliding Plasmas in Air

When two, or more, laser produced plasma plumes are forced to collide there are two extremes in the resulting outcome, (i) the plasmas may interpenetrate, or, (ii) a layer of stagnated plasma is formed at the collision front. The degree of interpenetration (or stagnation) is determined by the so-called 'collisionality parameter' which is the ratio of the separation of the individual 'seed' plasmas to the ion-ion mean-free path. Previous work on colliding plasmas *in vacuo* show that when 'stagnation layers' are formed, they exhibit an enhancement in plasma emission duration and a reasonably uniform spatial distribution of electron density, electron temperature and atomic/ionic density. These characteristics have made stagnation layers of interest to the laser plasma community, however to date research has been almost exclusively *in vacuo*.

This work concerns experimental efforts to produce similar conditions for plasmas formed on solid targets in air at atmospheric pressure. This was realised by creating plasmas on the walls of V-shaped aluminium targets irradiated by a single, defocused laser pulse. Channels of varying vertex angles (namely, 30°, 60°, 90°) were employed to alter the relative collisional velocity of the expanding plumes and thus the collisionality parameter. The formation and evolution of the plasmas were tracked using time resolved imaging and spectroscopy. It was observed that the confined plasma plumes exhibited three distinct phases. For early time delays (<100 ns) they were similar to plasmas formed on flat targets with a rapidly expanding plasma front that separates from the primary plasma located close to the target vertex. At later times the primary plasma splits into two components, a stationary or stagnated plasma remaining close to the target vertex and a lobe-like plume. The stationary or stagnated plasmas exhibited some of the characteristics of stagnation layers in that they were formed at the collision plane, showed little sign of expansion, and exhibited reasonable spatial uniformity and slower rates of decay for various key plasma parameters. Furthermore line emission from plasmas formed within the V-channel targets had enhancements of intensity upwards of 20% over that of a single plume formed from a flat target.

Additionally, a compact, single shot, Fourier Transform Spectrometer was developed for recording weak spectral lines from laser produced plasmas and other pulsed sources. Details of the spectrometer design and its performance are also given in the thesis.

1 Introduction

1.1 Laser Produced Plasmas & LIBS

Laser produced (or induced or generated) plasmas have been of considerable interest since the invention of high powered lasers in the 1960s [1,2]. Research on laser plasmas is far reaching and comprises both fundamental and translational domains with applications such as pulsed laser deposition (PLD) [3], EUV sources for lithography [4], electron/ion beam generation [5], analytical spectroscopy [6], and quantitative analysis of samples [7] to name but a few.

Laser plasmas are formed when a surface is irradiated by laser light focussed to a high intensity. In this case material is ablated from the target to form a dilute vapour. If the intensity of the laser pulse is sufficiently high the vapour can be excited and ionised, thus forming a plasma. The properties of a laser plasma depend on many variables including the irradiance (W/cm^{-2}), laser wavelength [8], pulse duration, focussed spot size, target material and target geometry. During the lifetime of the laser plasma in the ablated plume, which consists of excited atoms and ions, various atomic processes occur and some of these atomic processes result in characteristic line emission from the atoms and ions present.

Laser induced breakdown spectroscopy or ‘LIBS’, is one of the analytical spectroscopy techniques that utilises this emitted line radiation from laser plasmas. The wavelengths present in the plasma emission spectrum allow the elemental composition of the target sample, on which the plasma was formed, to be determined. It is this analysis that makes LIBS somewhat unique: it is a contactless technique that can provide analysis of any material [9,10]. Due to the simplicity and relatively low-cost of a LIBS system, and also its capability to yield rapid in-situ analysis of a variety of samples, LIBS has become a widely used analytical technique even over more sensitive well-established techniques [10].

Typically one of the stated advantages of LIBS is that it does not require any sample preparation as a laser plasma can be formed on or in any material in any phase, be it solid, liquid or gas. However as the technique has matured, it is becoming increasingly more common for the sample to undergo some simple preparation. This has resulted in an improvement of performance and detection limits of LIBS [11] while offering more practical methods for some samples to be measured (in particular liquids). Jantzi *et al.* review some of the various sample preparation techniques used in LIBS [11], which include techniques such as compression of powders/loose materials into pellets [12], dehydration of solutions into films [12], suspension of liquids in gels [13], polishing of the target surface [14], and creation of target channels [15]. It is this latter type of sample preparation that was employed for the laser plasma studies which are the basis of this thesis.

As LIBS has matured, in addition to sample preparation many other methods and techniques have been developed with the aim to improve the performance of LIBS. Many of these techniques are discussed in the comprehensive LIBS review by Hahn and Omenetto [16], and include double-pulse LIBS [17], resonantly-enhanced LIBS [18], and magnetically confined LIBS [19]. LIBS is also being combined with a variety of other techniques such as Raman, fluorescence etc. Finally there is the method that this work is concerned with: colliding plasmas, in particular for the formation of stagnation layers [20] which are introduced briefly in the next section.

1.2 Colliding Plasmas and Stagnation Layers

The study of collisions between individual plasma plumes has been a distinct sub-field of laser plasmas since the mid-1970s, again covering both fundamental physics and some potential applications. The physical interactions and collisions between two (or more) plasmas can be used as a laboratory scale model of astrophysical phenomena [21], the design of indirect drive inertial confinement fusion hohlraums [22], the formation of molecules [23–25] and the formation of nanoparticles [26].

A stagnation layer is the result of colliding plasmas that, under certain conditions, as outlined by Rambo and Denavit and expressed in the form of a ‘collisionality parameter’ [27] (discussed in section 2.5), can decelerate abruptly at the plane where the two plasmas collided. This abrupt deceleration creates a build-up of material at this collision plane which can compress into a stagnation layer [28]. Stagnation layers formed *in vacuo* have been shown to yield an increase in the duration of emission compared to the case of a single plasma plume [29], a more uniform spatial distribution of atoms and ions [30] and in some cases an enhancement of intensity of line emission [23,31]. Since the properties of a stagnation layer depend on the collisionality parameter which in turn is dependent on the target geometry and also the parameters of the laser plasmas used in its formation (i.e., the seed plasmas) it is possible to have a degree of control over the layer. It has been shown that by controlling the properties of the seed plasmas the stagnation layer can effectively be tuned for shape, ionization balance, electron temperature and electron density [32,33]. Work by Delaney and Kelly [34], has shown that stagnation layers can lead to an enhancement in the limit of detection achievable for trace elements in Aluminium and Steel. Research to date on stagnation layers and colliding plasmas has been predominantly *in vacuo,* however there have been some efforts into investigating colliding plasmas in ambient air.

1.3 Colliding Plasmas in Ambient Air

Investigations of colliding plasmas in ambient air are still limited in number. Two studies can be highlighted as examples of the current research on this topic, namely Zhang *et al.* [35] and Yang *et al.* [36], however other work by Sánchez-Aké [37] and Bukin [38] are also worth noting.

In the experimental work by Zhang *et al.* [35] the seed plasmas are formed by tilting the laser focusing lens focus to create spherical aberration. This tended to break up the initial focus into a ‘multi-microfocus’ in air, specifically in Zhang et al, two major foci which formed two air plasmas along the optical axis of the focused laser beam. During expansion, the two air plasma plumes collided. Interferometry was used to track the shockwaves generated by the two seed (air) plasmas, and the phase shift observed within the interferograms was used to determine the electron density distribution within for this colliding air plasma system. Two regions of high electron density were observed, the first in the vicinity of the air plasma breakdown which was closest to the incident laser. This was attributed to plasma shielding (concept discussed in chapter 0). Zhang *et al.* stated that the second region was due to the formation of a stagnation layer. However they state that due to the plasmas being created in ambient air, it is the fast-moving shockwaves that collide. This results in a region of high air density in the wake of the shock waves which creates the appearance of an 'air stagnation layer'. It's an interesting study but clearly the technique would not give rise to the plethora of potential applications that stagnation layers formed from the colliding plasma plumes from a whole host of liquid and solid materials could have.

Work on colliding plasmas in air from Yang *et al.* [36] however was more typical of the work carried out in vacuo. In this case a pair of plasmas were formed on a flat aluminium slab target and allowed to expand. Again, interferometry was deployed to track the expanding shock wave and provide electron density distributions for the seed plasmas and the collision plane. This was supplemented with tracking the expanding shockwaves through techniques of Schlieren imaging and Shadowgraphy. Similar results to Zhang *et al.* are reported with a compression of the air between the shockwaves which resulted in a build-up of electron density as shown in Fig. 1.1 taken from reference [36]. At a distance of $1.45\ mm$ an increase in refractive index ($n = 1.006$) is visible indicating an electron density of $\sim 5 \times 10^{20}\ cm^{-3}$, almost double that of the gas behind the shock waves. Yang *et al.* attribute this to the formation of a stagnation layer of air. They do however, also claim

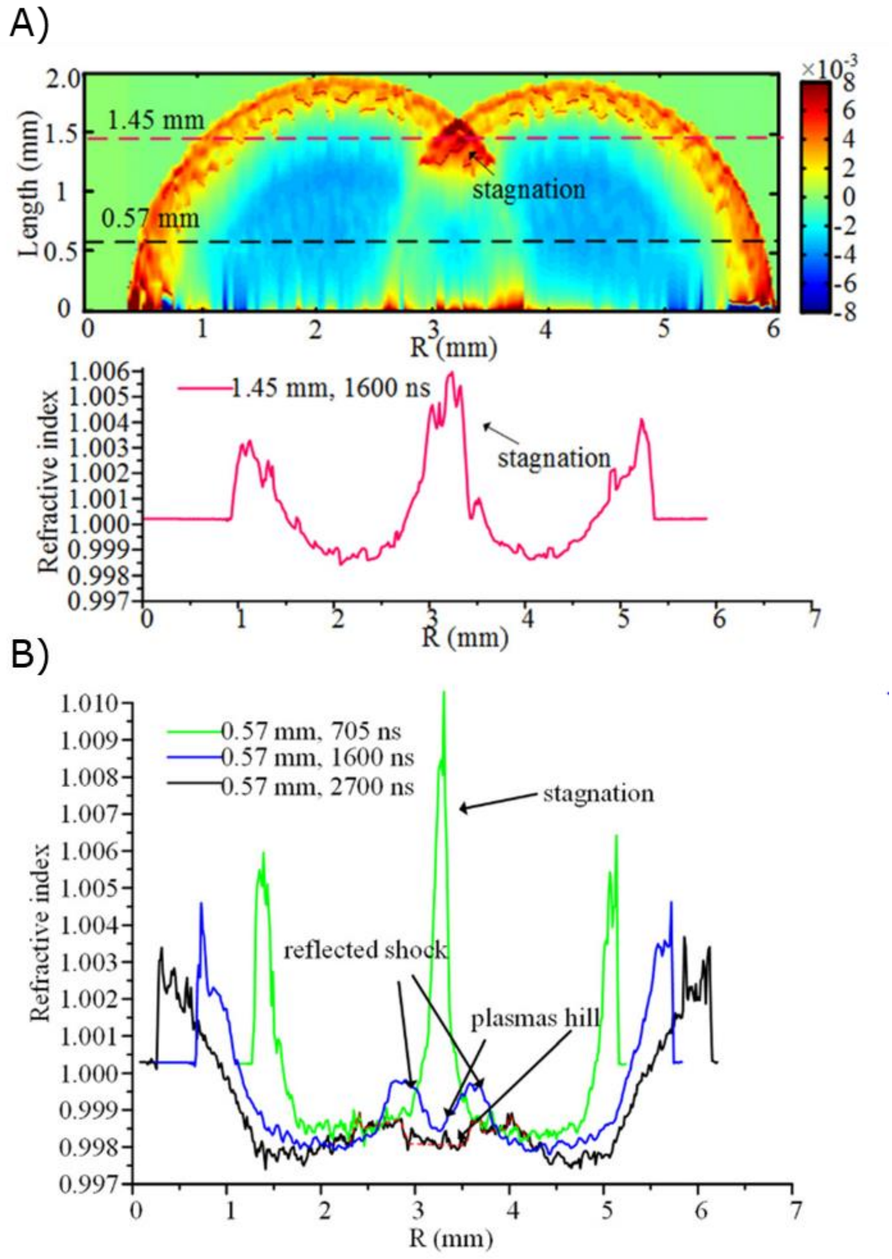

Fig. 1.1 Taken from [36]. A) 2D relative refractive index profile at $1600\ ns$. Below graph shows a lineout of the refractive index at $1.45\ mm$. B) Refractive index at $0.57\ mm$ for various time delays. Reflected shocks and plasmas hill can be seen.

to observe the formation of a soft stagnation layer closer to the target ($0.57\ mm$) formed by ablated material from the target. This is designated as a 'plasmas hill' in Fig. 1.1B at time delays of $1600\ ns$ and $2700\ ns$. They claim that as the stagnating air moves up and away from the target, the dissipated stagnation area was filled with free electrons near the target surface, hence indicating the expansion and collision of the two seed plasmas from the target material. This claim is somewhat questionable since the overall signal level in the ‘hill’ region is not much greater than the background fluctuation.

In summary work done to date is interesting but it has not been definitively shown that a stagnation layer, or plasma region exhibiting the beneficial stagnation layer properties, comparable to those observed in the *in vacuo* experiments, has been formed.

1.4 Fourier transform spectrometer for LIBS

Work was also carried out on the development of a compact single shot Wollaston prism Fourier transform spectrometer for LIBS. The motivation was to develop a spectrometer with a small footprint, an increased signal to noise ratio and high throughput for applications where weak spectral signals occur and also as an alternative to compact grating-based spectrometers for portable LIBS. This was realised through a Fourier transform spectrometer based on a design by Harvey and Padgett [39,40]. The Fourier transform spectrometer, by inherent design, does not require an entrance slit which limits the throughput of grating-based spectrometers.

1.5 Thesis Outline

This thesis is divided into seven chapters and a brief overview of each various chapter is presented below.

Chapter One presents the motivation for the work along with a brief introduction to the fields of LIBS and colliding plasmas.

Chapter Two discusses the theoretical background required for the analysis and discussion of the experimental results, including basic laser plasma theory, the main atomic processes occurring in plasmas, plasma equilibrium models and the line broadening mechanisms of the plasma atomic emission.

Chapter Three details the main experimental systems and set-ups used in this work, providing specifications and capabilities of the different apparatus used for the experiments on colliding plasmas in air.

Chapter Four presents results of the formation, evolution, and dynamics of the laser plasmas for the different target geometries through time-resolved imaging, both broadband and spectrally filtered.

Chapter Five outlines the results from the space and time-resolved optical emission spectroscopy for plasma diagnostics, specifically electron densities and temperatures for the different target geometries. The application of an ionization model to help interpret the results is discussed here also.

Chapter Six details work undertaken on the development of a compact single shot Wollaston prism Fourier transform spectrometer for low light level applications, including cases in LIBS where the spectral features are weak. The chapter is largely self-contained with basic theory, experimental set ups, and construction of the prototype spectrometer all discussed along with results from initial testing and use in a LIBS experiment.

Chapter Seven summarises the results presented in the thesis along with an outlook and suggestions for possible future work.

References

1. Eliezer S. The Interaction Of High-Power Lasers With Plasmas. London: Institute of Physics Publishing; 2002.

2. Cremers DA, Radziemski LJ. Handbook of Laser-Induced Breakdown Spectroscopy, Second Edition. Chichester: John Wiley & Sons, Incorporated; 2013. 432 p.

3. Smith HM, Turner AF. Vacuum Deposited Thin Films Using a Ruby Laser. Appl Opt [Internet]. 1965;4(1):147. Available from: https://www.osapublishing.org/abstract.cfm?URI=ao-4-1-147

4. Otsuka T, Kilbane D, White J, Higashiguchi T, Yugami N, Yatagai T, et al. Rare-earth plasma extreme ultraviolet sources at 6.5-6.7 nm. Appl Phys Lett. 2010;97(11).

5. Gu YJ, Zhu Z, Li XF, Yu Q, Huang S, Zhang F, et al. Stable long range proton acceleration driven by intense laser pulse with underdense plasmas. Phys Plasmas. 2014;21(6).

6. Khater MA, Van Kampen P, Costello JT, Mosnier JP, Kennedy ET. Time-integrated laser-induced plasma spectroscopy in the vacuum ultraviolet for the quantitative elemental characterization of steel alloys. J Phys D Appl Phys. 2000;33(18):2252–62.

7. Zhang W, Hu Z, Liu Y, Yang W, Chen H, Hu S, et al. Quantitative analysis of major and trace elements in NH4HF2-modified silicate rock powders by laser ablation - inductively coupled plasma mass spectrometry. Anal Chim Acta [Internet]. 2017;983:149–59. Available from: http://dx.doi.org/10.1016/j.aca.2017.06.039

8. Colombant D, Tonon GF. X-ray emission in laser-produced plasmas. J Appl Phys. 1973;44(8):3524–37.

9. Aragón C, Aguilera JA. Characterization of laser induced plasmas by optical emission spectroscopy: A review of experiments and methods. Spectrochim Acta - Part B At Spectrosc. 2008;63(9):893–916.

10. Cristoforetti G, Lorenzetti G, Legnaioli S, Palleschi V. Investigation on the role of air in the dynamical evolution and thermodynamic state of a laser-induced aluminium plasma by spatial- and time-resolved spectroscopy. Spectrochim Acta - Part B At Spectrosc. 2010;65(9–10):787–96.

11. Jantzi SC, Motto-Ros V, Trichard F, Markushin Y, Melikechi N, De Giacomo A. Sample treatment and preparation for laser-induced breakdown spectroscopy. Spectrochim Acta - Part B At Spectrosc [Internet]. 2016;115(January 2016):52–63. Available from: http://dx.doi.org/10.1016/j.sab.2015.11.002

12. Zheng L, Niu S, Khan AQ, Yuan S, Yu J, Zeng H. Comparative study of the matrix effect in Cl analysis with laser-induced breakdown spectroscopy in a pellet or in a dried solution layer on a metallic target. Spectrochim Acta - Part B At Spectrosc [Internet]. 2016;118:66–71. Available from: http://dx.doi.org/10.1016/j.sab.2016.02.007

13. Moncayo S, Rosales JD, Izquierdo-Hornillos R, Anzano J, Caceres JO. Classification of red wine based on its protected designation of origin (PDO) using Laser-induced Breakdown Spectroscopy (LIBS). Talanta [Internet]. 2016;158:185–91. Available from: http://dx.doi.org/10.1016/j.talanta.2016.05.059

14. Cabalín LM, Romero D, Baena JM, Laserna JJ. Effect of Surface Topography in the Characterization of Stainless Steel Using Laser-induced Breakdown Spectrometry. Surf Interface Anal. 1999;27(January):805–10.

15. Fallon C, Hayden P, Walsh N, Kennedy ET, Costello JT. Target geometrical effects on the stagnation layer formed by colliding a pair of laser produced copper plasmas. Phys Plasmas. 2015;22(9).

16. Hahn DW, Omenetto N. Laser-induced breakdown spectroscopy (LIBS), part II: Review of instrumental and methodological approaches to material analysis and applications to different fields. Appl Spectrosc. 2012;66(4):347–419.

17. Uebbing J, BRUST J, SDORRA W, Leis F, Niemax K. Reheating of a Laser-Produced Plasma By a 2Nd Pulse Laser. Appl Spectrosc [Internet]. 1991;45(9):1419–23. Available from: isi:A1991GR64600006

18. Goueguel C, Laville S, Vidal F, Chaker M, Sabsabi M. Resonant laser-induced breakdown spectroscopy for analysis of lead traces in copper alloys. J Anal At Spectrom. 2011;26(12):2452–60.

19. Shen XK, Lu YF, Gebre T, Ling H, Han YX. Optical emission in magnetically confined laser-induced breakdown spectroscopy. J Appl Phys. 2006;100(5).

20. Fallon C, Hayden P, Walsh N, Kennedy ET, Costello JT. The effect of wedge angle on the evolution of a stagnation layer in a colliding plasma experiment. J Phys Conf Ser. 2014;548(1).

21. Gregory CD, Howe J, Loupias B, Myers S, Notley MM, Sakawa Y, et al. Astrophysical Jet Experiments with Colliding Laser-produced Plasmas. Astrophys J [Internet]. 2008;676(1):420–6. Available from: http://stacks.iop.org/0004-637X/676/i=1/a=420

22. Vick D, Kado M, Yamamoto H, Nishiguchi A, Tanaka KA, Mima K, et al. Hydrodynamics of collisional structures in laser-produced plasmas. Phys Rev E. 1993;48(3):2308–12.

23. Al-Shboul KF, Hassan SM, Harilal SS. Molecular formation in the stagnation region of colliding laser-produced plasmas. Plasma Sources Sci Technol. 2016;25(6).

24. Sizyuk T, Oliver J, Diwakar PK. Mechanisms of carbon dimer formation in colliding laser-produced carbon plasmas. J Appl Phys. 2017;122(2).

25. Al-Shboul KF, Harilal SS, Hassan SM, Hassanein A, Costello JT, Yabuuchi T, et al. Interpenetration and stagnation in colliding laser plasmas. Phys Plasmas. 2014;21(1).

26. Gupta SL, Thareja RK. Photoluminescence of nanoparticles in vapor phase of colliding plasma. J Appl Phys. 2013;113(14).

27. Rambo PW, Denavit J. Interpenetration and ion separation in colliding plasmas. Phys Plasmas. 1994;1(12):4050–60.

28. Dardis J, Costello JT. Stagnation layers at the collision front between two laser-induced plasmas: A study using time-resolved imaging and spectroscopy. Spectrochim Acta - Part B At Spectrosc [Internet]. 2010;65(8):627–35. Available from: http://dx.doi.org/10.1016/j.sab.2010.03.005

29. Luna H, Kavanagh KD, Costello JT. Study of a colliding laser-produced plasma by analysis of time- and space-resolved image spectra. J Appl Phys. 2007;101(3).

30. Hough P. Laser, Optical and Electrical Diagnostics of Colliding Laser-Produced Plasma. [Ireland]: Dublin City University; 2010.

31. Harilal SS, Bindhu C V., Shevelko P, Kunze HJ. XUV diagnostics of colliding laser-produced magnesium plasmas. J Phys B At Mol Opt Phys. 2001;34(18):3717–26.

32. Cummins T, O'Gorman C, Dunne P, Sokell E, O'Sullivan G, Hayden P. Colliding laser-produced plasmas as targets for laser-generated extreme ultraviolet sources. Appl Phys Lett. 2014;105(4):1–5.

33. Hough P, Hayden P, Fallon C, Kelly TJ, McLoughin C, Yeates P, et al. Ion emission in collisions between two laser-produced plasmas. J Phys D Appl Phys. 2011;44(35).

34. Delaney B, Kelly TJ. From conversations with colleagues within the NCPST about ongoing research. Priv Commun.

35. Zhang H, Lu J, Ni X, Zhang H, Ni X. Optical interferometric analysis of colliding laser produced air plasmas Optical interferometric analysis of colliding laser produced air plasmas. 2015;063308(2009):1–6.

36. Yang Z, Wei W, Han J, Wu J, Li X, Jia S, et al. Experimental study of the behavior of two laser produced plasmas in air. 2016;073511(2015).

37. Sánchez-Aké C, Bredice F, Villagrán-Muniz M. Electric field-perturbation measurement of the interaction between two laser-induced plasmas. Rev Sci Instrum. 2012;83(2).

38. Bukin OA, Il'in AA, Kul'chin YN, Nagornyi IG, Pavlov AN, Bulanov AV. Interaction of laser plasmas upon optical breakdown in the normal atmosphere. Quantum Electron. 2006;36(6):553–6.

39. Padgett MJ, Harvey a R, Duncan a J, Sibbett W. Single-pulse, Fourier-transform spectrometer having no moving parts. Appl Opt. 1994;33(25):6035–40.

40. Harvey a. R. Stationary Fourier transform spectrometer for use as a teaching tool. Am J Phys [Internet]. 1994;62(11):1033. Available from: http://link.aip.org/link/?AJP/62/1033/1&Agg=doi

2 Theoretical Background

2.1 Plasma Definition

Plasma, often referred to as the fourth state of matter, is the name given to what is essentially an ionised gas. It is unique in that it must be created via an external source of energy and, due to interaction with our 'cold environment', it will decay unless this stimulation is sustained [1]. It is estimated that up to 99% of all matter in the universe is plasma, with stellar, interstellar and intergalactic material all including forms of plasma [2,3], along with the earth's ionosphere and the solar corona. Common day-to-day examples of plasmas include lighting, lightning, sparks, glow discharges and flames.

The definition of a plasma can be more precisely described as; a local assembly of atoms, ions, free-electrons and molecules with an overall neutral electric charge where the charged particles act collectively [4]. Equation (2.1) describes mathematically the criterion relating to overall charge neutrality, namely that the electron number density n_e is equal to the sum over all n_z, the density of ions in the charge state z [3,5].

$$n_e = \sum_z n_z z \tag{2.1}$$

However, this electrical neutrality differs significantly from that of neutral gas particles, whose interactions are both weak and short-ranged as it is due to a balance of charged particles; hence relatively strong and long-ranged Coulombic forces within the plasma exist, and this results in plasmas exhibiting their unique behaviour. Each particle can interact and hold influence over many of its neighbours resulting in what is seen as the defining 'collective response', where the charged particles within the plasma act as a collective in the presence of a perturbing force [3]. The collective response occurs over distances greater than the Coulombic force scale where the individual charged particles exhibit their influence. To understand how this response arises we need to look at the 'shielding effect' of electrons on ions in a plasma.

The shielding effect arises as electrons in the plasma will naturally tend to surround the positively charged ions while ions of like charge will tend to want to separate from each other [6]. These electron barriers electrically shield the area surrounding a charged ion. The distance at which an individual charge's influence is shielded is known as the Debye length λ_D [3,5–7]. This length in meters is expressed as:

$$\lambda_D = \left(\frac{\varepsilon_0 k_B T_e}{n_e e^2}\right)^{\frac{1}{2}} \tag{2.2}$$

where ε_0 is the permittivity of free space, k_B is the Boltzmann constant, T_e is the electron temperature of the plasma in kelvin, and e is the charge on the electron . It is only at scales when the Debye length is exceeded that the collective response of a plasma becomes of primary importance, indicating that a plasma is quasineutral; at large scales it behaves as an electrically neutral entity, while at small spatial scales, below the Debye length, effects from individual charged particles can be felt. Therefore a second characterising property of a plasma is that the plasma dimensions L should be significantly larger than the Debye length [5–7], i.e.

$$L \gg \lambda_D \tag{2.3}$$

Furthermore, it is rational to require that a threshold density of electrons is required for the shielding effect to become effective. This can be understood by invoking the concept of a Debye sphere, also referred to as the plasma parameter, where the number of electrons n_e in any given sphere with a radius equal to the Debye length should be greater than unity [3,5].

$$\frac{4}{3}\pi {\lambda_D}^3 n_e \gg 1 \tag{2.4}$$

For the plasma plumes concerned in this work where, after an expansion time of hundreds of nanoseconds, typically $n_e \approx 1.3 \times 10^{17}\ \mathrm{cm}^{-3}$ and $T_e \approx 1.5\ \mathrm{eV}$ which results in a Debye sphere with approximately 8.5 electrons, meeting this criterion.

It is also worth noting that for plasmas where the ion temperature T_i is non-zero, ions also contribute to the shielding effect, resulting in an ion Debye length λ_{Di} given by [5]:

$$\lambda_{Di} = \left(\frac{\varepsilon_0 k_B T_i}{n_i e^2}\right)^{\frac{1}{2}} \tag{2.5}$$

Possibly the most important collective response of a plasma arises from the electron oscillations within the plasma where the electrons oscillate collectively about their equilibrium positions caused following a disturbance. These oscillations are characterised by the plasma frequency denoted ω_p. This oscillatory motion is one mechanism contributing to quasineutrality [7]. When the charged particles are displaced due to the perturbation, the plasma becomes momentarily polarised [3] and the electric field created by this imposes a restoring force on each particle which results in a simple harmonic motion at the electron and ion plasma frequencies, ω_{pe} and ω_{pi} respectively [5]. Although both the electrons and ions exhibit oscillations, due to an inverse relationship with the particle mass, the heavier ions oscillate far more slowly than the electrons and hence the ions can often be assumed to be stationary [3,5]. Hence the plasma frequency can often be approximated by the electron plasma frequency only given by [5,7]:

$$\omega_p \approx \omega_{pe} = \left(\frac{n_e e^2}{m_e \varepsilon_0}\right)^{\frac{1}{2}} \qquad (2.6)$$

The plasma frequency plays a major role in the plasma response to incident radiation [3]. The dispersion relationship for an electromagnetic wave travelling through a plasma is given by [3]:

$$\omega^2 = {\omega_p}^2 + c^2 k^2 \qquad (2.7)$$

where ω is the angular frequency of the wave, c the speed of light, and k the propagation constant given by $k = {}^{2\pi}/_{\lambda}$. When the electromagnetic wave frequency is greater than the plasma frequency ($\omega > \omega_p$), k will be real and the wave propagates. If, however, the electromagnetic wave frequency is smaller than the plasma frequency ($\omega < \omega_p$), k will have an imaginary value and the wave will not propagate. In effect the plasma becomes reflective in much the way that a metal mirror becomes so due to the high density of free electrons at its surface. Plasma reflectivity is of considerable importance in the generation of laser plasmas because as reflectivity rises, the laser will begin to be shielded from the target surface. If the plasma becomes fully reflective it cannot absorb the incident photon energy. The point at which this happens is known as the critical density n_c and is given by:

$$n_c = \frac{\varepsilon_0 m_e \omega^2}{e^2} \approx \frac{10^{21}}{\lambda^2} \qquad (2.8)$$

Where ε_0 is the permittivity of free space, m_e and e the mass and charge of an electron, ω and λ the angular frequency and wavelength of the electromagnetic wave (in microns for density in cm^{-3}) [4,8].

2.2 Atomic Processes in Laser Plasmas

Many atomic processes occur in a plasma which facilitate the absorption, transport, and emission of radiation including the laser pulse used to create the plasma. Atomic processes can be placed into three main categories based on the initial and final states of the electrons involved; bound-bound, bound-free, and free-free transitions. The mechanisms by which energy transfer occurs via these processes can further be classified into radiative and collisional;

- *Collisional* - Those related to the transfer of energy between species within the plasma.
- *Radiative* - Those related to the transfer of energy between photons and species within the plasma.

There are ten key atomic processes of interest here which occur within a laser plasma. These are summarised in Table 2.1 and will be further discussed below. They involve both neutral atoms and ions, but in order to avoid confusion, transitions involving a neutral atom and processes involving conversion to/from a neutral atom will be used when describing these atomic processes.

Table 2.1 Summary of the main atomic processes in laser produced plasmas

Process	Excitation	De-excitation	Type
B ↔ B	Impact Excitation	Impact De-excitation	Collisional
B ↔ B	Photoabsorption	Spontaneous Decay	Radiative
B ↔ F	Impact Ionisation	3-Body Recombination	Collisional
B ↔ F	Photoionisation	Radiative Recombination	Radiative
F ↔ F	Bremsstrahlung	-	Collisional
F ↔ F	-	Inverse Bremsstrahlung	Radiative

2.1.1 Bound-Bound Processes

There are four main bound-bound processes of interest, two collisional and two radiative. These bound-bound processes typically describe transitions of electrons between bound quantum states within an atom. The atom remains in its initial state of ionisation is either excited or de-excited depending on whether energy has been absorbed or lost respectively.

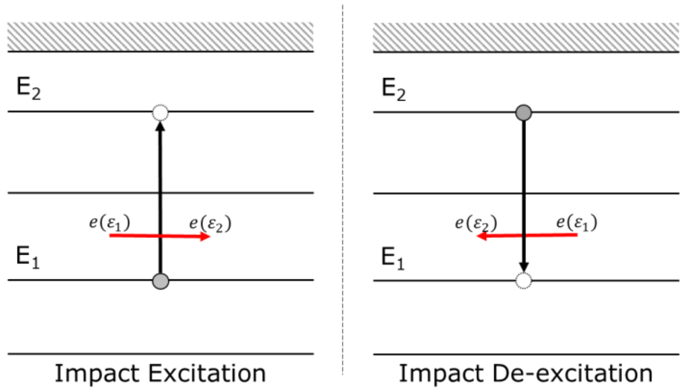

Fig. 2.1 Schematic of the atomic processes impact excitation (left) and impact de-excitation (right). E_1 *and* E_2 *are the lower and upper energy levels and* e *is a free electron with energies* (ε_1) *and* (ε_2) *where* $(\varepsilon_2) < (\varepsilon_1) \geq E_2 - E_1$.

The two bound-bound transitions shown in Fig. 2.1 involve collisional mechanisms; namely electron impact excitation and de-excitation. As these processes are typically driven by collisions with the more active free electrons [3], they can be represented by the simplified expressions (2.9) & (2.10):

$$A + e(\varepsilon_1) \rightarrow A^* + e(\varepsilon_2) \tag{2.9}$$

$$A^* + e(\varepsilon_2) \rightarrow A + e(\varepsilon_1) \tag{2.10}$$

Where A is the atom in its lower energy state, A^* represents the atom in an excited state and e is a free electron with energies (ε_1) and (ε_2) before and after the interaction respectively with $\varepsilon_1 > \varepsilon_2$. In impact excitation, illustrated by (2.9), an atom in a lower energy state undergoes excitation to a higher lying state E_2 due to the transfer of some or all kinetic energy from an incident free electron of energy (ε_1) to the bound electron within the atom during a collision [3]. Due to conservation of energy, any energy gained by the bound electron is correspondingly lost by the free electron in the collision resulting in the free electron having a lower kinetic energy (ε_2). Impact de-excitation given by (2.10), describes the inverse process, where an excited atom is induced to decay to a lower energy state during a collision with a free electron with energy (ε_2). This electron carries away the excess energy so that its new kinetic energy becomes (ε_1).

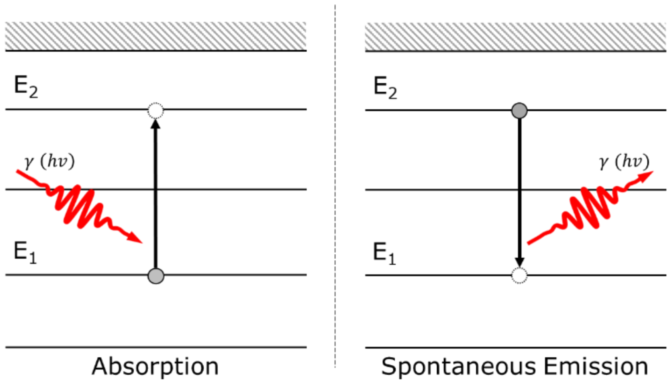

Fig. 2.2 Schematic of the atomic processes photoabsorption (left) and spontaneous emission (right) [5]. E_1 *and* E_2 *are the lower and upper energy levels and* γ *is a photon of energy* $hv = E_2 - E_1$*. These absorption processes may also occur with multiple photons however for simplicity only the single photon case is shown here.*

Like the collisional bound-bound processes, the radiative bound-bound processes of photoabsorption and spontaneous emission, shown in Fig. 2.2, are inverse processes. However, the radiative energy being absorbed/released is carried by a photon. These two processes can be described by expressions (2.11) & (2.12) [5];

$$A + \gamma \rightarrow A^* \qquad (2.11)$$

$$A^* \rightarrow A + \gamma \qquad (2.12)$$

where γ represents the incident/emitted photon. In the absorption process described by (2.11), an atom in a lower energy state becomes excited as a bound electron is promoted to a higher energy state E_2 following absorption of an incident photon with an energy $hv = E_2 - E_1$. The inverse of the photoabsorption process is spontaneous decay described by (2.12). An excited atom A^* relaxes when an electron moves from a higher E_2 to lower E_1 energy state via the emission of a photon γ with energy equal to the transition energy $hv = E_2 - E_1$ [5].

2.1.2 Bound-Free Processes

The four bound-free processes can be thought of as special cases of the bound-bound processes where the ionisation degree of the atom changes. Again, there are two collisional and two radiative pathways which can be thought of as inverse processes. The processes involve

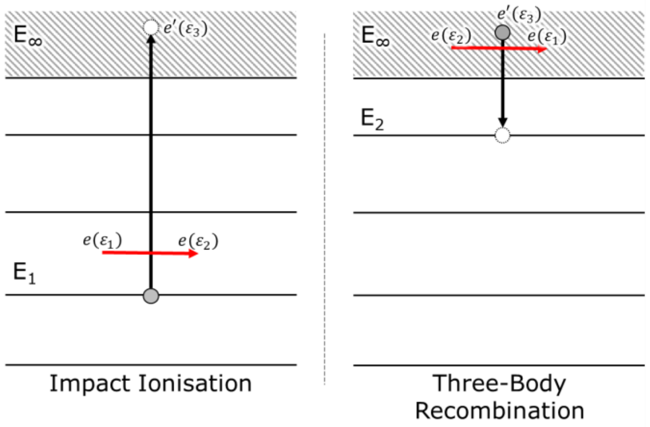

Fig. 2.3 Schematic of the atomic processes impact ionisation (left) and three-body recombination (right). E_1 *and* E_2 *are bound energy levels,* E_∞ *the continuum,* e' *is the captured/liberated free electron with energy*(ε_3) *and* e *is a second free electron with energies* (ε_1) *and* (ε_2)*.*

either the promotion of a bound electron above the ionisation limit thereby becoming a free electron with the atom undergoing ionisation, or recombination of a free electron with an ionised atom thereby lowering the degree of ionisation as the free electron becomes a bound electron.

Fig. 2.3 shows the collisional bound-free processes of impact ionisation and three-body recombination which can be described by the expressions (2.13) & (2.14) respectively.

$$A + e(\varepsilon_1) \rightarrow A^+ + e(\varepsilon_2) + e'(\varepsilon_3) \qquad (\ 2.13\ )$$

$$A^+ + e(\varepsilon_2) + e'(\varepsilon_3) \rightarrow A + e(\varepsilon_1) \qquad (\ 2.14\ )$$

Where A^+ is the ionised atom, e and e' are free electrons with energies (ε_1), (ε_2), and (ε_3). In impact ionisation, an incident free electron of energy $(\varepsilon_1) \geq (E_\infty - E_1)$ scatters off a bound electron within the atom. During this collision sufficient energy is transferred from the free electron to the bound electron for the latter to overcome its ionisation energy promoting it into the continuum above E_∞. The excited electron, no longer bound to the atom, becomes a second free electron e' with an energy $(\varepsilon_3) = (\varepsilon_1) - (E_\infty - E_1) - (\varepsilon_2)$, and the atom moves to a higher degree of ionisation.

The inverse process, as the name three-body recombination suggests, involves three particles; an ion and two free electrons (e and e'). This

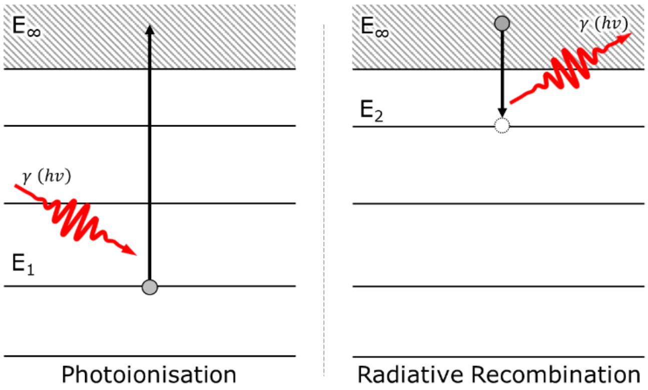

occurs in high density plasmas when it becomes statistically likely for two free electrons to enter the Debye sphere of an ion. One of the free electrons will be captured by the ion into a bound state E_2, reducing the ionisation degree of the ion by unity. This process releases a quantum of excess energy which can be absorbed by the second electron increasing its kinetic energy from (ε_2) to (ε_1). The bound electron at energy level E_2 may undergo further relaxation through bound-bound processes as described above until the atom has returned to its ground state.

Schematics of photoionisation and radiative recombination processes are shown in Fig. 2.4, and are represented by expressions (2.15) & (2.16) [5].

$$A + \gamma \rightarrow A^{+} + e \qquad (2.15)$$

$$A^{+} + e \rightarrow A + \gamma \qquad (2.16)$$

Photoionisation, sometimes known as the atomic photoelectric effect, occurs when an incident photon of energy $hv \geq (E_\infty - E_1)$ excites a bound electron into the continuum [5]. Radiative recombination occurs when a free electron is captured into a bound state E_2 of an ion. During this process a photon is released with an energy equal to that lost by the free electron during the capture process [5].

Fig. 2.4 Schematic of the atomic processes photoionisation (left) and radiative recombination (right) [5]. *E_1 and E_2 are finite energy levels, E_∞ the continuum, and γ represents a photon.*

2.1.3 Free-Free Processes

The free-free electron processes are denoted bremsstrahlung and inverse bremsstrahlung and represent excitation (acceleration) and de-excitation (deceleration) of free electrons within the vicinity of an ion resulting in a change in kinetic energy of the free electrons. The two processes are illustrated in Fig. 2.5 and described by expressions (2.17) & (2.18) [5]:

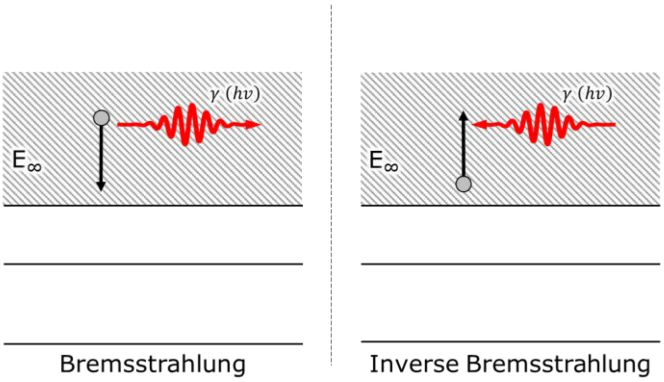

Fig. 2.5 Schematic of the atomic processes bremsstrahlung (left) and inverse bremsstrahlung (right) [5]. *E_∞ is the continuum, and γ is a photon of energy hv.*

$$e(\varepsilon_1) + A^+ \rightarrow e(\varepsilon_2) + A^+ + \gamma \qquad (2.17)$$

$$e(\varepsilon_2) + A^+ + \gamma \rightarrow e(\varepsilon_1) + A^+ \qquad (2.18)$$

where $(\varepsilon_1) > (\varepsilon_2)$. Bremsstrahlung or 'breaking radiation' refers to a process in which a free electron close to an ion is decelerated due to its interaction with the ion's Coulombic field, resulting in a photon being emitted as the free electron loses kinetic energy. Conservation of energy dictates that the energy of the photon emitted will be equal to that lost by the free electron $hv = (\varepsilon_1) - (\varepsilon_2)$. Inverse Bremsstrahlung occurs when a free electron in the vicinity of an ion absorbs a photon. The energy gained increases the kinetic energy of the free electron by an amount equal to the photon energy, $(\varepsilon_1) = (\varepsilon_2) + hv$.

2.1.4 Multiphoton Processes

It is worth noting that the radiative processes of photoabsorption, and photoionisation, described above as single photon interactions, can also occur when the photon energy is less than that of the transition if the radiation field is sufficiently intense, usually an external laser field. This refers to the case of multi-photon interactions where the energies of the photons 'stack' in order to reach above the transition energy. The number of photons n required is given by $n.hv \geq (E_\infty - E_2)$ where n is an integer number.

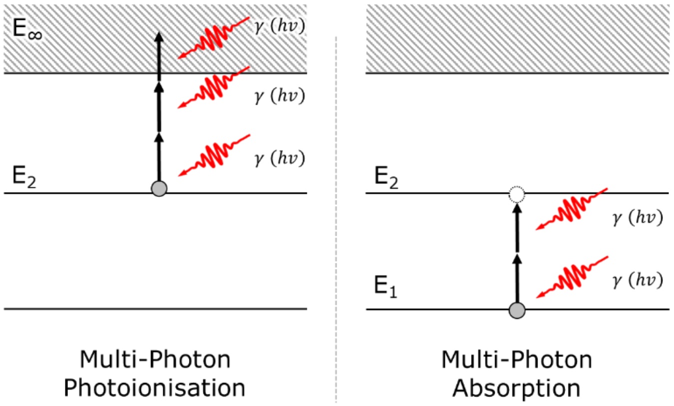

Fig. 2.6 Schematic of the atomic processes multi-photon photoionisation (left) and Multi-photon absorption (right). E_1 *and* E_2 *are finite energy levels,* E_∞ *the continuum, and* γ *is a photon of energy* $h\nu$*.*

2.3 Laser Plasma Formation

Laser plasmas are formed when a target material is irradiated by laser light with a focused intensity above some threshold value, typically close to $1\,GW.cm^{-2}$ for many metals. The properties of the laser plasma formed will greatly depend on the incident laser pulse parameters along with the material composition and geometry of the target. Laser wavelength, pulse duration, pulse shape, spot size, spot shape and intensity are all factors which influence the resulting properties of the plasma. Those target parameters that can influence the resulting plasma and its properties include composition, density, geometry, atomic weight, surface reflectivity, conductivity, etc.

The laser radiation absorbed and the resulting heating, melting, vapourisation, and plasma formation occur at a faster rate than the expansion of the ablated material for long pulse (few ns) laser drivers. A laser plasma can simplified into three main stages of formation [9]:

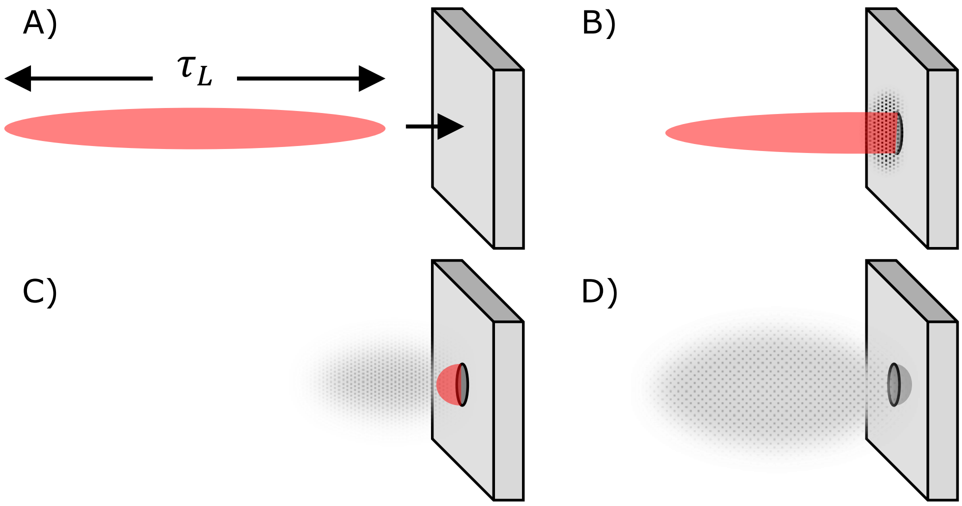

Fig. 2.7 Schematic of laser produced plasma formation. A) An incident laser pulse of duration τ_L is incident on a solid target. B) As the leading edge of the pulse interacts with the target surface, material is ablated, and a dilute plasma is formed. C) The remaining pulse energy excites the plasma and it expands isothermally. D) After the laser pulse has terminated the plasma will continue to expand adiabatically into the surrounding medium. Adapted from [4].

- Laser-matter interaction – The interaction of the laser pulse with target material, Fig. 2.7B
- Laser-plasma interaction – The interaction of the laser pulse with the plasma formed as it undergoes isothermal expansion, Fig. 2.7C
- Plasma expansion – The adiabatic expansion of the ablated plume into the surrounding medium after the laser pulse has terminated, Fig. 2.7D

This approximation implies that the energy transferred from the incident laser pulse is first converted to internal energy within the target and vapour cloud. From there, this internal energy then partially decays to kinetic energy of the ablated particles. Although not fully justified since some of these processes occur simutaneously, it does allow a simplifed picture of the plasma formation and expansion which can illustrated schematically in Fig. 2.7.

2.3.1 Laser-Matter Interaction

The laser-matter interaction phase can be thought of as a process of laser ablation, i.e. the removal of matter into a vapour cloud at the target surface. When the leading edge of a laser pulse is incident on a target some of the radiation is reflected from the surface while a portion penetrates the surface. The penetration distance is known as the skin depth δ, typically a fraction of the incident radiation wavelength, and is given by the expression:

$$\delta = \left(\frac{2}{\omega\mu\sigma}\right)^{\frac{1}{2}} \qquad (2.19)$$

Where ω is the angular frequency of the incident laser radiation, μ the magnetic permeability of free-space, and σ the conductivity of the target material [8]. For a $1064\,nm$ laser incident on an aluminium target surface, the skin depth is less than $10\,nm$.

Within this skin depth the radiation is absorbed by electrons through various processes such as photoabsorption, single photon photoionisation and multiphoton ionisation, all of which were described in section 2.2. The free electrons created can transfer energy into the bulk material down to a heat penetration depth L_{th} given by [8]:

$$L_{th} \approx (2D\tau_L)^{\frac{1}{2}} \qquad (2.20)$$

where D is the heat diffusion coefficient ($D = k/\rho C$), k is the thermal conductivity, ρ is the mass density, C is the specific heat capacity and τ_L is the pulse duration of the laser. For nanosecond lasers on metals the heat penetration depth is on the order of $\sim 1\ \mu m$, typically far greater than the skin depth ($L_{th} \gg \delta$) [8]. Hence, energy from an incident nanosecond pulse is transferred thermally from the material surface at a skin depth into the bulk material and the material undergoes phase changes from solid → liquid → vapour.

For completeness it is noted that in the case of pico- and femtosecond pulses, the pulse duration is so short that thermal conduction into the target can be often neglected and the heat penetration depth is approximately that of the skin depth ($L_{th} \approx \delta$). Hence ablation from picosecond and femtosecond pulses are generally considered direct solid to vapour transitions [4,8]. In what follows only the interaction of nanosecond duration pulses with matter will be considered.

During the phase change in the material of a target irradiated by a nanosecond pulse, vaporisation requires much more energy than melting. Hence, when the energy stored in the bulk material up to the heat penetration depth (per unit volume) becomes larger than the latent heat of evaporation per unit volume, evaporation will occur. An approximation to the ablation depth ΔZ_v of the evaporated material is given by:

$$\Delta Z_v \approx \frac{A_s(F_L - F_{th})}{\rho L_v} \tag{2.21}$$

Where A_s is the surface absorption coefficient, F_L is the laser fluence, F_{th} is the threshold fluence and L_v is the latent heat [8]. The threshold fluence is the minimum energy at which appreciable ablation takes place, typically to a depth L_{th} and can be approximated by [8]:

$$F_{th} \approx \frac{\rho C \Delta T_m L_{th}}{A_s} \tag{2.22}$$

where ΔT_m is the difference in the melting temperature of the material and its initial temperature. The threshold fluence will grow as the square root of the laser pulse duration ($\mathrm{F_{th}} \propto (\tau_L)^{\frac{1}{2}}$) and will also depend on the material's thermal and optical properties.

To account for this dependence on pulse duration, the threshold fluence $\mathrm{F_{th}}$ (Jcm^{-2}) is often converted into a laser power density (or intensity) and designated the 'breakdown threshold' $\mathrm{I_{th}}$ (Wcm^{-2}). In typical LIBS (Laser induced breakdown spectroscopy) experiments, breakdown thresholds of $10^8 - 10^{10}\ Wcm^{-2}$ [4] are found for solid targets and pure aluminium has been calculated to have a breakdown threshold of $\sim 1.75\ x\ 10^8\ Wcm^{-2}$ [4]. For a $20\ mJ$ pulse with a duration of $18\ ns$ focussed down to a spot size of $200\ \mu m$, typically used in this work, the irradances achieved were on the order of $10^9\ Wcm^{-2}$, and were comfortably able to breakdown the target material while still being lower than the breakdown irradiance (power density) for labororatory air, which is estimated to be on the order of $10^{10} - 10^{11}\,Wcm^{-2}$ [4].

2.3.2 Laser-Plasma Interaction

After the leading edge of the laser pulse has ablated material to form a diffuse plasma above the surface of the target, the plasma will begin to interact with the remaining part of the laser pulse, absorbing energy so that further excitation occurs. In addition, the plasma will begin to expand at the target surface.

The dominant laser-plasma interactions occur via photoionisation and inverse bremsstrahlung. The absorption due to photoionisation, where an incident photon excites and liberates a bound electron within an atom, has an absorption coefficient α_{PI} which can be calculated using [8]:

$$\alpha_{\mathrm{PI}} = \sigma_{PI} n_N \approx \sum_N 2.9 \times 10^{-17} \frac{(\varepsilon_N)^{\frac{5}{2}}}{(hv)^3}\, n_N \quad [cm^{-1}] \tag{2.23}$$

Where σ_{PI} is the photoionisation cross section (typically on the order of $\approx 10^{-17}\,cm^2$), hv the photon energy (eV), ε_N and n_N are the ionisation energy (eV) and number density (cm^{-3}) of the excited species in state N respectively, and the summation is performed for all bound states 'N' that satisfy the condition $hv > \varepsilon_N$. If the laser photon energy does not exceed the ionization threshold then free electrons are produced by multiphoton ionization where the ionization rate will scale as I^n where n is the number of photons absorbed in the process. For infrared lasers this is the dominant photoionisation process.

As photoionisation occurs, the plasma undergoes further ionisation which in-turn gives rise to an increase in the electron density and hence free electrons which can go on to be further excited through inverse bremsstrahlung. Inverse bremsstrahlung refers to the absorption of incident laser radiation by free electrons in the vicinity of an ion. The absorption coefficient for inverse bremsstrahlung α_{IB} is given by [8]:

$$\alpha_{\mathrm{IB}} = \sigma_{IB} n_e = \frac{4}{3}\left(\frac{2\pi}{3k_B T_e}\right)^{\frac{1}{2}} \frac{z^2 e^6}{hcm_e^{3/2} v^3} n_i g_{ff}\left(1 - \exp\left(-\frac{cv}{k_b T_e}\right)\right) n_e \qquad (2.24)$$

Where σ_{IB} is the inverse Bremsstrahlung cross section, n_e and n_i are the electron and ion densities (cm^{-3}) respectively, e and m_e the electron charge and mass, z the ion charge, k_b Boltzmann's constant, and T_e the electron kinetic temperature (K). g_{ff}, known as the Gaunt factor, is introduced in a more exact theory of the absorption coefficient and is usually assumed to be 1 by Kramer's rule [8]. As free electrons absorb energy via inverse bremsstrahlung continues they go on to excite the plasma further through collisional processes such as electron impact ionisation. Eventually the plasma will reach the critical density n_c (section 2.1) and the plasma will become opaque to the incident radiation, which will begin to be reflected from the critical density layer. During this phase the plasma will expand, thereby lowering the electron density, the laser can penetrate the plasma plume and the plasma will begin to absorb laser radiation yet again. This cyclical process of absorption and expansion will repeat for the duration of the laser pulse. During the laser pulse the expansion of the plasma can be considered as isothermal since, although the plasma expands and hence increases in volume, it will have a constant temperature as the expansion time is far greater than the heating time.

2.3.3 Plasma Expansion

As the plasma expands it begins to cool as thermal energy is rapidly converted into kinetic energy, and this point the plume expansion can be described by the adiabatic expansion model introduced by Singh and Narayan [9]. In this model the plasma is approximated by an ideal gas at high pressure and temperature, which is suddenly allowed to expand into vacuum having been confined to a small volume. Their expression for the expansion of the plasma in vacuum is given by:

$$X(t)\left[\frac{d^2X}{dt^2}\right] = Y(t)\left[\frac{d^2Y}{dt^2}\right] = Z(t)\left[\frac{d^2Z}{dt^2}\right] = \frac{k_B T_0}{m}\left[\frac{X_0 Y_0 Z_0}{X(t)Y(t)Z(t)}\right]^{\gamma-1} \qquad (2.25)$$

where X_0, Y_0, Z_0, and T_0 are the initial orthogonal edges of the plasma and plasma temperature once the laser pulse has terminated, k_B is Boltzmann's constant, m is the mass of the atomic species, and γ is the ratio of the specific heat capacities at constant pressure and volume [9]. As the expression is dependent on the species mass, the lighter, and consequently faster, electrons will expand at a faster rate ahead of the heavier ions, hence the electrons will move to the outer regions of the plasma and a charge separation will occur [10] creating an ambipolar field. It can also be seen that the expansion velocities will depend on the initial dimensions of the plasma, with the highest velocities in the direction of the smallest dimension. The initial dimensions of the plasma will be large on the surface of the target due to the spot size (typically $100 - 200\,\mu m$), and much smaller normal to the target from the isothermal expansion (typically a few μm), the typical plasma scale length. Therefore, the expansion velocity will be greater normal to the target, leading to an anisotropic expansion of the plasma, creating the characteristic elongated laser plasma shape [9].

2.3.4 Plasma Expansion Under Atmospheric Conditions

When a laser plasma is formed in the presence of a background gas it follows similar processes to that of a plasma formed in vacuum, having the three distinct stages of formation. However, due to the presence of the background gas, the processes become more complex. Harilal *et al* [11] state that there are typically three main differences observed when a plasma expands into a background gas, (i) the formation of a *shock front* propagating into the gas, (ii) a spatial confinement of the plume caused by interactions of the expanding plasma with the gas slowing the plume expansion, and (iii) an increase in fluorescence due to enhanced collisions at the expansion front along with inter-plume collisions.

During the laser-matter interaction phase the laser heats and excites the target and evaporation occurs. During this phase of continuous heating and ablation, high thermal pressure builds within the plasma which is suddenly released. This sudden release of energy drives a hemi-spherical shock front, or *blast wave,* into the surrounding medium [12]. This shock front also imparts momentum to the air behind the shock front creating a powerful *compression wave* and thus, the plasma begins to expand towards the laser and the laser-plasma interactions begin to occur. During the laser-plasma interaction in air three different types of waves can be generated, laser-supported combustion (LSC) waves, laser-supported detonation (LSD) waves, and laser-supported radiation (LSR) waves [4,13]. The three waves are distinguished on the basis of pressure, velocity and their effects on the plasma expansion and they are strongly dependant on the incident laser pulse intensity. Fig. 2.8A shows a plasma expanding towards the laser pulse in a gas medium, there are three main regions of interest; (i) the plasma volume, the bulk material comprising the hot plasma, (ii) the absorption zone, a dilute plasma where the main absorption processes occur, and (iii) the shock front formed in the laser-matter interaction.

At lower laser intensities LSC waves are produced. In this case both energy deposited in the atmosphere by the shock front and energy from the plasma volume radiation are required to move the absorption zone towards the laser beam [4]. This results in the absorption zone and plasma volume being coupled into one region which is preceded by the shock front. At intermediate intensities LSD wave are produced. In the case of an LSD wave the shock front is stronger than that of an LSC wave and has sufficient energy to heat the gas leading to absorption of the laser beam without additional heating from the plasma. As such, the absorption zone does not need to be coupled to the plasma volume but is found right behind the shock front, moving at the same velocity. The plasma volume and absorption zone create two distinct regions,

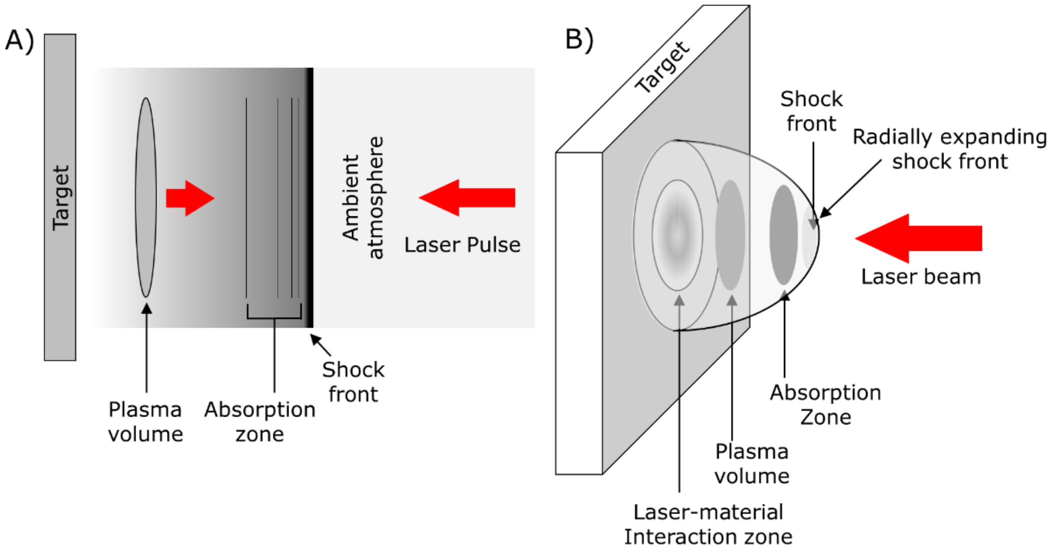

Fig. 2.8 Schematic diagrams of A) The development of a laser plasma from a solid surface. The absorption zone, plasma volume and shock front are all labelled. B) A laser-supported detonation (LSD) wave, the shock wave preceding the absorption zone and plasma front and the three zones are separated. Figures recreated from [4].

compared to the LSC wave case where they were required to be coupled as one [4,13]. This separation of the plasma volume and absorption zone can be seen in Fig. 2.8B, which shows an LSD wave expanding.

At the highest intensities where LSR waves are formed, the plasma formed is so hot that the radiation from the plasma is sufficient to heat the ambient gas to temperatures where laser absorption begins, even before the shockwave has arrived. Hence the absorption zone and plasma volume will couple once more, expanding outwards [4].

For intensities not much greater than the breakdown threshold I_{th}, such as those used in this work, the plasma, formed in air at atmospheric pressure, is typically in the LSD regime [4]. Therefore as the expansion of the plasma will depend strongly on the expansion of the shock front [12] in order to model plasma expansion, we must take into account the shock front position R at a time after plasma ignition t, which can be described by the Sedov-Taylor or *point explosion* model. This model has slight variations [11,14,15] but can be given in its general form as:

$$R = \xi_0 \left(\frac{E_0}{\rho_0}\right)^{\frac{1}{2+\nu}} t^{\frac{2}{2+\nu}} \qquad (2.26)$$

Where E_0 is the amount of energy released in the explosion, ρ_0 the ambient gas density and ξ_0 is a constant determined by the gas specific heat ratio. The parameter v describes the geometry of the wave having a value of 1, 2, or 3 for planar, cylindrical, or spherical waves respectively. Equation (2.26) can be further simplified to:

$$R = \alpha t^n \tag{2.27}$$

which can be fitted to experimental values of R as a function of time and the values of α and n determined from that fit. n has a value of 0.4, 0.5, or 0.667 for a spherical, cylindrical or planar shock front.

While the plasma expands, as mentioned previously, a confinement due to the background gas occurs and the plume begins to decelerate as the pressure exerted by the surrounding gaseous medium begins to make a greater contribution to its confinement. This is not accounted for in the point explosion model and hence a drag-force model must be incorporated to account for this deceleration and the eventual stopping of the plume expansion, which is due to collisions with the background gas. The drag model states that [11]:

$$R = R_0[1 - \exp(-\beta t)] \tag{2.28}$$

Where R_0 is the stopping distance of the plasma plume, and β is the slowing coefficient such that $R_0\beta = v_0$, where v_0 is the initial velocity. Thus a combination of the point explosion and drag-force models is typically needed to describe the expansion of a laser plasma into a background gas of ambient air, with the point explosion model being used for early stages and the drag-force model being used for later stages in the lifetime of the plasma $(> 500\,ns)$ [11].

The other notable difference seen in the case of a laser produced plasma expanding into a background gas at atmospheric pressure is an enhancement in emission from the different atomic species in the plasma during the expansion phase. This enhancement is due to collisions with the ambient gas molecules increasing electron density via ionization and hence the probability of electron impact excitation and recombination processes [11].

2.4 Plasma Equilibrium

In order for a plasma to exist in a *complete state of thermodynamic equilibrium* (CTE) it must meet certain criteria [3,16]:

- The Maxwell velocity distribution law approximates the motion of particles within the plasma, electrons, ions and neutral species.
- The Boltzmann formula describes the population distributions between the electronic states of any atom or ion in the plasma, i.e., the excitation balance.
- The Saha equation describes the ratio of ions with charge z relative to those with charge $(z-1)$, i.e., the ionization balance.
- The Planck radiation distribution function specifies the intensity distribution of the emitted radiation.

In plasmas that are in CTE there exists a balance between every atomic process. Each process that takes place has a corresponding inverse process that must occur to maintain this balance, e.g., the rate of collisional excitation must be equal to the rate of collisional de-excitation. However, it is very rare for complete thermal equilibrium to be achieved, especially in terrestrial plasmas [3,16,17].

By the very presence of the radiation emitted from a plasma, energy is lost from the system and CTE is therefore not possible. Thus, other equilibrium models have been developed to describe plasmas in different regimes. These models employ more flexible criteria and can better describe the nature of real laboratory and astrophysical plasmas. The three thermodynamic models most commonly used to describe plasmas are:

- Local Thermodynamic Equilibrium (LTE)
- Coronal Equilibrium (CE)
- Collisional Radiative Equilibrium (CRE)

The applicability of the three models is largely dictated by the electron density of the plasma. LTE is very similar to CTE and is typically applied to hot plasmas of high density. When dealing with low density plasmas

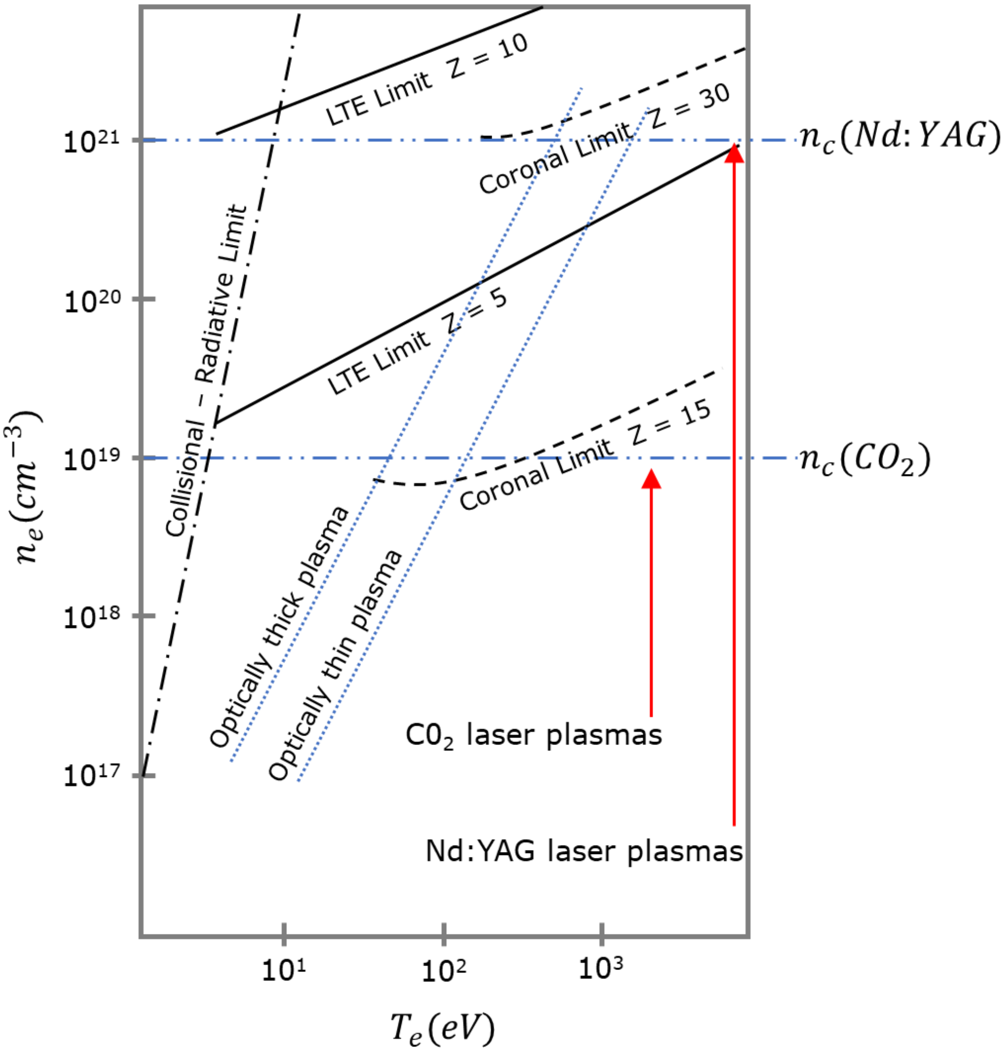

Fig. 2.9 Criteria for applicability of different thermodynamic equilibrium models for laser plasmas. Adapted from [18]

typically the CE model is used. The CRE model is used to describe the intermediate region between LTE and CE, and at its upper and lower density limits overlaps with the LTE and CE models respectively.

To help illustrate this, Fig. 2.9 is a phase (n_e , T_e) diagram, showing the regions of applicability of each model highlighting the various limits imposed on electron temperature for a given electron density and vice versa [18]. Also shown are the critical densities for CO_2 and Nd:YAG lasers where the plasma will become reflective to the incident laser light as discussed in section 2.1.

2.4.1 Local Thermodynamic Equilibrium (LTE)

LTE describes a model where collisional atomic processes dominate the system's behaviour. It is very similar to CTE in that is also requires the velocity distribution, the (atomic) level population distributions, and ionisation distribution to be given by Maxwell velocity distribution, the Boltzmann formula and the Saha equation respectively. As the system is dominated by collisional processes the radiation distribution is not governed by Planck's equation and it is assumed to be insignificant in determining plasma equilibrium [3]. In addition LTE also differs from CTE in that the temperature need not be uniform and the plasma homogeneous, and as the name would suggest, local equilibria are sufficient for this model to be valid [17]. When the plasma is in LTE, the processes of electron impact excitation & ionisation are equal to the rate of collisional de-excitation and three-body recombination. For this to hold true, the electron density must be high enough for the collisional processes to become statistically favoured over their radiative counterparts by at least an order of magnitude. This condition puts a lower boundary on the electron density n_e for LTE to hold true, given by the McWhirter criterion [19]:

$$n_e \geq 1.6 \times 10^{12} T_e^{\frac{1}{2}} \chi^3 \tag{2.29}$$

Where T_e is the electron temperature and χ is the excitation potential (eV) of the transition under consideration. For laser plasmas concerned in this work (common Al transitions with $T_e \approx 1.5\, eV$) this results in a lower limit for the electron density $n_e \geq 6.5 \times 10^{15}\ cm^{-3}$.

2.4.2 Coronal Equilibrium (CE)

The CE model is deployed for low electron density plasmas. These plasmas are often found in astrophysical situations such as solar coronas, hence the naming convention. In the CE case, excitation and ionisation are caused by electron collisions but are balanced by de-excitation and radiative recombination processes [3,16–18]. The plasma must be optically thin to this emitted radiation so that re-absorption is negligible. As densities are low, the collisional excitation rates will be low, allowing the atoms time to relax through spontaneous radiative processes and hence most atoms will be found to be in the ground state, leaving excited state populations negligible. Thus, the Boltzmann and Saha formulae may not hold in the CE model. However, the velocity distribution is still assumed to be Maxwellian [16,18]. The application of the CE model is limited to low density plasmas and an estimation of this density can be obtained from:

$$n_e \leq 5.6 \times 10^8 (z+1) T_e^{\frac{1}{2}} \exp\left[\frac{1.162x10^3 (z+1)^2}{T_e}\right] \qquad (2.30)$$

Where z is an ionic charge and T_e is given in (eV). Thus, it can be seen that the LTE and CE models are indeed regimes at opposite ends of the density spectrum, therefore the CRE model was required for the intermediate region between them.

2.4.3 Collisional Radiative Equilibrium (CRE)

From [18] the Collisional Radiative Equilibrium model is described as bridging the LTE and CE models. This model observes that the main mechanisms of ionisation and recombination, as discussed in section 2.2, are collisional and radiative. Hence, includes a balance of collisional and radiative processes. However, if these processes become dominated by collision processes the model will tend to that of LTE.

From this equilibrium model Colombant and Tonon [18] introduce a collisional radiative ionisation model. This ionisation model is based on a rate equation determined by balancing collisional and radiative processes [16]. The rate equation for the population of ions of charge $z + 1$ is given by.

$$\begin{aligned} \frac{dn_{z+1}}{dt} &= n_e n_z S(z, T_e) - n_e n_z [A] + n_e n_z [B] \\ A &= S(z+1, T_e) + \alpha_R (z+1, T_e) + n_e \alpha_{3B} (z+1, T_e) \qquad (2.31) \\ B &= \alpha_R (z+2, T_e) + n_e \alpha_{3B} (z+2, T_e) \end{aligned}$$

Where n_e and n_z are the electron and ion densities, T_e the electron temperature, and z the charge state. S, α_R, α_{3B} are the coefficients of collisional ionisation, radiative recombination and three-body recombination respectively and can be determined by equations (2.32), (2.33), & (2.34)[18]:

$$S = \frac{9 \times 10^{-6} \xi_z \left(\frac{T_e}{\chi_z}\right)^{1/2}}{\chi_z^{3/2} \, (T_e/\chi_z)} \exp\left(-\frac{\chi_z}{T_e}\right) \tag{2.32}$$

$$\alpha_R = 5.2 \times 10^{-14} \left(\frac{\chi_z}{T_e}\right)^{1/2} z \left[0.429 + \frac{1}{2}\log\left(\frac{\chi_z}{T_e}\right) + 0.469\left(\frac{T_e}{\chi_z}\right)^{1/2}\right] \tag{2.33}$$

$$\alpha_{3B} = 2.97 \times 10^{-27} \, \frac{\xi_z}{T_z \chi_z}\left(4.88 + \frac{T_z}{\chi_z}\right) \tag{2.34}$$

ξ_z refers to the number of atoms in the outmost layer corresponding to the charge state z, and χ_z is the ionisation potential.

These values for these coefficients can be computed using measured time and space resolved plasma parameters of electron densities and electron temperatures. By investigating these rates along with which recombination processes dominate within the plasma can give further insight to the plasma behaviour.

2.5 Colliding Plasma Plumes

When a pair of expanding laser plasmas collide two extreme scenarios may occur, namely interpenetration or stagnation. If interpenetration occurs, the two plasmas stream through one another with the plasma constituents undergoing binary collisions. If they stagnate, each expanding plasma will decelerate abruptly at the collision plane, resulting in a build-up of plasma material. As time progresses this material will be compressed by following material giving rise to a region of increased temperature and density, a so-called stagnation layer [20]. Fig. 2.10 below illustrates the concepts of A) interpenetration and B) stagnation of two plasmas.

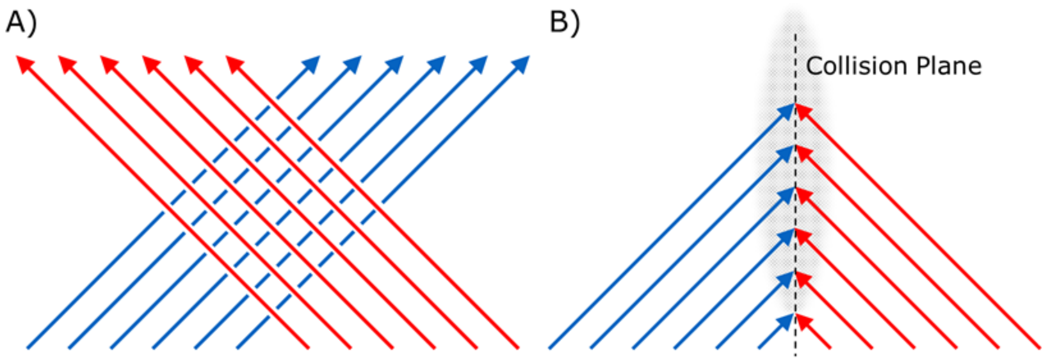

Interpenetration Stagnation

Fig. 2.10 Examples of two expanding plasma plumes exhibiting A) Interpenetration and B) Stagnation. In interpenetration the plasma constituents will pass through one another with the main interactions being binary collisions. At the other extreme the plasma plumes decelerate rapidly at the collision front and stagnate. The remaining material from the plumes accumulate at the collision plane and so the density starts to rise even further. For the case of two expanding plasmas, interpenetration or stagnation may occur depending on the collisionality parameter ζ*.*

Interpenetration is most likely to occur when the relative collisional velocity of the plasma plumes is high, and the density is modest, whereas stagnation is preferred when the relative velocity is small and the plume density at the collision front is high. Typically, a combination of these processes occurs and in order to describe to what extent colliding plasmas interpenetrate or stagnate, Rambo and Denavit introduced a "collisionality parameter" ζ, given by the ratio of the separation between the two colliding plasmas D to the ion-ion mean free path (MFP) λ_{ii}:

$$\zeta = D/\lambda_{ii} \tag{2.35}$$

It is also worth noting that the ion-electron MFP is much larger than the ion-ion MFP for medium atomic number laser plasmas, hence the contributions from the ion-electron MFP can be ignored. Substituting for the ion-ion MFP λ_{ii} we obtain equations (2.36) [21] and (2.37) [22] in terms electron temperature or collisional velocity respectively.

$$\zeta = \frac{\frac{8}{3}\left(\frac{\pi}{2}\right)^{\frac{1}{2}} n_i q^4 D z^2}{T_e^2} \tag{2.36}$$

$$\zeta = \frac{4\pi n_i q^4 z^4 \, D \ln \Lambda_{1\to 2}}{m_i^2 v_{12}^4} \tag{2.37}$$

where n_i and T_e are the density and electron temperature of the seed plasmas, q the elementary charge, z the average ionisation state of the plasma, m_i the ion mass, v_{12} the relative plasma collision velocity, and $\ln \Lambda_{1\rightarrow 2}$ the Coulomb logarithm.

From the strong dependence on collisional velocity, and notable dependence on ion charge state, ion density, and plasma separation an experimental set up can be designed to manipulate the collisionality parameter in order to increase the probability of stagnation or interpenetration occurring. Typically, when the MFP is larger than the plasma dimensions and the collisionality parameter is less than unity ($\zeta < 1$) interpenetration will dominate. Conversely stagnation will dominate when the MFP is small and the collisionality parameter is greater than unity ($\zeta > 1$) [20,23].

2.6 Optical Emission from Laser Produced Plasmas

Laser plasma radiation consists of both continuum and line emission. Continuum or broadband emission arises from free-bound and free-free interactions and will dominate in the early stages of plasma lifetime ($0 - 150\,ns$), when the plasma is hot, and dense, and consequently recombination processes are favoured. At mid to late plasma radiative lifetimes line emission, arising from bound-bound processes, is observed as the plasma begins to cool and excited atoms decay lower energy states. It is this line emission that typically holds the most useful information on the plasma environment, not only on the atomic and/or molecular species present, but also on the plasma conditions where line intensities and line profiles act as sensitive sensors of their local plasma conditions and can be used to extract plasma parameters such as electron temperature and density.

2.6.1 Line Broadening

The angular frequency of radiation ω emitted in a bound-bound transition between two discrete energy levels E_1 and E_2 is given by:

$$\omega_{21} = \frac{E_2 - E_1}{\hbar} \qquad (2.38)$$

Where $E_2 > E_1$, and $\hbar$ is Planck's constant divided by 2π. From this relationship the line emitted might be expected to be infinitely sharp, however this is not the case due to line broadening. The three main forms of line broadening of concern in laser plasmas are; natural broadening, Doppler broadening, and Stark broadening.

Natural Broadening

Natural broadening arises from the Heisenberg uncertainty principle which states that one cannot determine simultaneously the exact energy and lifetime of a transition. The finite lifetime leads to a spread of possible energies of the order of $\hbar/2\tau$, where τ is the lifetime of the state. As there is a finite lifetime of excited states there is a finite probability for a photon to be emitted within the energy interval centred about $E_2 - E_1$. Natural broadening results in a Lorentzian intensity distribution $\mathcal{L}(\omega)$ about the central frequency ω_0 given by the expression [4,24]:

$$\mathcal{L}(\omega) = \frac{\Gamma}{2\pi} \frac{1}{(\omega - \omega_0)^2 + (\Gamma/2)^2} \qquad (2.39)$$

Where $\Gamma/2$ is the Full Width at Half Maximum (FWHM) of a normalised Lorentzian profile. Natural line broadening results in the minimum possible spectral linewidth that can result from a spectral measurement, and hence it is smaller than that of other broadening mechanisms in laser plasmas (on the order of $10^{-5}\,nm$). Typically it is beyond the recording capabilities of most laboratory spectrometers.

Doppler Broadening

Doppler broadening results from the shift in observed wavelength of a spectral line due to the motion of the emitter with respect to the observer. An effective shortening of the wavelength or *blueshift* occurs when the emitter is moving towards the observer causing a bunching of waves. On the other hand, when the emitter is moving away from the observer an elongation of waves effectively increases the wavelength resulting in a *redshift.* In frequency terms a blueshift corresponds to a frequency upshift and conversely a redshift represents a frequency downshift. The Doppler shift $\Delta\omega$ for a wave observed to have angular frequency ω, different from the emitted wave frequency ω_0 is given by:

$$\Delta\omega = \omega - \omega_0 = \omega_0 \frac{v}{c} \tag{2.40}$$

Where v is the non-relativistic velocity of the emitter and c the speed of light. The sign of the shift (positive or negative) depends on the sign (direction with respect to observer) of the velocity. Since emitting species move randomly within a plasma plume (ignoring any directed motional shifts due to the expansion of the plume), Doppler broadening creates a spread of observed frequencies. With the assumption of a Maxwellian velocity distribution a spectral line having a Gaussian profile given by equation (2.41)[24] will result:

$$\mathcal{G}(\omega) = \frac{1}{\sqrt{2\pi}\sigma} \exp\left(-\frac{1}{2}\left(\frac{\omega - \omega_0}{\sigma}\right)^2\right) \tag{2.41}$$

where σ is the FWHM of the Gaussian line profile. Doppler broadening has a significant contribution in high-temperature or low-Z element plasmas where the velocities of emitting species are likely to be large. The relationship between the FWHM of a Doppler broadened line profile and the temperature of the plasma and atomic mass of the emitting species is given by [25]:

$$\Delta\lambda_{D\frac{1}{2}} = 7.16 \times 10^{-7} \lambda_0 \left(\frac{T}{m}\right)^{\frac{1}{2}} \tag{2.42}$$

Where λ_0 is the centre wavelength (nm), m the atomic mass of the emitting atom, and T the temperature (K), again assuming a Maxwellian velocity distribution. For the quite low temperature aluminium plasmas presented in this work this results in a small contribution to the overall line broadening budget of c.a. $0.007\,nm$. Of course, a line profile may become asymmetric if, in addition to the normal isotropic velocity distribution, there exists a motional contribution with a preferred direction, e.g., if the plasma is viewed along its axis of expansion, normal to the target.

Pressure Broadening

Pressure broadening occurs due to interactions between the emitter and the surrounding species and there are three classes depending on the nature of the interacting species;

- Resonance – Interactions of the same type of atom
- Van der Waals – Interactions with a different type of atom
- Stark broadening – Interaction with a charged particle

For laser plasmas the mechanism of greatest interest is Stark broadening, since, by definition, a high-temperature and high-density plasma is comprised mainly of charged particles. The collisions involving the emitting species (atoms and ions) with electrons occur on a very short timescale and are thus the most important, dominating Stark broadening in hot and dense plasmas. The ion-emitter collisions take place over a significantly longer timescale, that is to say that the electron-emitter collision frequency is significantly greater than the ion-emitter frequency. The FWHM a Stark broadened line is related to the electron density by the expression [26]:

$$\Delta\lambda_{S\frac{1}{2}} = 2w\left(\frac{n_e}{10^{16}}\right) + 3.5A_i\left(\frac{n_e}{10^{16}}\right)^{\frac{1}{4}}\left(1 - 1.2N_D^{-\frac{1}{3}}\right)w\left(\frac{n_e}{10^{16}}\right) \qquad (\ 2.43\ )$$

where w is the electron impact parameter ($\text{Å}/cm^{-3}$), n_e the electron density (cm^{-3}), A_i is the ion broadening parameter and N_D the number of particles in the Debye sphere. The first term on the right-hand side is the expression for electron-emitter contribution and the second term the ion-emitter contribution. In the case of a nonhydrogenic ions, Stark broadening is typically dominated by electron-emitter collisions and the expression (2.43) can be reduced to [26,27]:

$$\Delta\lambda_{S\frac{1}{2}} = 2w\left(\frac{n_e}{10^{16}}\right) \qquad (\ 2.44\ )$$

In the case of a hot and dense plasma, Stark-shifting of the energy levels involved in a transition can also contribute to the broadening of the resulting emission line. A Stark-shift occurs when the electric field from neighbouring particles perturbs the energy levels of the emitter, causing a shift in the observed wavelength. This shift is given by [17]:

$$\Delta\lambda_{shift} = d\left(\frac{n_e}{10^{16}}\right) + 2A_i\left(\frac{n_e}{10^{16}}\right)^{\frac{1}{4}}\left(1 - 1.2N_D^{-\frac{1}{3}}\right)w\left(\frac{n_e}{10^{16}}\right) \qquad (2.45)$$

where d is the calculated shift parameter, the amount a spectral line is shifted by the plasma field felt by the emitter. Equations (2.44) & (2.45) may only be applied when the conditions $N_D > 2$ and $A_i < 0.5$ are satisfied [28].

2.6.2 Gaussian, Lorentzian and Voigt Profiles

As described in section 2.6.1, line emission from a laser plasma will tend to undergo three forms of broadening, Doppler broadening resulting in a Gaussian line profile, and Natural and Stark broadening, resulting in a Lorentzian line profile. Therefore, the resulting line profile is best approximated by a Voigt profile, a convolution of Gaussian and Lorentzian functions, given by the expression:

$$\mathcal{V}(\omega) = \mathcal{G}(\omega_0 - \omega) \otimes \mathcal{L}(\omega_0 - \omega) \qquad (2.46)$$

Where $\mathcal{L}(\omega)$ and $\mathcal{G}(\omega)$ are the Lorentzian and Gaussian functions given by equations (2.39) and (2.41) respectively, and $\otimes$ denotes the convolution operation. A Voigt profile is best described as Gaussian around the central frequency ω_0 but tending towards Lorentzian as the wings of the profile are approached, owing to the wider wings of the Lorentzian profile. Fig. 2.11 shows a plot of all three profiles with the Gaussian and Lorentzian having equal FWHM and area, while the Voigt is the convolution of the two. It can be seen that the Gaussian has a narrower width than the other profiles.

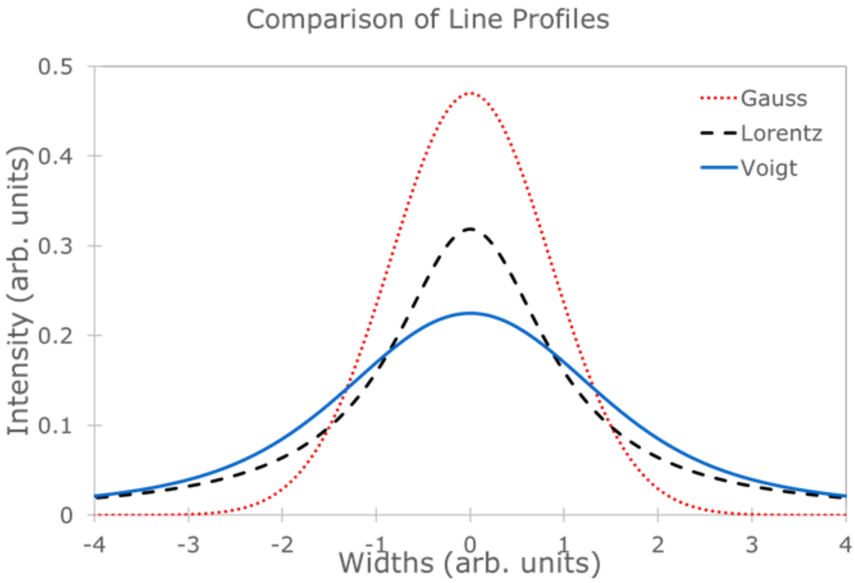

Fig. 2.11 Gaussian and Lorentzian profiles with equal full-width half max values. The Voigt profile is the result of the convolution of the Gaussian and Lorentzian functions. Recreated from [4].

It is also worth mentioning that in any real spectral measurement it is most important to take into the account the instrumental broadening which should be experimentally determined from a known narrow linewidth light source (e.g., a low pressure spectral lamp) for a series of wavelengths over the spectral range to be covered [17].

2.6.3 Electron Density

There are many purely spectroscopic methods for the determination of electron density of a laser plasma, from Stark widths and shifts, and relative line intensities[1] [17]. The method chosen for determining the electron density for this work was to use the Stark widths of the spectral lines. This would leave the relative line intensities method to be used for temperature calculations as will be discussed in the next section.

To obtain the electron densities the Stark widths were obtained by fitting selected spectral lines (for which the Stark parameters were available in the literature) with a Voigt profile, further details of which are discussed in the results in section 0. The Gaussian component of this

---

[1] This measurement would require knowledge of the electron temperature T_e, therefore as discussed in section 2.6.4, this method will instead be used with the electron density n_e to calculate electron temperature T_e.

profile is dominated by the instrument function, while the Lorentzian component is dominated by Stark broadening. Hence the FWHM of the Lorentzian component can be used to determine the Stark width ($\Delta\lambda_{S\frac{1}{2}}$). Rearranging equation (2.44) to isolate the electron density yields:

$$n_e = \frac{2w}{\Delta\lambda_{S\frac{1}{2}} \times 10^{16}} \qquad (2.47)$$

This method of determining electron density also has the benefit that Stark widths are relatively insensitive to ion and electron temperatures [17] compared to the other methods which are more sensitively dependent on electron temperature.

2.6.4 Electron Temperature

Similar to electron densities, there are many spectroscopic methods to determine electron temperature. Some quick but crude ways of estimating electron temperature can be achieved by noting the maximum ionisation degree of the plasma from any of the lines present in the spectra at a given time. For quite high temperature laser plasmas Colombant and Tonon [18] have shown that for $T_e > 30\,eV$, $z \sim [A.T_e(eV)]^{\frac{1}{3}}$ where A is the dominant ion stage and z is the atomic number. They have also shown that, assuming collisional radiative equilibrium to pertain in a plasma, the electron temperature before expansion can be approximated by [18]:

$$\mathrm{T(eV)} \approx 5.2 \times 10^{-6} m^{\frac{1}{5}} (I\lambda^2)^{\frac{3}{5}} \qquad (2.48)$$

where m is the atomic mass, λ the laser wavelength (μm), and I the irradiance on target (Wcm^{-2}). This approximation is seen to be valid for the duration of the laser pulse [18] and provides an estimate of the initial plasma temperatures on the order of $2 - 3\,eV$ for laser irradiances on the order of $10^9\ Wcm^{-2}$ on aluminium from an Nd:YAG laser operating at its fundamental $1064\,nm$ wavelength, typical of the experiments carried out in this work.

For a more accurate method of temperature determination the Doppler widths of the spectral lines can be used by rearranging equation

(2.42). However as mentioned, the Gaussian component which includes the Doppler width is also broadened by the instrument function which for most compact spectrometers is significantly larger than the thermal component. Thus, the most common method for determining electron temperature is to use a measurement of relative line intensities. There are three main approaches [17]; (i) line-to-line ratios within the same charge state, (ii) line-to-line ratios of successive charge states, and (iii) line-to-continuum ratios.

Line-to-line ratios within the same charge state

In an optically thin laser plasma a spectrally integrated emission line intensity I_{nm} is given by [17]:

$$\mathrm{I}_{nm} \approx \frac{\hbar\omega_{mn}}{4\pi} A_{nm} N_m \ell \qquad (2.49)$$

Where ω_{mn} is the emission frequency, A_{nm} the atomic transition probability, N_m the excited state population distribution, and ℓ the line of sight length. Assuming a state of LTE, the relative state populations are determined by the Boltzmann equation [17]:

$$\frac{\mathrm{N_m}}{N_n} = \frac{g_m}{g_n} \exp\left(-\frac{E_m - E_n}{k_B T_e}\right) \qquad (2.50)$$

which leads to an expression for the ratio of the integrated emission line intensities arising from the two-level populations given by:

$$\frac{\mathrm{I}_m}{I_n} \approx \frac{\omega_m A_m g_m}{\omega_n A_n g_n} \exp\left(-\frac{E_m - E_n}{k_B T_e}\right) \qquad (2.51)$$

where the two individual spectral lines of interest are denoted by the subscripts m and n. Rearranging this equation for electron temperature gives:

$$k_B T_e \approx (E_n - E_m) \times \left(\ln\left(\frac{I_m \omega_n A_n g_n}{\mathrm{I}_n \omega_m A_m g_m}\right)\right)^{-1} \qquad (2.52)$$

This method is not without fault though, due to the small differences in excitation energies, theoretical uncertainties, and experimental errors. Thus it is difficult even under ideal situations to obtain errors in the measurement of $< 10\%$ [17]. This accuracy can be improved somewhat, down to approx. 5%, by measuring intensity ratios for some spectral series and plotting the logarithms of the relative intensities as a function of the excitation energies of the upper levels. This will produce a Boltzmann plot [17] which will be an approximately straight line with the reciprocal of the slope permitting extraction of the plasma temperature. The Boltzmann plot, although expected to yield a smaller error, is still challenging if errors below 10% are required, especially if only a few spectral lines and energy levels are accessible.

Line-to-line ratios of successive charge states

Due to the not insignificant errors associated with temperature determination using line ratios within the same charge state and the Boltzmann plot methods, it is often more accurate to use the line ratios of successive charge states. The larger energy separation of the ionisation energy E_∞, yields separations greater than $k_B T_e$, reducing the percentage error to as low as 1% in some cases [17]. Griem has shown that for intensity ratios of successive charge states, e.g., from an atom I_2 and the following ion I_1 the intensity ratio is given by [17]:

$$\frac{\mathrm{I}_1}{I_2} \approx \frac{A_1 g_1 \omega_1}{A_2 g_2 \omega_2}\left(4\pi^{\frac{3}{2}} a_0^3 n_e\right)^{-1}\left(\frac{k_B T_e}{E_H}\right)^{\frac{3}{2}} \exp\left(\frac{E_2 - E_1 - E_\infty + \Delta \mathrm{E}_\infty}{\mathrm{k_B} T_e}\right) \qquad (2.53)$$

where $A\,(s^{-1})$ is the atomic transition probability of each line, g the statistical weight of the upper level, $\omega\,(Rad/sec)$ the angular frequency of each line, $a_0\,(cm)$ the Bohr radius, $n_e\,(cm^{-3})$ the electron density, $E_H\,(eV)$ the ionisation energy of the Hydrogen atom, $E_1\,(eV)$ and $E_2\,(eV)$ the excitation energies of the successive ion stages, $E_\infty\,(eV)$ the ionisation energy of the lower ionic stage and $\Delta E_\infty\,(eV)$ the high-density correction factor which accounts for shifts in ionisation energy due to strong electric fields.

Line-to-continuum ratios

The final line intensity ratio method employs the ratio of the emissivity of a neutral atomic line ε_{ℓ} to the background continuum emissivity $\varepsilon_{\lambda,c}$, and is given by the formula [28]:

$$\frac{\varepsilon_{\ell}}{\varepsilon_{c}} = \frac{3^{\frac{3}{2}} h^{4} c^{3} \varepsilon_{0}^{3}}{4 e^{6} k} \frac{A_{21} g_{2}}{U_{i}(T)} \frac{\lambda_{c}^{2}}{\lambda_{\ell}} \frac{\exp\left(\frac{E_{\infty} - E_{2} - \Delta E_{\infty}}{k_{B} T_{e}}\right)}{\xi\left(1 - \exp\frac{-hc}{\lambda k_{B} T_{e}}\right) + G \exp\frac{-hc}{\lambda k_{B} T_{e}}} \quad (2.54)$$

Where $A_{21}\ (s^{-1})$, g_{2}, and $E_{2}\ (eV)$ are the transition probability, statistical weight of the upper level and upper level energy of the neutral atom transition respectively, $U_{i}(T)$ is the partition function for the ion, λ_{ℓ} and λ_{c} the wavelengths of the line and continuum emission respectively, ε_{0} the permittivity of free space, e the electronic charge, G the free-free Gaunt factor and ξ is the free-bound correction factor. This method again assumes that LTE holds for the plasma in question and is highly applicable in the early stages of a plasma where line emission and continuum emission are of comparable intensity.

Therefore, for the work presented here, due to the limited range of applicability of the line-to-continuum ratio method and the inherent error of the line-to-line ratios within the same charge state, the line-to-line ratios for successive charge states method was chosen for electron temperature determination.

This method is also not without its challenges, as can be seen from equation (2.53). To get a solution for electron temperature $k_{B} T_{e}$ is not straightforward and there are two main approaches to do so with both first requiring the electron density to be determined. This was done using the Stark broadening method as discussed in section 2.6.3. The first approach is to calculate intensity ratios as a function of electron temperature resulting in an electron density curve for each specific density as shown in Fig. 2.12. For each measured electron density and intensity ratio, the value of the electron temperature can be read directly off the plot.

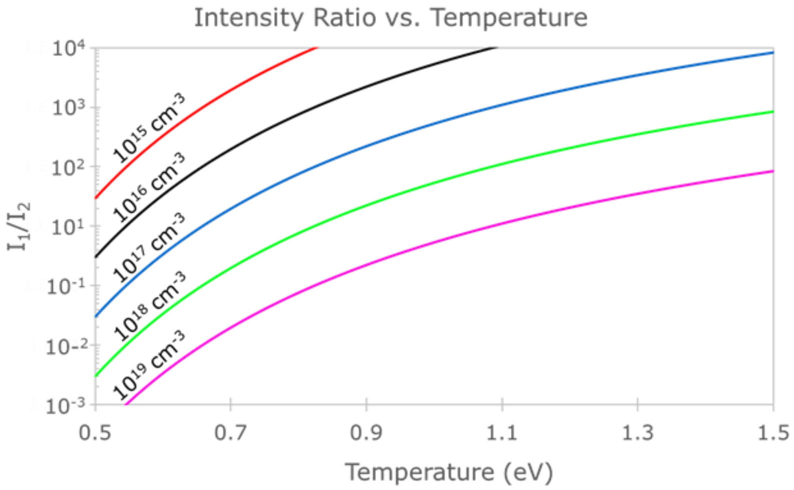

Fig. 2.12 Simulated solution to equation (2.53) from the ratio of the Al^+358.7 nm and Al 396.1 nm transitions for a range of electron densities.

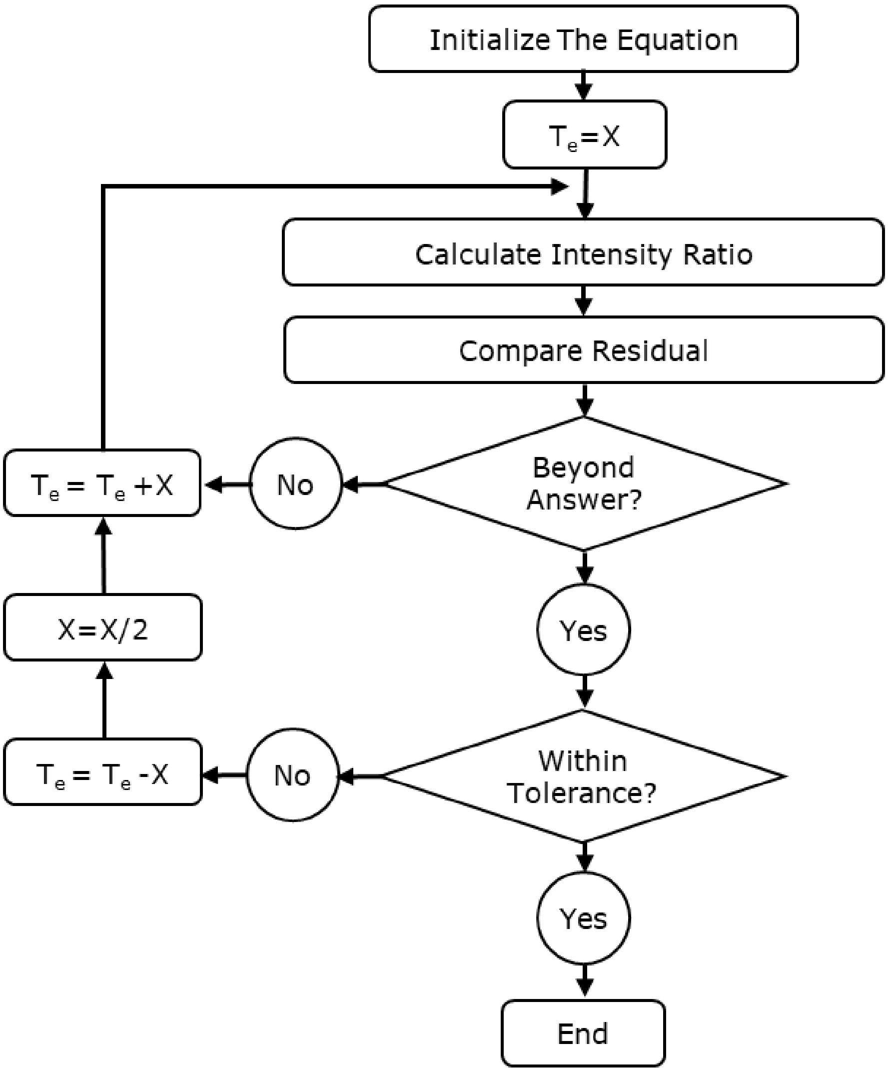

Fig. 2.13 Flow chart of the numerical method used to solve for the electron temperature in equation (2.53). The electron temperature is varied until the calculated intensity ratio is within a tolerance of the recorded value.

The other approach is to use a simple numerical method to systematically vary the temperature value until a line intensity ratio, within a set tolerance, is obtained. A basic flow chart of the numerical method used is shown in Fig. 2.13. The program initialises equation (2.53) with the recorded intensity ratio. An initial temperature value of X is set and the resulting intensity ratio calculated. This is then compared to the recorded intensity ratio and, if it is not beyond the desired value, the temperature value is increased by an amount X and the new intensity ratio is calculated and compared again. Once the calculated intensity ratio has passed the desired (goal) value the residual is compared to see if the current solution is within the allowed tolerance. If the solution is within tolerance the program ends and the solution is taken. If it is not within tolerance, the program undoes the last temperature increase, halves the X value and increases the temperature by this now smaller amount.

Although the program is not the most efficient numerical method, it will converge on a solution for the temperature value with high accuracy and with modern processing power is essentially instantaneous. In essence, both the look up or numerical solving methods will result in the same outcome. However the numerical method is faster while yielding and can allow for a more accurate result, hence it was the method employed in this work.

2.7 Summary

This chapter included the basic theory and principles of laser plasmas required for the discussion of the results in subsequent chapters. The main atomic processes, plasma parameters and equilibrium models were discussed along with a description of the formation and expansion of laser plasmas. The differences between a plasma expanding *in vacuo* and in a gas at atmospheric pressure conditions are introduced along with the concept of the formation of regions of stagnated plasma or so-called stagnation layers by colliding plasmas.

Along with the theory of laser plasmas, the underlying concepts of the different diagnostic techniques employed to investigate the laser plasmas in this work were introduced along with the different plasma parameters that they can yield.

References

1. Morozov AI (Alekseĭ I. Introduction to plasma dynamics. Illustrate. CRC Press; 2013. 815 p.
2. Fujimoto T. Plasma Spectroscopy. Birman J, Edwards SF, Friend R, Rees M, Sherrington D, Veneziano G, editors. Plasma Polarization Spectroscopy. Kyoto: Clarendon Press Oxford; 2008. 29-49 p.
3. Carroll PK, Kennedy ET. Laser-produced plasmas. Contemp Phys. 1981;22(1):61–96.
4. Cremers DA, Radziemski LJ. Handbook of Laser-Induced Breakdown Spectroscopy, Second Edition. Chichester: John Wiley & Sons, Incorporated; 2013. 432 p.
5. Eliezer S. The Interaction Of High-Power Lasers With Plasmas. London: Institute of Physics Publishing; 2002.
6. Goldston RJ, Rutherford PH. Introduction to Plasma Physics. London: Institute of Physics Publishing; 1995.
7. Bittencourt JA. Fundamentals of Plasma Physics. 3rd ed. Springer, New York. New York: Springer; 2004.
8. Amoruso S, Bruzzese R, Spinelli N, Velotta R. Characterization of laser-ablation plasmas. J Phys B. 1999;32(14):R131.
9. Singh RK, Narayan J. Pulsed-laser evaporation technique for deposition of thin films: Physics and theoretical model. Phys Rev B. 1990;41(13):8843–59.
10. Hough P, McLoughin C, Kelly TJ, Hayden P, Harilal SS, Mosnier JP, et al. Electron and ion stagnation at the collision front between two laser produced plasmas. J Phys D Appl Phys. 2009;42(5).
11. Harilal SS, Bindhu C V., Tillack MS, Najmabadi F, Gaeris AC. Internal structure and expansion dynamics of laser ablation plumes into ambient gases. J Appl Phys. 2003;93(5):2380–8.

12. Rui Z, Zhong-Cheng L, Bing H, Hong-Chao Z, Rong-Qing X, Jian L, et al. Mechanism of laser-induced plasma shock wave evolution in air. Chinese Phys B. 2009;18(5):1877–83.

13. Singh JP, Narayan Thakur S, Russo RE, Mao XL, Yoo JH, Gonzalez JJ, et al. Laser-Induced Breakdown Spectroscopy. 1st ed. Singh JP, Narayan Thakur S, editors. Amsterdam: Elsevier; 2007.

14. Freiwald DA, Axford RA. Approximate spherical blast theory including source mass. J Appl Phys. 1975;46(3):1171–4.

15. Hough P, Kelly TJ, Fallon C, McLoughlin C, Hayden P, Kennedy ET, et al. Enhanced shock wave detection sensitivity for laser-produced plasmas in low pressure ambient gases using interferometry. Meas Sci Technol. 2012;23(12).

16. Chung HK, Lee RW, Chen MH, Ralchenko Y. The How To for FLYCHK @NIST. 2008.

17. Griem HR. Principles of Plasma Spectroscopy. Haines MG, Hopcraft KI, Hutchinson IH, Surko CM, Schindler K, editors. Cambridge University Press (2005). Cambridge University Press; 1997.

18. Colombant D, Tonon GF. X-ray emission in laser-produced plasmas. J Appl Phys. 1973;44(8):3524–37.

19. P. MRW. Plasma Diagnostic Techniques. New York: Academic Press; 1965.

20. Dardis J, Costello JT. Stagnation layers at the collision front between two laser-induced plasmas: A study using time-resolved imaging and spectroscopy. Spectrochim Acta - Part B At Spectrosc [Internet]. 2010;65(8):627–35. Available from: http://dx.doi.org/10.1016/j.sab.2010.03.005

21. Rambo PW, Denavit J. Interpenetration and ion separation in colliding plasmas. Phys Plasmas. 1994;1(12):4050–60.

22. Chenais-Popovics C, Renaudin P, Rancu O, Gilleron F, Gauthier JC, Larroche O, et al. Kinetic to thermal energy transfer and interpenetration in the collision of laser-produced plasmas. Phys

Plasmas. 1997;4(1):190–208.

23. Sizyuk T, Oliver J, Diwakar PK. Mechanisms of carbon dimer formation in colliding laser-produced carbon plasmas. J Appl Phys. 2017;122(2).

24. Salzmann D. Atomic Physics in Hot Plasmas. Oxford University Press; 1998.

25. Konjevic N. Plasma broadening and shifting of non-hydrogenic spectral lines: Present status and applications. Phys Rep. 1999;316(6):339–401.

26. Abdellatif G, Imam H. A study of the laser plasma parameters at different laser wavelengths □. Spectrochim Acta Part B. 2002;57:1155–65.

27. Yeates P, Kennedy ET. Spectroscopic, imaging, and probe diagnostics of laser plasma plumes expanding between confining surfaces. J Appl Phys. 2010;108(9).

28. Aragón C, Aguilera JA. Characterization of laser induced plasmas by optical emission spectroscopy: A review of experiments and methods. Spectrochim Acta - Part B At Spectrosc. 2008;63(9):893–916.

3 Experimental Systems

3.1 Spectron Laser System

The laser system used in this work was a Spectron™ SL803 class-4 Q-Switched Nd:YAG laser, shown in Fig. 3.1, producing linearly polarised pulses with a FWHM pulse width of approximately $18\,ns$. The SL803 utilises both an oscillator and amplifier to achieve high pulse energies of up to $850\,mJ$ when operating at maximum power. The amplifying medium in each of the oscillator and amplifier is a rod of crystalline yttrium aluminium garnet ($Y_2Al_{12}O_{12}$) doped with neodymium ions (Nd^{3+}), abbreviated to Nd:YAG, which gives a fundamental wavelength of $1064\,nm$. A summary of the SL803s parameters can be seen in Table 3.1.

Table 3.1 Specification of the Spectron™ SL803 Laser System

Spectron SL803	
Lasing Medium	Nd:YAG
Wavelength	1064 nm (Fundamental)
Energy	350 mJ (850 mJ Max)
Pulse Length	18 ns (± 1 ns) FWHM
Repetition Rate	1 Hz
Trigger Jitter	< 1 ns

The principle of the Q-switched laser is that an electro-optic Q-switched shutter is positioned within the laser cavity to prevent stimulated emission from occurring within the laser rod which in turn leads to a substantial population inversion between the upper and lower levels of the lasing transition. When the Q-switch is triggered the shutter becomes transparent and the photons can traverse the laser cavity depleting the population inversion producing an intense and short (few ns to few $10\,ns$) laser pulse [1]. Essentially it is a process of changing the quality factor of the laser cavity from one of heavy losses to one of high quality, hence the naming convention Q-Switch. The SL803 uses an active Q-Switch which is made up of a polariser, Pockels cell and quarter-wave plate [2]. As the lasing medium is optically pumped via the flashlamps, a beam propagates within the laser cavity

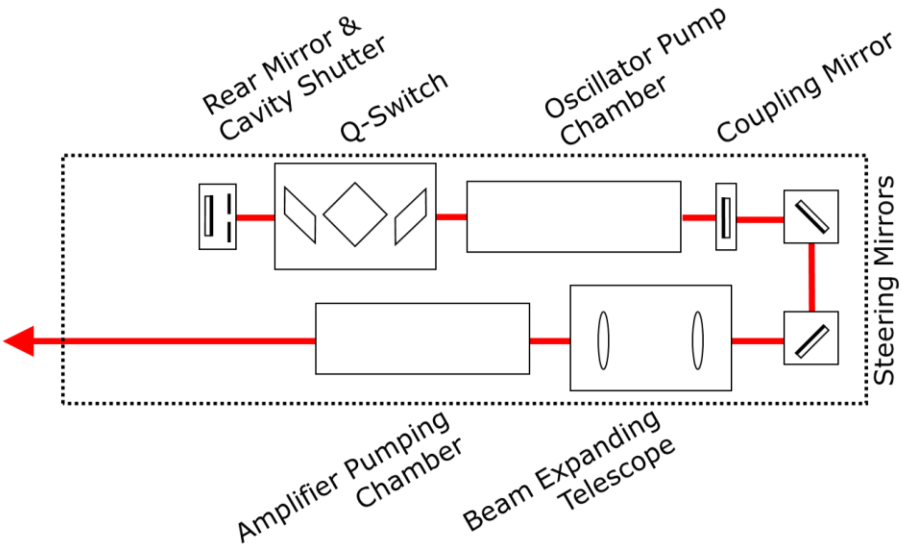

Fig. 3.1 Schematic of the Spectron™ SL803 laser system. The SL803 is a Q-Switched Nd:YAG laser with an oscillator and an amplifier. [2]

making a double pass through the Q-switch assembly. On the first pass the light will be horizontally polarised. It then passes through the Pockels cell, which has a voltage applied across it to act as a ¼-wave plate, and so the light becomes circularly polarised. The circularly polarised light then reflects off the rear cavity mirror and passes back through the Pockels cell thereby becoming vertically polarised and hence blocked by the polariser so that laser oscillation cannot proceed. When the Q-Switch is activated, the ¼-wave plate voltage on the Pockels cell is suddenly dropped to zero and light can freely propagate within the cavity. As result, lasing can occur [2]. The Pockels cell is triggered at the point of peak population inversion in order to maximise optical output and ensure a good pulse to background light contrast (i.e., no pre- or post-lasing).

As the experiments for this thesis were carried out in air at atmospheric pressure the laser pulse energy was reduced to $350\,mJ$ via lowering the pump energy of the amplifier. Furthermore, twin attenuators, shown schematically in Fig. 3.2, were incorporated into the laser beam path in order to have full control over the already reduced pulse energy. Each attenuator is comprised of a ½-waveplate and cube polariser. The ½-wave plate rotates the polarisation of the incident pulse so that a

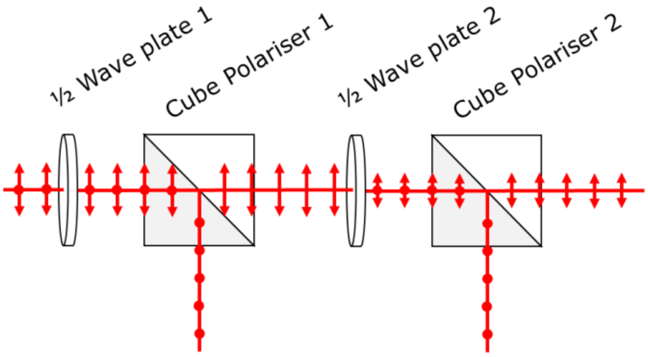

Fig. 3.2 Basic schematic of the ½-Wave plate polariser attenuator pairs. Stacking two of these systems allows fine control of the laser pulse energy without changing the beam profile.

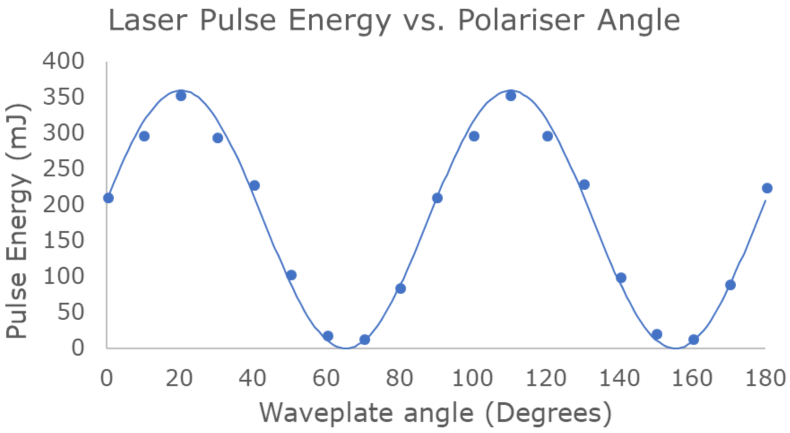

Fig. 3.3 Spectron SL803 (average) pulse energy vs. ½-waveplate angle. Experimentally measured using a Coherent PowerMax PM30 power meter.

relative angle θ between the incident (polarised) laser pulse and the cube polariser is formed. Rotating the ½-waveplate by an angle θ results in a rotation of the polarisation plane of the laser by 2θ. Hence from Malus's law the intensity exiting the cube polariser is given by the expression:

$$I = I_0 \cos^2 2\theta \tag{3.1}$$

where I is the intensity of the pulse transmitted through the polariser and I_0 is the pulse intensity incident on the half waveplate.

Fig. 3.3 shows the resulting calibration curve for average pulse energy as a function of the ½-waveplate angle, which was experimentally measured using a Coherent™ PowerMax PM30 power meter. Each point on the plot is the result of averaging 20 pulses for each ½-waveplate position.

3.2 Fast Imaging and Intensified CCD (ICCD) Cameras

A major part of the work presented here is concerned with plasma formation, evolution and interactions with both the laser field and ambient air. The first diagnostic of choice to investigate these interactions is time resolved (or gated) imaging which permits the spatial evolution of the plasma to be recorded as a function of time, i.e., to track its spatial evolution.

Fast imaging of laser plasmas is a widely deployed technique and if the imaging is performed by applying a fast-electronic shutter to gate the camera sensor, the emission of the plasma can be both spatially and temporally investigated. This opens the possibility to track the plasma plume's evolution and expansion by setting the gate width (exposure time) t_g to a few nanoseconds and varying the delay in the camera acquisition t_d with respect to the incident laser pulse, as shown in Fig. 3.4.

Using gate widths of just a few nanoseconds and noting that the optical signal intensity of the plasma will decay rapidly as the plasma relaxes requires the use of ICCD cameras. Two different intensified charge coupled device (CCD) cameras were used during this work for time-resolved imaging and spectroscopy. The spectrometer system was provided (on loan) from Andor Technology™ comprising a Kymera spectrograph with a high resolution intensified camera (for beta testing in the DCU laboratory). More information on the spectrometer will be given in section 3.3.

For the imaging experiments an Andor™ DH5H7 ICCD (intensified CCD) model camera with 512×512 pixels was used. The pixels on the CCD chip were each $24\,\mu m \times 24\,\mu m$ in size, resulting in an active imaging area of $12.3\,mm \times 12.3\,mm$. The DH5H7 ICCD utilises an intensifier, which is coupled to the CCD via a fibre optic stub and allowed for reliable optical gate widths (exposure times) as low as $10\,ns$.

The high (spatial) resolution intensified camera utilised in the spectroscopy measurements and was an Andor™ iStar sCMOS model

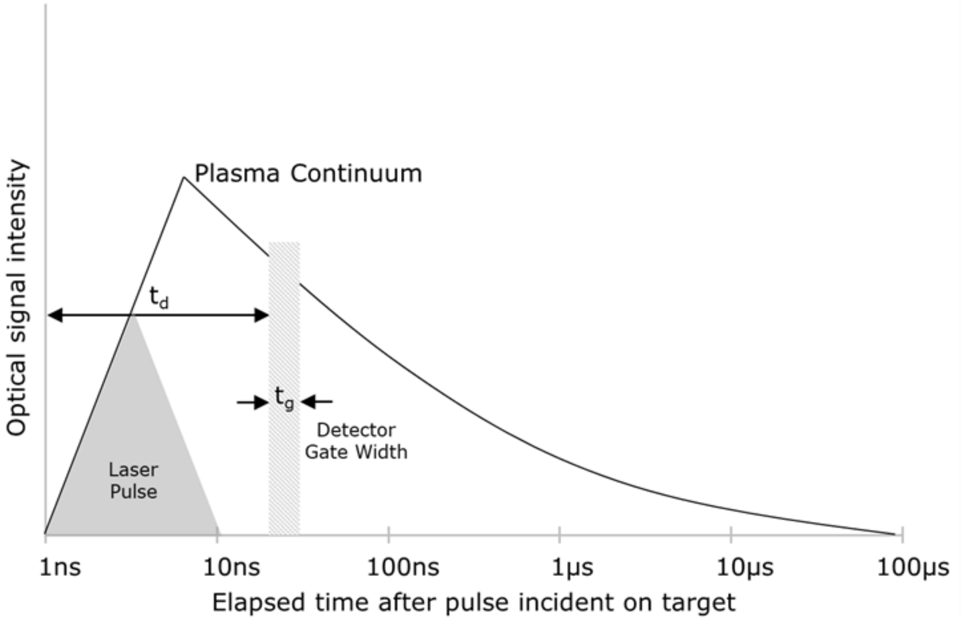

Fig. 3.4 Schematic of the optical signal intensity vs. elapsed time after the pulse from the laser. It can be seen that during the first ~10 ns the optical signal intensity rises sharply before relaxing over time as the plasma evolves. Also shown are the laser pulse duration and detector gate width t_g, which is delayed by some time t_d with respect to the laser pulse. Recreated from [4].

camera. The iStar has a CMOS sensor with 2560×2160 pixels, with pixel sizes of $6.5\,\mu m \times 6.5\,\mu m$ resulting in an active imaging region of $16.6\,mm \times 14\,mm$. Again, the sensor is coupled to the intensifier via a fibre optic coupler and the iStar sCMOS was capable of exposure times down to $2\,ns$.

The Andor Technologies™ intensifier used in both cameras consists of three main components Fig. 3.5 [3]:

- A photocathode
- A micro-channel plate (MCP)
- An output phosphor screen.

The photocathode is coated onto the inside surface of an input window. When an incoming photon strikes the photocathode an electron is emitted via the photoelectric effect. This photoelectron is accelerated towards the MCP via an electric field.

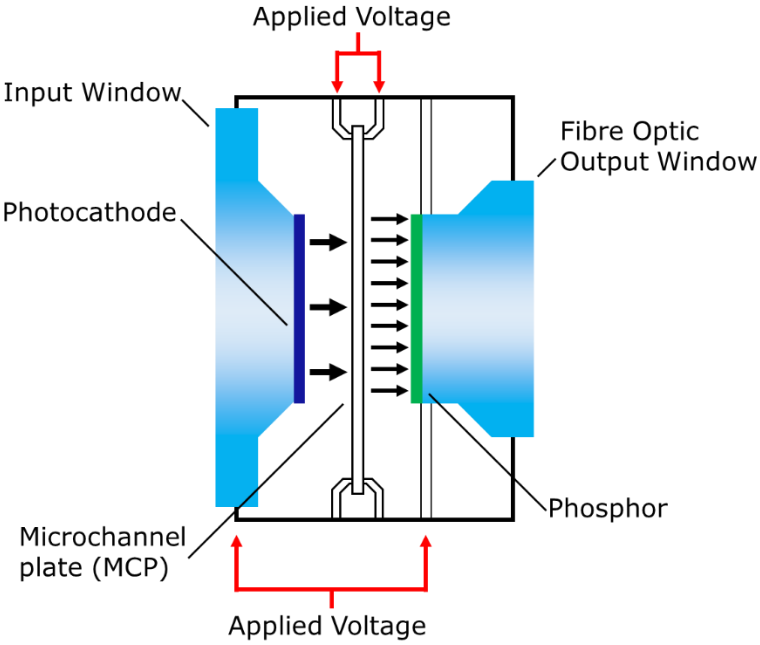

Fig. 3.5 Schematic of the Andor™ image intensifier. An incoming photon strikes the photocathode which emits an electron. The electron is accelerated down one of the MCP channels, colliding with the sidewalls, creating secondary electrons, as it does so. Thus a weak optical image, focused onto the photocathode, results in a bright electron replica at the output of the MCP. The electron image strikes the phosphor to form a corresponding bright optical image which is focused onto the camera CCD sensor. The number of secondary electrons emitted can be varied by controlling the applied voltage on the MCP allowing control of the gain. Image recreated from [3].

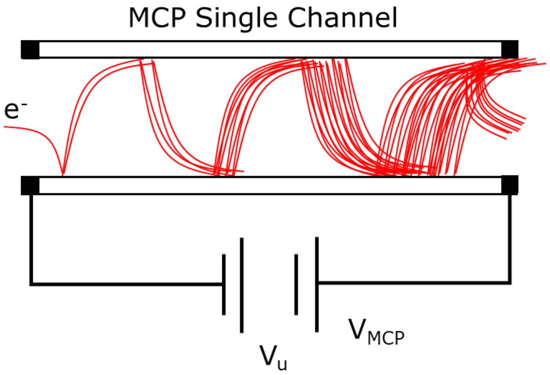

Fig. 3.6 Schematic view of an MCP Single Channel amplification process. As an incoming electron e^- cascades down the channel it produces a series of secondary electrons via impact ionisation. Recreated from [3].

The MCP is a thin disk comprised of a honeycomb-like array of glass channels, each $\sim 10\,\mu m$ in diameter. Each channel is internally coated with a secondary electron emitting material. Thus the MCP acts as a matrix of photomultiplier tubes. A high voltage, V_u, is applied across the MCP, on the order of $0.5\,kV$ to $1k\,V$, so that an incoming photoelectron will cascade down the channel, producing an avalanche of secondary

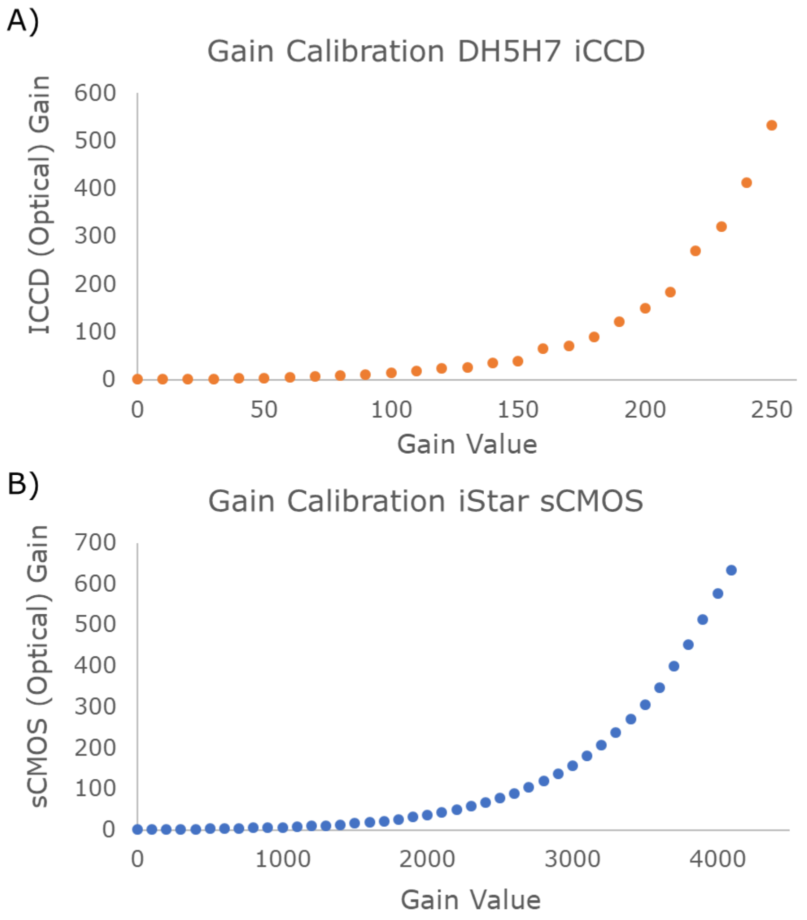

Fig. 3.7 Gain calibration curves for A) Andor™ DH5H7 ICCD and B) Andor™ iStar sCMOS cameras of recorded HeNe 632.8 nm over a range of gain settings.

electrons via impact ionisation resulting in an amplification or gain of the electron signal as seen in Fig. 3.6. This gain in electron number, and hence the final optical gain, can be controlled by varying the voltage across the MCP. Gating the MCP for a short period of time results in a fast optical shutter (on the order of nanoseconds), with the signal during the gate opening time being intensified while signal outside of this gate time will fall below the detection limit of the CCD or CMOS readout sensor.

Secondary electrons created will go on to strike and excite a phosphor screen. The phosphor screen is coated onto a coherent fibre optic window which is coupled to the CCD detector. The function of the phosphor is to convert the incident electron pattern into a visible light pattern which can be focused onto and read out from the camera sensor.

The gain in signal achievable from the intensifiers on the two cameras used in this work was on the order of $\times 600$ and was experimentally determined using a HeNe laser as a source. Emission from the $632.8\,nm$ laser was measured as a function of the camera gain setting and plots of the optical gain vs. the camera gain setting were constructed (Fig. 3.7.). These calibration plots allowed for relative intensity corrections when comparing images acquired at different gains for each ICCD.

3.3 Kymera Spectrometer

Perhaps the most powerful diagnostic tool for laser plasmas is optical emission spectroscopy (OES). Laser plasmas although short-lived, are bright luminous sources of spectral information. Spectra can be recorded in time-integrated mode or, in combination with fast-imaging, as time-resolved data. It is here where the full potential of spectroscopy as a plasma diagnostic tool is realised. Time-resolved spectra provide an insight into the atomic processes occurring within the plasma and analysis of the resulting spectra allows important parameters such as plasma temperature and density in the mid to late phases of the radiative lifetime of a plasma to be extracted.

High-resolution spectroscopy studies were performed using an Andor Technologies™ Kymera 328i Spectrograph. This spectrometer was provided on loan by Andor Technologies™ along with a high resolution iStar sCMOS intensified camera as part of a beta test program. The Kymera spectrograph itself, shown schematically in Fig. 3.8, uses a Czerny-Turner optical layout with astigmatism-corrected toroidal focussing mirrors, providing flat field imaging capability. It has a focal length of $328\,mm$ and a numerical aperture of $F/4.1$ [4]. As the spectrometer was stigmatic, it yielded spatial resolution along the direction of the entrance slit.

The Kymera 328i has a number of useful features including a quad-grating turret, adaptive focus, and fully automated control for high repeatability in wavelength selection. The quad-grating turret allowed

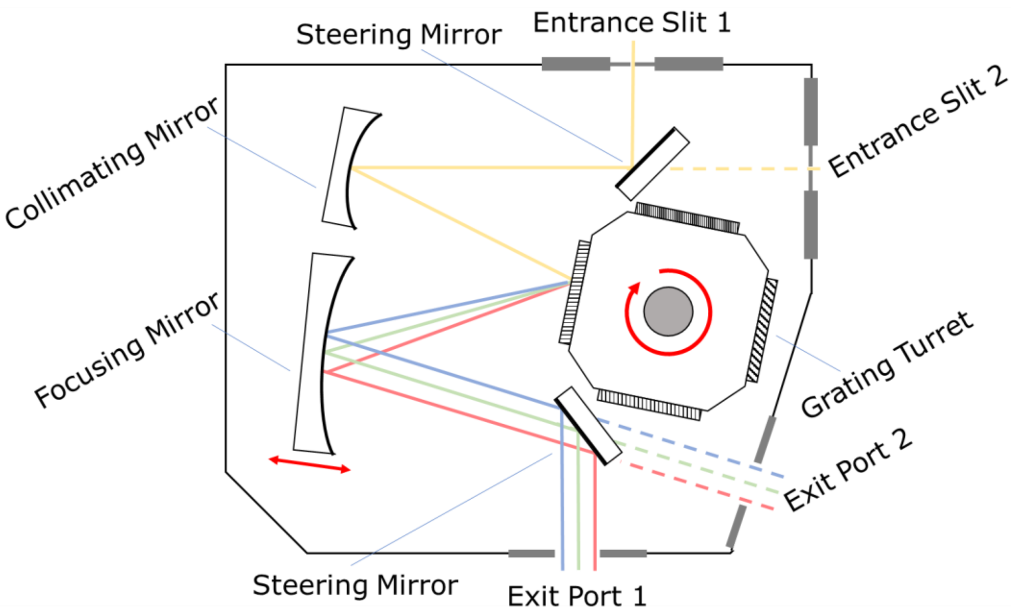

Fig. 3.8 Schematic of the Andor Technologies™ Kymera 328i spectrograph. The Kymera 328i uses a Czerny-Turner layout and has a focal length of 328 mm and a numerical aperture of f/4.1.

seamless swapping between gratings, without the need to recalibrate the spectrometer after each change. The four gratings loaded into the Beta test model were blazed for the UV-VIS region and ranged between 300 lines/mm and 2400 lines/mm. The resulting wavelength windows and FWHM instrumental widths obtained experimentally are shown in Table 3.2.

Table 3.2 Grating specifications for the Andor Technologies™ Kymera 328i spectrometer. Window size and FWHM linewidths were obtained experimentally using Cd & Hg gas discharge lamps.

	Blaze Wavelength (nm)	Lines/mm	Window size (nm)	FWHM (nm)
Grating 1	Holographic 250	1800	21.35	0.15
Grating 2	300	300	164.16	1.5
Grating 3	300	1200	36.56	0.8
Grating 4	Holographic 220	2400	16.3	0.08

This range of gratings allowed low resolution but broad sweeps of the UV-VIS region (ca. $164\,nm$ wide window) using Grating 2 (300 lines/mm) all the way up to high-resolution measurements ($0.08\,nm$ FWHM) using Grating 4 (2400 lines/mm), albeit with a much narrower wavelength window captured by the ICCD (ca. $16\,nm$). Adaptive focus is a patented feature that utilises a stepper motor on the focussing mirror to

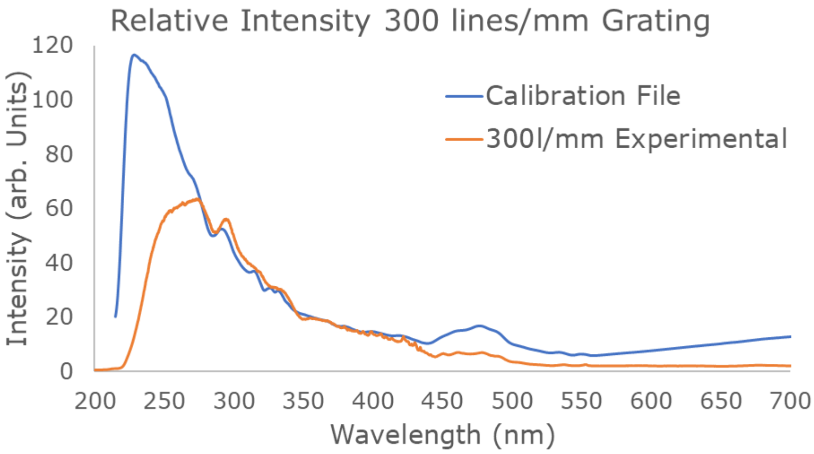

Fig. 3.9 Comparison of Ocean Optics™ Deuterium-Halogen lamp calibration file with experimental data recorded with Grating 2 (300 lines/mm) for relative intensity correction.

automatically optimise the focus of the spectrometer when swapping between gratings to ensure optimum spectral resolution for each grating, as opposed to an intermediate (compromise) focus for all four gratings [4]. Automated control of the grating turret position allows single-grating and grating-to-grating centre wavelength repeatability down to $4\,pm$ and $10\,pm$ respectively, ensuring confidence in the calibration and obviating the need to manually calibrate between gratings after each change. Wavelength calibration was performed using well known emission lines from Cd and Hg gas discharge bulbs for the UV-VIS region. For relative intensity calibration a certified Ocean Optics™ deuterium-halogen lamp was used. The experimentally recorded irradiance of the deuterium-halogen lamp is compared against the calibration file and a correction factor $\alpha(\lambda)$ can be calculated as:

$$\alpha(\lambda) = \frac{Measured\ Spectrum}{Calibration\ Spectrum} \qquad (3.2)$$

This was repeated for the various gratings used within this work. An example of the differences found between the calibration file and the experimentally recorded data is shown in Fig. 3.9. Using this relative intensity calibration data for different centre-wavelength regions, all experimental spectra can be normalised to each other so that line intensity ratios can be confidently used when extracting electron temperatures from them.

3.4 Target Geometries

The target design for colliding plasma experiments under atmospheric pressure air conditions began by building from previous work within the research group [5–10]. V-shaped channels of different angles would allow the relative collisional velocity of the two seed plasmas to be varied and compared as can be seen in Fig. 3.10A. Due to the additional confinement when working in a background gas at atmospheric pressure, sharper angles of 30°, 60°, and 90° were chosen to ensure that the relative collisional velocity was high, and the seed plasmas would not be hindered from interacting with one another by the intervening high-pressure air. The V-channel would also permit the formation of the two seed plasmas, with one forming on each of the channel walls. This eliminates the need to split the beam with prisms or similar optics while also decreasing the distance between the seed plasmas to minimum values. This did however require the laser to have a somewhat larger focussed spot size to ensure both walls of the V-channel were irradiated as shown in the schematic Fig. 3.10B.

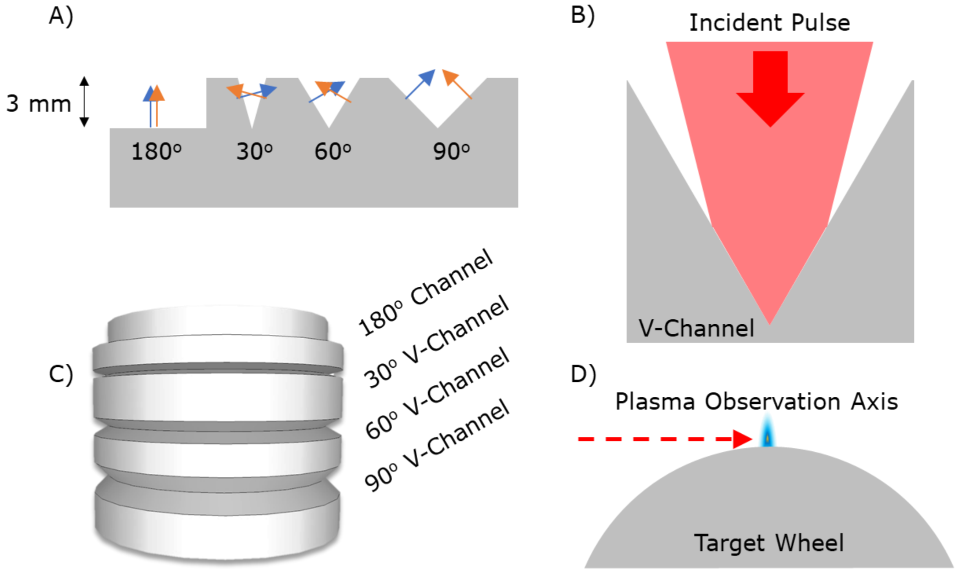

Fig. 3.10 A) Schematic of the target design, 30°, 60°, and 90° V-channels and a 180° flat target. B) Schematic of incident laser impinging on the two walls of a V-channel. C) Design for the actual target wheel used in the experiments shown in this work. D) Plasma observation direction with relation to target wheel.

The final targets were made cylindrical with the angles of choice and a 180° flat target for comparison purposes, cf. Fig. 3.10C. The cylindrical shape provides a large target area for multiple laser shots, but also the observation axis could be chosen orthogonal to the target ensuring the plasma was not blocked. The target wheel was mounted in a rotatable holder to expose a fresh target surface after each shot to the laser and this was then mounted onto an XYZ translation stage for fine alignment with respect to the laser focus.

3.5 Optical Delivery System

During the investigation into colliding plasmas in air under atmospheric conditions there were two main experimental setups used, a fast imaging setup, and an optical emission spectroscopy (OES) setup. The laser optical delivery system for each of these setups did not change and is shown in Fig. 3.11. The laser system used was the Spectron™ SL803 Nd:YAG (detailed in section 3.1) operating at its fundamental $1064\,nm$ wavelength. The attenuators were used to bring the pulse energy down to $20\,mJ$, which was sufficiently low that air breakdown

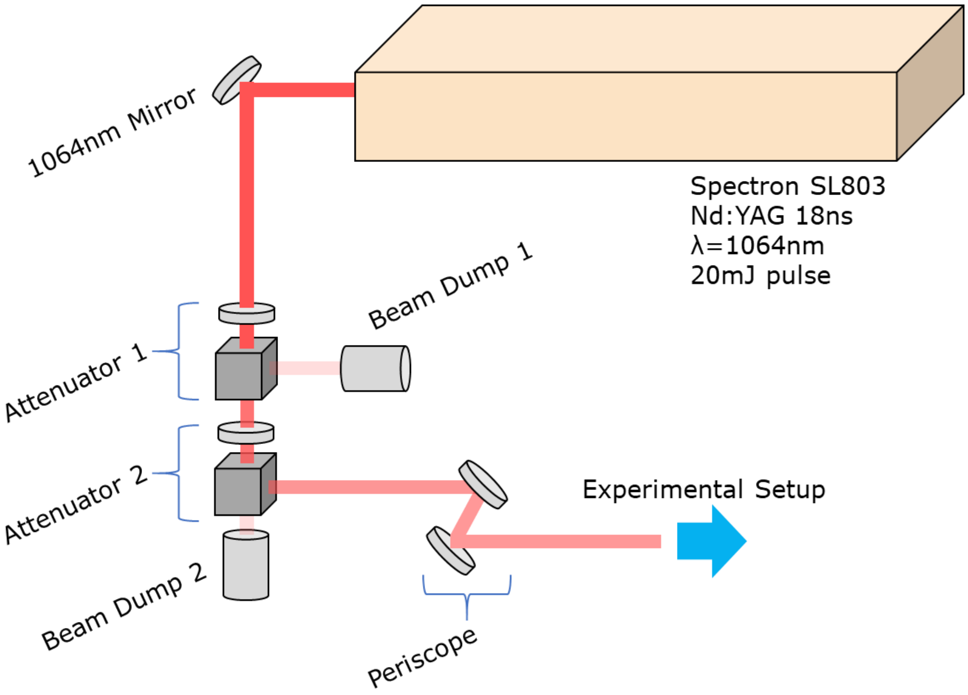

Fig. 3.11 Schematic of the optical delivery system used in the imaging and spectroscopy experiments for colliding laser plasmas in air .

would not occur while being comfortably above the breakdown threshold for the aluminium target surface. Excess beam energy was sent to two teflon beam dumps. The $20\,mJ$ pulse was sent through a periscope to bring the laser beam to the height of the optical components on the experimental bench ready for experiments.

The laser flashlamps were externally triggered via a Quantum Composers™ model 9514 pulse generator running at pulse repetition frequency of $1\,Hz$. The Q-Switch delay was set to a $160\,\mu s$ for optimum giant pulse production. Further details of the system synchronisation and timing can be found in section 3.8.

3.6 Fast Imaging Setup

The fast imaging setup can be seen in Fig. 3.12. After the laser pulse passes through the optical delivery system it is focussed onto the target using a plano-convex lens of focal length $75\,mm$. The emission from the resulting plasma was collected and imaged onto the Andor™ DH5H7 ICCD through a relay lens system comprising two $\phi 25\,mm$ bi-convex UV fused silica (UVFS) lenses, shown schematically in Fig. 3.13A. The relay lens system works not only to image the plasma plume onto the ICCD but can also be used to magnify the image. The first lens L_1 is placed a distance equal to the focal length of the lens f_1 from the object. The resulting parallel rays are then collected and focussed onto the camera sensor by the second lens L_2. The camera is placed at a distance corresponding to the focal length of the second lens f_2. The magnification of the system is equal to the ratio of the focal lengths of the lenses, i.e., $f_2\,/\,f_1$. The two UVFS lenses used had focal lengths of $f_1 = 50\,mm$ and $f_2 = 150\,mm$ resulting in a magnification of $3\,\times$. In order to check for a sharp focus, a backlit pin was placed at the laser target interaction zone and imaged onto the camera. Sample images are shown in Fig. 3.13B where the pin is in sharp focus within the 60° V-Channel. Another sample image is shown in in Fig. 3.13C where a clear ruler with millimetre rulings was backlit with a white light source and imaged onto the ICCD. This image was used to transform the scale

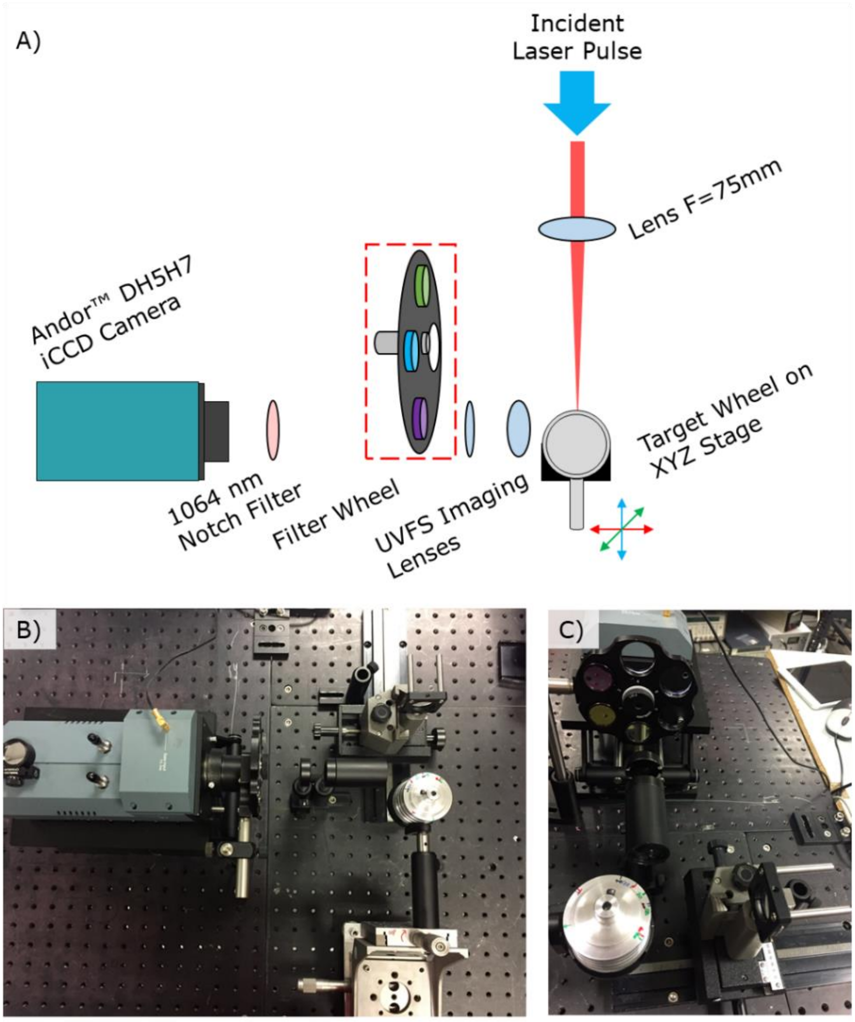

Fig. 3.12 Schematic of the fast-imaging experimental setup along with corresponding photographs from the laboratory. The filter wheel shown in the dashed box was removed when undertaking broadband imaging.

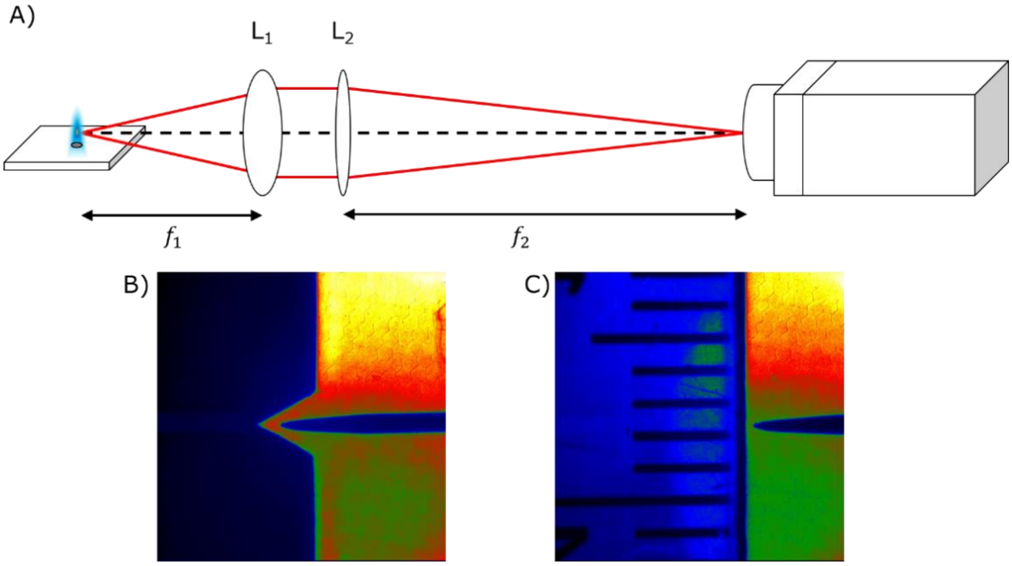

Fig. 3.13 A) Schematic of the lens relay system. The object is placed at a distance equal to the focal length of lens 1 (f_1) and the image will be formed at a distance equal to the focal length of lens 2 (f_2). The magnification of the system will be approximately in the ratio f_2/f_1. B) Backlit sample image of a pin in the 60° V-channel. C) Backlit sample image of a clear ruler and pin.

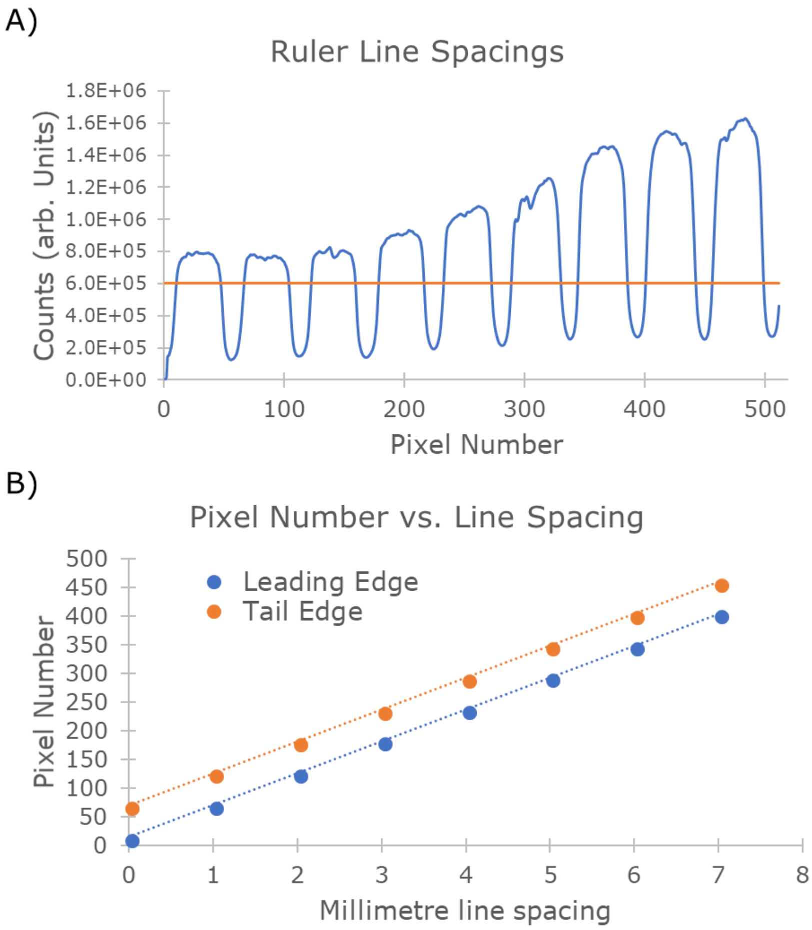

Fig. 3.14 A) Binned data of millimetre ruler spacings from backlit image. B) Plots of the pixel number vs. line spacings to extract number of pixels per millimetre for spatial calibration.

of the images recorded from pixel number to mm. The image of the ruler is binned over the region of the rulings and plotted in Fig. 3.14A, where each of the local minima corresponds to a dark ruling. As the backlighting field was not flat, the image intensity is not uniform and hence a threshold level at which to make measurements was required, shown via the orange line in the plot. When the intensity crossed this threshold the corresponding pixel number was noted and plotted against the corresponding ruling location (Fig. 3.14B). Two lines are created each corresponding to the leading edge and trailing edge respectively, the slope of which determines the average number of pixels corresponding to one millimetre, hence allowing calibration of pixel number terms of mm.

For the spectrally resolved fast imaging experiments, narrow bandpass filters were introduced via the filter wheel to isolate the plasma emission

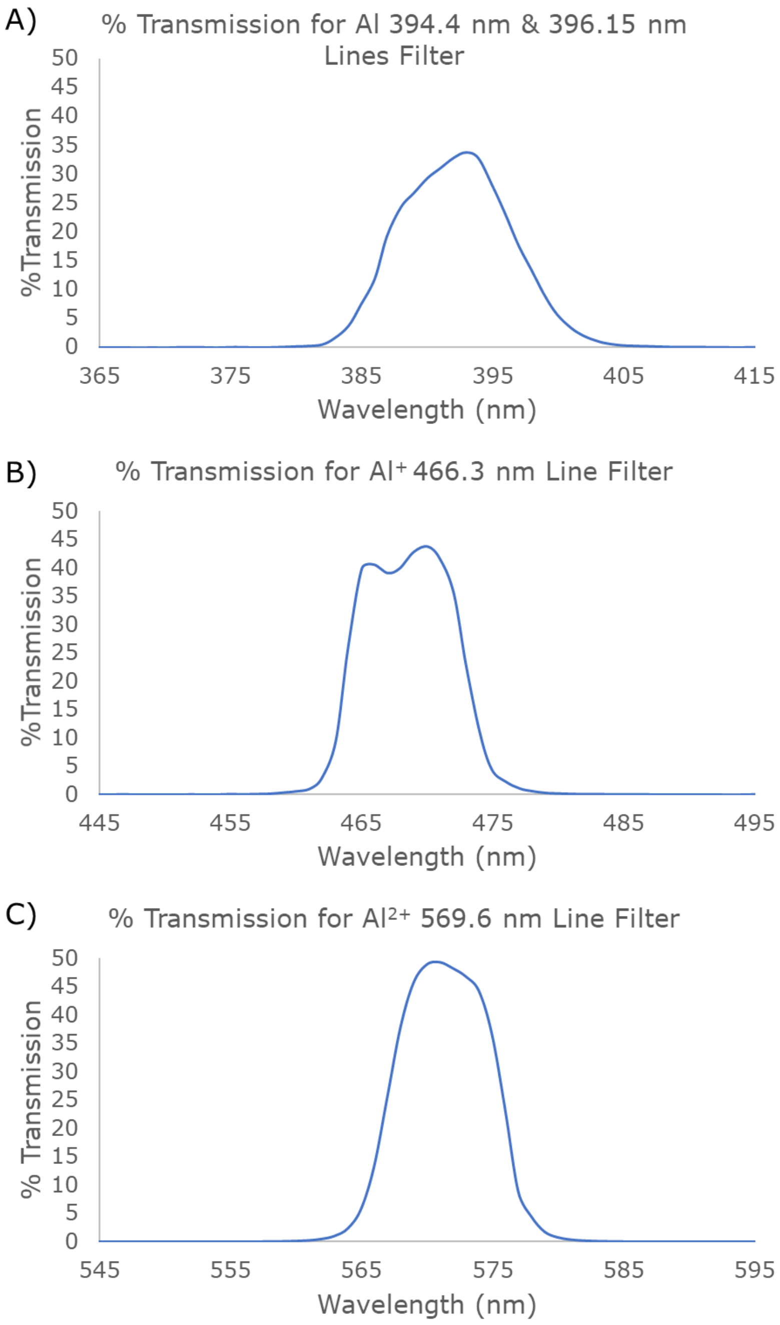

Fig. 3.15 Transmission curves for narrow bandpass filters used in the filtered imaging of A) Al 394.4 nm & 396.15 nm lines, B) Al^{+} *466.3 nm line, and C)* Al^{2+} *569.6 nm line.*

due to specific transitions of the neutral atom or ions. Only radiation from these transitions reaches the camera and so the spatial evolution of different excited state atoms/ions could be monitored over time. The filters used covered the neutral $Al^0\ 394.4\,nm$ and $396.15\,nm$ lines, the $Al^+\ 466.3\,nm$ line, and the $Al^{2+}\ 569.6\,nm$ line. The transmission curves for these filters are shown in Fig. 3.15.

In addition to the bandpass line filters, during acquisition of both the broadband and filtered images a series of 1%, 10%, and 30% neutral density filters were used to prevent ICCD saturation during the early, and hence bright, stages of the plasma plume evolution. In addition, all imaging was performed with a $1064\,nm$ notch filter used to block scattered laser light from the camera.

In order to correct for all of the different filters used, transmission data for the filters was obtained with the aid of a UV-VIS spectrophotometer and the corrected image intensity I_0, was determined as:

$$I_0 = I \times \left(T_N T_{Nd} T_{Bp}\right)^{-1} \tag{3.3}$$

Where I is the intensity recorded by the camera and T_N, T_{Nd}, and T_{Bp} are the transmissions of the notch filter, neutral density filter, and bandpass filter present respectively. This intensity correction was made during the image analysis along with gain correction and background subtraction.

3.7 Optical Emission Spectroscopy (OES) Setup

Fig. 3.16 shows the system used for the optical emission spectroscopy. As before the laser is focussed onto the target wheel with a lens of focal length $75\,mm$. The relay lens system collects and images the optical plasma radiation onto the entrance slit of the Andor™ Kymera 328i spectrograph (described in section 3.3). Again, magnification was determined by imaging a backlit ruler through the spectrometer with the slit open to its maximum width. This allowed the image pixel values to be spatially transformed into mm. As the spectrograph allowed space resolution along the slit direction, a dove prism could be introduced to the system in order to rotate the plasma image through 90°, so that the expansion of the plasma could be aligned with the entrance slit, as shown in Fig. 3.17.

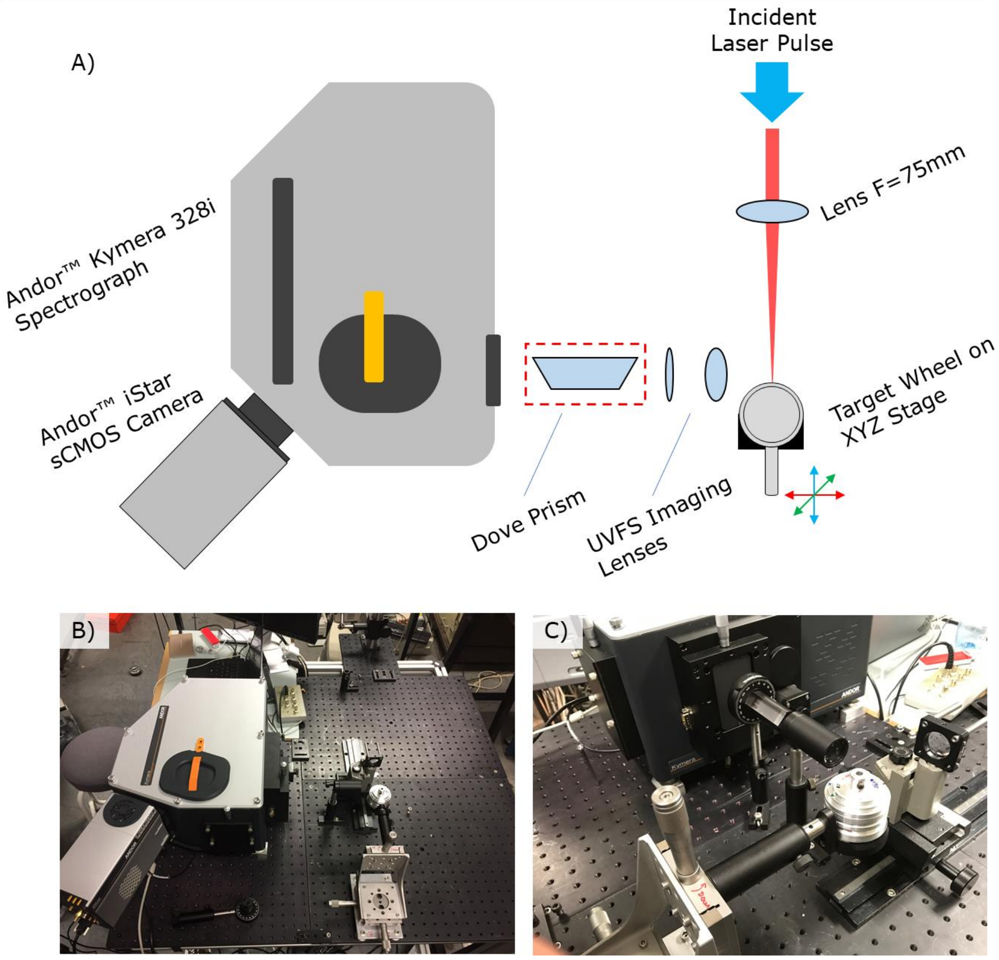

Fig. 3.16 Schematic of the optical emission spectroscopy experimental setup along with corresponding photographs from the laboratory. The dove prism shown in the dashed box was added/removed as needed.

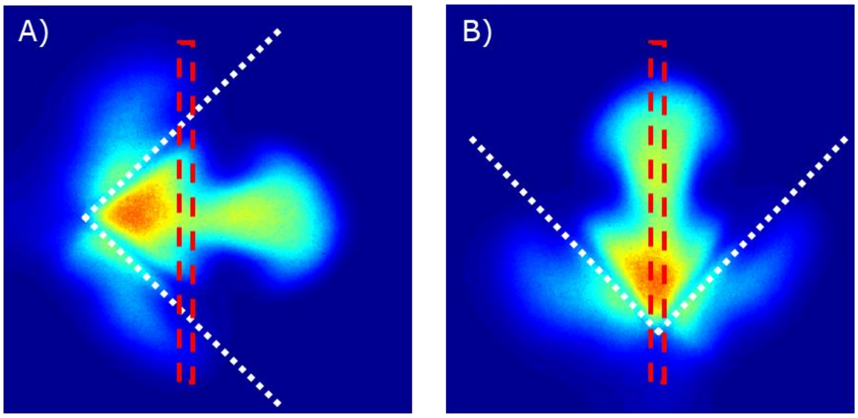

Without Dove Prism

With Dove Prism

Fig. 3.17 Function of the dove prism. With the dove prism present the image of the plasma is rotated 90^o so that the plasma expansion is directed along the entrance slit of the spectrograph.

3.8 Synchronisation and Timings

In order to synchronise laser pulses with the gated intensified cameras for the time resolved measurements, the laser flashlamps and Q-Switch were externally triggered using a timing system shown in Fig. 3.18. This comprised two delay generators, in combination with AND gates and an inverting amplifier. One delay generator was used to control the laser (Quantum Composers Plus model 9514) and the other was used to control the gate duration and delay of the intensified CCD cameras (Stanford instruments model SG535).

A $15\,V$ active-low signal, with a duration of $10\,\mu s$, firing at a pulse repetition rate of $1\,Hz$ was delivered to the laser flashlamps from channel-A of delay generator 1. Channel-B was set to deliver a $10\,\mu s$ TTL pulse at a pulse repetition rate (PRF) of $1\,Hz$ with a delay of $160\,\mu s,$ to one input of AND gate 1, the output of which was coupled to laser Q-Switch trigger input via an inverting amplifier and also connected to one input of AND gate 2. Channel C was fed to one input of AND gate 2, the output of which was used to trigger delay generator 2. To open the AND gates, and allow the Q-switch to be triggered, yielding an optical pulse, a $1000\,\mu s$ TTL trigger signal is sent from the 'FIRE' output of the Andor trigger box to one input of the AND gate 1. This opens the AND gate and results in the next $10\,\mu s$ TTL signal from channel B passing through to the inverting amplifier to become a $15\,V$ active-low pulse of $10\,\mu s$ duration to activate the Q-Switch, thereby firing the laser.

For the camera synchronisation the output from the first AND gate is coupled to the second AND gate along with a $10\,\mu s$ TTL pulse from channel-C from delay generator 1. Channel-C is synchronised to channel-B with a delay corresponding to the time it takes the laser pulse to pass through the optical delivery system and is represented as t_0 in the timing diagram. This is determined experimentally and is on the order of nanoseconds.

The output of the second AND gate is fed to the external trigger for the second delay generator, and a pulse from that delay generator is sent to the camera gate with a duration equal to the gate width

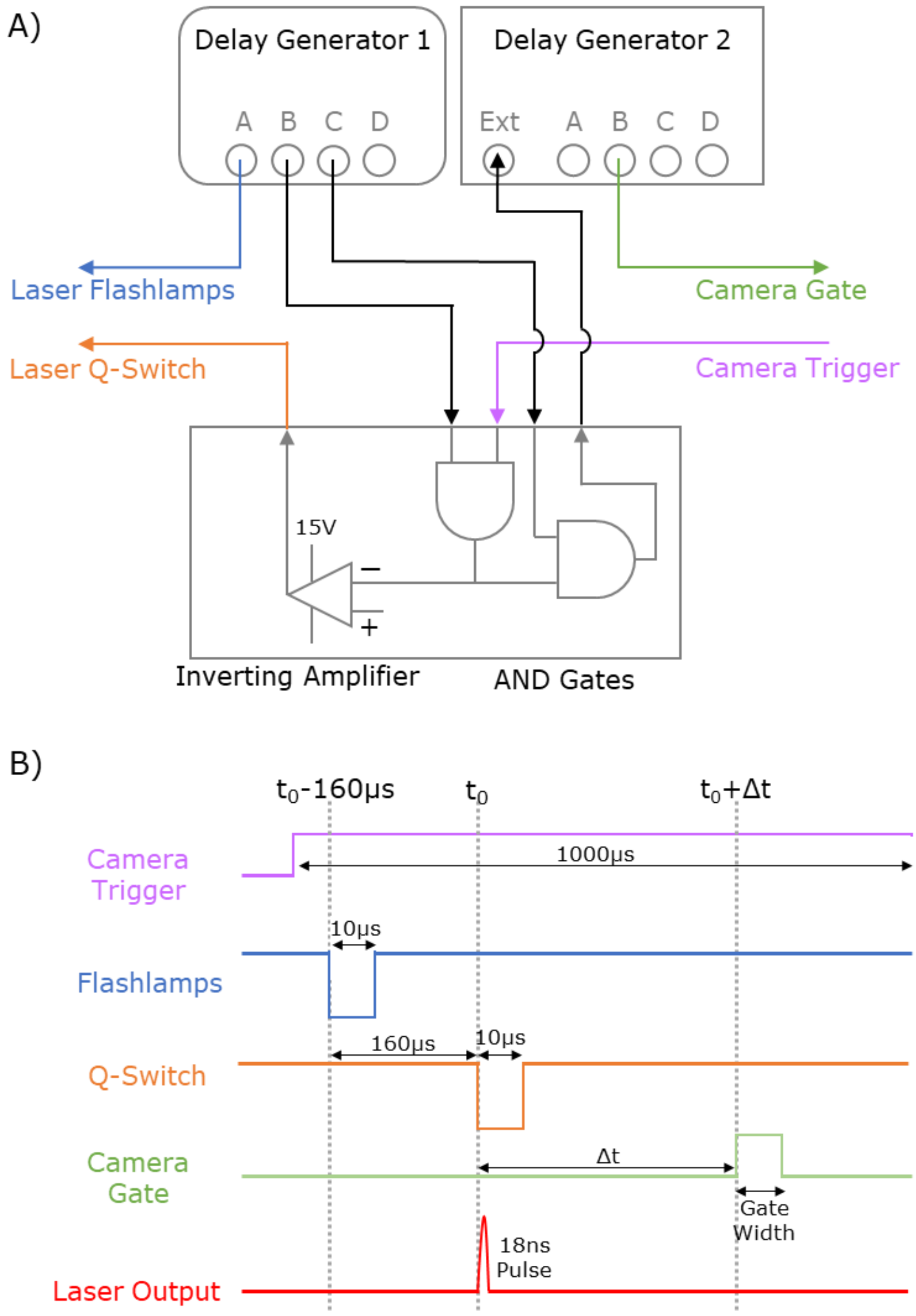

Fig. 3.18 A) Timing and synchronisation system for the laser plasma experiments undertaken B) Corresponding timing diagram. Δt, the time delay between the triggering of the laser Q-Switch and the ICCD is swept throughout the experiment to obtain time resolved plasma images.

(typically $10\,ns$ for this work). This gating pulse can be further delayed by introducing a time delay Δt allowing time resolved images and spectra to be obtained.

3.9 Summary

Presented in this chapter was an overview of the experimental systems used in this work. The main components such as the Spectron™ SL803 laser system, the Andor intensified cameras, and the Andor Kymera 328i spectrograph were all described along with providing key information of the instrument performance and calibration.

The experimental set-ups used for the fast imaging and optical emission spectroscopy were also presented and discussed along with a basic description of the synchronisation and timing diagram required to perform the time resolved experiments.

References

1. Cremers DA, Radziemski LJ. Handbook of Laser-Induced Breakdown Spectroscopy, Second Edition. Chichester: John Wiley & Sons, Incorporated; 2013. 432 p.
2. SL800 Series Pulsed Nd:YAG User Manual. Rugby, Warwickshire: Spectron Laser Systems; 1996.
3. New iStar ICCD User Guide. Andor Technology; 2012.
4. Kymera 328i User Guide. Andor Technology; 2017.
5. Fallon C. Optical Diagnostics of Colliding Laser Produced Plasmas : Towards Next Generation Plasma Light Sources. Dublin City University; 2013.
6. Hough P. Laser, Optical and Electrical Diagnostics of Colliding Laser-Produced Plasma. [Ireland]: Dublin City University; 2010.
7. Kavanagh KD. Image and Spectroscopy of Laser produced Colliding Plasmas. Dublin City University; 2006.
8. Luna H, Kavanagh KD, Costello JT. Study of a colliding laser-produced plasma by analysis of time- and space-resolved image spectra. J Appl Phys. 2007;101(3).
9. Fallon C, Hayden P, Walsh N, Kennedy ET, Costello JT. The effect of wedge angle on the evolution of a stagnation layer in a colliding plasma experiment. J Phys Conf Ser. 2014;548(1).
10. Dardis J, Costello JT. Stagnation layers at the collision front between two laser-induced plasmas: A study using time-resolved imaging and spectroscopy. Spectrochim Acta - Part B At Spectrosc [Internet]. 2010;65(8):627–35. Available from: http://dx.doi.org/10.1016/j.sab.2010.03.005

4 Imaging Colliding and Confined Plasmas

4.1 Colliding Plasmas

As discussed in section 2.5 Rambo and Denavit [1] introduced the concept of the collisionality parameter ζ, which indicates the degree of interpenetration versus stagnation occurring when two (or more) plasma plumes collide. Therefore, control over the collisionality parameter is desirable as it permits one to adjust the 'hardness' of the stagnation at the collision plane, among other parameters such as the temperature and density of the plasma at the collision plane or front, which, under appropriate conditions, may be stagnated and hence form a stagnation layer. For laser produced plasmas formed on metals *in vacuo*, using our typical laser parameters, an appreciable degree of stagnation is expected and hence we tend to observe stagnation layers formed at the collision front or plane. However, working within a background medium of air at atmospheric pressure is more challenging, for example the potential for air breakdown exists. This in turn limits the laser fluences that can be used during the experiment to ensure the plasma is formed from the target material and not the background gas as was the case in [2]. Referring to previous work undertaken within the DCU research group [3–8] and the broader literature [9,10], it has been shown that varying the target geometry is a commonly used method to manipulate the (relative) collisional velocity and hence the collisionality parameter and hardness of the stagnation which occurs. Thus, V-channel targets with varying angles (30°, 60°, 90°) were fabricated from aluminium to study the effect of angle on the plasma formed in air. The comparatively small angles of 30° and 60° were chosen to increase the relative collisional velocity as a means to overcome the increased confinement of the plasma due to working in air at ambient pressure (i.e., at $1\ atm.$). When laser plasmas are collided *in vacuo* for the formation of stagnation layers, typically the incident laser pulse is split in order to form the two seed plasmas. This is generally realised by means of a beam splitting optic such as a wedge or bi-prism, as shown in Fig. 4.1A. A proof of concept experiment was set up to investigate this method, however, as seen in the corresponding

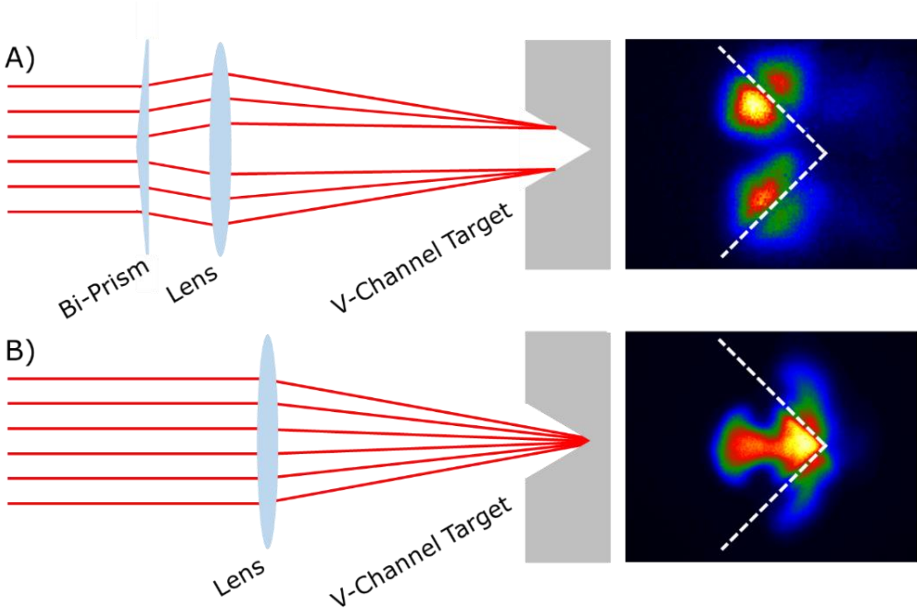

Fig. 4.1 Schematic diagram of the two methods investigated for colliding laser plasmas in air, along with two sample images recorded $500\,ns$ *after the incident laser showing the expansion of the plasma at that time. The gatewidth was* $10\,ns$*. A) Typical method used in previous work in vacuo for splitting the incoming laser to form two discrete seed plasmas on the V-channel walls. B) Method investigated here which uses a soft focus of the incoming laser to encompass the two walls of the V-channel, forming two seed plasmas with close to zero separation.*

plasma image, the separation between the seed plasmas was too great for plasma-plasma interactions to occur as the confinement due to the air hindered plasma expansion. It was realised that in order to maximise the chances of an interaction between the two seed plasmas, the separation between them would need to be as small as possible. This consideration led to the eventual method employed in this work, namely using a soft focus of the laser resulting in an overall spot size that could be increased to encompass both walls of the V-channel at the vertex without the need for a beam splitting optic. This method permitted the formation of a plasma on each of the walls of the V-channel expanding normally which could collide/interact with one another. This is shown in Fig. 4.1B where the corresponding plasma image shows the presence of a plasma plume at the centre plane, exhibiting complex spatial structure and extending from the vertex of the V-channel.

Images of the craters formed on the different V-channel targets were obtained using a microscope with a magnification of $42\times$ to confirm that the laser was indeed impinging on both walls of the V-channels as shown

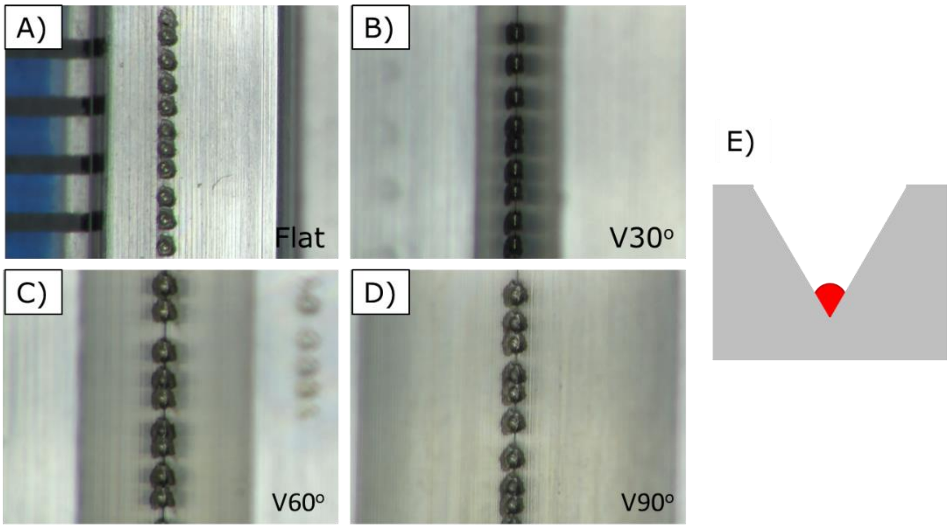

Fig. 4.2 Crater images of A) Flat, B) 30° V-channel, C) 60° V-channel, and D) 90° V-channels viewed under a microscope with a magnification of 42.39×. The spot sizes were measured to be on the order of 200 μm along with some melting visible around the craters. E) Indication of crater position in targets

in Fig. 4.2. From these images the laser spot size was found to be on the order of $200\,\mu m$ in diameter.

With this proof of concept experiment showing promising evidence of plasma-plasma interactions, a fast imaging investigation was carried out to determine if this single soft focus on the vertex of the V-channel target did indeed lead to the formation of a stagnation layer in air, or at least a region of confined and stagnated plasma that would replicate some of the desirable properties of stagnation layers like sustained light emission and greater homogeneity with respect to plasma density and temperature.

4.2 Broadband Fast Imaging

A time resolved broadband fast imaging experiment was set up as described in section 3.6. Plasmas were created in air at atmospheric pressure using the Spectron™ SL803 operating at its fundamental wavelength of $1064\,nm$ with a pulse energy of $20\,mJ$. Using the Andor™ DH5H7 iCCD camera, time resolved images were recorded with a gatewidth (shutter speed) of $10\,ns$ to allow insights into the formation and expansion dynamics of the plasma plumes for each of the 30°, 60°, and 90° V-channel targets along with a standard flat target as a reference 'single plume'. This would allow any enhancement or variation from the single plume behaviour to be seen. Sample images of the plasmas formed are presented for each target showing the plasma plume evolution for selected time delays while the full expansion series can be found in Appendix 0. The intensities of these broadband images were normalised at each time-step for ease of comparison between targets. As a result, some images have been increased in intensity (multiplied by a factor) to preserve their contrast as shown in the bottom left hand corner. Target positions have also been added to the images for ease of interpretation and to make clear that light perceived to be coming from behind the target is due to reflections off the aluminium target surface.

The expansion of the plasma was estimated from the luminous plume front position, obtained from horizontal lineouts taken from the centre of the broadband images along an axis normal to the target centre point (or vertex for grooved targets). The expansion length was defined as the distance from the target at which the emission intensity of the plasma had dropped to 5%[2] of the peak plasma emission intensity relative to the initial plasma position on the sensor at time $t = 0\,ns$. This data was tabulated and used to create a luminous expansion plot for each target. The data was also fitted with point explosion and drag force models to determine the appropriateness of each for different phases of the plasma expansion. The formulae for the point explosion and drag force models are given by equations (2.27) and (2.28) [11] and were discussed in section 2.3.4.

$$R = \alpha t^n \tag{2.27}$$

$$R = R_0[1 - \exp(-\beta t)] \tag{2.28}$$

Once again for the best fit to a plasma expanding in air at atmospheric pressure, a combination of both models should be required as the point explosion model tends to agree well with the plasma expansion during

---

[2] This boundary of 5% was determined from the experimental data since for other targets it was seen that there were more complex images exhibiting a dimmer region intervening region where, although counts were well above the background (by 10^3-10^4), was being washed out by an intense bright region creating an artefact, namely an abrupt dip in plasma dimensions when the typical boundary of 1/e (~37%) was used.

early times after plasma formation, while at later times, the drag force model exhibits better agreement with experimental data.

Results from the single plume expansion will be detailed in section 4.2.1 first to provide a reference of the behaviour exhibited by a laser plasma expanding into ambient air. The expansion behaviour of the V-channel targets will follow in section 4.2.2, and a comparison between the various targets will be discussed in section 4.2.3.

4.2.1 Single Plume (Flat Target) Expansion

Fig. 4.3 shows images of plasmas, formed on a flat target, recorded at time delays of $40\,ns$ and $100\,ns$. A series of images of the single plume plasma expansion can be seen in Fig. 4.4 along with the corresponding luminous expansion data in Fig. 4.5. From the luminous expansion data, it can be seen that there is an apparent flattening-off in the plasma expansion in the $60 - 80\,ns$ time delay interval. It is proposed that this is due to the presence a two-component expansion at the beginning of the plasma expansion. Similar behaviour was seen by Wu *et al* [12] who report the presence of two components in the early expansion as shown in Fig. 4.3, a fast 'plasma front' and a slower 'primary plasma'. This is attributed to the formation of a laser supported detonation (LSD) wave, as discussed in section 2.3.4 where, during the laser pulse, the plasma front absorbs more energy than the primary plasma as shielding effects become pronounced. The first component, the plasma front, coupled to the shock wave, expands rapidly outwards due to the extra energy absorbed while the primary plasma is left to slowly expand as a second component, resulting in the observed plume splitting.

Shortly after the termination of the laser pulse the plasma front is seen to cease expanding allowing the slower primary plasma to expand into the decaying plasma front Fig. 4.3B.

From the first $\sim 40\,ns$ of the luminous expansion data (Fig. 4.5), the plasma is seen to expand rapidly, and this is attributed to the faster plasma front expanding towards the laser pulse. Once the laser pulse terminates, the plasma front can no longer gain further energy to

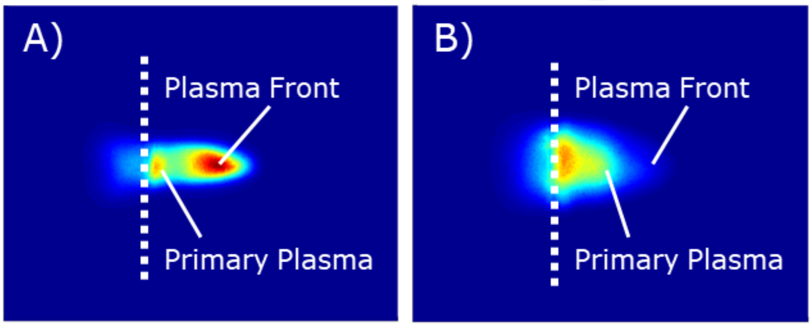

Fig. 4.3 ICCD images of the initial plasma with the plasma front and primary plasma components indicated. Images are from the flat Al target at A) 40 ns and B) 100 ns.

oppose the confinement of the surrounding air at atmospheric pressure, and the plasma front expansion decelerates and also begins to cool down through radiation losses. As the plasma front cools, the primary plasma, expands at a slower rate behind the plasma front and begins to be become more noticeable with both components visible in the $60\,ns$ image, Fig. 4.4B.

While the primary plasma expands into the stationary plasma front, the luminous expansion halts and even dips at $\sim 70\,ns$. This is due to the emission from the plasma front decaying and, as a result, the bright primary plasma becomes the ‘leading edge’ of the luminous expansion. This switching of the leading edge occurs due to the primary plasma becoming very distinct from the plasma front as can be seen at a time delay of $100\,ns$, Fig. 4.4C.

In addition to the effective halting of the luminous plasma expansion, Wu *et al* [12] report that interactions with the plasma front material, along with confinement by the atmospheric pressure air surrounding it, creates a deceleration of the primary plasma plume from a time delay of $\sim 130\,ns$ onwards. During this deceleration the plasma begins to cool and the intense continuum emission decays, which is evident from the intensity reduction at a time delay of $160\,ns$, Fig. 4.4D. In addition, it can be seen that although the preferred direction of expansion is normal to the target surface, considerable lateral expansion has occurred, and the plasma has taken a cone shape that one would expect from a laser plasma expanding in air.

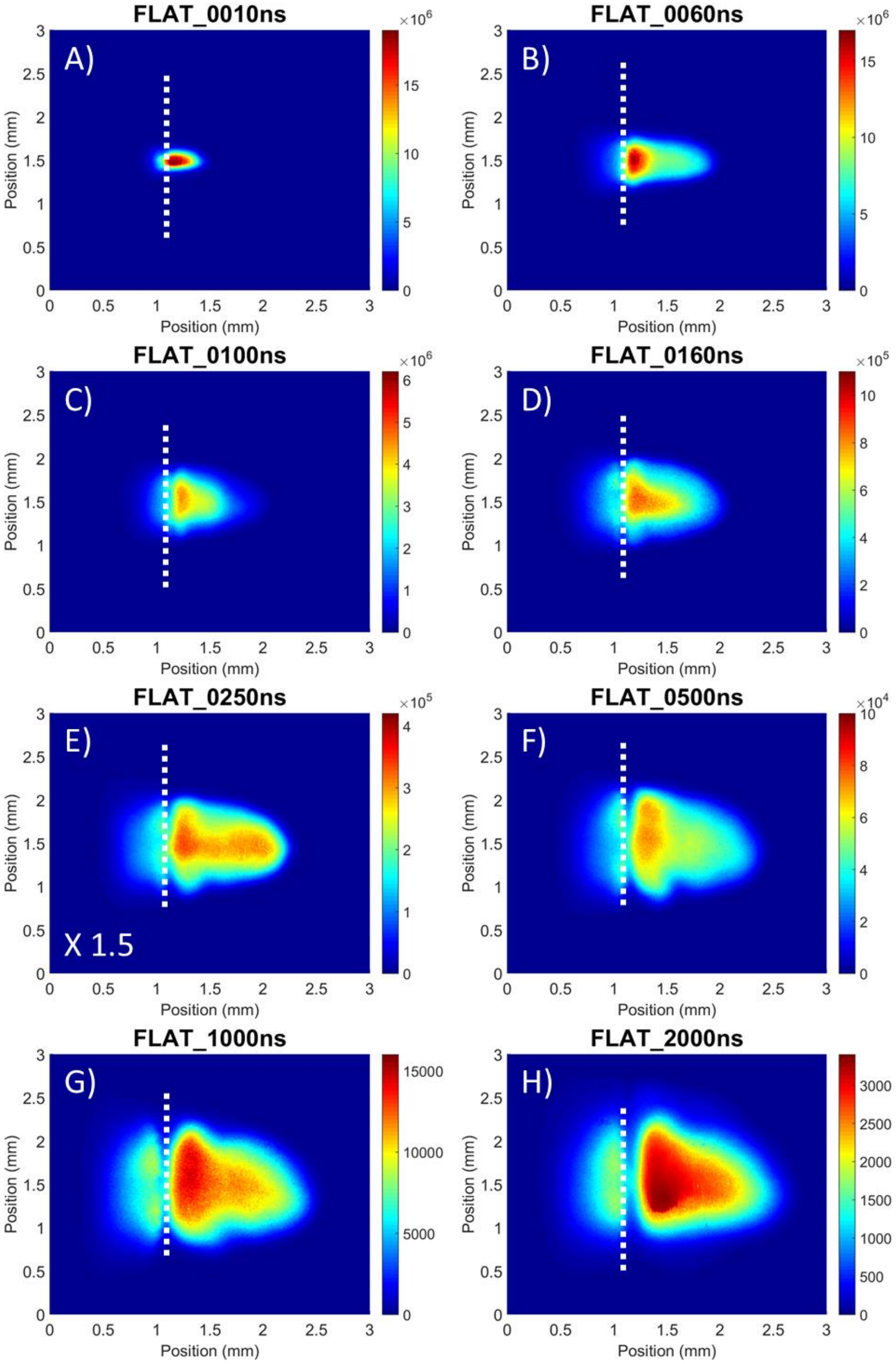

Fig. 4.4 Sample images of the evolution of a laser plasma created on the Flat target. The broadband images have been normalised at each time-step across all targets for ease of comparison. The ICCD gatewidth was 10 ns.

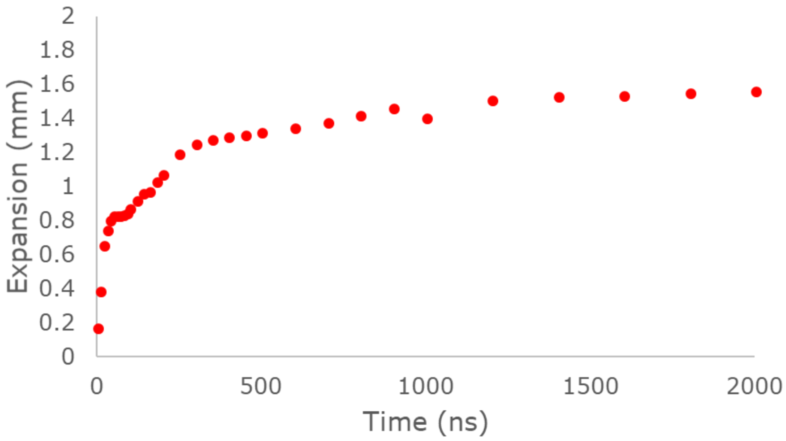

Fig. 4.5 The luminous plume expansion of a laser plasma in air from a flat target.

The image corresponding to a time delay of $250\,ns$, Fig. 4.4E, is composed of strong line emission from the plasma species with the continuum emission having mostly abated by this time. A sharp interface between the plasma plume and the background can be seen due to strong confinement as the plasma expands into the air at ambient pressure. As this expansion continues, it begins to slow down and eventually stop at a time delay of $\sim 400\,ns$ leaving the plasma to slowly diffuse into the surrounding air, seen in the image at a time delay of $500\,ns$ Fig. 4.4F. At later time delays ($> 500\,ns$) the intense emission falls off as the plasma cools and the more highly charged ions have recombined with electrons to form a plume dominated by neutral and singly charged species. Eventually the expansion of the luminous plasma levels off, and at a time delay of $2000\,ns$ it is seen to have grown to $1.5 - 1.6\,mm$ in length. This maximum extent of the plasma plume is known as the 'stopping distance' and from the literature it is shown to be dependent on many parameters such as laser pulse energy, laser wavelength [13] and background gas pressure [11,14]. The stopping distance achieved from the flat target is in good agreement with Hussein *et al* who report a stopping distance of $\sim 1.6\,mm$ for a $25\,mJ$ $1064\,nm$ pulse on a flat Al target [13].

4.2.2 V-channel Target Expansion

Luminous plume expansion data for the V-channel targets is shown in Fig. 4.6. The expansion behaviour of the 90° and 60° V-channels, seen

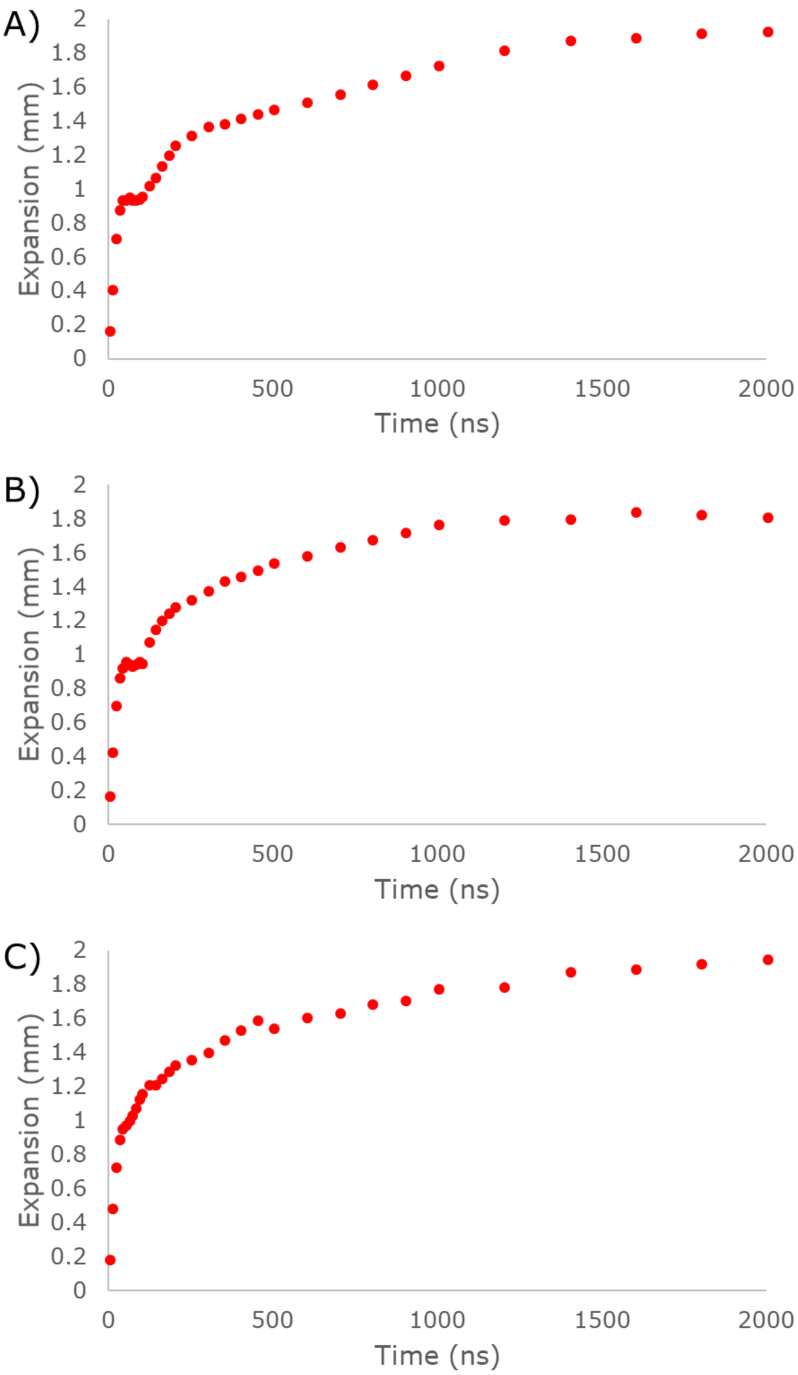

Fig. 4.6 The luminous plume expansion of a laser plasma in air from the A) 90º B) 60º C) 30º V-channel targets.

in Fig. 4.6A and B respectively, follows closely that seen for the flat target plasmas at early times. The formation of an LSD wave, resulting in plume splitting, occurring due to the rapid expansion of a plasma front component while a slower moving primary plasma component follows on, is also clear from corresponding images (Fig. 4.7). Again, this plasma front expansion terminates shortly after the end of the laser pulse, having reached a distance of $\sim 1\,mm$ within the first $\sim 40\,ns$ of the plasma expansion. As the plasma front emission decays, the slower moving primary plasma becomes more noticeable as it expands into the plasma front and the two distinct components can be seen from the corresponding images at a time delay of $60\,ns$, Fig. 4.7A and Fig. 4.7C for the 90° and 60° V-channel targets respectively. As the plasma front cools, the luminous expansion front effectively swaps to the leading edge of the primary plasma forming the dip in plasma expansion plots (Fig. 4.6A and Fig. 4.6B) again centred at a time delay of approximately $\sim 80\,ns$. In the images corresponding to a time delay of 100 ns, Fig. 4.7B and Fig. 4.7D, it can be seen that the plasma front emission has decayed considerably with the plasma front barely visible as the primary plasma emission dominates the image as it continues to expand across the full field of view of the ICCD. The 30° V-channel case is somewhat different. From the luminous expansion plot Fig. 4.6C, it can be seen that there is no dip or levelling off in the early plasma expansion present. It is still very likely that the two-component expansion is present in this case. However it is not as distinct perhaps due to an almost complete overlap of emission from the plasma front and the primary plasma components. It is worth highlighting that at early time delays, for example $60 - 100\,ns$ in Fig. 4.7, there seems to be a trend that the primary plasma expands further the more confined it is by the target at any given time. It is thus proposed that, as the vertex angle decreases, plasmas formed on the target walls reach the collision plane more quickly where lateral motion is then converted to an outward motion. Hence the narrower the vertex angle, the greater the primary plasma expansion velocity and spatial extent, at least at these early times.

It is at time delays $> 100\,ns$ that differences between the V-channel targets and the flat target begin to become more evident with the former showing greater directionality due greater confinement and hence, lower lateral expansion. This is a good indication that collisions within the plasma are indeed occurring. As mentioned earlier, plasmas expanding from each wall of the V-channel targets will collide at a collision plane or surface. Typically they do so in the vicinity of the centre of the V-channel, and the opposing lateral velocity components will

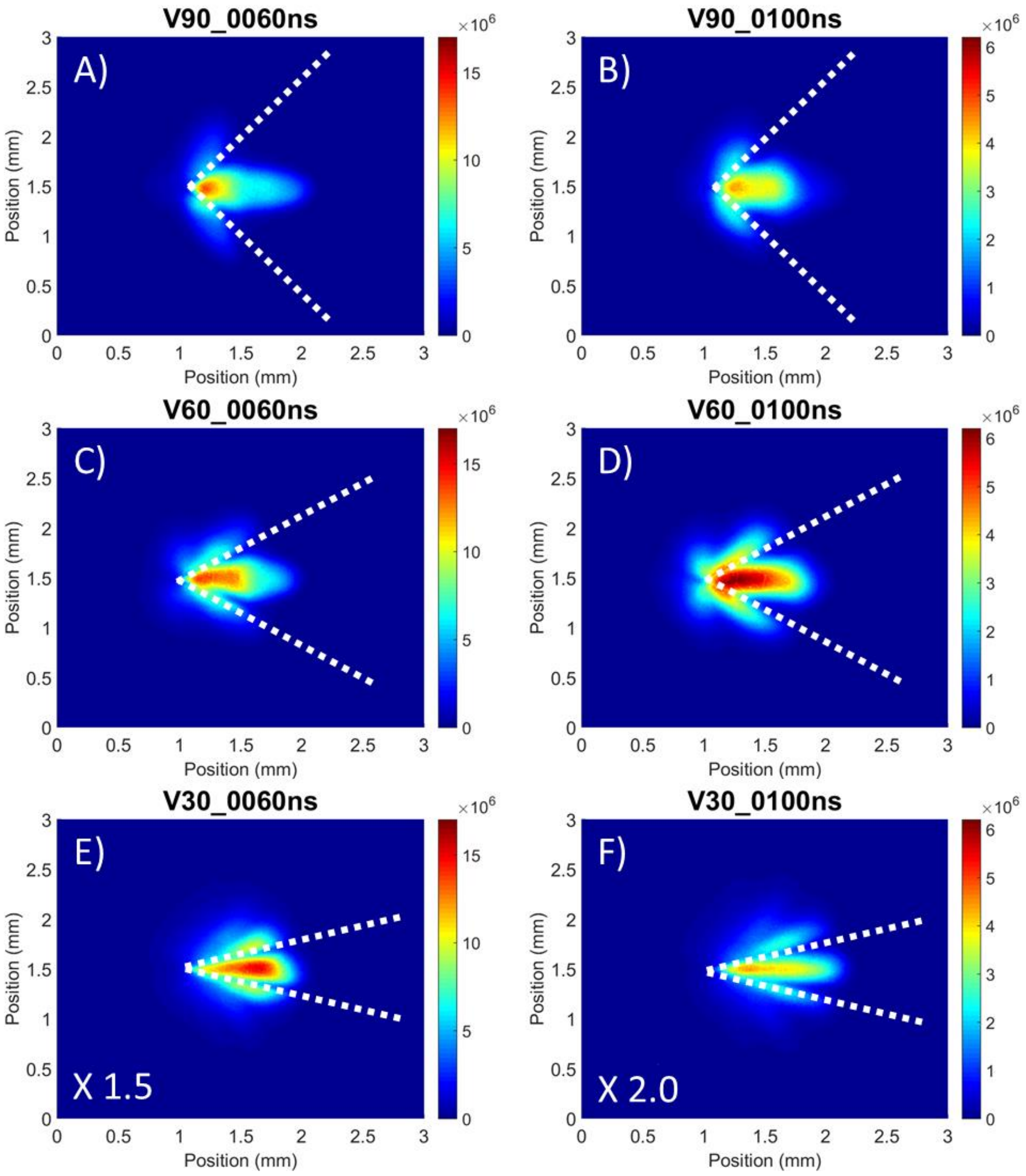

Fig. 4.7 Sample images of the evolution of a laser plasma created on the V-channel targets at $60\,ns$ *and* $100\,ns$*. The broadband images have been normalised at each time-step across all targets for ease of comparison. The ICCD gatewidth was 10 ns.*

cancel. This results in stagnated plasma formation and a net outward growth of the plasma away from the target, with little or no lateral component of expansion and hence greater directionality in the plasma plume expansion.

This imposed directionality persists over the plasma lifetime and, at a time delay of 160 ns, it can be seen from the images in Fig. 4.8 that the V-channel plasmas are far more cylindrical in shape than the cone shape that was exhibited by the flat target plasma at this time delay. Confinement by the background air is also evident due to the sharp plasma air interface both in the lateral and outward directions. This

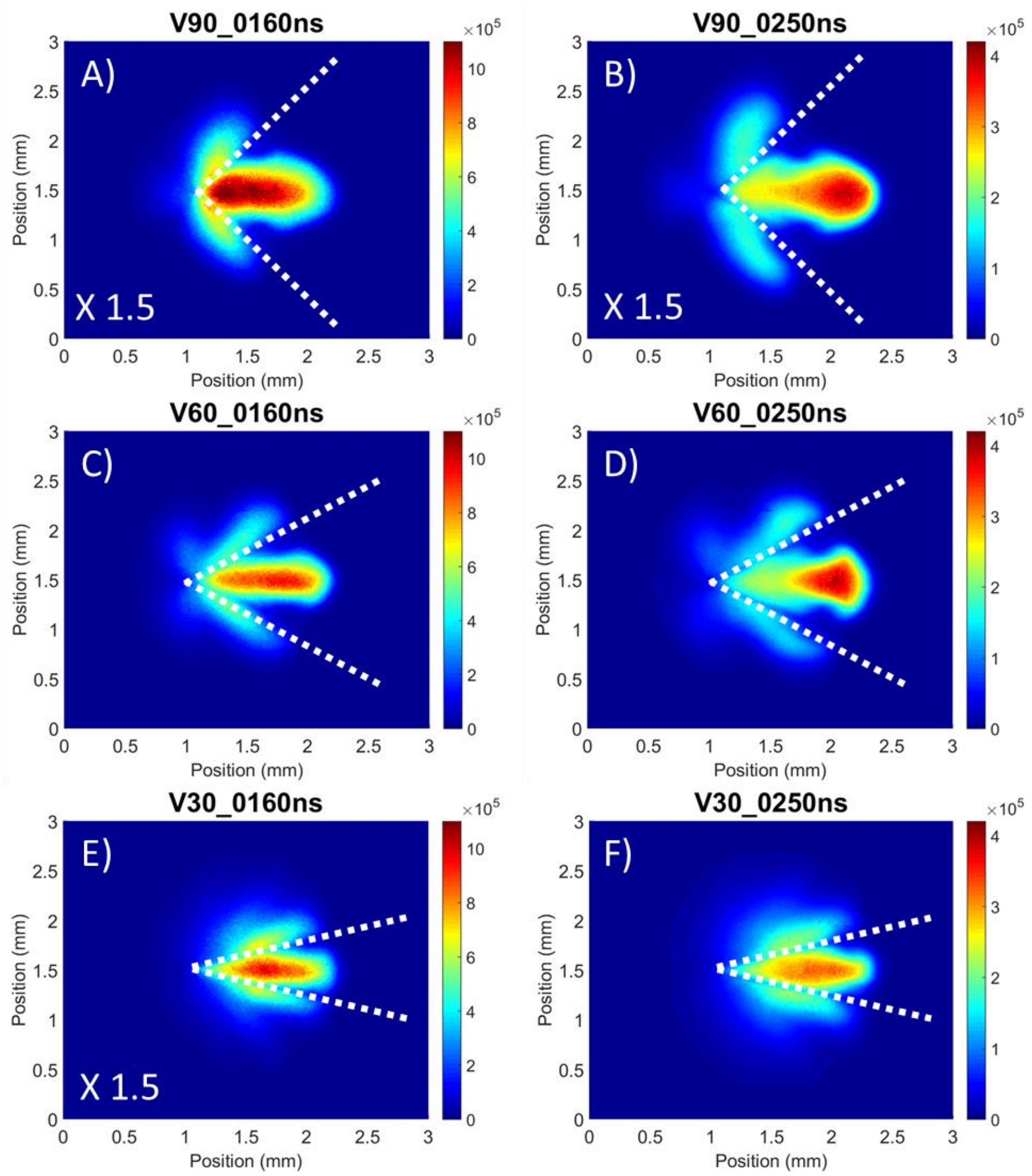

Fig. 4.8 Sample images of the evolution of a laser plasma created on the V-channel targets at $160\,ns$ and $250\,ns$. The broadband images have been normalised at each time-step across all targets for ease of comparison. The ICCD gatewidth was 10 ns.

confinement of the outward expansion slows not only the plasma expansion, as seen from the deceleration in the luminous plasma expansion plots, Fig. 4.6, but in the 90° and 60° V-channel targets it creates a build-up at the leading edge of the plasma, that is evidenced by the formation of a lobe-like plasma plume component at the leading edge of the plasma, evident in Fig. 4.8A and Fig. 4.8C. At a time delay of $250\,ns$, the primary plasma is seen to have split into two distinct plasma components, as seen in Fig. 4.8B and D. These two components consist of the lobe-shaped plasma region at the leading edge of the plume, now distinct and separate from the component of plasma

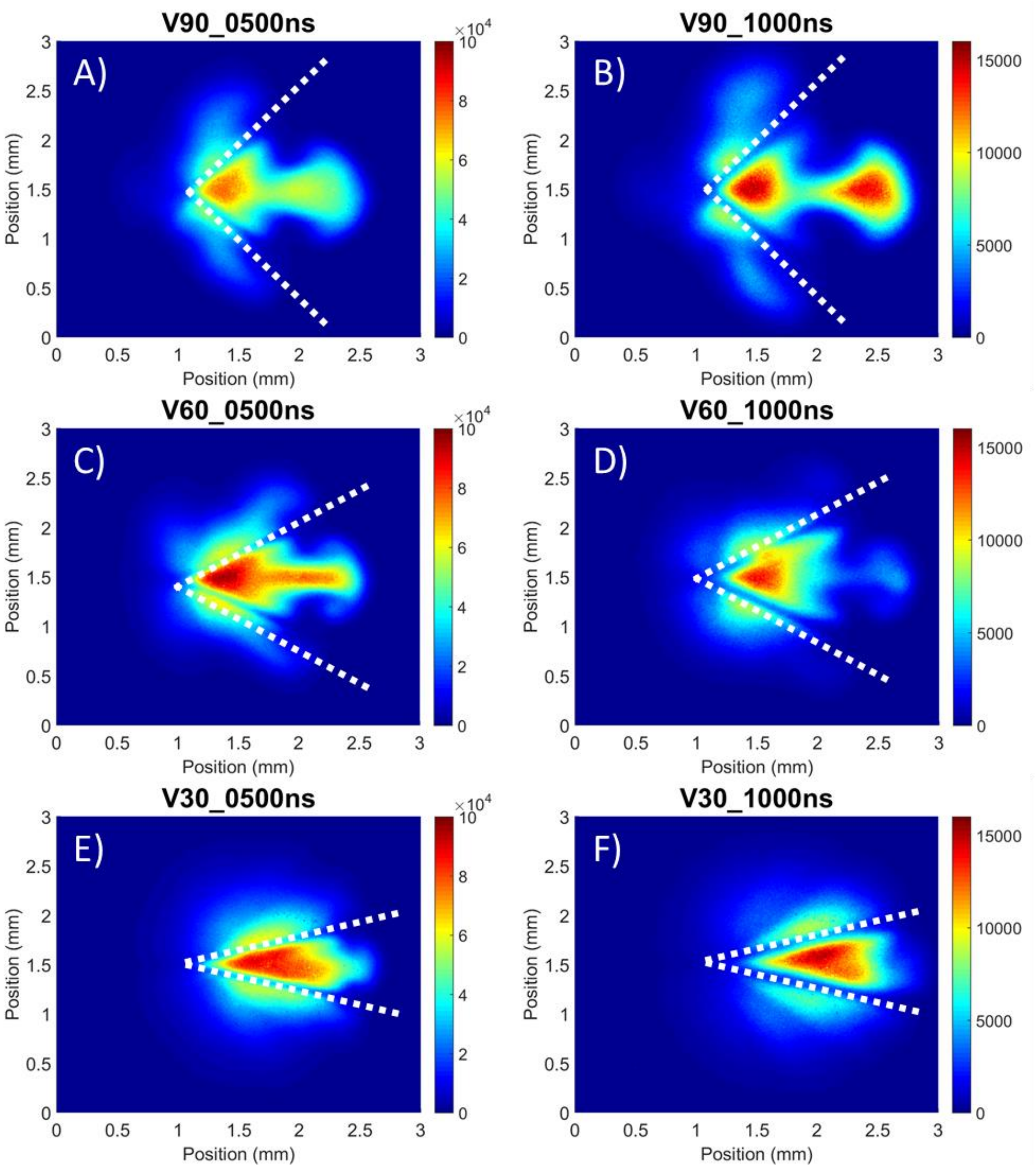

Fig. 4.9 Sample images of the evolution of a laser plasma created on the V-channel targets at $500\,ns$ *and* $1000\,ns$*. The broadband images have been normalised at each time-step across all targets for ease of comparison. The ICCD gatewidth was 10 ns.*

confined to the vicinity of the target vertex. At later time delays ($> 500\,ns$) in Fig. 4.9A and C, it can be seen that the plasma component within the target vertex remains somewhat stationary, showing little or no expansion. This is in contrast to the lobe-shaped plasma plume component that expands away from the target. It is proposed that this lobe-shaped plasma component is the result of the following. The component of the plasma plume located near the vertex of the target is of high density and creates a pressure gradient which exerts a force on the plasma region further from the target. The region coalesces into a lobe which then moves away from the target over time under the applied

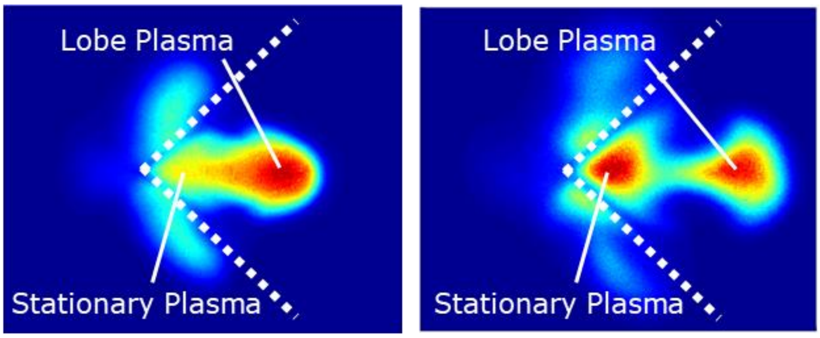

Fig. 4.10 ICCD images of the plasma with the lobe plasma and stationary plasma components indicated. Images are from the 90° V-channel Al target at A) 250 ns and B) 1000 ns.

pressure. This leads to the appearance of the two plasma components in the images recorded at long time delays, one a 'stationary plasma', close to the target vertex and the other, the moving 'plasma lobe' which are labelled in Fig. 4.10 and this nomenclature of stationary plasma and plasma lobe/column[3] will be used to refer to these corresponding plasma components within the thesis. At longer time delays, when the stationary plasma and plasma lobe have separated, the electron density and degree of ionisation in both components will be low and so the Debye length will be long. Hence, we do not expect Coulombic forces to play a major role in the separation of each of these plasma components.

Unlike the 60° and 90° V-channel targets, at $160\,ns$, Fig. 4.8E, the 30° V-channel does not seem to exhibit any indication of the appearance of the early stages of a separate plasma lobe. In fact no distinct plasma lobe is formed at any time delay. Further, as time proceeds, expansion of the plasma plume away from the target continues to slow, and signs of lateral expansion become evident, with the plasma expanding to fill the target vertex region at a time delay of $\sim 250\,ns$, Fig. 4.8F. Within the time delay range of $250 - 500\,ns$ the plume evolves into a stationary plasma, similar to those seen in the target vertex of the 60° and 90° V-channels. In addition the component of the plasma plume protruding into the ambient air assumes a flat and well-defined front edge. This stationary plasma undergoes no further expansion and exhibits quite

---

[3] For the 60° V-channel the plasma lobe was seen to take on more of a columnar shape at later delays and hence at these stages it will be referred to as plasma column.

uniform emission while the plasma cools (cf. Fig. 4.9B and D, corresponding to a time delay of $1000\,ns$).

4.2.3 Comparison of Targets

Over the course of the plasma lifetime there are many similarities and differences between the targets, both in relation to the flat target and between the various V-channel targets. At very early time delays ($< 60\,ns$) all targets seem to show similar behaviour[4] i.e. a two-component expansion, albeit it is less obvious from images of the 30° V-channel case. This plume splitting is attributed to the formation of an expanding LSD wave with the plasma front coupled to the shockwave, while the second primary plasma component expands at a lower velocity in its wake. With this two-component expansion it is found that a single fit to the full expansion data range was, as one would expect, not satisfactory and two separate fits of the point explosion model to the luminous front data were required, one for the plasma front and one for the primary plasma.

Table 4.1 Fitting parameters obtained by fits to the point explosion model for the plasma front. R^2 is the corresponding correlation coefficient from the fit.

	A	n	R^2
Flat	0.11	0.46	0.95
V90°	0.12	0.48	0.94
V60°	0.12	0.48	0.95
V30°	0.13	0.46	0.97

These two fits are show in Fig. 4.11 for the 90° and 30° V-channel targets and Fig. 4.12 for the flat and 60° V-channel targets. Fit parameters for the *plasma front* expansion are given in Table 4.1 and it is clear from the best fit n values that all of the targets tend towards a

---

[4] This taking into account our assumption of the 30° V-channel still having a two-component expansion as mentioned in section 4.2.2.

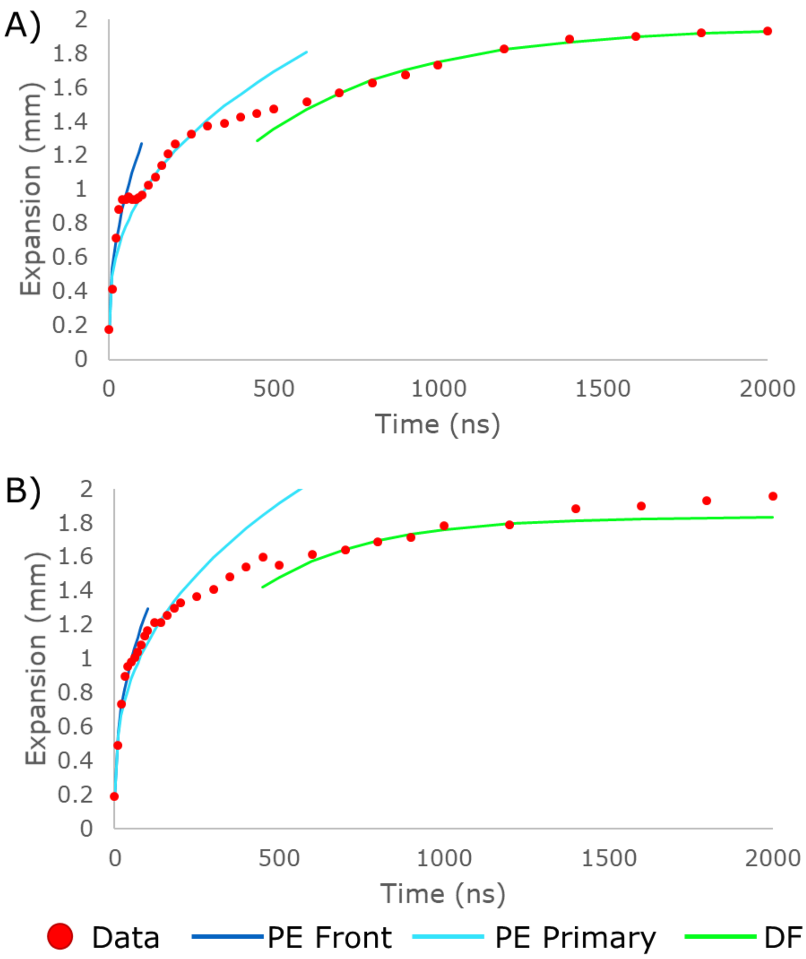

Fig. 4.11 Fits to the luminous expansion data for the A)90º and B) 30º V-channel targets. Point explosion models were fitted to the plasma front (PE Front) and primary plasma (PE Primary) for the early delay times while the drag force model (DF) was fitted at later time delays.

cylindrical expansion (0.4-spherical, 0.5-cylindrical, 0.667-planar). This is consistent with the observation that the plasma fronts have a fast, outward expansion, along the incident laser direction, with little evidence of lateral expansion. The A values are dependent on the energy of the point explosion and it can be seen that the V-channel targets all show a modest, but distinct increase in this energy as the vertex angle decreases. When the velocities were calculated for time delays of $0-60\,ns$, this increase in point explosion energy was seen to result in an increase of initial velocity of up to $\sim 24\,\%$.

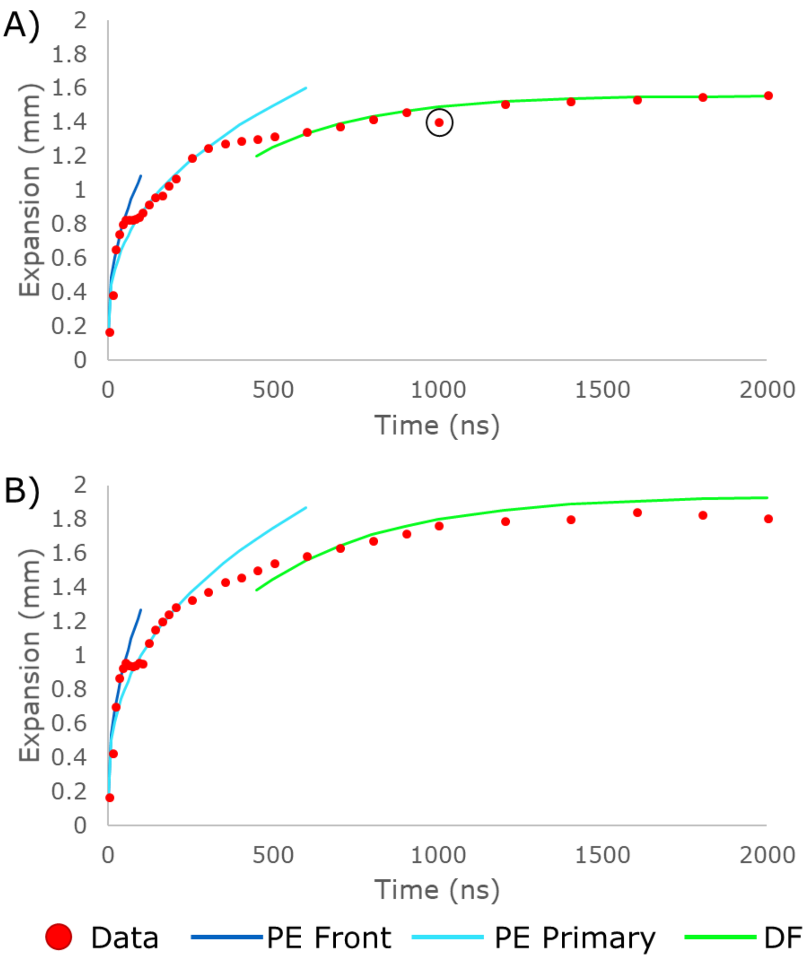

Fig. 4.12 Fits to the luminous expansion data for the A)Flat and B) 60º V-channel targets. Point explosion models were fitted to the plasma front (PE Front) and primary plasma (PE Primary) for the early delay times while the drag force model (DF) was fitted at later time delays. The circled data point in the flat target data is determined to be an outlier and hence was omitted from the corresponding fits.

Table 4.2 Comparison of average velocities for the initial expansion $0-60\,ns$ *of the different target geometries.*

	Average Velocity 0-60 ns	% Increase
Flat	$1.10 \times 10^6\ cm.s^{-1}$	N/A
V90º	$1.31 \times 10^6\ cm.s^{-1}$	19%
V60º	$1.29 \times 10^6\ cm.s^{-1}$	18%
V30º	$1.36 \times 10^6\ cm.s^{-1}$	24%

The initial velocity values are shown in Table 4.2 where it can be seen that the velocity values for the 90º and 60º V-channel targets are very similar, as one would expect from the a values.

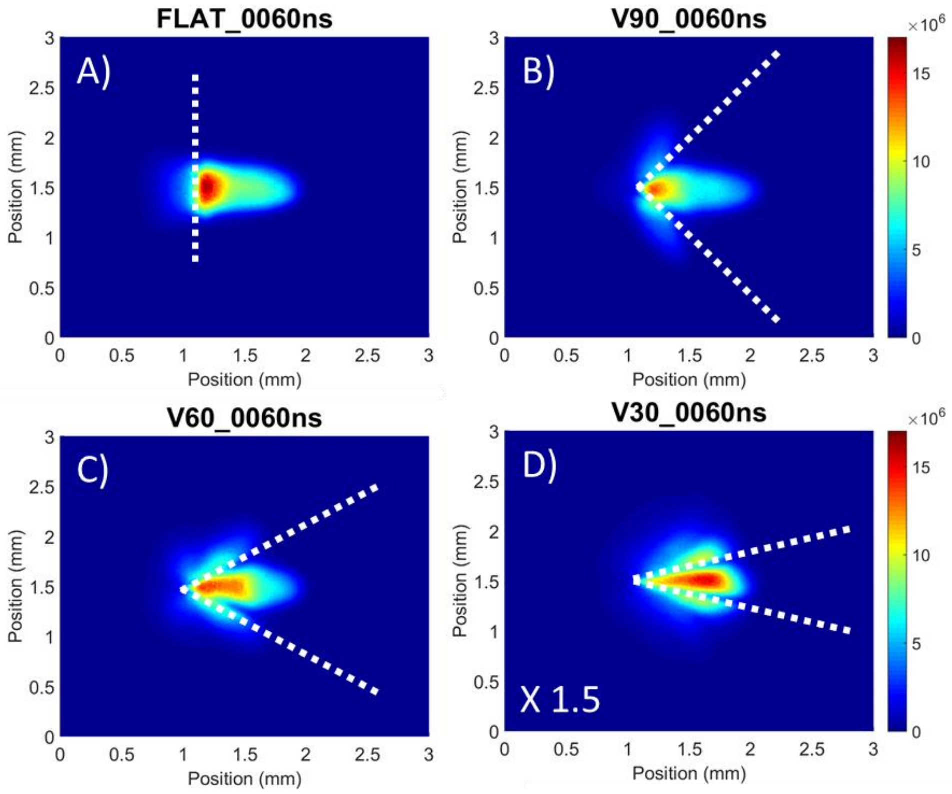

Fig. 4.13 Broadband images of the expanding plasma 60 ns after the arrival of the laser pulse on target for the four different targets. Image intensities are normalised with correction factors show bottom left where required.

*Table 4.3 Fitting parameters obtained by fits to the point explosion model for the primary plasma. *Indicates that the value was forced to this value by the boundaries set in the fitting. R^2 is the corresponding correlation coefficient from the fit.*

	A	n	R^2
Flat	0.11	0.41	0.98
V90°	0.13	0.40	0.97
V60°	0.13	0.4*	0.90
V30°	0.14	0.4*	0.91

After the initial rapid expansion of the plasma front, the primary plasma which expands at a slower rate, becomes dominant. Table 4.3 shows the point explosion model fits to the *primary plasma* expansion data for all four targets.

It can be seen that the expansion at this time is quite spherical with n values of ~ 0.4. however for the 60° and 30° V-channel targets this value is forced to the lower boundary of 0.4, resulting in a poorer R^2 value compared to the other fits. If the n parameter is not constrained in this fashion, the n values take rather unphysical values closer to 0.3 than 0.4.

Notwithstanding the applied constraints, the trend in the A values show yet again that the V-channel targets give rise to an increase in point explosion energy. This is consistent with the images in Fig. 4.13 (time delay of $60\,ns$). As the target vertex angle decreases, the point explosion energy increases, the primary plasma expands farther away from the target extending to distances of approximately $0.82\,mm$, $0.72\,mm$, $0.57\,mm$, and $0.52\,mm$ for the 30°, 60°, 90°, and flat targets respectively. This increase in the primary plasma expansion rate, as hypothesised earlier, supports the proposition that the 30° V-channel target does not show a dip in the luminous expansion data since the primary plasma and the plasma front have expanded at similar rates. Looking at the two point explosion fits corresponding to the primary plasma and plasma front expansions in the 30° V-channel case, Fig. 4.11B, it can be seen that the fitted curves overlap each other smoothly, while for the other targets the two curves are distinct and exhibit a short flat region in the luminous expansion plots as the most distant luminous front swaps from the plasma front to the primary plasma. This can be seen most clearly in the 90° V-channel data (Fig. 4.11A).

At $160\,ns$, as seen in Fig. 4.14, the V-channel targets were stated to display a higher degree of lateral confinement resulting in plasma widths as low as half of that for the flat target plasma plumes (cf. values in Table 4.4.). A trend is seen that as the target geometry becomes tighter the confinement of the plasma increases.

Table 4.4 Comparison plasma widths at 160 ns of the different target geometries.

	Plasma width at $160\,ns$ (mm)	% Decrease
Flat	0.89	N/A
V90°	0.64	28%
V60°	0.51	43%
V30°	0.45	49%

However, as the plasma remains confined, even when not in contact with target walls, it is proposed that this is not just due to geometric

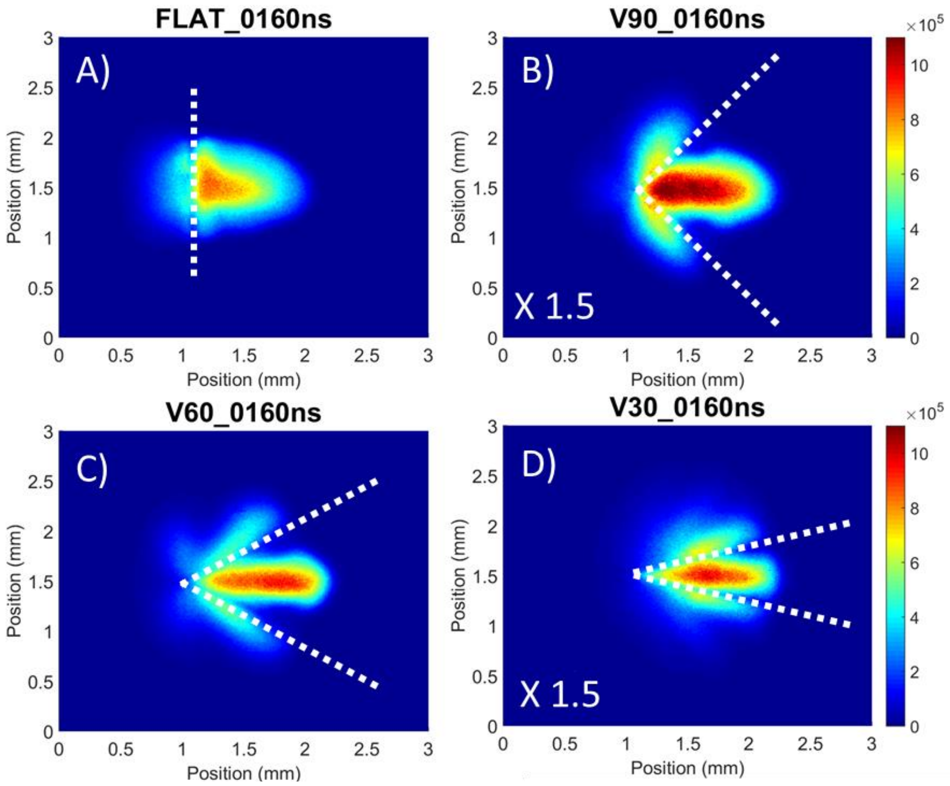

Fig. 4.14 Broadband images of the expanding plasma 160 ns after the laser pulse arrived at the target for the four different targets. Image intensities are normalised with correction factors show bottom left where required.

confinement but also arises from the plasmas formed on the target walls. As a result we can state that the tighter the target angle the higher the confinement. When the plasma material arrives at the collision plane the faster lateral expansion components in the 30° and 60° V-channel targets form well-defined regions or 'harder' stagnation, while the slower lateral components from the 90° V-channel forms a less-defined 'softer' stagnation [7]. Also visible from the images at a time delay of $160\,ns$ is the early stages of the formation of the separate plasma lobe component seen in the 60° and 90° V-channel targets. This is the early stage formation before it separates to become a distinct and spatially separate feature at longer time delays, Fig. 4.14B and C. As the plasmas continue to expand, the behaviour of the lobe component of each plasma begins to vary. In the 90° V-channel target case the plasma lobe moves away separating from the stationary plasma, while in the 60° V-channel case the sides of the lobe-shape expand somewhat, and it forms into a plasma column extending away from the stationary plasma. This difference in behaviour is possibly due to the enhanced confinement of the 60° V-channel plasma, which results in the hotter material remaining columnar in shape rather than spreading over the whole lobe, as observed in the 90° V-channel target case. By $600\,ns$ it can be seen from the luminous expansion plots, Fig. 4.11 and Fig. 4.12, that the plasmas have slowed down considerably as evidenced by the flattening of curves as each plasma has approached its stopping distance [11,13,14].

As described in the literature [2,12,15], it is at these later time delays that the drag force model is typically more appropriate. The fitting parameters obtained with the drag force model, for time delays in excess of $600ns$, are shown in Table 4.5.

Table 4.5 Parameters obtained by fits to the drag force model for times ≥ $600\,ns$. R^2 is the corresponding correlation coefficient from the fit.

	R_0	β	R^2
Flat	1.56	3.0×10^{-3}	0.986
V90°	1.95	2.2×10^{-3}	0.983
V60°	1.84	3.1×10^{-3}	0.976
V30°	1.94	2.5×10^{-3}	0.941

The 30° and 90° V-channel targets have a smaller slowing parameter β and hence it is no surprise that they also exhibit the farthest stopping distances R_0 of 1.95 mm and 1.94 mm respectively. It is somewhat unexpected that the 60° V-channel would have such a variation in slowing parameter, however this may be attributed to the fact that these measurements are based on luminous plasma front position. The emission from the plasma column in the 60° V-channel target is seen to decay away at late time delays and as such this would have a negative going impact on the luminous plasma front position. Hence the 60° V-channel is seen to have a somewhat smaller stopping distance of $1.84\,mm$.

By $1000\,ns$ the plasmas have all but stopped expanding and peak intensities are all approximately equal in all cases. However it can be seen that each of the V-channel targets exhibits strikingly different behaviours. The 90° V-channel target has two bright regions of intense

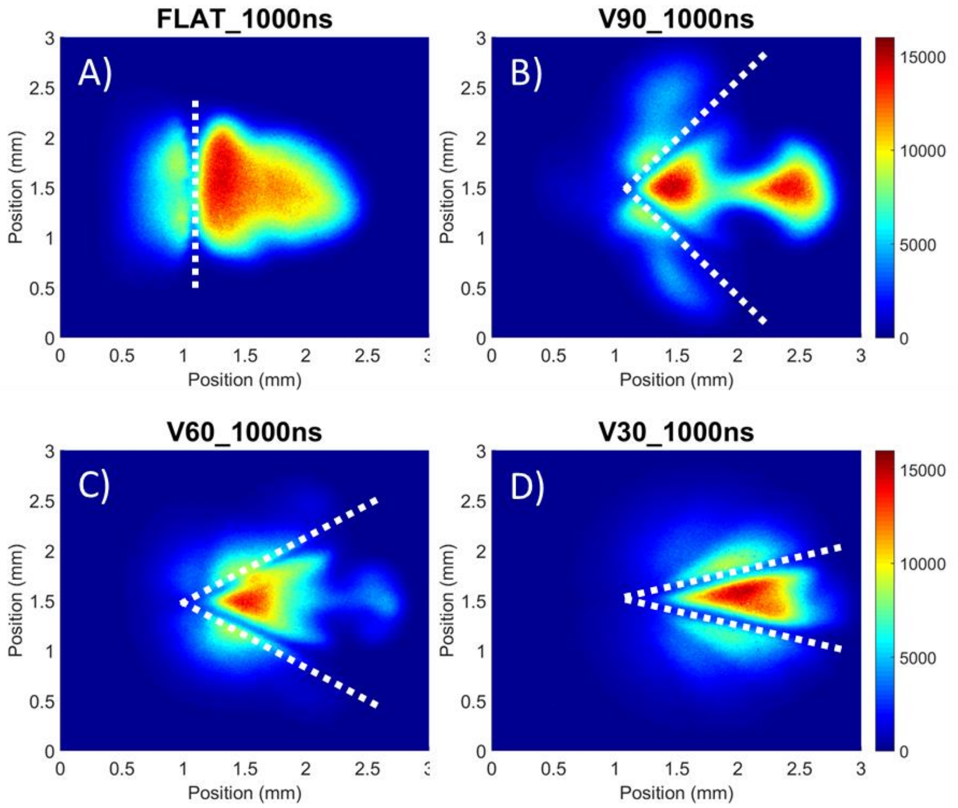

Fig. 4.15 Broadband images of the expanding plasma 1000 ns after the laser pulse arrived at the target for the four different targets. Image intensities are normalised with correction factors show bottom left where required.

emission, the extended plasma lobe and the stationary plasma located near the V-channel vertex. The 60° V-channel target has intense emission from the stationary plasma while in contrast to the 90° V-channel case, the plasma column displays much weaker emission. The 30° V-channel did not show any indication of a distinct separate lobe formed at any time delay and the entire plasma appears to behave as one stationary plasma. It is worth pointing out that the stationary plasmas within the V-channels at this point all exhibit similarities in emission intensities and distribution.

It is at time delays beyond $1000\,ns$ that the intensities of the images for the different targets begin to decay at different rates. The 30° and 60° V-channel target intensities fall away at the fastest rates, while the 90° V- channel target is closer to the flat target case. This can be seen that in the images recorded at a time delay of $2000\,ns$, Fig. 4.16, where the 60° and 30° V-channel targets have peak intensities of approximately 900 counts, three times lower than the flat and 90° V-channel cases. This decrease in emission from the V-channel targets at the late time

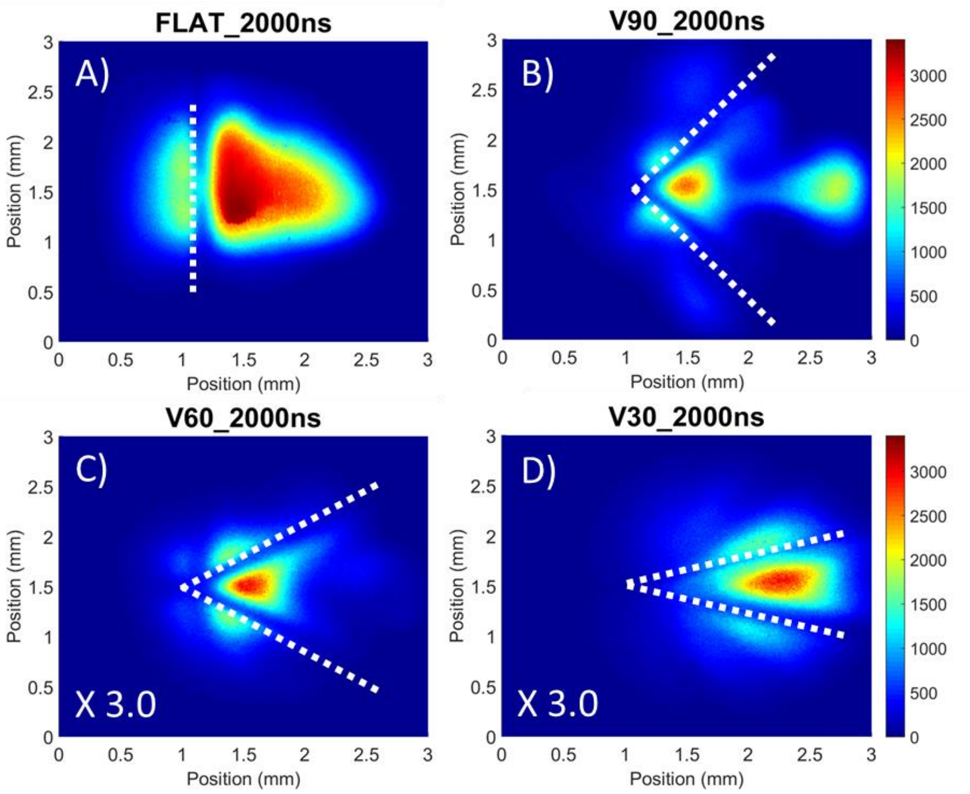

Fig. 4.16 Broadband images of the expanding plasma 2000 ns after the laser pulse began for the four different targets. Image intensities are normalised with correction factors show bottom left where required.

delays is proposed to be due to confinement of the targets. It was seen that the V-channel targets had an early increase in emitted radiation and this was attributed to confinement increasing the recombination rates, with this recombination scaling inversely and increasing as the target angle decreased. It is proposed that the increased recombination rates for the 60° and 30° V-channel target plasmas means that the radiative losses occur more quickly for these cases than the less well confined flat and 90° V-channel cases.

Turning to the individual stationary and lobe plasmas, and looking at rather long time delays when they have been separated for some time ($> 1000\,ns$), it is observed that the plasma lobe emission intensity decays more quickly than the emission intensity for the stationary plasma, particularly for the 60° V-channel target case, where the plasma column is not visible in the corresponding image at 2000 ns, Fig. 4.16C.

It is worth noting that the stationary plasmas form at what would be the location of the collision plane from the initial plasmas expanding from the target walls. They exhibit many of the characteristics one would expect from a stagnation layer. They are stationary showing little to no expansion, they have quite uniform intensity distributions which decay more slowly than regions further from the target vertex, e.g. in the lobe plasma region. Uniformity of plasma parameters, which can be only inferred from broadband intensity images, will be discussed in the next chapter, Chapter 0. However before doing so, spectrally filtered imaging is investigated on the route to a more complete spectroscopic study of these multicomponent plasmas.

4.3 Spectrally Resolved Fast Imaging

In addition to time resolved broadband fast imaging, filters corresponding to transitions of different ion stages Al $(394.4\,nm\,\&\,396.15\,nm)$, Al^{+} $(466.3\,nm)$, and Al^{2+} $(569.6\,nm)$ were used to perform spectrally resolved fast imaging. Further details of the filters can be found in section 3.6. The objective was to track the spatial evolution of an individual charge state within the plasma. Due to the narrow gate-width of the ICCD and the transmission efficiencies of the filters used, images could only be obtained for time delays up to $500\,ns$. Beyond this time delay the images became very noisy and it was difficult to extract usable information from them.

4.3.1 Single Plume Filtered Imaging

Sample images from the single plume filtered imaging are shown in Fig. 4.17 where the gate width is $10\,ns$ as it was in the broadband image study. For early time delays there appears to be no significant differences in the intensity distributions for neutral and ionised species as can be seen in Fig. 4.17 A-C. The observation is as one would expect by taking into account the fact that the early plasma emission is dominated by continuum radiation and hence no spectral signature of any specific charge state will be present.

As the continuum emission decays, the line emission appears and grows in importance so that the images begin to show a variation in intensity

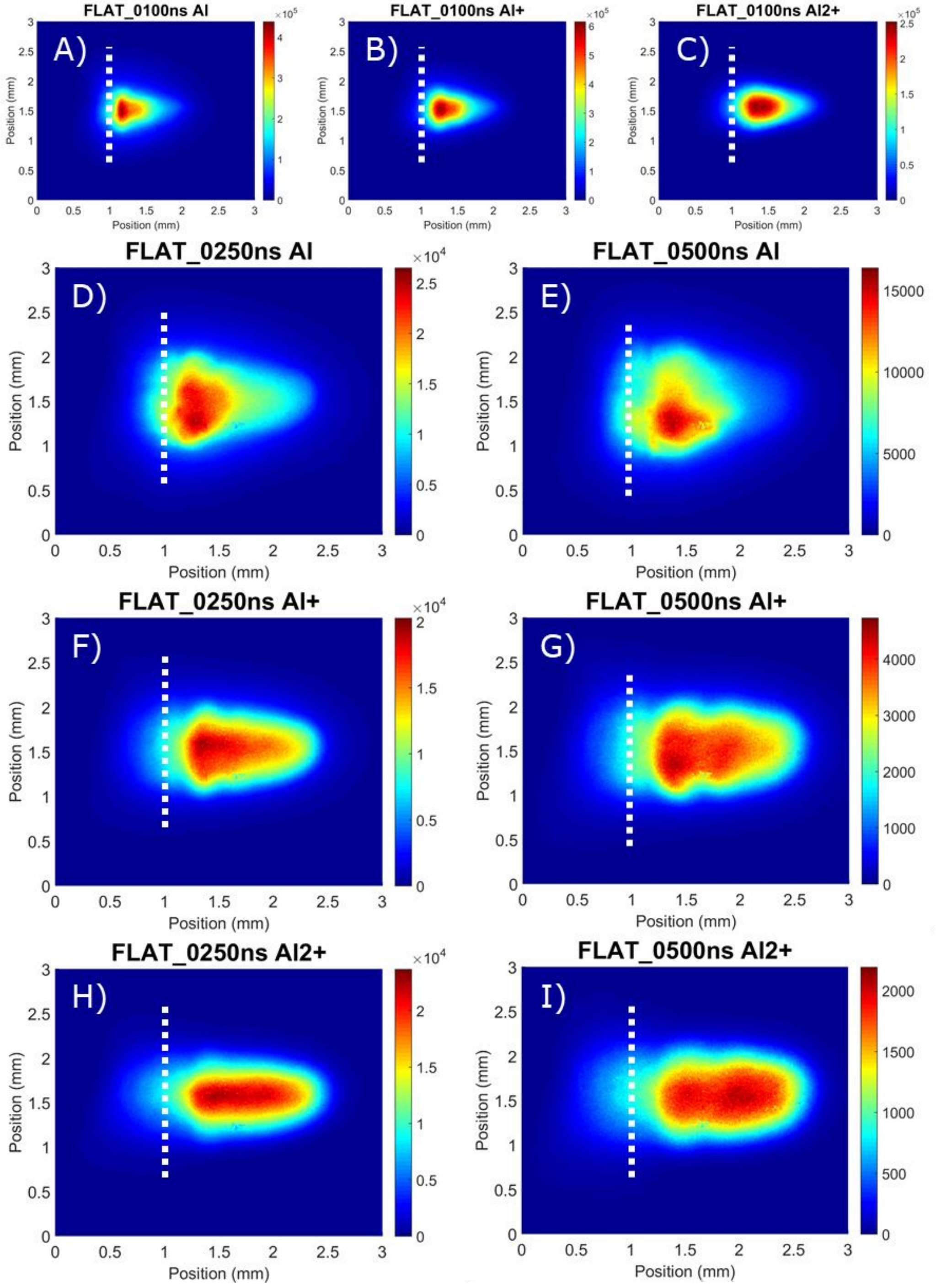
FLAT_0100ns Al

FLAT_0100ns Al+

FLAT_0100ns Al2+

FLAT_0250ns Al

FLAT_0500ns Al

FLAT_0250ns Al+

FLAT_0500ns Al+

FLAT_0250ns Al2+

FLAT_0500ns Al2+

Fig. 4.17 Spectrally filtered images of the flat target showing the different distributions of the Al, Al$^+$, and Al^{2+} species as the plasma evolves.

distribution between the charged states which is present, for example, in the images at a time delay of 250 ns, Fig. 4.17D, F, and H. As mentioned in section 2.3.3, electrons tend to move away from the target more rapidly than ions. This results in an ambipolar field which imposes an attractive force on the charged ions, accelerating them in a forward direction, resulting in an ion stage distribution that depends on charge state. The slower neutral Al atoms tend to stay close to the target while the Al^{+} ions will move away more quickly and the Al^{2+} species more quickly still. This trend, whereby the more highly ionised an atom the faster it accelerates, can be seen throughout the literature [11,16,17]. At a time delay of $500\,ns$ not only is there a variation in the spatial distribution of the different species present, but it is replicated also in the relative emission intensity. Comparing the percentage drop in the peak intensity between time delays of $250 - 500\,ns$, the neutral Al was seen to exhibit a decrease of $\sim 40\%$ while the Al^{+} and Al^{2+} exhibited values of $\sim 75\%$ and $\sim 90\%$ respectively. This is attributed to the charged species undergoing recombination as the plasma expands and cools resulting in a reduction in the number density of more highly charged ions and an increase in neutral atoms. This can be seen in Fig. 4.17E, G, and I, while the processes leading to electron-ion recombination will be discussed in section 5.3 of the next chapter.

4.3.2 V-channel Targets Filtered Imaging

Spectrally filtered imaging of the plasma evolution of the V-channel targets shows similar behaviour to the flat target case at a time delay of $100\,ns$, with the intensity distributions exhibiting no significant differences between the spatial distribution of the charge states, again attributed to the intense broadband continuum radiation at early time delays ($< 150\,ns$) which masks the spectral signatures of the different ion stages. As time progresses, and the continuum emission decays away, evidence of a spatial distribution starts to appear. Fig. 4.18 shows sample images of the 90° V-channel target emission, at a time delay of $250\,ns$ where strong Al^{2+} emission is found within the plasma lobe at the leading edge of the plasma (Fig. 4.18 H), while the neutral Al^{0} emission is predominantly located close to the target vertex in the vicinity of the stationary plasma (Fig. 4.18 D), and the Al^{+} emission bridges these two regions (Fig. 4.18 F). So in contrast to all other target geometries, the 90° V-channel target is seen to exhibit three well separated regions in spatial distribution of charge states at this time delay.

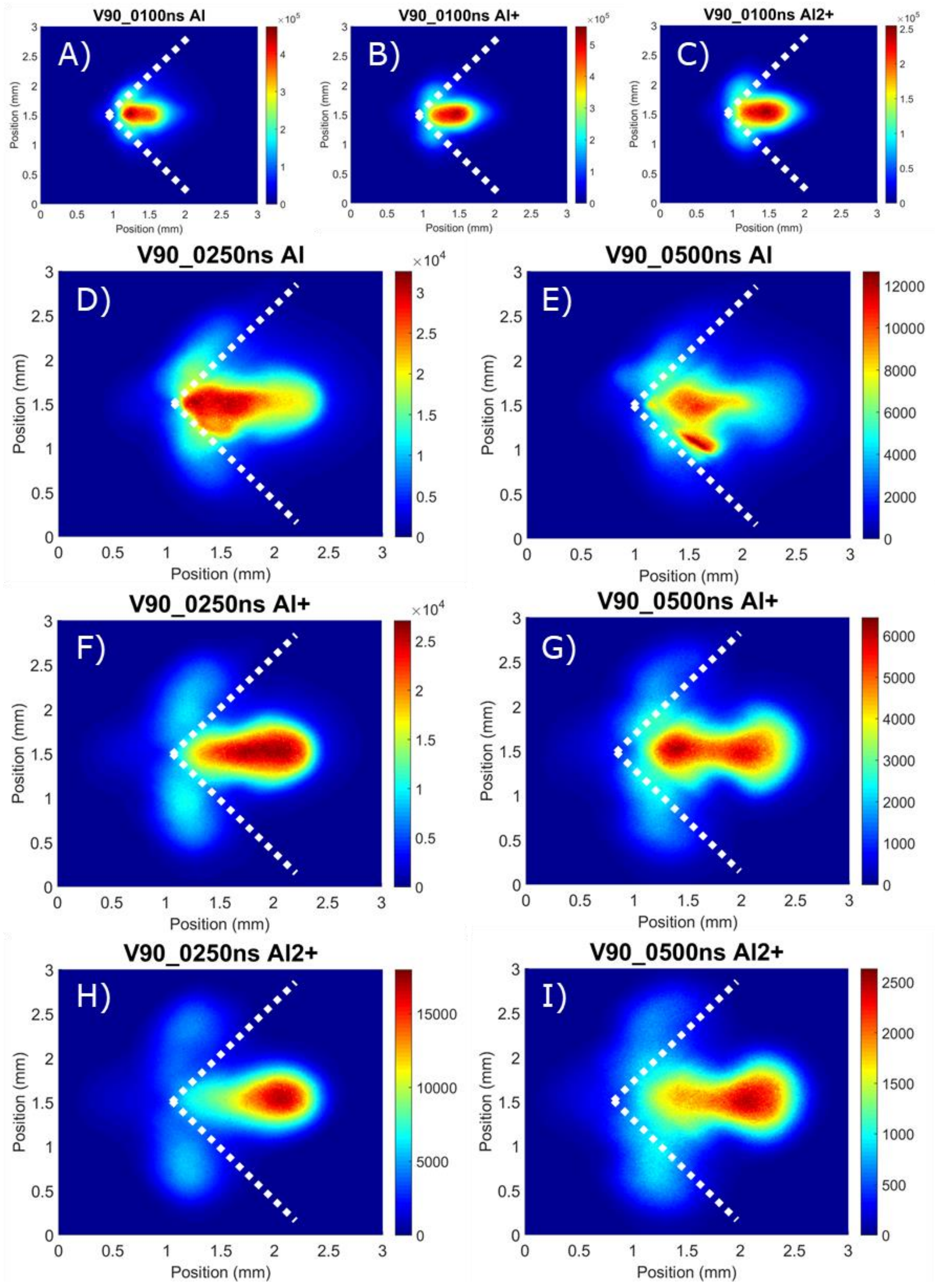

Fig. 4.18 Spectrally filtered images of the 90^{O} V-channel target showing the different distributions of the Al, Al^{+}, and Al^{2+} species as the plasma evolves.

At a time delay of $500\,ns$, the plasma lobe appears to cool faster than the stationary plasma and the strong emission from Al^{+} and Al^{2+} ions decays to levels comparable with the stationary plasma, resulting in a flattening of the intensity distribution across the plasma plume similar to that seen in the flat target case at this time delay.

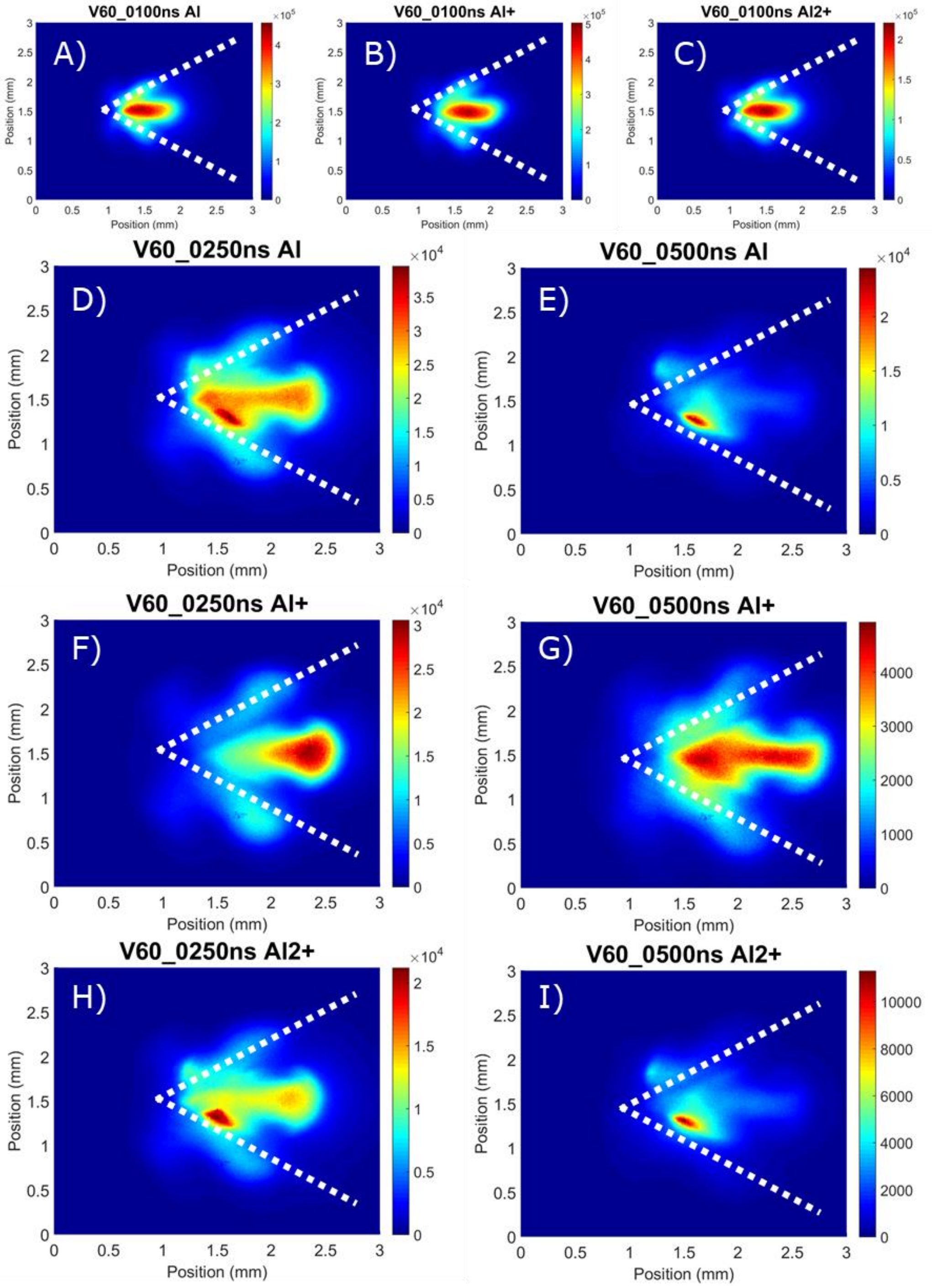

Fig. 4.19 Spectrally filtered images of the 60^O V-channel target showing the different distributions of the Al, Al+, and Al2+ species as the plasma evolves.

Sample images for the 60° and 30° V-channel targets are shown in Fig. 4.19 and Fig. 4.20 where continuum radiation dominates the spectral distribution at short time delays $(< 150\,ns)$, similar to that for the flat and 90° V-channel targets, with no means to extract the spatial distribution of individual charge states. As the continuum emission intensity declines (circa $120\,ns$) the formation of localised spots of

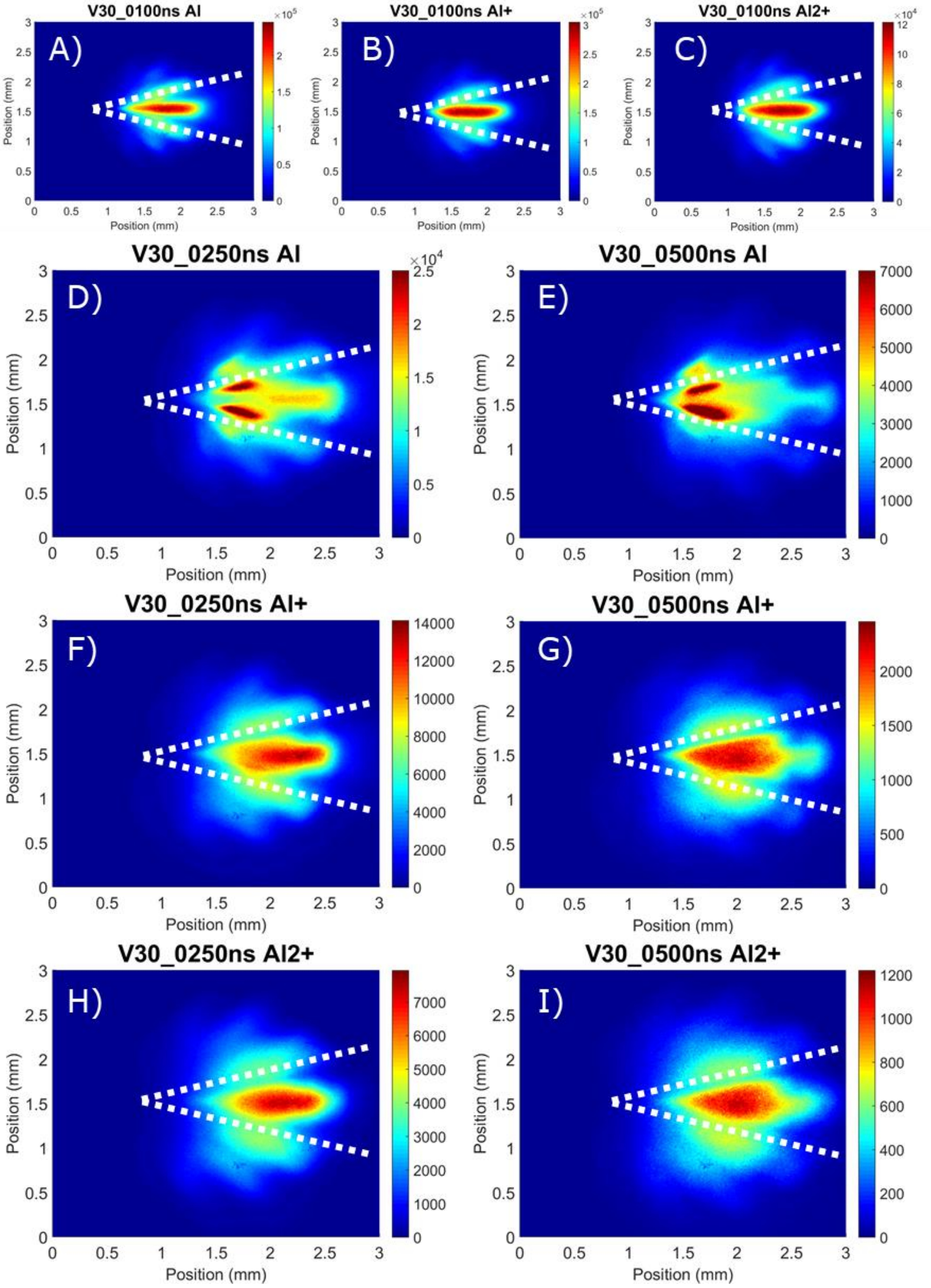

Fig. 4.20 Spectrally filtered images of the 30^O V-channel target showing the different distributions of the Al, Al$^+$, and Al^{2+} species as the plasma evolves.

intense emission at the target walls become visible within the Al^0 spatial distributions. At time delays in the range $200 - 250\,ns$, the emission from these localised spots begin to exceed that of the main plasma plume, as seen in Fig. 4.19D and Fig. 4.20D. At $500\,ns$ the emission from these bright spots dominates the images, reducing the contrast between the stationary plasma and plasma column, Fig. 4.19E and especially Fig.

4.20E. These bright spots were also seen in the 90° V-channel neutral Al^0 images, Fig. 4.18D and E. However they were not as strong as those in the 60° and 30° V-channel Al^0 images. It is proposed that these bright spots are due to the phenomenon of 'forced recombination', which will be discussed in section 4.3.3.

The Al^{2+} images from the 60° V-channel target plasma also exhibit evidence of forced recombination which can be seen in Fig. 4.19H and I. Their presence hinders a measurement of the spatial distributions of the Al^0 and Al^{2+} at the later $500\,ns$ time delay. However at a time delay of $250\,ns$ the charge state distribution differs from the 90° V-channel target case, with both the Al^0 and Al^{2+} emission displaying rather uniform intensity across the plasma length, as seen in Fig. 4.19D and H. The Al^+ emission does not display evidence of forced recombination as there is no clear sign of bright spots. In this sense it is closer to the flat and 90° V-channel targets, with intense emission at the front of the plasma at a time delay of $250\,ns$, Fig. 4.19 F, showing strong localisation of Al^+ in that region of the image before it evolves into a more uniform distribution across the plasma, seen in Fig. 4.19H. Again this is attributed to the plasma column cooling faster than the stationary plasma. Notwithstanding the presence of bright spots due to the forced recombination on the Al^0 images, the 30° V-channel target images do not show any significant spatial variation between the charged species, with emission being quite evenly distributed over most of the plasma volume for Al^0, Al^+ and Al^{2+} as evident from the various images in Fig. 4.20.

4.3.3 Forced Recombination Within the V-Channel Targets

Bright spots of intense emission located at the target walls are seen in the neutral Al filtered imaging of the V-channel targets (and Al^{2+} of the 60° V-channel target). As the plasma evolves these bright spots begin to become quite prominent in the images with sustained intense emission. As mentioned earlier, it is proposed that this phenomenon is

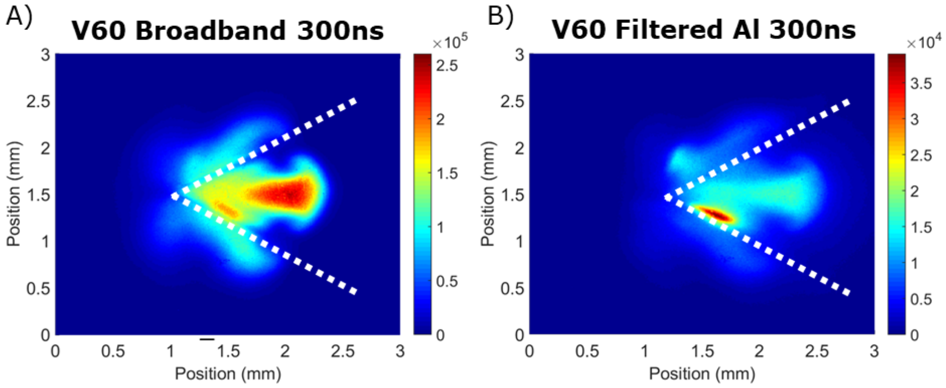

Fig. 4.21 Sample images showing the presence of the bright spots from forced recombination in A) Broadband fast imaging and B) Filtered Al Neutral fast imaging

the result of forced recombination, a mechanism whereby enhanced emission is observed when plasmas collide with ‘cold’ electron donor surfaces increasing recombination rates [19,20]. This is usually performed by introducing a forced recombination wall/tamper (typically a metallic material) into the path of an expanding laser plasma, however it has also been reported to occur from the surfaces of confining cavity targets [18] as is the case proposed here. At the plasma-target interface there will be an increase in the population of excited neutral Al^0 species as Al^+ ions recombine with electrons donated from the target wall. It is proposed that the bright spots are due to the emission of these excited Al^0 species.

Although evident in all V-channel targets, the 90° V-channel does not exhibit this phenomenon to the same extent as the 60° and 30° V-channel targets. This leads one to believe that the mechanism is dependent on confinement of the plasma, with some sources [18,20] suggesting it may be the result of a hydrodynamic compression at the target surface increasing the ion density that drives this forced recombination. It can be expected that a tighter confinement by the V-channel targets will increase this hydrodynamic compression .

It should be noted that although forced recombination was strongly evident in the filtered imaging, it was not as evident in the broadband imaging. It appeared only in a few images such as the $300\,ns$ image shown in Fig. 4.21 for the 60° V-channel target plasma. This is most likely due to strong emission from other charge states dominating the broadband images.

4.4 Summary

In this chapter results from both broadband and filtered time-resolved fast imaging were presented in order to better understand the expansion dynamics of plasmas formed on the various flat and grooved targets with the goal of the formation of stagnated/confined plasmas layers under atmospheric pressure air conditions that could exhibit the properties of stagnation layers.

Results from the time resolved broadband fast imaging experiments showed that all targets seem to exhibit similar behaviour initially with the formation of an LSD wave. This results in a two-component expansion, the fast plasma front rapidly expands into the background air stopping at approximately $60\,ns$ at a distance of $1\,mm$. It is at this time that the second slower component, the primary plasma, becomes more noticeable as the plasma front decays away. This two-component expansion at the early time delays led to the requirement to invoke of two different plasma expansion models to represent the full set of plume expansion data, as seen in Fig. 4.11 and Fig. 4.12. It was observed that as the target angle decreased the energy extracted from the point explosion model fits increased, and this was evident from the increases in initial velocity of the plasma front and primary plasma components. At longer time delays ($> 600\,ns$) the expansion was seen to be better described by the drag force model, with the V-channel targets showing greater final stopping distances of up to $0.5\,mm$ greater than the flat target.

During the expansion of the plasma, the 90° and 60° V-channel targets were seen to exhibit the formation of a lobe at the leading edge of the plasma at circa $\sim 160\,ns$. This build up of plasma material far from the target vertex was seen to extend outwards and separate from the plasma forming two new components, the stationary plasma and the plasma lobe/column. As the stationary plasma was found close to the target vertex at what would be the location of the collision plane from the initial plasmas expanding from the target walls, along with exhibiting many of the characteristics one would expect from a stagnation layer (little to no expansion, uniform intensity, slower decay rates), it was determined that these stationary plasmas would require further investigation and plasma diagnostics performed to confirm that they could indeed be used as proxies for stagnation layers.

Results from the time resolved, spectrally filtered, fast imaging showed the presence of a spatial distribution of the various species within the plasmas, with the charged Al^{2+} species moving towards the leading edge of the plasma while the neutral Al^0 species stayed close to the target surface in each case. The Al^+ ions were seen to bridge these regions with a good distribution over the length of the plasma while showing a slight preference towards the leading edge.

In addition to the spatial distribution of charged species, some evidence for forced recombination at the target walls was also obtained from the filtered imaging, with the plasma from the V-channel targets showing spots of intense Al^0 emission due to interactions with the target walls.

References

1. Rambo PW, Denavit J. Interpenetration and ion separation in colliding plasmas. Phys Plasmas. 1994;1(12):4050–60.

2. Cristoforetti G, Lorenzetti G, Legnaioli S, Palleschi V. Investigation on the role of air in the dynamical evolution and thermodynamic state of a laser-induced aluminium plasma by spatial- and time-resolved spectroscopy. Spectrochim Acta - Part B At Spectrosc. 2010;65(9–10):787–96.

3. Fallon C. Optical Diagnostics of Colliding Laser Produced Plasmas : Towards Next Generation Plasma Light Sources. Dublin City University; 2013.

4. Hough P. Laser, Optical and Electrical Diagnostics of Colliding Laser-Produced Plasma. [Ireland]: Dublin City University; 2010.

5. Kavanagh KD. Image and Spectroscopy of Laser produced Colliding Plasmas. Dublin City University; 2006.

6. Luna H, Kavanagh KD, Costello JT. Study of a colliding laser-produced plasma by analysis of time- and space-resolved image spectra. J Appl Phys. 2007;101(3).

7. Fallon C, Hayden P, Walsh N, Kennedy ET, Costello JT. Target geometrical effects on the stagnation layer formed by colliding a pair of laser produced copper plasmas. Phys Plasmas. 2015;22(9).

8. Dardis J, Costello JT. Stagnation layers at the collision front between two laser-induced plasmas: A study using time-resolved imaging and spectroscopy. Spectrochim Acta - Part B At Spectrosc [Internet]. 2010;65(8):627–35. Available from: http://dx.doi.org/10.1016/j.sab.2010.03.005

9. Al-Shboul KF, Hassan SM, Harilal SS. Molecular formation in the stagnation region of colliding laser-produced plasmas. Plasma Sources Sci Technol. 2016;25(6).

10. Al-Shboul KF, Harilal SS, Hassan SM, Hassanein A, Costello JT, Yabuuchi T, et al. Interpenetration and stagnation in colliding laser

plasmas. Phys Plasmas. 2014;21(1).

11. Harilal SS, Bindhu C V., Tillack MS, Najmabadi F, Gaeris AC. Internal structure and expansion dynamics of laser ablation plumes into ambient gases. J Appl Phys. 2003;93(5):2380–8.

12. Wu J, Wei W, Li X, Jia S, Qiu A. Infrared nanosecond laser-metal ablation in atmosphere: Initial plasma during laser pulse and further expansion. Appl Phys Lett. 2013;102(16).

13. Hussein AE, Diwakar PK, Harilal SS, Hassanein A. The role of laser wavelength on plasma generation and expansion of ablation plumes in air. J Appl Phys. 2013;113(14).

14. Farid N, Harilal SS, Ding H, Hassanein A. Emission features and expansion dynamics of nanosecond laser ablation plumes at different ambient pressures. J Appl Phys. 2014;115(3).

15. Amoruso S, Bruzzese R, Spinelli N, Velotta R. Characterization of laser-ablation plasmas. J Phys B. 1999;32(14):R131.

16. Hough P, McLoughlin C, Harilal SS, Mosnier JP, Costello JT. Emission characteristics and dynamics of the stagnation layer in colliding laser produced plasmas. J Appl Phys. 2010;107(2).

17. Ursu C, Gurlui S, Focsa C, Popa G. Space- and time-resolved optical diagnosis for the study of laser ablation plasma dynamics. Nucl Instruments Methods Phys Res Sect B Beam Interact with Mater Atoms [Internet]. 2009;267(2):446–50. Available from: http://dx.doi.org/10.1016/j.nimb.2008.10.057

18. Yeates P, Kennedy ET. Spectroscopic, imaging, and probe diagnostics of laser plasma plumes expanding between confining surfaces. J Appl Phys. 2010;108(9).

19. Miyamoto S, Amano S, Inoue T, Nica P-E, Shimoura A, Kaku K, et al. EUV Source Developments on Laser-Produced Plasmas using Cryogenic Xe and Lithium New Scheme Target. Proc SPIE. 2006;6151(132):21–3.

20. Nagano A, Inoue T, Nica PE, Amano S, Miyamoto S, Mochizuki T.

Extreme ultraviolet source using a forced recombination process in lithium plasma generated by a pulsed laser. Appl Phys Lett. 2007;90(15):1–4.

5 Optical Emission Spectroscopy (OES) of Colliding Plasmas in Air

Chapter 4 focused on time-resolved broadband and filtered imaging which provided useful information on the temporal evolution and expansion rates of the luminous plumes, and the spatial distribution of various ion stages for plasma formed on the four different target configurations. However, to obtain more detailed information on other key plasma parameters, additional diagnostics are needed. This chapter focuses on one such technique – time and spatially resolved optical emission spectroscopy (OES), as described in sections 3.3 and 3.7.

OES is one of the most powerful diagnostic techniques and, from the resulting spectra, parameters such as electron temperature and density can be extracted. In addition, OES has the advantage that the intensity of individual spectral lines or continua over narrow spectral ranges can be extracted, as opposed to the entire bandwidth of a spectral filter in the imaging mode.

The spectroscopic set-up used in this work comprised an Andor™ Kymera 328i spectrograph equipped with an Andor™ iStar sCMOS imaging camera, enabling space resolved spectroscopic measurements, with control over the delay and gate width of the camera. This allowed a series of spectra to be obtained at various stages of the plasma evolution, all formed under the same conditions. From these spectra space and time resolved electron density and temperature maps were built.

From the imaging data presented in Chapter 4, two regions of interest (labelled with continuous white lines in Fig. 5.1) for the spectroscopic study were determined. Spectra recorded along the Y-direction provide information on the plasma plume along its expansion direction. On the other hand, in the X-direction the slit was positioned at the interface region between the stationary plasma and the expanding component of the plasma ($\sim 0.7\ mm$ from the target vertex). It is also the site at which

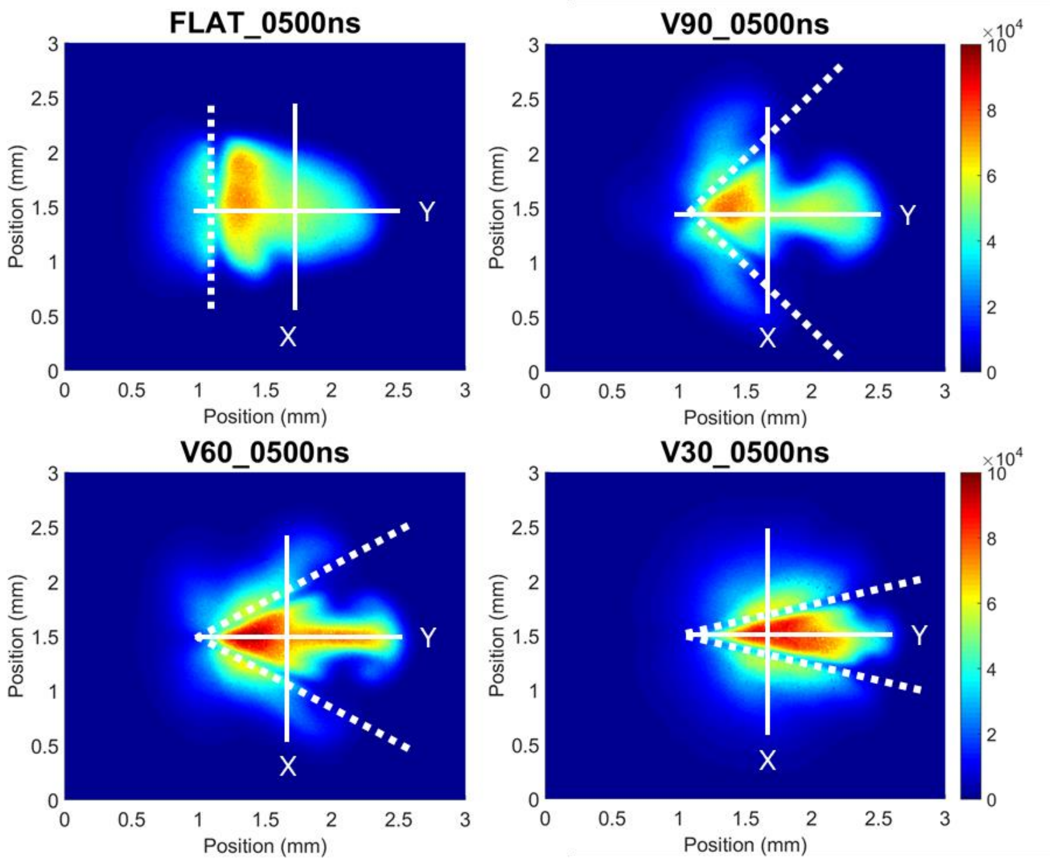

Fig. 5.1 Slit positions for spectroscopic measurements on plasmas formed on the different targets along the X- and Y-directions.

hot spots were observed in some of the images shown in section 4.3 and which may be the result of forced recombination. For the X-direction a relay lens system was used to focus the regions of interest onto the entrance slit of the spectrometer, with a magnification of $\sim 3\times$, while for the Y-direction the same imaging system was used, in conjunction with a Dove prism to rotate the image of the plasma plume so that it was aligned with the entrance slit direction (see section 3.7).

Section 5.1 gives a brief overview of the different Al lines present in the spectra along with the time delays at which they were visible/resolvable. The spatial distribution of the $Al^{+}\ 358.7\ nm$ and $Al^{0}\ 396.15\ nm$ emission lines are discussed in Section 5.2. In Section 5.3 details of the extracted electron densities and electron temperatures are given, along with the application of the collisional radiative ionisation model (discussed in section 2.4.3). Finally section 5.4 provides a discussion of the emission from the various targets highlighting key benefits found from colliding plasmas in air.

5.1 Broad Spectral Band Time Resolved Optical Emission Spectroscopy

An initial study of the emission from each target was performed using a using the $300l/mm$ grating which provided a spectral window width of $164.16\,nm$ resulting in a measured instrument function of c.a. $1.5\,nm$ FWHM, see section 3.3. This allowed the identification of spectral regions of interest for a higher resolution study focused on the determination of electron densities and temperatures, and on the general trends in the spatial distribution of lines emitted by atoms in neutral and lowly charge states in plasmas formed on the different targets.

5.1.1 Overview of space integrated, time resolved spectra along the Y-direction

The objective here is to illustrate the time evolution of the main features of the spectrally resolved, spatially integrated emission along the fast axis of expansion of the plasma plume. The main focus is on the 90° V-channel target simply to illustrate the typical spectra obtained for Al plasmas formed in air. The corresponding spectra recorded for the other targets are presented in Appendix C, while the data extracted from these spectra will be used throughout the chapter.

Fig. 5.2 shows sample spectra from time resolved, low resolution OES performed on the 90° V-channel target with the spectrometer slit positioned along the Y-direction. The spectrometer was set at a centre wavelength of $400\,nm$ and the spectral data were integrated along the entire length of the plasma expansion axis. Lines were identified with the aid of the National Institute of Standards and Technology (NIST) atomic spectra database lines [1] and tagged with their corresponding element and ion stage labels. For the spectra recorded at time delays of $100\,ns$ & $150\,ns$, strong continuum emission is observed, in addition to intense emission from the background air plasma with many nitrogen and oxygen lines present. This makes the isolation of Al emission lines,

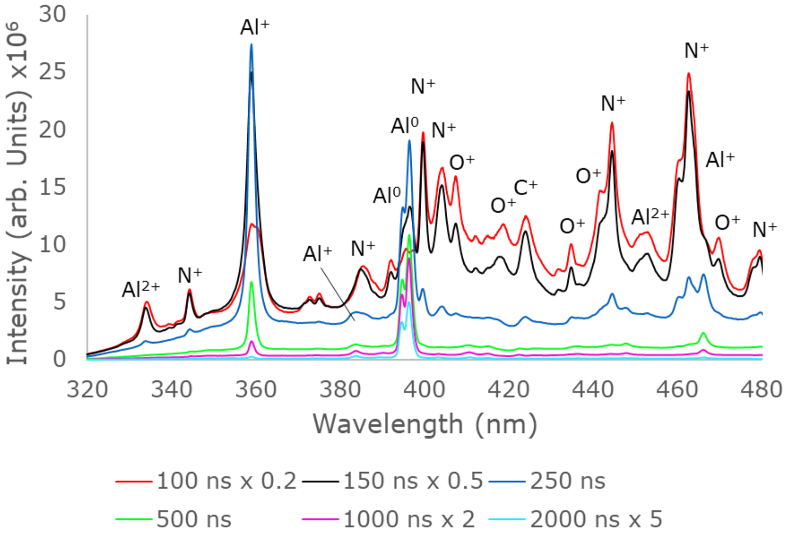

Fig. 5.2 Time resolved optical emission spectra of the 90° V-channel target in the wavelength range 320 nm – 480 nm with slit positioned in Y-direction. Lines have been tagged with their corresponding elements for reference.

which are required for obtaining electron temperatures and densities, extremely difficult at the early times in the radiative lifetime of the plasma.

This dominance of the continuum and air emission over the Al lines of interest also highlights an advantage of OES over filtered imaging. In section 4.3 it was observed that the images showed little difference between charge state distributions for the aluminium species at early time delays. However, with the additional spectral information provided by OES, one can now conclude that those images alone could not be used to track Al species in the plasma due to the large amounts of continuum and air emission present in the spectral bands of the filters used.

From the spectra shown in Fig. 5.2, the following Al emission lines were chosen as markers for further investigation of the various stages of the plasma evolution:

1) The Al^{2+} $334.85\,nm$ $[2p^6 6p(^2P_{3/2}) - 2p^6 4d(^2D_{5/2})]$ line is only present at the hotter, earlier stages for the plasma, with significant emission in the time delay range from $100 - 250\,ns$.

2) The $Al^{+}\ 358.7\,nm\ [3s4f(^{3}F_{2}) - 3s3d(^{3}D_{2})]$ line is present for the majority of the plasma life-time, covering the time delay range $100 - 2000\,ns$.
3) The $Al^{+}\ 466.3\,nm\ [3s4p(^{1}P_{1}) - 3p^{2}(^{1}D_{2}\,)]$ line is resolvable from the N^{+} emission after $250\,ns$, and is present for the majority of the plasma life-time, from $250 - 2000\,ns$.
4) The Al^{0} doublet consisting of the $394.4\,nm$ and $396.15\,nm$ lines from the $3s^{2}4s(^{2}S_{1/2}) - 3s^{2}3p(^{2}P_{1/2})$ and $3s^{2}4s(^{2}S_{1/2}) - 3s^{2}3p(^{2}P_{3/2})$ transitions is present from $150 - 2000\,ns$.

Further discussion on the plasma emission intensity and its temporal evolution is included in section 5.4.

5.1.2 Spatially Resolved Spectra along the X-Direction

As the Kymera spectrograph was stigmatic, it also provided spatial resolution along the slit direction. Spectra in the X-direction could be used to further investigate the bright spots seen in the filtered imaging in section 4.3. It was proposed that these spots, found at the target walls of the V-channel targets, were due to *forced recombination*. Yeates [2] suggests that this phenomenon is due to a hydrodynamic confinement of the plasma plume at the target walls which in turn act as electron donors and increases the formation of excited species in the local vicinity.

Fig. 5.3 shows spatially resolved spectra of the 60° V-channel and Flat targets along with corresponding line profiles for the $Al^{0}\ 394.4\,nm$ and $396.15\,nm$ emission lines at a time delay of $500\,ns$. It can be seen that in both spectra only the $Al^{0}\ 394.4\,nm$ and $396.15\,nm$ emission is present with little to no evidence of emission from the continuum and background gas species. Furthermore from the line profiles it can be seen that the

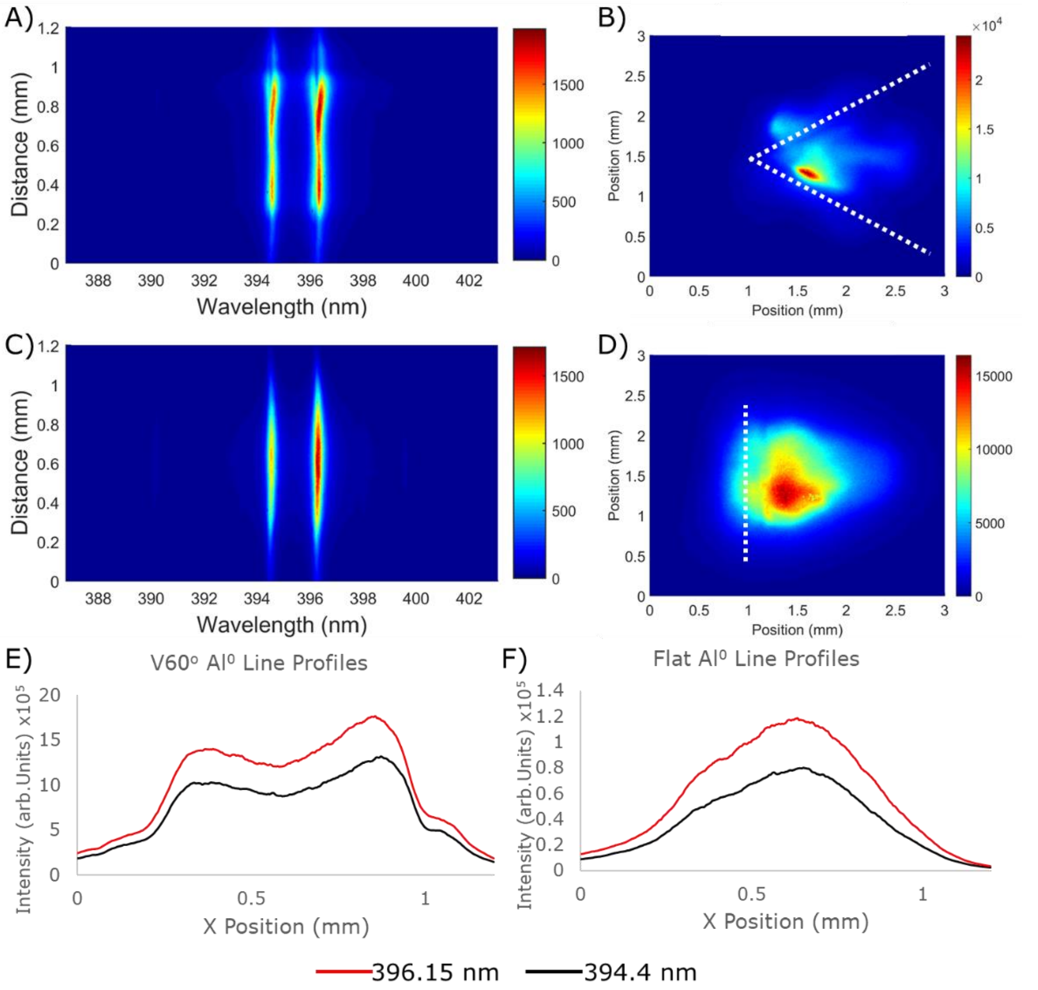

Fig. 5.3 Sample spectra from X-direction of Al^0 394.4 nm and 396.15 nm doublet for the A) 60° V-channel and C) Flat targets at a time delay of 500 ns. B) and D) show corresponding Al^0 filtered images, while E) and F) the spatial profiles of the emission lines within the spectra to aid comparison.

flat target Fig. 5.3D shows a central bright region which tails off in each direction. The 60° V-channel Fig. 5.3B however, shows distinct lobes of high intensity coming from the target walls[5] for both Al^0 emission lines. This result shows that the appearance of bright spots in some of the plasma images cannot be due to the background gas since this behaviour is not seen in the case of the flat target and is hence attributed to the presence of the confining target walls.

---

[5] The spectrum shown here exhibits bright spots close to both target walls, whereas in the filtered imaging only one bright spot was noted at one of the walls.

5.2 Spatial Distributions of Al^+ 358.7 nm and Al^0 396.15 nm Line Emission

As the Kymera spectrograph provided spatial resolution, the distribution of the $Al^+\ 358.7\,nm$ and $Al^0\ 396.15\,nm$ emission within the plasma could be investigated by taking lineouts from the temporally and spatially resolved spectra corresponding to the $Al^0\ 396.15\,nm$ and $Al^+\ 358.7\,nm$ lines, respectively. A sample set of the corresponding results from space resolved spectra recorded along the Y-direction, for the flat and 90^O V-channel targets can be seen in Fig. 5.4 while the 60^o and 30^o V-channel targets are shown in Fig. 5.5. The spatial profile of the $Al^+\ 358.7\,nm$ emission is shown by the orange lines, while the $Al^0\ 396.15\,nm$ represented by the blue lines.

It can be seen that at a time delay of $100\,ns$ the profile of the flat target (Fig. 5.4A) shows a peak in the intensity distribution close to the target (ca. $0.3\,mm$) for both emission lines which tails off gradually away from the target ($>\ 1.0mm$). At the front of the tail-off region a subtle second peak or shoulder in the emission profile can be seen for both lines, but more clearly in the case of the Al^+ feature. This is attributed to collisions of the of the plasma plume with the background gas at the leading edge of the plume where kinetic energy is converted into both ionization and excitation. Electrons formed in the former process will lead to a local increase in electron density and also contribute to a corresponding increase in impact excitation. The overall shape of the spatial distribution for both emission lines persists right up to the longest time delay shown (cf. $2000\,ns$ Fig. 5.4L) with only the relative intensities of the two species showing any significant variation, that of a peak close to the target surface which tails off gradually to a second component due to the confinement of the plasma.

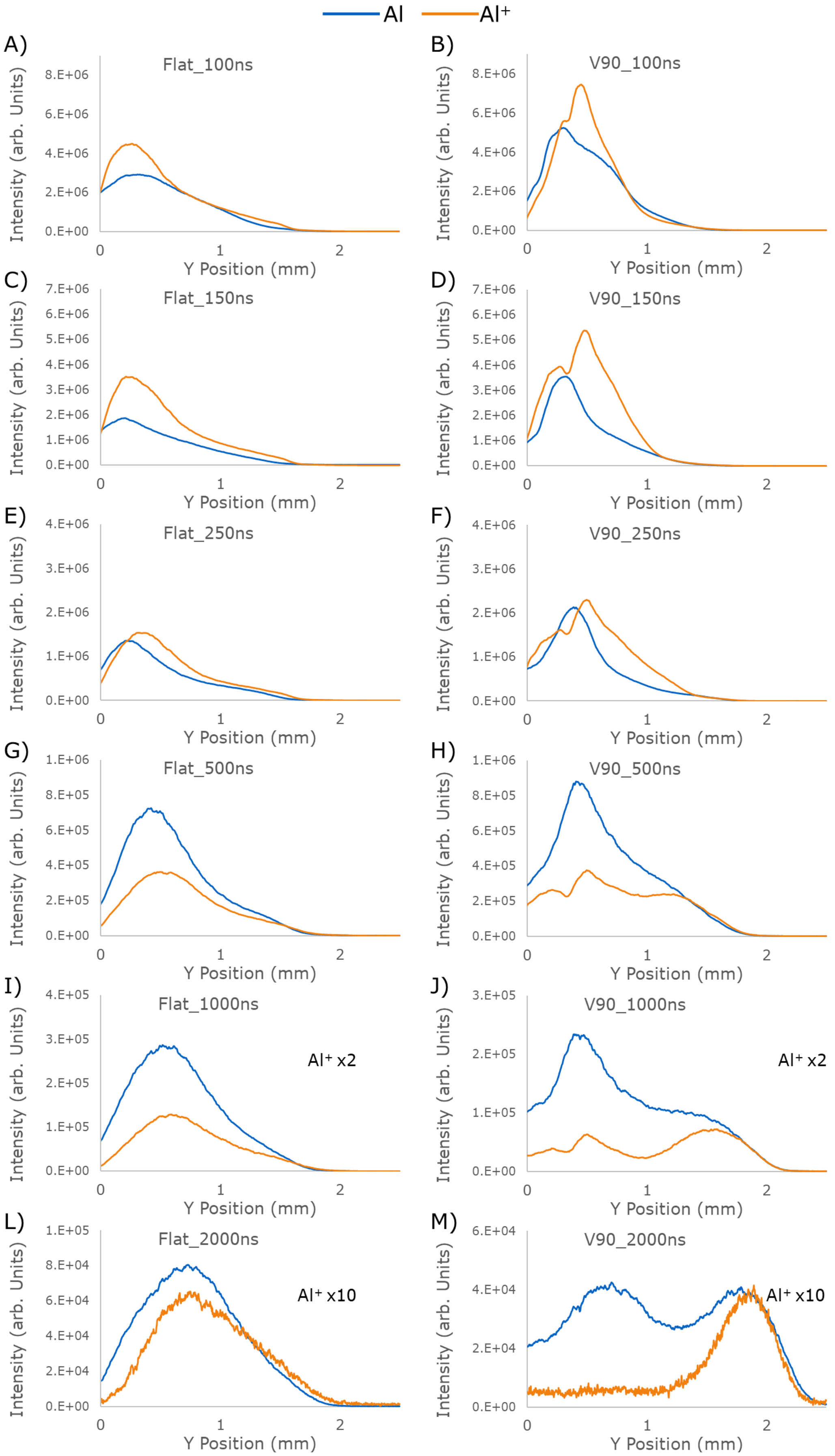

Fig. 5.4 Time resolved spatial distributions of the Al^0 396.15 nm *and* Al^+ 358.7 nm *line emission along the Y-direction for the Flat and 90° V-channel targets.*

Some specific divergences from this general behaviour include the following. At $250\,ns$, Fig. 5.4E, the Al species have separated with the Al^+ emission seen to extend farther from the target than the Al^0 emission. This is in accordance with the spatial distribution of charge states previously discussed in the filtered imaging, section 4.3.1.

Beyond $250\,ns$ the intensity of the Al^0 emission become more intense than the Al^+ line and the peaks in the spatial distributions of the two species begin to shift away from the target surface as the plasma expands. The two peaks are seen to follow one another closely in time and space with the Al^+ peak seen to be slightly ahead of the Al^0 peak at $500\,ns$, Fig. 5.4G, and $1000\,ns$, Fig. 5.4I.

Turning now to the 90° V-channel target, for the early time delays of $100\,ns$ and $150\,ns$, a double peaked spatial distribution of the Al^+ line emission is observed Fig. 5.4B and D. The individual peaks in this case are both strong and well-defined. The larger peak (at $0.8\,mm$), observed at these short delays, may be due to the early stages of the plasma lobe formation (build-up of hot material at the leading edge of the plasma which was seen in the broadband imaging Fig. 4.8A). Both the Al^0 and Al^+ emission also show strong emission with peak intensities nearly twice that of the flat target case at these corresponding times. It can also be seen that the spatial distribution of both species is more confined in the 90° V-channel target case with the leading edge exhibiting a steeper slope than for the flat target case. At a time delay of $150\,ns$, Fig. 5.4D, it can also be seen that the Al^+ emission is seen to extend further out than the Al^0 emission, as expected from the filtered imaging results in section 4.3.2. The emission distributions seen in Fig. 5.4F, corresponding to a time delay of $250\,ns$, show an increase in the relative intensity of Al^0 along with a broadening of the outer Al^+ peak as the Al^+ rich plasma lobe moves further away from the target.

At a time delay of $500\,ns$, Fig. 5.4H, the spatial distribution of the Al^+ emission has changed significantly. The Al^0 line emission is overall stronger, and it has expanded to be comparable in width to the Al^+ emission distribution. There is a now a clear triple peak structure in the spatial distribution of the Al^+ emission. The first two peaks remain localised within the stationary plasma, and the third peak corresponding to the plasma lobe. This peak has now grown relatively stronger and has moved away, giving rise to the significant separation of the plasma lobe and stationary plasma.

At later time delays, Fig. 5.4J & M), the Al^0 emission splits into a double peak structure, namely the stationary and lobe-like plasma regions, in which the ionised species in both having largely recombined into excited Al^0 species. The Al^+ emission, on the other hand is largely confined to the plasma lobe, and hence the ratio of Al^0 to Al^+ emission in the plasma lobe follows more closely that of the flat target case than the stationary plasma (although at lower values). At $2000\,ns$ there is no Al^+ emission from the stationary plasma as can be seen from the spatial profile which exhibits only one peak emanating from the plasma lobe. This further supports the hypothesis that the stationary plasmas exhibit different behaviour from a single plasma plume (flat target case).

From the 60° V-channel target spatial distributions (seen in Fig. 5.5) at early time delays $100\,ns$, Fig. 5.5A, and $150\,ns$ Fig. 5.5C) similar behaviour to the 90° V-channel target case can be seen with distinct double peaks, with the outermost peak or shoulder attributed to the formation of the plasma lobe. It is clear that the peak in the Al^+ spatial distribution is observed further from the target than the Al^0 peak for these early time delays.

As the plasma lobe moves away from the stationary plasma, the strong Al^0 shoulder at $\sim 0.8\,mm$ is seen to have decayed quite significantly so that by a time delay of $250\,ns$, Fig. 5.5E, the spatial distributions of the Al^0 and Al^+ in the plasma lobe ($> 1.0\,mm$) are seen to be approximately equal. At this time delay the Al^0 species have already begun to exhibit more intense emission, earlier than that observed from the flat and 90° V-channel cases.

As time continues and the plasma lobe decays, the strong Al^0 emission is seen to persist while the peak of its intensity distribution moves out to a distance of $0.5\,mm$ where it remains for the rest of the observed

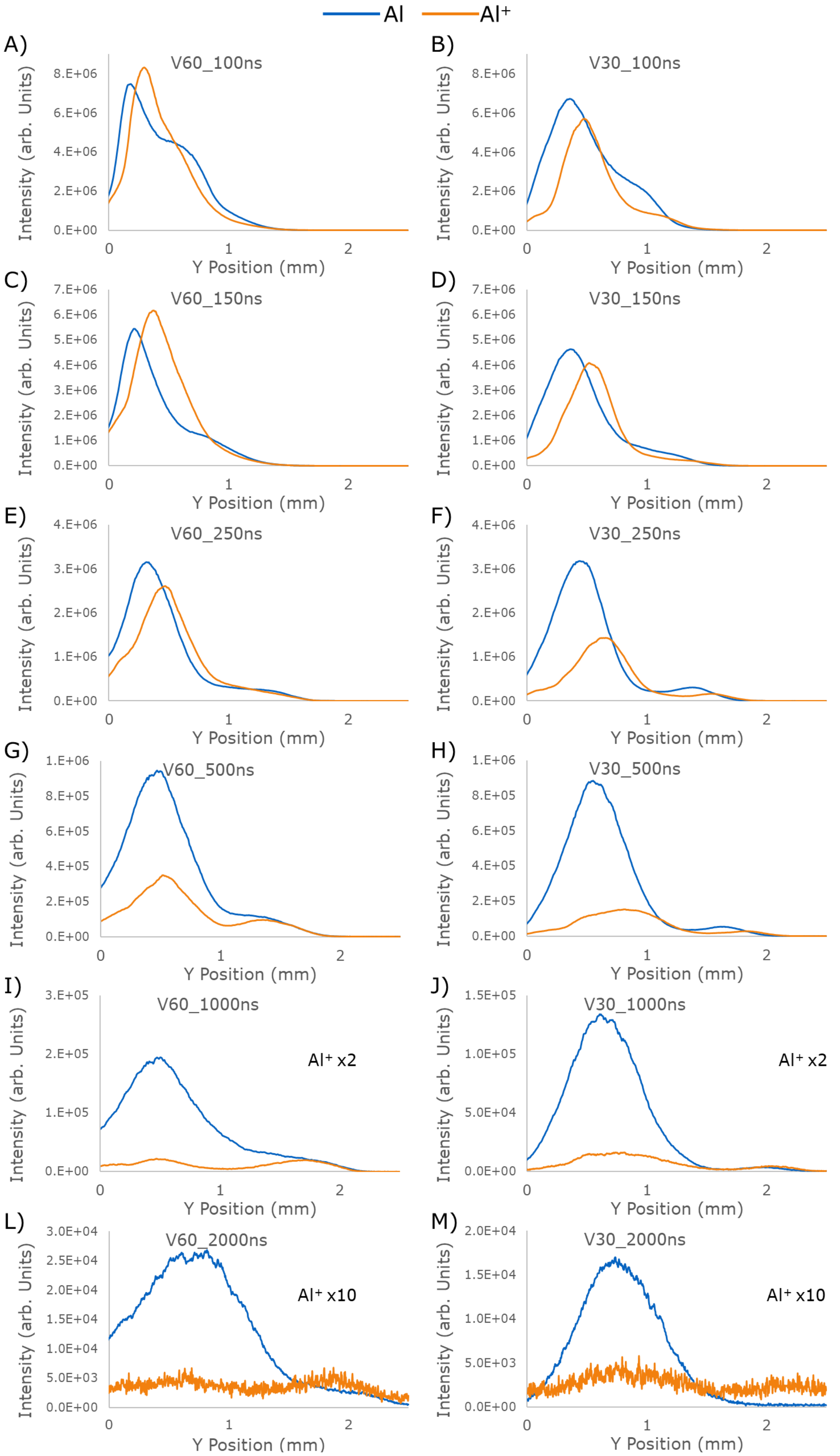

Fig. 5.5 Time resolved spatial distributions of the Al^0 396.15 nm *and* Al^+ 358.7 nm *line emission along the Y-direction for the 60º and 30º V-channel targets.*

time delays (c.f. Fig. 5.5 G, I, L). The Al^{+} peak, decays much more rapidly with relative intensity ratios between the Al^{0} and Al^{+} emission deviating from that observed from the flat target case. It is notable that the neutral distribution profile mimics that of the flat target at very long delays, being essentially one broad peak extending.

The 30° V-channel target is quite unique in that it is the only target where the peak intensity of the Al^{0} is greater than the Al^{+} for all time delays recorded. The initial two component distribution for both species can be seen again at $100\,ns$, Fig. 5.5B, however, the strong peaks in the spatial distributions are seen to be centred farther from the target vertex for this time delay at $0.4\,mm$ and $0.6\,mm$, for Al^{0} and Al^{+} respectively. Hence it is now clear that the early splitting of the peaks in the emission profiles increases as the target vertex angle decreases. As the plasma at the leading edge extends away from the target, a lobe can be seen quite clearly in the spatial distribution at $250\,ns$, Fig. 5.5F.

At the later time delays ($\geq 500\,ns$) the relative intensities of the Al^{0} to Al^{+} emission lines from the stationary plasma region were also seen to depart from the behaviour exhibited by the flat target. The line emission ratio from the extended plasma lobe, albeit derived from very weak lines, is again seen to follow more closely the flat target emission.

5.3 Spatio-Temporal Electron Temperatures & Densities

High resolution spectra (using the $2400\,l/mm$ grating (Grating 4 Table 3.2) which yielded a measured instrument function of c.a. $0.08\,nm$ FWHM with a window width of $16.3\,nm$) were obtained in order to determine the spatial and temporal electron temperature and density variations for the plasmas formed on each of the four target configurations for the X- and Y-directions. Time-resolved spectra of key lines of interest were recorded, including those at $Al^{+}\,358.7\,nm$, $Al^{0}\,394.4\,nm$ and $Al^{0}\,396.15\,nm$. These lines were chosen as they exhibited

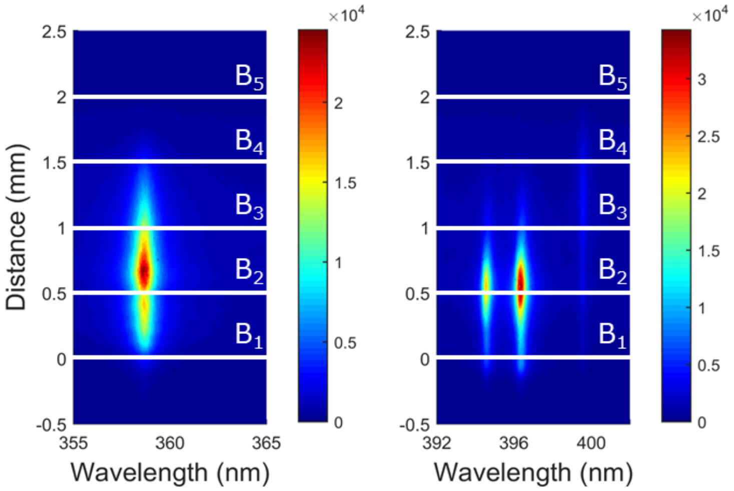

Fig. 5.6 Bin positions along the Y-direction where each bin corresponds to a height of 0.5 mm to provide reasonable space resolution. Sample spectra in the figure are for the 90°V-channel target at 250 ns.

strong persistent emission during the OES experiments, ideal for optical diagnostics experiments over long periods during the lifetimes of the plasmas formed.

As described in section 2.6.3, Stark broadening of spectral lines can be used to determine the electron density of a plasma. Using the electron density values, along with the relative line intensities, one can determine the corresponding electron temperatures. Therefore, in order to obtain values of the line intensities and Stark broadened widths the spectra first need to be analysed and Voigt profiles fitted to the measured lineshapes. The corresponding spectral analysis is outlined below.

The intensity corrected spectra were opened in MATLAB™ [3] and were trimmed to the region of interest (ROI). Next the spectra were spatially transformed from pixel number vs. wavelength (nm) to position (mm) vs. wavelength (nm).

In order to obtain spatial resolution the spectra were then split into five boxes along the plasma expansion direction[6], as shown in Fig. 5.6, and the data within each section binned. The binned data was tabulated and saved to *.txt* files for line profile fitting.

---

[6] In the Y-direction this was at set intervals of $0.5\,mm$, while in the X-direction this was at set to be 1/5th of the expansion width and hence varied for each target.

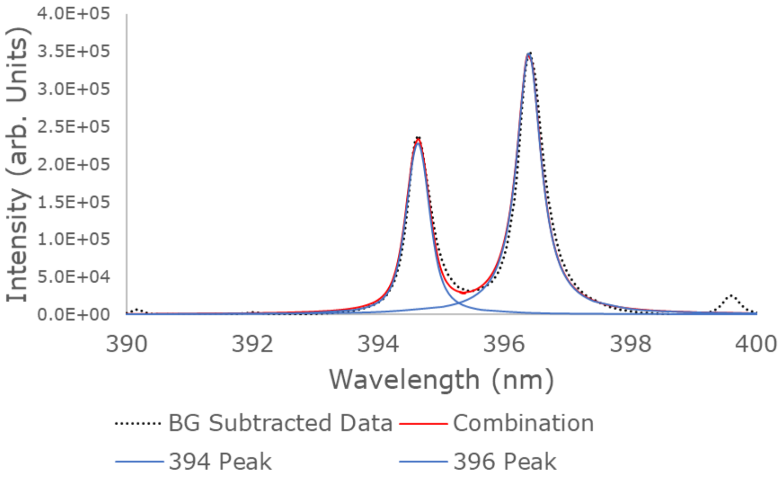

Fig. 5.7 Aluminium doublet spectrum with corresponding Voigt peak fits using Origin. From the fit parameters integrated line intensities and Stark broadened FWHM values could be obtained.

Fitting was performed using the *Peak Analyzer tool* in the plotting package Origin [4]. In order to obtain a more accurate fit to the spectral lines, prior baseline continuum emission subtraction was required. The baseline was determined by the *asymmetric least squares smoothing method* which proved the most robust approach within the peak analyser tool when dealing with the irregular baselines present in some of the spectra.

Once the baseline was determined and subtracted, Voigt profiles could be fitted to the spectra. Peaks were determined by the Origin software and a threshold limit of 20% of maximum intensity was set so that weak peaks were omitted. An example of the Voigt fits to the Al^0 doublet at $394.4\,nm$ and $396.15\,nm$ can be seen in Fig. 5.7 for the bin B_2 of the spectrum in Fig. 5.6. The fitting parameters from these Voigt fits could be extracted and tabulated for the electron temperature and density calculations.

For the electron density calculations, the Stark broadening of the spectral lines results in a Lorentzian profile. This profile and the corresponding full width at half maximum (FWHM) were then used with equation (2.43) to obtain a value for the electron density. Equation (2.43) is repeated here for convenience as:

$$n_e = \frac{2w}{\Delta\lambda_{S\frac{1}{2}} \times 10^{16}} \qquad (2.43)$$

Table 5.1 Electron impact parameter w *values for the spectral lines of interest*

Spectral Line	Transition	$w\ (\text{Å}.10^{-16}.cm^{-3})$
Al^{+} 358.7 nm	$3s4f(^3F_2) - 3s3d(^3D_2)$	0.288
Al 394.4 nm	$3s^24s(^2S_{1/2}) - 3s^23p(^2P_{1/2})$	0.037
Al 396.15 nm	$3s^24s(^2S_{1/2}) - 3s^23p(^2P_{3/2})$	0.038

The electron impact parameter values w $(\text{Å}.10^{-16}.cm^{-3})$ for each of the spectral lines of interest were taken from references [5–7] and are shown in Table 5.1. The Al^{+} 358.7 nm line has a large impact parameter, some ten times greater than the other lines, since it is comprised of many lines. However this blended line has been used in the literature for these measurements [8,9], and reference [9] gives the corresponding corrected atomic data for these lines to be used as a single blended line.

Once the electron densities were obtained, they were used to determine the electron temperature, as described in section 2.6.4. The intensity ratios from successive ionization stages can be used to solve equation (2.49) for the electron temperature:

$$\frac{I_2}{I_1} \approx \frac{A_2 g_2 \omega_2}{A_1 g_1 \omega_1}\left(4\pi^{\frac{3}{2}} a_0^3 n_e\right)^{-1}\left(\frac{k_B T_e}{E_H}\right)^{\frac{3}{2}} \exp\left(\frac{E_2 - E_1 - E_\infty + \Delta E_\infty}{k_B T_e}\right) \qquad (2.49)$$

The main lines used for the plasma temperature determination were the Al^{+} 358.7 nm and Al^{0} 394.4 nm and the various atomic parameters required were taken from [9] and are included in Table 5.2.

Table 5.2 Transition probability constants for the spectral lines of interest.

Spectral Line	g	$E\ (ev)$	$A\ (s^{-1})$
Al^{+} 358.7 nm	15	15.302	2.35×10^8
Al 394.4 nm	2	3.1427	4.99×10^7
Al 396.15 nm	4	3.0004	9.85×10^7

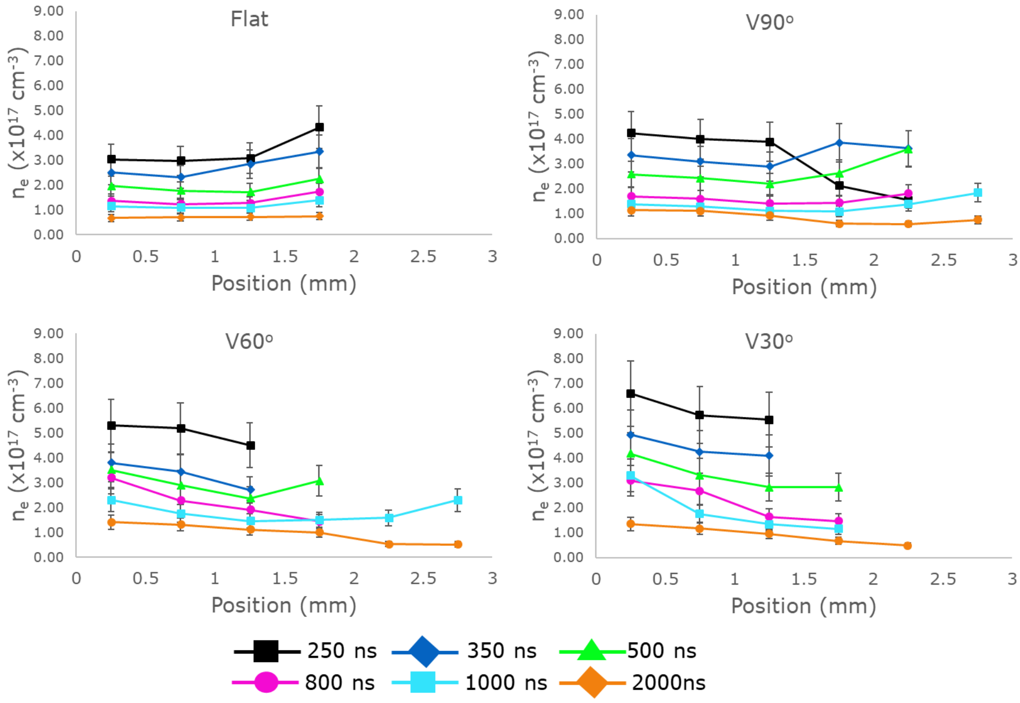

Fig. 5.8 Comparison of the measured spatio-temporal electron densities for the different targets along the Y-direction.

5.3.1 Electron Density Measurements

Fig. 5.8 shows a comparison of the electron densities in the Y-direction for the different targets for some sample time delays. An average of the densities obtained from the Al^{+} $358.7\,nm$ and Al^{0} $394.4\,nm$ lines were used for these values. Due to the strong continuum radiation emitted by the plasmas at early time delays, measurements could only be made at time delays from $250\,ns$ onwards.

From Fig. 5.8 it can be seen that the V-channel targets show an increase in electron density over the flat target, as expected for spatially confined plumes. It can also be seen that at $250\,ns$ the electron densities measured increase as the target angle decreases, with the 30° V-channel target exhibiting the largest electron density, especially at early time delays (Fig. 5.8D). The V-channel targets all show high electron density in the $0.0 - 0.5\,mm$ region, i.e., the stationary plasma, with a gentle negative gradient along a spatial extent of $0.0 - 1.5\,mm$ in each case.

As time progresses and the plasma lobes within the V-channel targets expand and electron densities at the leading edge of the plasmas increase so that an upswing in electron density can be seen from all

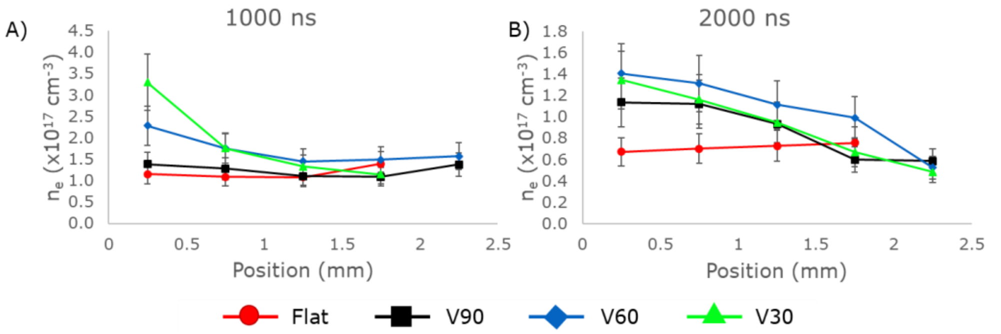

Fig. 5.9 Electron densities of the different targets along the Y-direction at time delays of A) $1000\,ns$ *and B)* $2000\,ns$ *.*

V-channel targets at $350\,ns$ (Fig. 5.8B-D). The minimum in electron density for this time delay appears at a distance of ca. $1\,mm$ from the target vertex so that the electron density profile for each of the V-shaped targets take on a bow-like shape.

At a time delay of $500\,ns$ the stationary plasmas exhibit a higher relative electron density due to a more gradual decay than the other plume regions (plasma lobe and intermediate region). This gradual flattening of the electron density profile is particularly visible in the 60° and 30° V-channel targets, Fig. 5.8C and D. Beyond the stationary plasma region, at distances $> 1\,mm$, it can be seen that the electron density of the V-channel targets tends towards values comparable to the flat target plasma at time delays exceeding $1000\,ns$ (c.f. Fig. 5.9). This outer region of the plasma plume was already shown to behave in a similar fashion to plasmas formed on the flat target in section 5.2, and is similar to the behaviour that was observed by Zeng *et al* in [10], i.e., higher electron density within the cavity region of target while the extended portion of the plasma plume exhibited electron densities closer in value to that of a single laser plasma.

In the case of electron densities in the X-direction, one can see a number of differences between the flat and V-channel targets. Sample data corresponding to various time delays are shown in Fig. 5.10. The V-channel target data again shows evidence of the effect of confinement of these plasmas with increased electron density over the flat target, especially for the 60° and 90° V-channel targets. In addition to this general increase in electron density over the flat target, there are regions of higher electron density close to the target walls with minimum

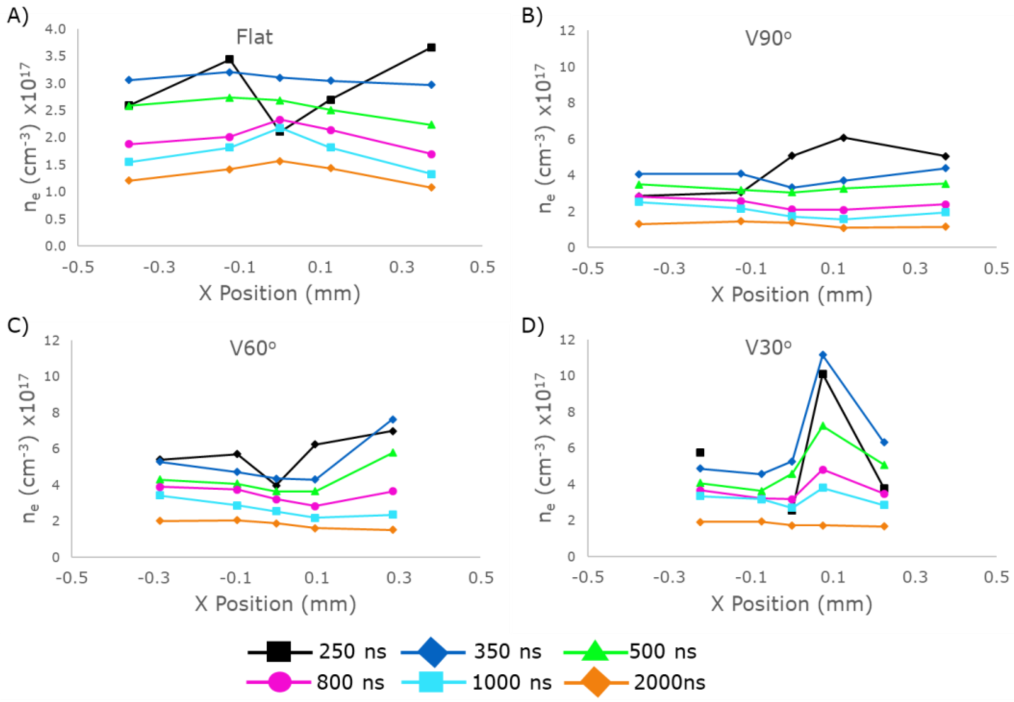

Fig. 5.10 Comparison of the measured spatio-temporal electron densities for the different targets along the X-direction.

at the centre plane where one would expect to find the stationary plasma for all V-channel targets. The flat target does not exhibit any evidence of this effect and in contrast the electron density has a much more gradual gradient, with the central hot core of the plasma exhibiting the higher densities. We propose that the higher electron density near the target walls arises from forced recombination where the metal surface acts as a source of bath of additional electrons which gives rises to a local increase in electron density.

The 30° V-channel is distinctive in the sense that the electron density distribution is quite asymmetric for all but the longest time delay. There is evidence of a trend in increasing asymmetry with deceasing opening angle of the target. Fig 4.20 does show evidence of asymmetric hot spots in the atomic aluminium images for a number of time delays and so that this is mapped here onto the electron density is perhaps not too surprising.

From both X- and Y-direction data it can be seen that along with the differences discussed above, plasma confinement by the V-channel targets also has an impact on electron density with the more confined

30° V-channel plasmas exhibiting typically higher electron densities, followed by the 60° and 90° V-channels.

5.3.2 Electron Temperature Measurements

Fig. 5.11 shows samples of the measured electron temperatures for the Y-direction. Due to the weak $Al^{+}\ 358.7\ nm$ and $Al^{0}\ 394.4\ nm$ line emission in some regions of the plasma at particular time delays, it was not possible to make reliable line profile fits. Hence it was not possible to make electron temperature calculations in all cases and consequently some data points do not appear in the plots below.

All of the targets show similar electron temperatures with differences at each corresponding position lying within an interval of width ca. $0.1\ eV$. It can be seen that typically the 90° V-channel target, Fig. 5.11B, exhibits higher electron temperatures, while the flat and 60° V-channel targets initially have similar electron temperatures for positions $> 0.5\ mm$. As the plasmas expand it can be seen that the 60° V-channel target cools faster than the flat target. In fact, the tighter that plasma confinement, the fast the electron temperature drops, with the 60° and 30° V-channel targets exhibiting the lowest electron temperatures at a given time delay (Fig. 5.11 C and D). This trend, whereby the greater the plasma confinement , the more rapid the electron temperature decays with time was also seen by Zeng *et al*, [10] and Yeates *et al*, [2].

In all cases the spatial distribution of electron temperature is quite flat, albeit slightly bowed with slightly higher values at the stationary or stagnated plasma region close to the target and further out in the lobe-like plasma region. This increase of electron temperature at the leading edge can once again be attributed to collisions with the background gas, which can release excess hot electrons at the collision front.

There is one slight caveat on the above discussion. It was found that the relative intensities of the $Al^{0}\ 394.4\ nm$ and $396.15\ nm$ lines, which end on the spin orbit split ground states of aluminium were not always in the statistical ratio of $2:1$. This was particularly noticeable at large

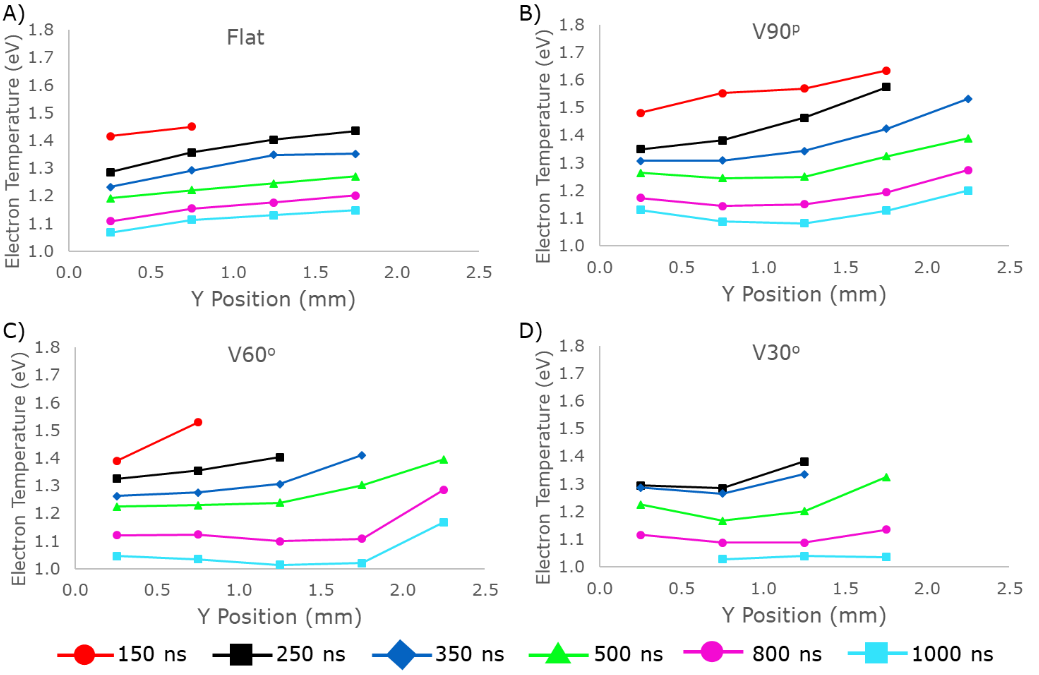

Fig. 5.11 Measured spatio-temporal electron temperatures for the different targets along the Y-direction.

distances from the target and at later time-delays ($> 1000\ ns$) with ratios going as low as $1.5{:}\,1$ in some cases. However this is mainly due to self-absorption on the stronger $396.15\ nm$ emission line ($3/2$ – $1/2$ transition) while the $394.4\ nm$ emission line ($1/2$ – $1/2$ transition) is significantly less affected due to its lower gf value.

Hence the electron temperature values obtained should be reliable and can still be used to track space-time trends in these key plasma parameters. In addition to the electron densities, they can also be used within the collisional radiative model by Colombant and Tonon [11] to obtain and track trends in the rates for recombination and ionisation processes in plasmas formed on the various targets. However the values obtained from the collisional radiative model should only be used to observe trends and ratios rather than a measure of the absolute rates.

5.3.3 Collisional Radiative Ionisation Model Rates

The electron densities and temperatures obtained in sections 5.3.1 and 5.3.2 are used here, with a code [12] based on the collisional radiative ionisation model of Colombant and Tonon [11], to calculate ionization and recombination rates. This collisional radiative ionisation model was discussed in section 2.4.3 and is based on the rate equation (2.31) which includes collisional ionisation (S), radiative recombination (α_{RR}), and three-body recombination ($\alpha_{3B}n_e$).

Fig. 5.12, Fig. 5.13, and Fig. 5.15 show the collisional ionisation ($\mathrm{Al}^0 \rightarrow \mathrm{Al}^+$), radiative recombination ($\mathrm{Al}^+ \rightarrow \mathrm{Al}^0$), and three-body recombination ($\mathrm{Al}^+ \rightarrow \mathrm{Al}^0$) rates for the various targets on position-time colour maps for time delays of $150 - 1000\,ns$ along the Y-direction. Due to the large variation in the rates, their values are presented on a $\log_{10}$ scale. Fig. 5.14 shows a time resolved comparison for the various rates for the different targets, integrated over the range 0.0 – $0.5\,mm$ along the Y-direction, extracted from these maps. It can be seen from these plots that the V-channel targets exhibit an increase of all rates over the flat target case. Also seen is a trend whereby the various rates increase as the target confinement increases.

The flat target case shows quite comparable rates for radiative recombination and three-body recombination Fig. 5.14A. Initially three-body recombination is the stronger recombination mechanism . However this is short lived, and the two rates equalise at $\sim 700\,ns$ while radiative recombination becomes the more favoured for the remainder of the time delay range.

It is proposed that this behaviour is due to three-body recombination having a dependence on electron density and therefore at the early time delays, when electron density is high, three-body recombination becomes the stronger mechanism. However, as the electron density drops over time, three-body recombination rates decay at a faster rate than radiative recombination which then becomes the dominant mechanism. From Fig. 5.12A, Fig. 5.13A, and Fig. 5.15A , it can be also be seen that the flat target case shows uniform behaviour for all three rates with reasonably similar values and a slight increase away from the target surface in the vicinity of the plasma-air boundary.

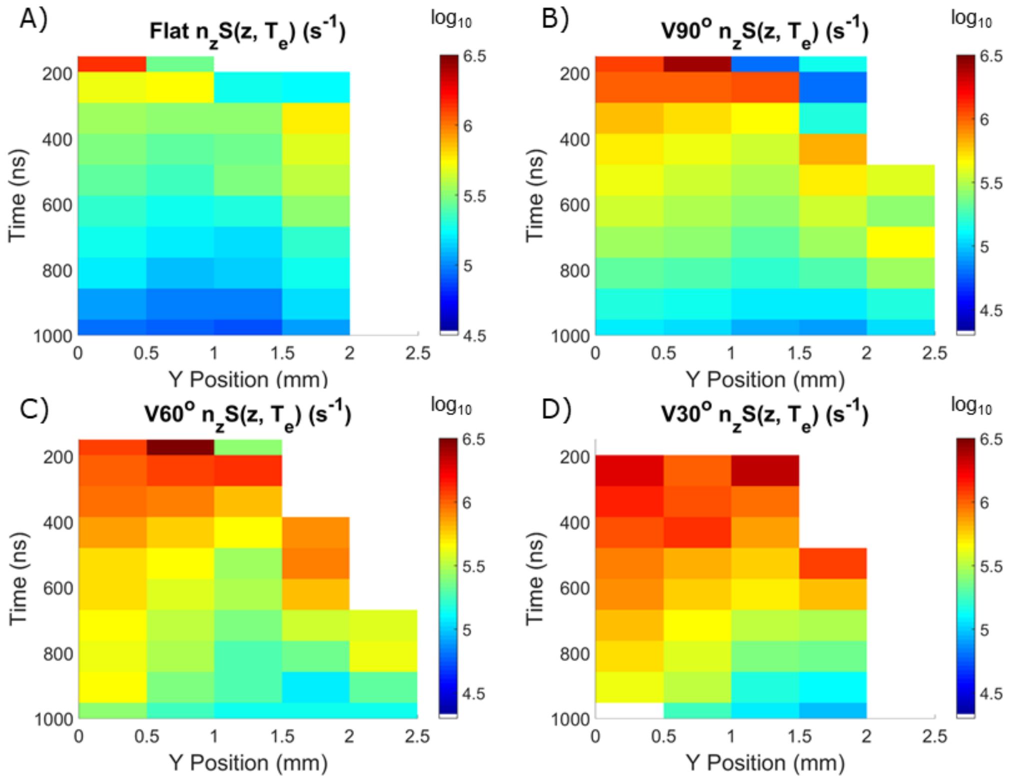

Fig. 5.12 Time position maps along the Y-direction for Al^0 collisional ionisation rates ($Al^0 \rightarrow Al^+$) for the various targets. Rates are shown as $\log_{10}$ values to preserve contrast.

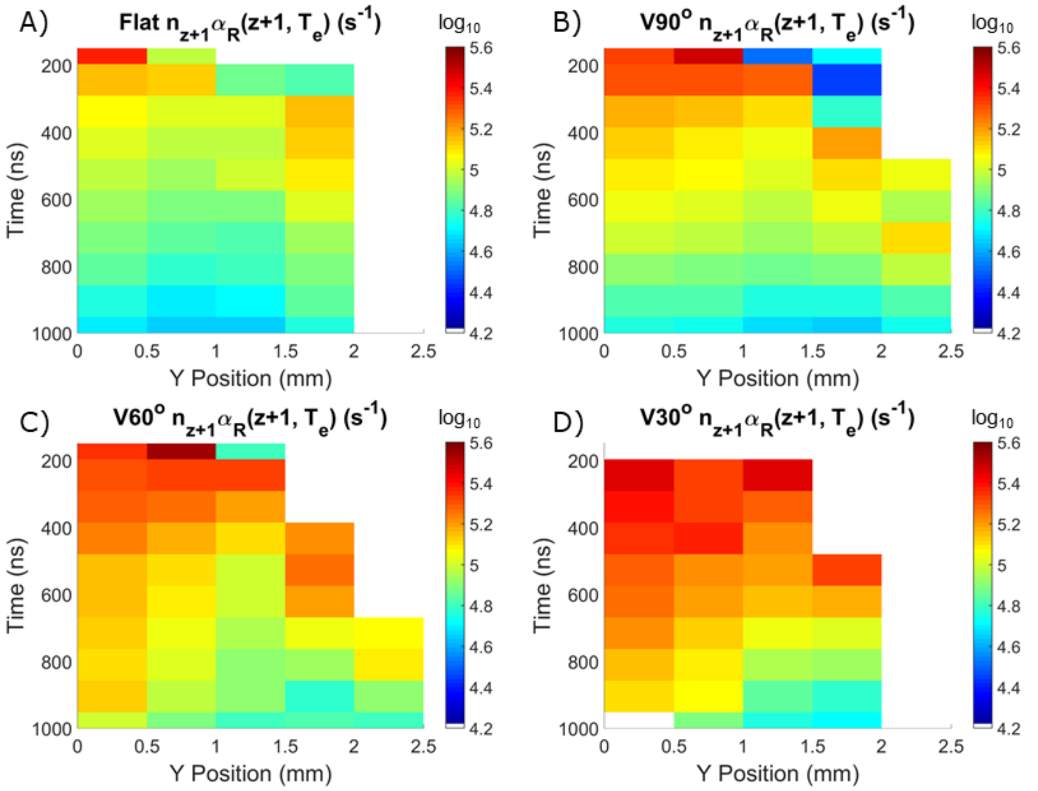

Fig. 5.13 Time position maps along the Y-direction for Al^+ radiative recombination rates ($Al^+ \rightarrow Al^0$) for the various targets. Rates are shown as $\log_{10}$ values to preserve contrast.

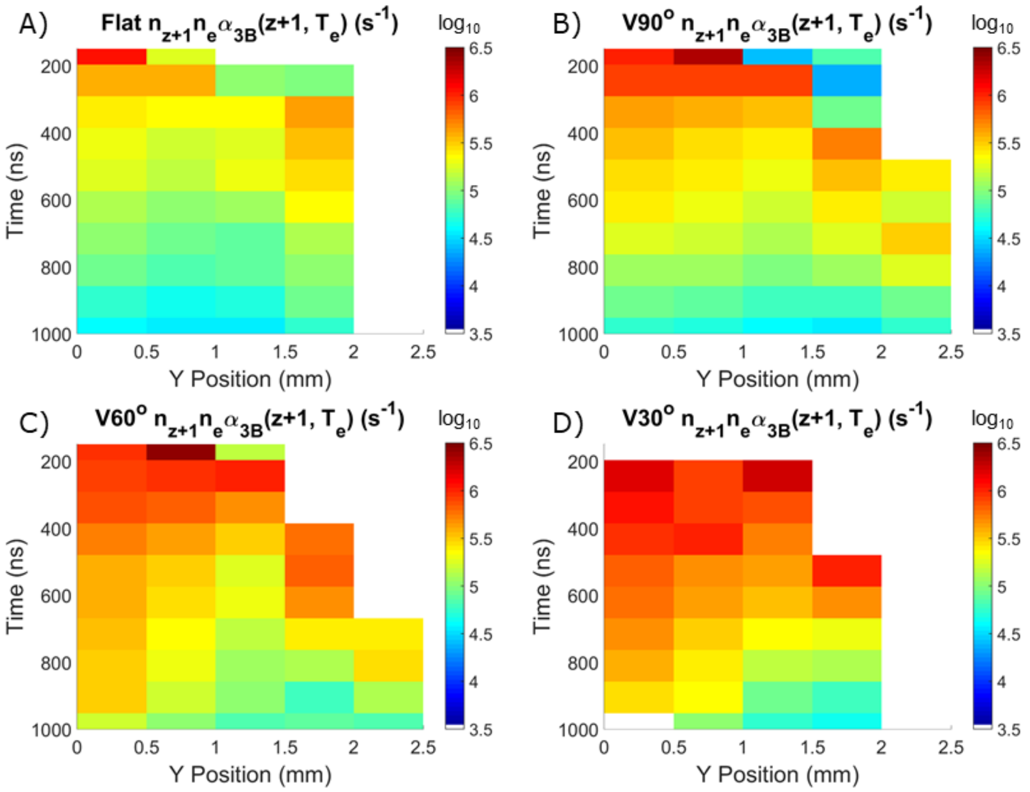

Fig. 5.14 Comparison of the various ionisation and recombination rates ($Al^0 \leftrightarrow Al^+$) as a function of time for the different targets. Data points obtained by integrating over the range $0.0 - 0.5\,mm$ along the Y-direction.

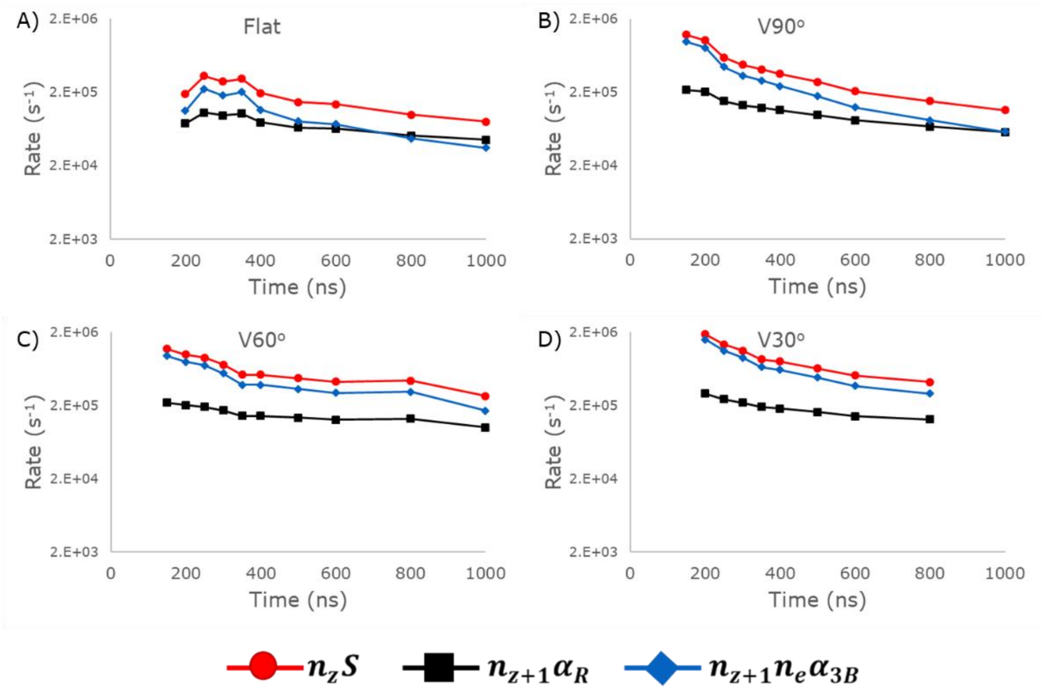

Fig. 5.15 Time position maps along the Y-direction for Al^+ three-body recombination rates ($Al^+ \rightarrow Al^0$) for the various target. Rates are shown as log_{10} values to preserve contrast.

The V-channel targets differ from the flat target case and also exhibit somewhat different behaviours between the different target geometries. From Fig. 5.14B three-body recombination is the more favoured recombination mechanism for the 90° V-channel target at $150\,ns$ with a rate some $\times 4.5$ greater than for radiative recombination. As the electron density decreases, just as in the flat target case, the three-body recombination rate is seen to correspondingly fall away at a faster rate than the radiative recombination. However it is not until the end of the time delay range studies, i.e., at $1000\,ns$ that the rates for the two mechanisms become equal, different to the $700\,ns$ time delay observed for this to occur in the flat target case. From the time-space maps, Fig. 5.12B, Fig. 5.13B, and Fig. 5.15B, it can be seen that the plasma lobe has a strong influence on the various rates at the leading edge of the plasma. The plasma lobe position can be tracked as it moves into the various position bins with a strong increase in all rates. This can be seen at $250\,ns$ for the range $1.0 - 1.5\,mm$, and at $400\,ns$ for $1.5 - 2.0\,mm$. The stagnated or stationary plasma is also an interesting region with rates in the $0.0 - 0.5\,mm$ range showing a slower rate of decay than those in the $0.5 - 1.5\,mm$ region and those for the flat target.

The 60° V-channel (Fig. 5.14 C) shows similar behaviour to the 90° V-channel target with an initially increase larger value for the three-body recombination rate of more than $\times 4$ over radiative recombination. However, unlike the 90° V-channel target the rates do not equalise within the time delay range covered here with the three-body recombination rate still displaying an increase of almost $\times 2$ over the radiative recombination rate at $1000\,ns$. Although initially all rates are similar to the corresponding 90° V-channel target values, at the longest time delays, the 60° V-channel rates are all larger, indicating a more gradual fall off ionization and recombination rates. From Fig. 5.15C and the time-position maps for the 60° V-channel target, Fig. 5.12C, Fig. 5.13C, and Fig. 5.14C, the stationary plasma is seen to exhibit a rather slow roll-off in all rates at the mid to late time delays ($> 350\,ns$).

Fig. 5.14D shows the 30° V-channel target case where the rates exhibit behaviour similar to the 60° V-channel target case, including the strong dominance of three-body recombination and higher values for all rates at early time delays compared to the other targets. It can also be seen that, just like the 60° V-channel target case, the three-body recombination rate is greater than the radiative recombination rate for all time delays and is a factor of 2 larger even at a delay as long as $800\,ns$. Measurements out to $1000\,ns$ were not possible due to the weakness of the spectra recorded there. Similar to the 90° and 60° V-channel target cases, the time-position maps for the 30° V-channel target, Fig. 5.12D, Fig. 5.13D, and Fig. 5.15D, show that the stationary plasma close to the target vertex retains higher rates for collisional ionisation, radiative recombination and three-body recombination over the positions further from the target at most time delays.

Comparing the different targets it can be seen that the more tightly confined the target the greater the values of the ionisation and recombination rates for comparable space and time values. Yeates [2], states that tighter confinement results in an increase in electron density and hence the rate of ion-electron collisions. As collisions increase, one would expect a corresponding increase in the collisional processes of collisional ionisation and three-body recombination.

5.4 Comparison of Line Emission for Different Targets

Fig. 5.16 shows the time evolution of the intensity of the $Al^{+}\ 358.7\,nm$ and $Al^{0}\ 396.15\,nm$ lines from the OES for the four different target geometries. The emission lines from the raw spectra (found in Appendix C) have been integrated to obtain line intensities. The line intensities are normalised to the flat target plasma corresponding values in order to observe variations in the relative intensities of the Al^{0} and Al^{+} lines as a function of time delay exhibited by the V-channel target plasmas.

At $150\,ns$, deviations from the flat target can be seen for all V-channel targets. The 30° V-channel shows a significant decrease in intensity for the $Al^{+}\ 358.7\,nm$ line, while the 60° and 90° V-channel targets show an

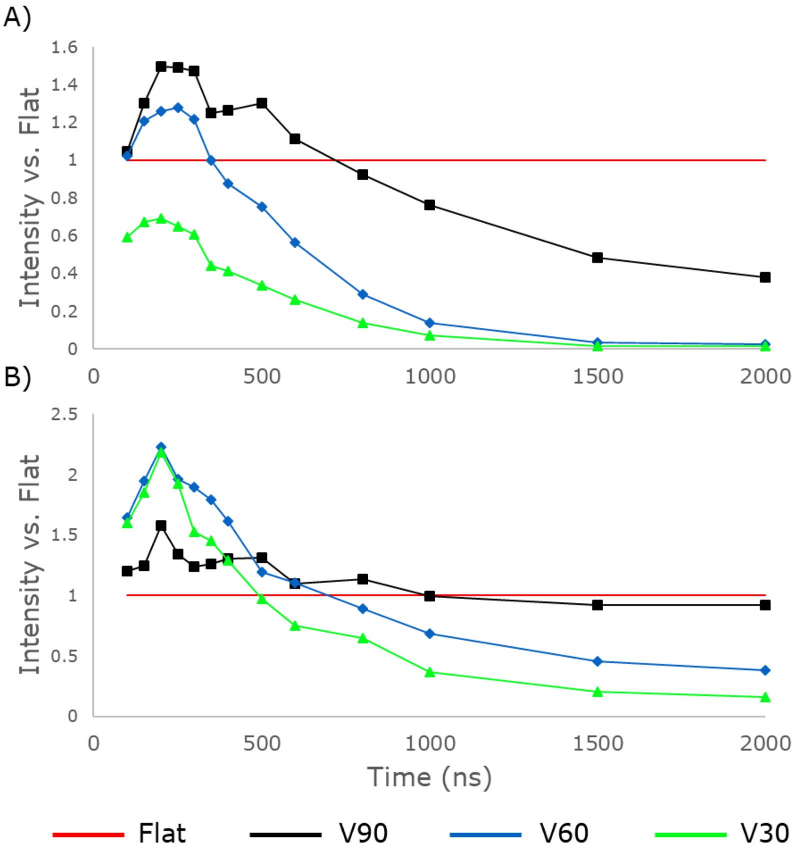

Fig. 5.16 Comparison of spatially integrated line intensity as a ratio of the V-channel target values to the flat target emission intensity for A) $Al^+ \, 358.7 \, nm$ *and B)* $Al \, 396.15 \, nm$ *lines as a function of time delay.*

enhancement over the flat target emission at this time delay for this line. From Fig. 5.16A this enhancement is on the order of $\sim 20\%$.

Looking now at the $Al^0 \, 396.15 \, nm$ emission line, again at $150 \, ns$, Fig. 5.16B, all V-channel targets exhibit strong enhancement of emission for this feature with intensity gains on the order of 25%, 95%, and 85% for the 90°, 60°, and 30° V-channel targets respectively.

The increase in emission for both the $Al^+ \, 358.7 \, nm$ (for the 90° and 60° V-channel targets) and $Al^0 \, 396.15 \, nm$ (for all V-channel targets) lines is seen to continue for quite some time, with intensities only falling below the flat target baseline some hundreds of nanoseconds later. The $Al^+ \, 358.7 \, nm$ line decays more rapidly than the $Al^0 \, 396.15 \, nm$ line as one would expect. The time delays at which each V-channel target intensity falls below the flat target emission for the $Al^+ \, 358.7 \, nm$ (t_{Al^+}), and $Al^0 \, 396.15 \, nm$ (t_{Al}) lines are given in Table 5.3.

Table 5.3 Time delays at which the emission of the V-channel targets fall below the flat target emission for the Al^{+} $358.7\,nm$ $(t_{Al^{+}})$*, and* Al^{0} $396.15\,nm$ $(t_{Al^{0}})$ *lines.*

Target	$t_{Al^{+}}$	$t_{Al^{0}}$
V90	700 ns	1000 ns
V60	350 ns	700 ns
V30	N/A	500 ns

The table also shows that the intensity of the Al^{0} line emission from V-channel target plasmas drops below the flat target baseline and decreases with increasing confinement, with the more tightly confining 30° and 60° V-channel targets falling below that of the flat target at earlier time delays. This trend differs slightly for the Al^{+} emission, in that the 30° V-channel target had not shown an enhancement in Al^{+} emission within the observed time-delays. However Al^{+} emission from the 60° V-channel target is seen to fall below that of the flat target emission before the 90° V-channel target which follows the trend that the decay of emission intensity is dependent on the degree of plasma confinement by the target.

Although plasmas formed on the flat target exhibit stronger emission than the V-channel targets for both the Al^{+} $358.7\,nm$ and Al^{0} $396.15\,nm$ lines at the later time delays, it is important to realise that at the time delays at which the V-channel plasma spectra have decreased in intensity compared to the flat target plasma, a significant portion of the total emission will have already taken place. In order to investigate this further, it was desired to temporally integrate the Al^{+} $358.7\,nm$ and Al^{0} $396.15\,nm$ line intensities. However, simply summing the various spectra acquired would not be an accurate representation of the total emission because, although the spectra were all recorded at gate widths of $10\,ns$, they were recorded at varying time delay intervals over the time delay range $100 - 2000\,ns$. Since the sampling intervals were smaller, and hence more numerous for early delay times, there would consequently be a bias towards the V-channel targets that show stronger emission in the early and mid-lifetimes. Therefore, in order to obtain a more accurate comparison, the data was integrated via the MATLAB™ [3] *trapz* function which uses trapezoids to integrate the area between data points and would result in a more fair comparison between

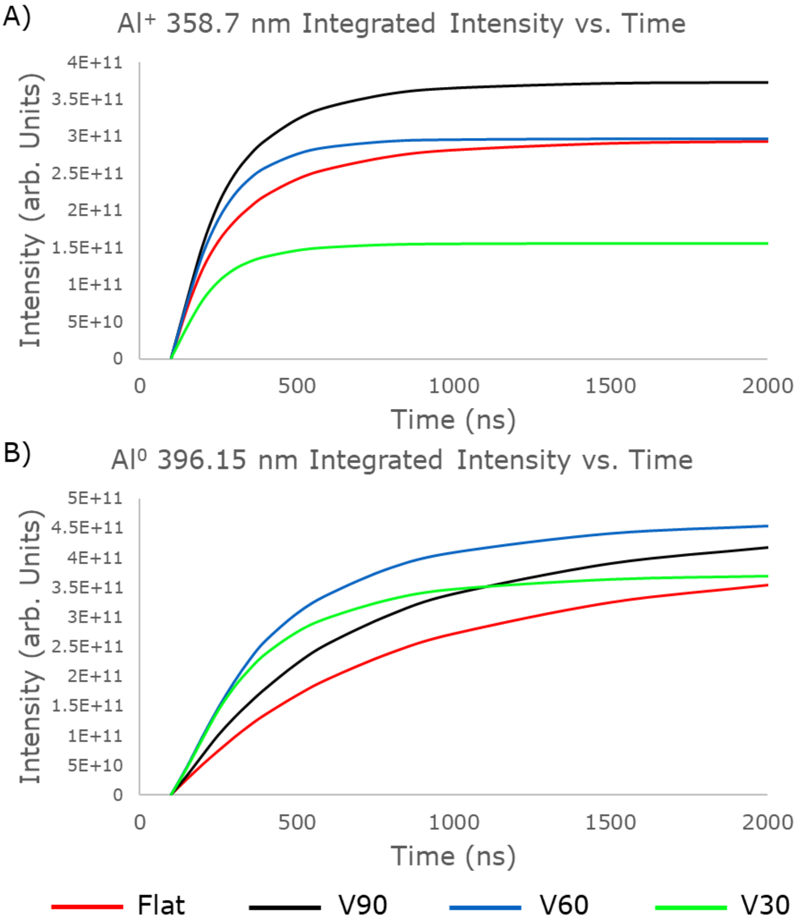

Fig. 5.17 Integrated intensities of A) Al^+ 358 nm line and B) Al 396 nm line. Intensities are integrated via the trapezoidal method over 100 – 2000 ns to give a more accurate depiction of the total emission.

the targets by taking into account the entire time series. The data was integrated up to each time delay in order to track the integrated emission and is shown in Fig. 5.17 with a summary of the final integrated intensities provided in Fig. 5.18.

It can be seen that for the Al^+ $358.7\,nm$ line, Fig. 5.17A, emission from all V-channel targets begins to plateau at a time delay of ca. $500\,ns$, since by this time the line emission has decayed significantly, and any further emission is not sufficient to vary the total accumulated counts by any large measure. The plasma formed on the 30° V-channel target shows significantly weaker $358.7\,nm\,Al^+$ emission, being some 47% lower than the flat target plasma case and having never shown any enhancement for this line within the time interval covered. The 60° V-channel target shows early enhancement of the $358.7\,nm\,Al^+$ emission over the flat target, with an increase in integrated emission of up to 20%

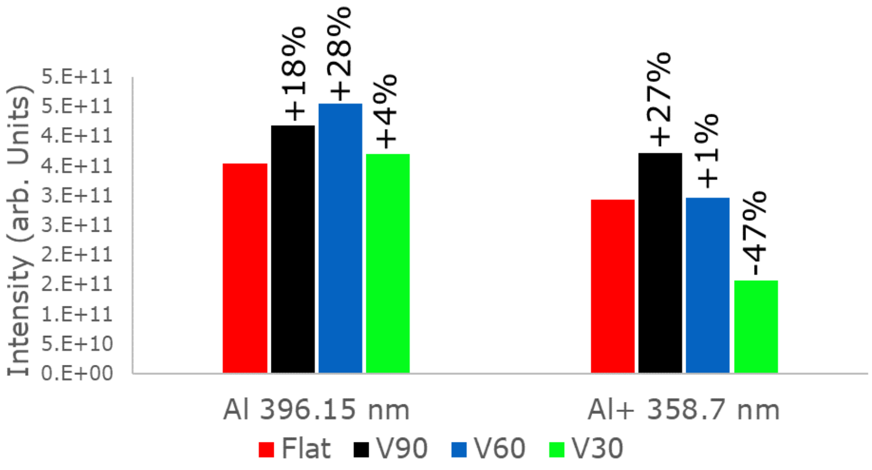

Fig. 5.18 Integrated line intensities for the various targets showing comparisons with the flat target. The percentage difference for the V-channel targets with respect to the flat target are included for ease of comparison.

at $300\,ns$. However, due to the 60° V-channel target emission levelling-off at a time delay of c.a. $600\,ns$, by the end of the time series at $2000\,ns$ the integrated intensities of the flat and 60° V-channel targets are approximately equal with a variation of just $+1\%$, well within error limits.

The 90° V-channel target is the only target to show a significant enhancement over the flat target for the $Al^{+}\,358.7\,nm$ line by the end of the time interval over which emission data was accumulated. A consistent increase of $25-30\%$ was observed for all time delays and at $2000\,ns$ the gain in time integrated emission is $+26\%$.

From the neutral $Al^{0}\,396.15\,nm$ line emission Fig. 5.17B, a much more gradual rise in the integrated intensity can be seen for all targets, which is expected as, from section 5.1.1, the neutral doublet does not appear strongly until time delays of $>150\,ns$ and exhibits intense emission for most of the plasma lifetime. Unlike the emission from the $Al^{+}\,358.7\,nm$ line, by the end of the time series the $Al^{0}\,396.15\,nm$ line emission has only levelled-off for the 30° V-channel target. The flat target plasmas exhibit the weakest emission for the period shown while the 30°, 60°, and 90° V-channel targets show enhancements on the order of $+18\%$, $+28\%$, and $+5\%$ respectively.

It can be seen that plasmas formed on the 30° V-channel target show strong early enhancement for the $Al^{0}\,396.15\,nm$ line over the flat and 90° V-channel target plasmas and that this emission levels off, leaving the still increasing 90° V-channel emission to surpass it at $\sim 1100\,ns$. The flat target does not overcome this early stage enhancement within the time delay range shown, but with a longer time delay range it is doubtful that it would not surpass the 30° V-channel emission. The 60° V-channel $Al^0\ 396.15\,nm$ emission shows a strong enhancement over the other target configurations at nearly all times, with only the 30° V-channel target having similar intensities at the earliest time delays in the series. $Al^0\ 396.15\,nm$ emission from the 90° V-channel target shows an increase in integrated emission over the flat target of 18% by the end of the measurement time series, i.e., at $2000\,ns$[7].

The final investigation into the emission of the various targets was to determine the signal to background ratio (SBR) for the emission lines of interest. The purpose is to investigate whether the emission enhancement is due to a gain in line signal or just an enhancement in total flux from the target. The background was determined by integrating a spectral region of continuum emission, adjacent to the lines of interest, of width equal to the linewidths. Fig. 5.19 shows the ratio of the V-channel SBRs to the flat target SBR for the $Al^+\ 358.7\,nm$ and $Al^0\ 396.15\,nm$ lines. In the $Al^+\ 358.7\,nm$ SBR data, Fig. 5.19A, it can be seen that only the 90° V-channel target exhibits any enhancement in SBR, observed for time delays in the range of $200\,ns\ - 700\,ns$. As previously mentioned these early time delays are a key period for measurement as it corresponds to most of the period when most of the radiation is emitted. The 60° and 30° targets however, do not show this enhancement. In fact both targets exhibit substantial decreases in SBR, indicating an increase in background continuum intensity is present without a corresponding increase in line emission.

From the $Al^0\ 396.15\,nm$ SBR data, Fig. 5.19B, it can be seen that unlike the $Al^+\ 358.7\,nm$ SBR data, the 90° and 60° V-channel target plasmas show an enhancement in SBR over the flat target for the whole time delay range with a small dip below the flat target at a time delay of

---

[7] Enhancements of +27%, +65%, +46% were obtained for the 90°, 60°, & 30° V-channel targets for the $Al^0\ 396.15\,nm$ emission line when just summing the emission from the acquired spectra.

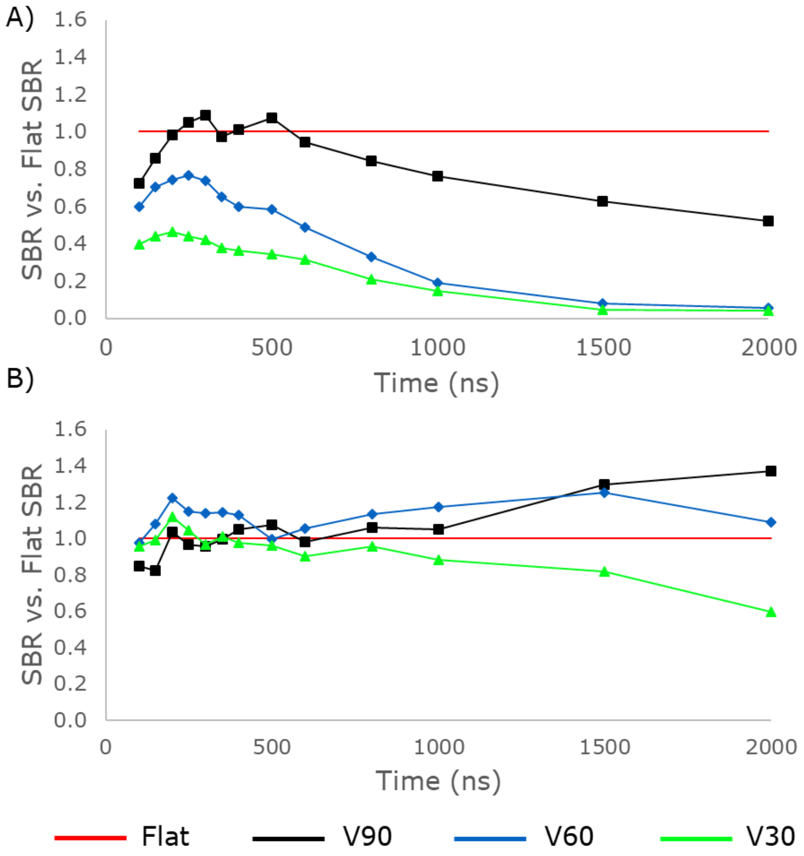

Fig. 5.19 Comparison of signal to background ratios of the V-channel targets with the flat target as a function of time for the A) Al^{+} 358.7 nm and B) Al 396.15 nm lines.

$\sim 500\ ns$. This clear increase in SBR shows that the enhancement of the emission seen in the 90° and 60° V-channel targets is indeed due to an increase in Al^{0} 396.15 nm line signal strength.

This observation contrasts with the 30° V-channel target which, although exhibiting an SBR that is close to the flat target, shows a decrease in SBR for most of the time delay range covered before decreasing even more significantly at later time delays as the emission dies off.

5.5 Summary

It was seen in this chapter that the stationary plasmas continue to exhibit behaviour one might expect from stagnating plasma. From the spatial distribution of the $Al^{+}\ 358.7\ nm$ and $Al^{0}\ 396.15\ nm$ emission lines, which were in good agreement with the filtered imaging from section 4.3, the intensity ratios were seen to differ from the flat target single plume in the vicinity of the stationary plasmas. On the other hand the lobe like plasma component beyond a distance of $ca. 1\ mm$ instead which exhibited behaviour more similar to the single plume case.

The electron density measurements showed that all V-channel targets experienced an increase in electron density due the plasma plume confinement. In addition, the stationary plasmas exhibited a slower rate of decay of electron density than the other plume regions (the plasma lobe and intermediate region), as one would expect from a stagnating plasma. A similar trend was observed for the electron temperature with the stationary plasma exhibiting a more gradual decay than the other plasma regions. However, unlike the electron density, the electron temperature of all regions within the V-channel targets are seen to cool at a faster rate than the flat target case.

The collisional-radiative ionisation model was used to extract rates of ionisation and recombination. It was seen that the stationary plasmas exhibited a slower roll off for these various rates, along with exhibiting an increase of up to an order of magnitude over the corresponding rates from the flat target case. In addition it was seen that at time delays $> 700\ ns$ the preferred recombination mechanism for the flat target was radiative recombination, while for the stationary plasmas this was seen to be three-body recombination.

It is a combination of exhibiting behaviour of stagnating plasma along with differences in the behaviour of the single plume flat target case that leads to the conclusion that these stationary plasmas are the result of both a colliding plasma system and plasma confinement and of hence potentially of further research interest.

The bright spots seen in the filtered imaging section 4.3 were further investigated and in section 5.1.2 were confirmed to be the presence of strong Al^0 emission extending from the target walls and not due to background gas species. Furthermore, in section 5.3.1 it was observed that these regions also show an increase in electron density at the target walls. It is a combination of these factors, along with the literature presented in the discussion in section 4.3.3, that leads to the conclusion that these bright spots could be due to forced recombination at the target walls.

Finally from the investigation into the emission from the various targets, the 90° and 60° V-channel targets show enhancement in emission over the flat target. The 90° V-channel target shows an enhancement of both the Al^+ $358.7\,nm$ $(+27\%)$ and Al^0 $396.15\,nm$ $(+18\%)$ emission lines, with corresponding increases in SBR, while the 60° V-channel target only shows enhancement from the Al $396.15\,nm$ emission $(+28\%)$ along with the increase in SBR. This increase in SBR is of key merit for analytical spectroscopy applications such as LIBS, as an enhancement in SBR should allow a lower limit of detection. The 30° V-channel target however, did not show any increase in SBR for either of the measured emission lines along with the increase in signal for the Al^0 $396.15\,nm$ only being on the order of $+4\%$.

References

1. NIST Atomic Spectra Database [Internet]. 2009. Available from: https://www.nist.gov/pml/atomic-spectra-database
2. Yeates P, Kennedy ET. Spectroscopic, imaging, and probe diagnostics of laser plasma plumes expanding between confining surfaces. J Appl Phys. 2010;108(9).
3. MATLAB. Massachusetts: MathWorks Inc; 2015.
4. OriginPro 2016. Northampton: OriginLab Corporation; 2016.
5. Heuschkel J, Kusch HJ. Stark Broadening and Shift of Singly Ionized Aluminium Lines. Astron Astrophys. 1973;25:149–51.
6. Roendigs G, Kusch HJ. Electron impact broadening of aluminum I-lines. Astron Astrophys. 1979;71(1–2):44–6.
7. Konjevic N, Wiese WL. Experimental Stark widths and shifts for spectral lines of neutral and ionized atoms. J Phys Chem Ref Data. 1990;19(6):1307–85.
8. Abdellatif G, Imam H. A study of the laser plasma parameters at different laser wavelengths □. Spectrochim Acta Part B. 2002;57:1155–65.
9. Kelleher DE, Podobedova LI. Atomic transition probabilities of aluminum. A critical compilation. J Phys Chem Ref Data. 2008;37(2):709–911.
10. Zeng X, Mao SS, Liu C, Mao X, Greif R, Russo RE. Laser induced plasma diagnostics of pulsed laser ablation in a cavity. 2003;58:1–24.
11. Colombant D, Tonon GF. X-ray emission in laser-produced plasmas. J Appl Phys. 1973;44(8):3524–37.
12. Hayden P. Plasma Parameter Calculator. Dublin; 2016.

6 Development of a Wollaston Prism Fourier Transform Spectrometer for LIBS Applications

Along with the formation of stagnation layers in air, work was undertaken on the development of a compact Fourier Transform (FT) spectrometer with no moving parts for use in LIBS. The objective was to build a compact spectrometer with a higher throughput than the conventional grating-based devices, for detecting weak LIBS lines and which could record a spectrum from a single laser shot. Its design is discussed in this chapter highlighting both its merits and areas for improvement. Comparison tests with the Stellarnet® EPP2000, a commercial compact grating spectrometer of similar size, have been conducted. The prototype FT spectrometer is shown to exhibit higher sensitivity as a result of improved optical throughput.

6.1 Fourier Transform Spectroscopy

In conventional dispersive spectroscopy, the spectrum is measured directly in the frequency domain. However with Fourier Transform spectroscopy a temporal/spatial interferogram is recorded [1]. The spectral distribution of an incident source can be determined by the power spectrum of the Fourier Transform of the interferogram recorded [2]. In Fig. 6.1 interferograms corresponding to three synthetic spectra in the frequency domain can be seen. A monochromatic source will result in a simple interferogram in the form of a sine wave. A dichromatic source on the other hand will result in an interferogram comprising a sum frequency modulated by a lower difference frequency as seen in the interferogram. Finally, a broadband or complex spectrum will result in an interferogram with few fringes which quickly decay as the various components destructively interfere.

There are two main advantages associated with Fourier Transform spectroscopy, namely the Fellgett and Jacquinot advantages. The Fellgett (or ‘multiplex’) advantage [3] pertains to a FT spectrometer since all frequencies are simultaneously measured. This allows the

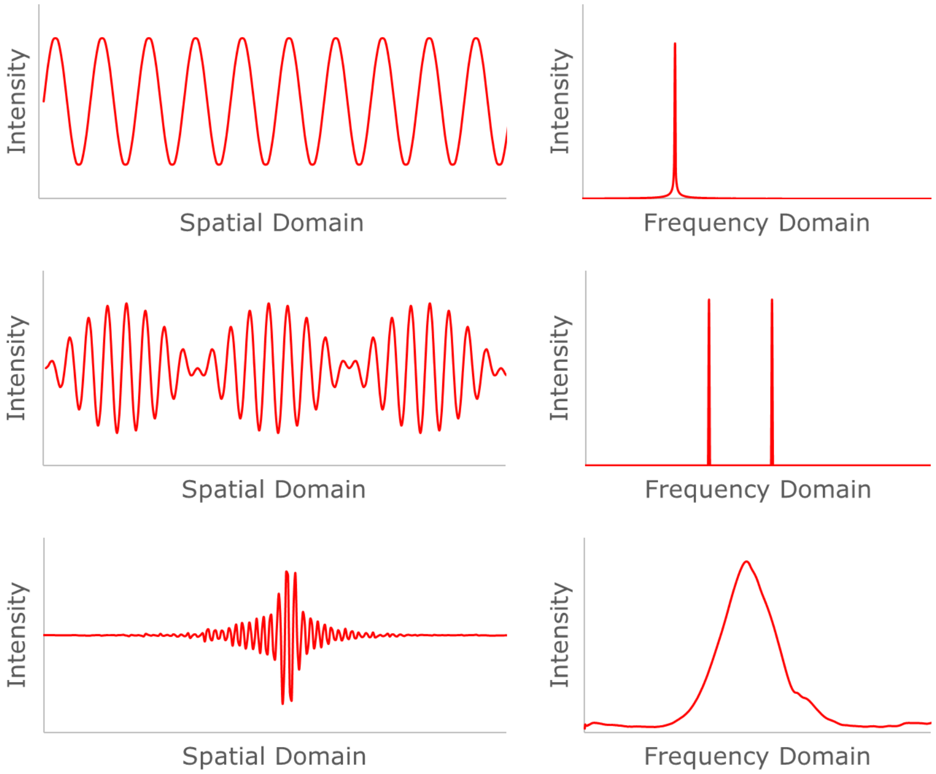

Fig. 6.1 Interferograms and their corresponding Fourier transforms. a) A single wavelength source and sharp peak spectrum. b) A dual wavelength source resulting in a spectrum with two sharp peaks. c) A broadband source with it's corresponding continuum or band spectrum. Recreated from [9]

signal to be recorded more rapidly or with better signal to noise performance, compared to dispersive (grating) spectrometers.

The Jacquinot (or 'throughput') advantage [4] arises from the fact that a FT spectrometer does not require an entrance slit. The resolution of a FT spectrometer is dependent only on the total number of fringes or optical path difference recorded. Hence the throughput is limited only by the apertures and transmission of the optical components and can thus be much higher than grating spectrometers with entrance slits.

Both advantages ultimately lead to an expected increase in the signal to noise ratio SNR over traditional dispersive spectrometers, which makes FT spectrometers ideal for situations where low light levels are a feature of the experiment or application.

In summary FT spectrometers do not measure in the frequency domain, but instead measure an interferogram in either the spatial or temporal domain and use the Fourier Transform to transform this data directly into the spatial frequency or (temporal) frequency domain.

6.2 The Wollaston Prism

The prototype FT spectrometer design is based on the original work of Padgett *et al.* [1,2], and records an interferogram in the spatial domain. The design employs a Wollaston prism, a birefringent optic which is described below.

Birefringence or ‘double refraction’ occurs when a medium exhibits different refractive indices for the propagation of light in different directions relative to the optic axis (OA) and is a property of anisotropic crystals. Light beams with an electric field component parallel to the OA are labelled ‘extraordinary rays’ and have a corresponding ‘extraordinary refractive index’, n_e, while beams with electric fields perpendicular to the OA are labelled ‘ordinary rays’ and have a corresponding ‘ordinary refractive index’, n_o. Common birefringent materials are calcite, quartz and α-BBO. This property of birefringence is the basis for the Wollaston prism.

A Wollaston prism is formed by bringing together two optical wedges (with angles α) of a birefringent material that are symmetric but have their optic axes orthogonal to one another and to the direction of propagation. In Fig. 6.2 below the optic axes are along the X & Y directions and the beam propagates along the Z-axis.

As the beam enters the first wedge of the Wollaston prism it can be resolved into two orthogonal linear polarisation components that propagate co-linearly [1]; the ordinary ray which is perpendicular to the OA and the direction of propagation, and the extraordinary ray which is parallel to the OA and also perpendicular to the direction of propagation. These rays will experience different refractive indices (n_o & n_e respectively) and hence will have different phase velocities [1]. At the interface between the wedges, the beams will ‘switch’ and the ordinary

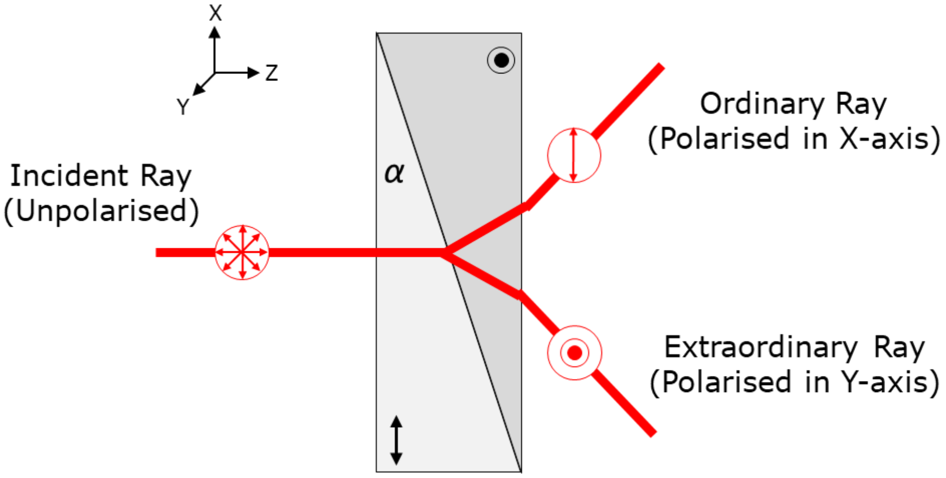

Fig. 6.2 Schematic diagram of a Wollaston prism I. Unpolarised light enters the Wollaston prism and splits into two orthogonal polarisation components. Each of the components experiences two instances of refraction, one at the interface of the two wedges and the second when exiting the prism into the air

ray becomes the extraordinary ray while the extraordinary ray becomes the ordinary ray. This is because the optic axis in the second crystal is orthogonal to the that in the first prism.

The initial ordinary ray effectively moves from a material of refractive index n_o to n_e and similarly the initial extraordinary ray moves from a material of refractive index n_e to n_o. As such the beams will experience a change in refractive index and will be refracted according to Snell's law;

$$\theta_{Ordinary} = \sin^{-1}\left(\frac{n_o}{n_e}\sin\alpha\right) \tag{6.1}$$

$$\theta_{Extraordinary} = \sin^{-1}\left(\frac{n_e}{n_o}\sin\alpha\right) \tag{6.2}$$

This results in a splitting of the two rays as one of the rays refracts towards the normal while the other ray refracts away from the normal. As the two rays exit the prism there will be a second refraction and the rays will split further.

This is the first property of Wollaston prisms; when a single incident beam propagates through the prism the beam will split into two diverging beams that are orthogonally polarized. If the incident beam is linearly polarised to lie in a plane oriented at 45° with respect to the X and Y axes in Fig. 6.2, the resulting pair of diverging beams will also be of equal intensity [1].

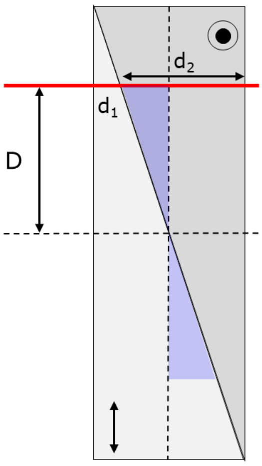

Fig. 6.3 Schematic diagram of a Wollaston prism II. In the centre of the Wollaston prism the optical path lengths within each prism are equal and there is no net phase shift between the ordinary and extraordinary rays. However, if you move a finite distance D away from the centre the optical path length of one prism becomes larger (d2>d1) and an optical path difference (and hence phase shift) between the prisms will be introduced.

The second property of the Wollaston prism is that it also introduces a linear phase shift between the two rays: In the first wedge the ordinary and extraordinary rays propagate colinearly with different phase velocities, this in turn creates a phase shift δ_1 between the two beams depending on the optical path through the wedge d_1:

$$\delta_1 = \frac{2\pi}{\lambda}.\Delta n d_1 \tag{6.3}$$

Where λ is the wavelength of the incident ray Δn is the difference in refractive indices (or the so-called 'birefringence') $\Delta n = |n_e - n_o|$.

Within the second wedge, as the refractive indices experienced by the two orthogonally polarised beams are opposite to the first wedge, there will be an opposing phase shift introduced δ_2. The resulting phase shift δ for both wedges can be given as

$$\delta = \delta_1 - \delta_2 = \frac{2\pi}{\lambda}.\Delta n(d_1 - d_2) \tag{6.4}$$

Assuming a small angle approximation that the path in the second prism d_2 is approximately equal to the path perpendicular to the exit face of second prism for the prisms used in these systems, $d_1 - d_2$ can be substituted for by $2D\tan\alpha$, where D is the distance from the centre of the prism as shown in Fig. 6.3 and α is the wedge angle of the Wollaston prism. Therefore the resulting phase shift for a Wollaston prism of wedge angle α at a distance D from the centre of the prism can be expressed as [2]:

$$\delta = \frac{2\pi}{\lambda}.2D\Delta n \tan(\alpha) \tag{6.5}$$

At the exact centre of the prism ($D = 0$), the two optical paths are equal and hence substituting into (6.5) we can see that the effective optical path difference is zero. This is the point of zero retardation and is similar to the point when the two arms of a Michelson interferometer are identical in length.

For beams of a finite width substituting into equation (6.5) will yield a linear change in phase shift across the beam as a function of D. This creates an interference plane that, when imaged through an analyser at 45°, will form straight line fringes as the beams will constructively and destructively interfere due to the linear phase shift. This spatial interferogram is the basis of the Wollaston prism spectrometer.

6.3 WPFT Spectrometer

6.3.1 Prototype WPFT Spectrometer Design

As mentioned above the Wollaston Prism Fourier Transform (WPFT) spectrometer design is based on the original work of Padgett *et al.* [1,2]. The basic idea is as follows: when a Wollaston prism is placed between two polarisers set at 45° with respect to the optic axes of the prism, straight line interference fringes are observed, this interference pattern is a representation of the spectral distribution of the incident source.

The basic design of the prototype can be seen in Fig. 6.4 and its operation is as follows: Incident light enters the system and falls onto a polariser. The polariser is set at 45° to the vertical direction and so the exiting light is plane polarised also at 45° to the horizontal and vertical directions. The light then passes through the Wollaston prism where it is split into diverging beams that are orthogonally polarised at 0° and 90°. Since the light incident on the Wollaston prism was plane polarised

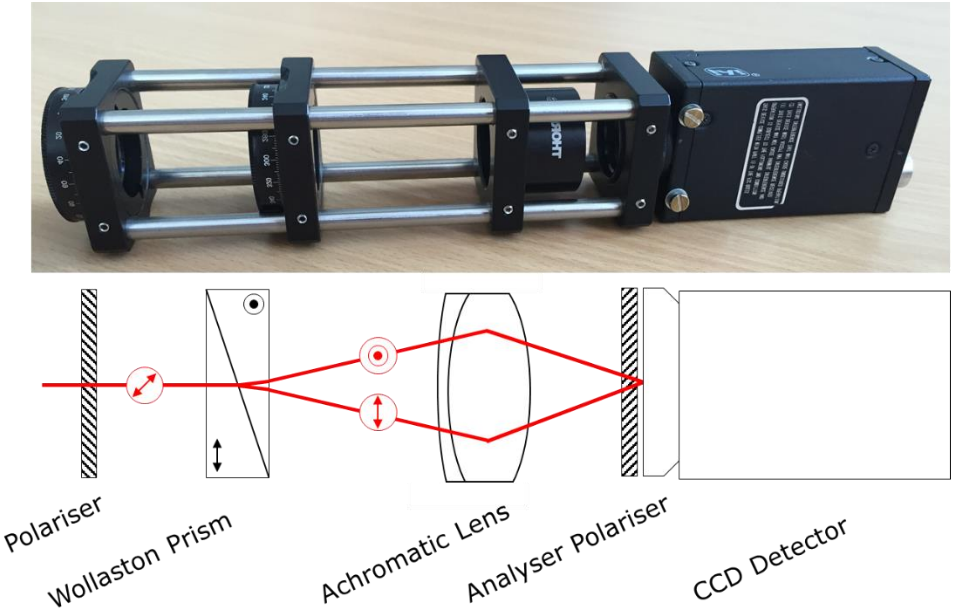

Fig. 6.4 Photo and corresponding schematic of the prototype WPFT spectrometer in the linear achromat based configuration. The system is housed in a Thorlabs™ 30 mm cage system with one-inch optics making the system compact and rugged.

at 45° to the vertical, the two component beams will be of equal intensity.

For an incident light beam of a finite width the Wollaston prism also introduces a linear phase shift between the two orthogonally polarised components of the incident beam, as described by equation (6.4), which forms an interferogram on passing through an *analyser* set at 45°. The interferogram is formed in space as the spectral components move in and out of phase with each other across the face of the prism. This interferogram has been reported to be formed at a plane inside the Wollaston prism [2]. Therefore, an imaging optic, such as an achromatic lens or curved aluminium mirror, is introduced to image the interferogram onto an array detector. The detector records the interferogram and the image is processed using the Fourier transform to obtain the spectral distribution of the incident light.

6.3.2 Interferogram Analysis

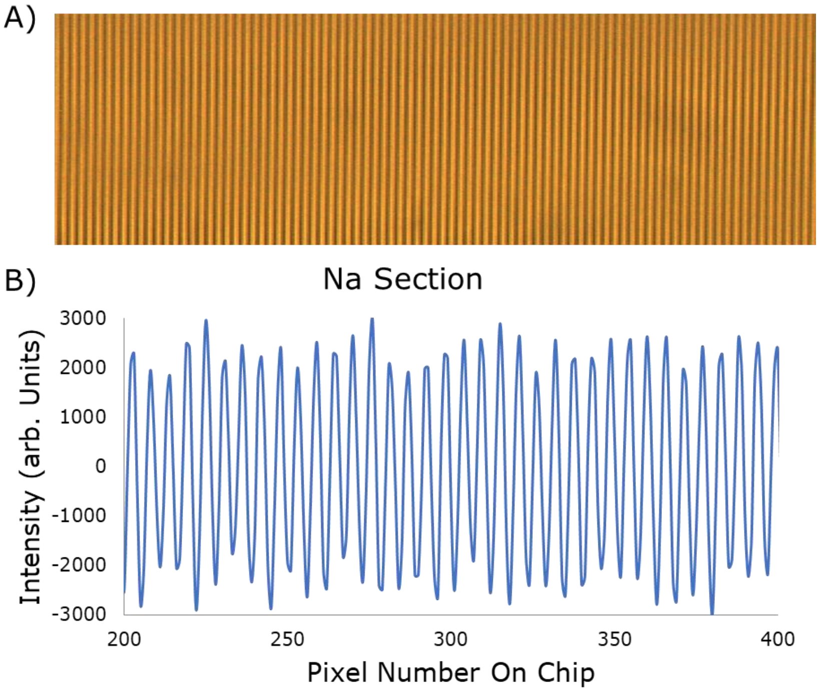

Fig. 6.5 A) Sample section taken from a Sodium (Na) discharge lamp interferogram recorded using the prototype WPFT spectrometer and the Point Grey FLEA®3 FL3-U3-88S2C-C machine vision camera. B) Sample section of the corresponding 1-D intensity plot.

In order to analyse the resulting interferogram images, a MATLAB™ [5] program was used. The basic outline of the code is as follows. The user selects interferograms for analysis and each interferogram is then analysed one by one. The JPEG image of the interferogram for the example shown in Fig. 6.5A is opened and loaded into the workspace.

This converts the RGB colour JPEG into an N×M×3 matrix of ASCII values. (An N×M matrix for each of the three colour profiles; Red, Blue & Green). This three-dimensional colour matrix is then converted into a grayscale two-dimensional N×M matrix using the built-in *rgb2gray* function[8]. The N×M matrix is then full vertically binned to give an N×1

---

[8] When using a monochrome camera like the JAI™ CM-140-GE-UV the JPEG will be loaded directly as a M×N matrix and hence this step is not required

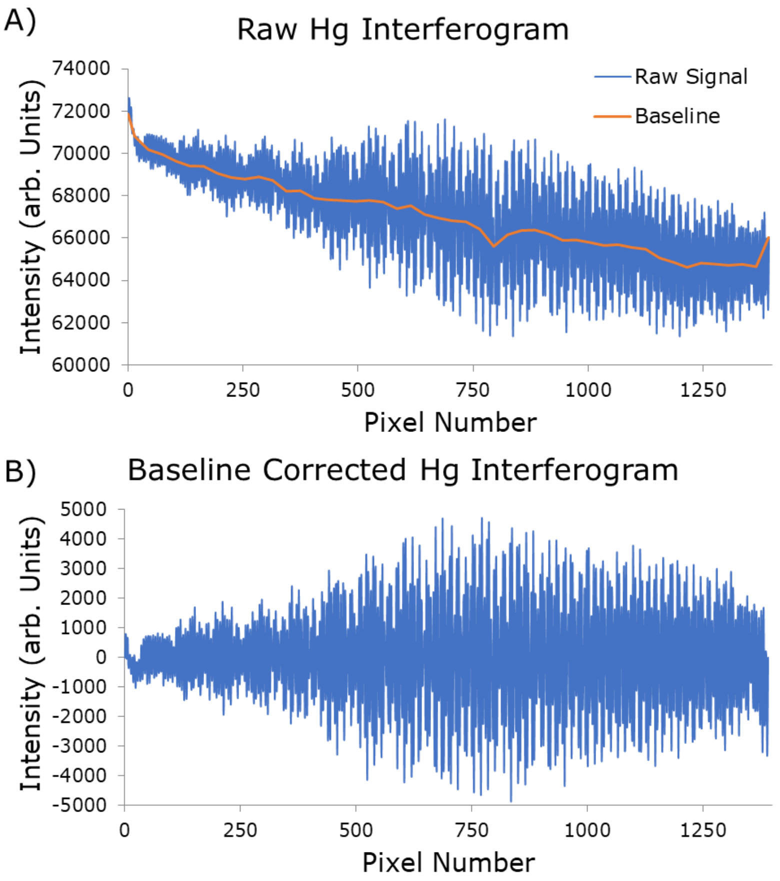

Fig. 6.6 A) A raw Mercury (Hg) interferogram, with corresponding baseline calculated using a moving average. B) The baseline corrected Mercury interferogram which is now flat and centred about zero.

dimensional matrix of the intensity as a function of horizontal position along the detector. This effectively averages out some of the noise which results in a cleaner interferogram.

When the intensity vs. pixel number is plotted the baseline can be large and non-uniform and so it can show up as low frequency artefacts in the Fourier transform. To account for this, the baseline is determined by a moving average of the signal with a boxcar width of 20-30 pixels. This baseline can then be subtracted away leaving a cleaner more 'ideal' interference pattern, that is centred about zero as shown in in Fig. 6.5B. The process of baseline subtraction is shown in Fig. 6.6. This is a computationally light yet effective way to subtract an irregular background that changes from shot to shot.

The Fourier transform of this interference pattern is taken using the built-in *FFT* function within MATLAB™, and the resulting power spectrum will determine what spatial frequencies are present in the interferogram.

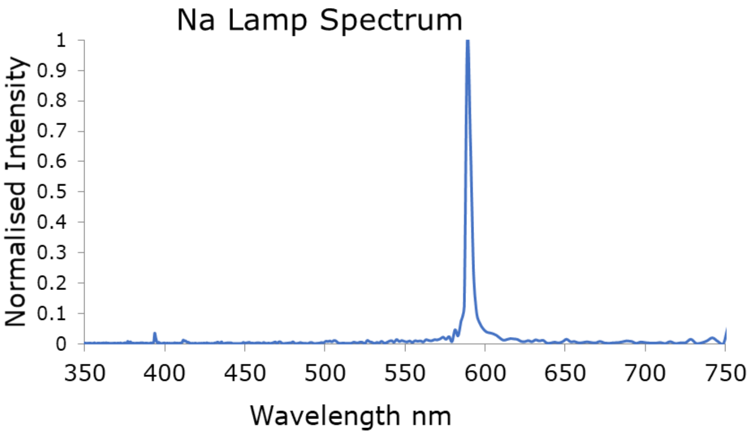

Fig. 6.7 Sample Sodium (Na) discharge lamp spectrum. As the two Na-D lines are separated by only a fraction of 1 nm, they are not resolved here, nor indeed are they by grating based compact spectrometers with similar spectral coverage and size.

These spatial frequencies can be related back to wavelength values λ by the expression:

$$\lambda = \frac{2Nx(n_e - n_o)\tan\alpha}{i_\lambda M} \tag{6.6}$$

where N is the number of horizontal pixels on the camera detector of pixel width x, n_e and n_o the extraordinary and ordinary refractive indices, α the wedge angle of the Wollaston prism, M the magnification of the interferogram image, and i_λ is the pixel number from the power spectrum for the given wavelength, and is related to the spatial frequency of the fringes in real space v_d by:

$$v_d = \frac{i_\lambda}{Nx} \tag{6.7}$$

Therefore, we can transform the x-axis of the power spectrum from spatial frequency to wavelength, leaving us with the typical Intensity vs. Wavelength spectrum commonly obtained from spectrometers. Before plotting the final processed spectrum, the code can also normalise the spectrum to aid in comparison of the data obtained to that from other spectrometers. An example of a normalised sodium spectrum can be seen in Fig. 6.7.

6.3.3 Prototype WPFT Spectrometer Construction

The prototype WPFT spectrometer can be seen in the photo in Fig. 6.4. It is constructed from a Thorlabs $30mm$ cage system using one-inch diameter optics which results in a spectrometer that is compact, auto-aligned, and rugged while having a large throughput. The main components of the spectrometer are discussed below:

Camera

As the resolution of a Fourier transform spectrometer is dependent on sampling as many fringes as possible while meeting or exceeding the Nyquist criterion, a camera with as many pixels as possible in the horizontal direction is highly desirable. Other factors important in selecting a camera were that it would need to be small and compact for a portable device, that it would be sensitive in the desired UV-VIS region ($200\,nm - 700\,nm$) and have sufficient dynamic range to record spectra over a large line intensity range. This proved to be very difficult to find as there are limited options for economical cameras capable of recording in the UV region while still having a high-resolution sensor.

Following a period of desk research, the JAI™ CM-140GE-UV shown in Fig. 6.8A was found to be the best compromise between size, spectral sensitivity, and dynamic range. As a machine vision camera, the JAI CM-140GE-UV is compact and versatile. It is equipped with a Sony ICX407BLA UV-sensitive CCD with high quantum efficiency which allowed an effective operating spectral range of $200\,nm$ – $1000\,nm$ [6] as can be seen from Fig. 6.8B. The sensor has a pixel count of $1340(H) \times 1040(V)$, which although was lower than desired, was found to sample enough fringe pairs for adequate resolution when implemented into the prototype WPFT spectrometer. This however did require a trade-off, namely that the spectral range covered by the prototype would be decreased, with the spectral range now not only

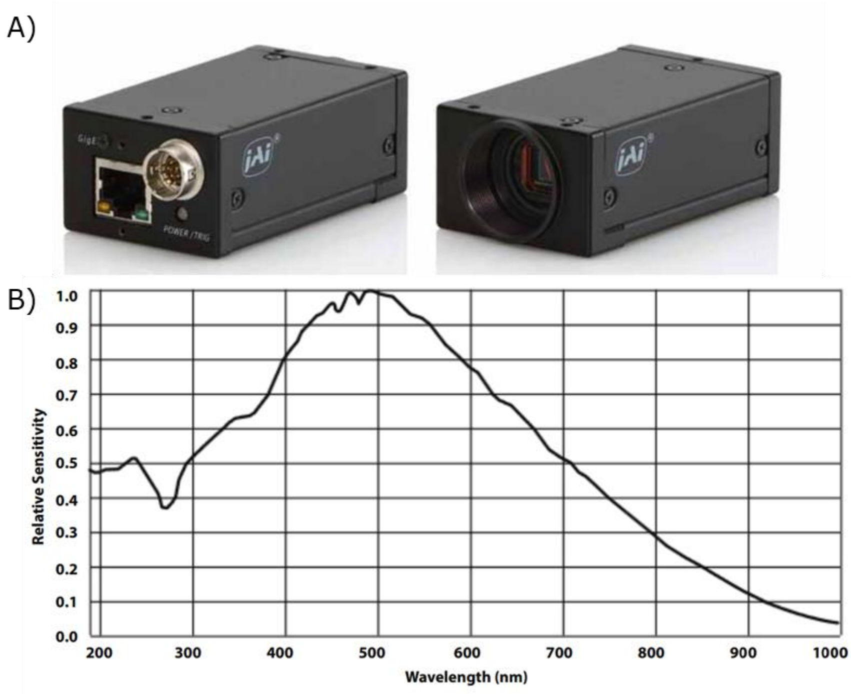

Fig. 6.8 The JAI™ CM-140GE-UV Machine vision camera. This camera is equipped with a UV sensitive Sony ICX407BLA sensor with 4.65µm square pixels and a horizontal by vertical pixel count of 1340(H) × 1040(V). B) The JAI™ CM-140GE-UV Relative Sensitivity vs. Wavelength graph is ßtaken from [6].

dependant on the transmission of the optics, but on the Nyquist criterion[9] for the lower wavelength limit, while the upper wavelength limit is determined by the optic or when the resolution was deemed too poor, typically $750\,nm$.

To meet a desired resolution of better than $2\,nm$ for the whole wavelength range, ideally the detector would need to sample > 300 fringe pairs at all wavelengths. Using equation (6.6) and assuming a linear relationship, for an upper wavelength of $700\,nm$ to have 300 fringe pairs a lower wavelength of $200\,nm$ would have ~ 1050 fringe pairs. However due to the strong non-linear wavelength dependence of the birefringence in the UV region of the spectrum, the number of fringe pairs created at $200\,nm$ will generally be far greater than in the visible region. This means that a camera with many thousands of pixels would be required to meet the Nyquist criterion for the desired resolution right throughout the UV-VIS region. Further details on the prototype WPFT

---

[9] The Nyquist sampling criterion is a well-known principle in signal analysis, that the sampling rate of a signal must be greater than twice the frequency of the highest frequency component in the signal to be restored.

spectrometer's resolution and how the number of fringes required for the desired resolution were determined are given in section 6.5.1.

Wollaston prism

The Wollaston prism is the heart of the prototype WPFT spectrometer; it creates the linear phase shift that forms the interferogram and once the camera had been chosen it was possible to match a Wollaston prism to it to give optimal performance. The prism was selected to provide the largest number of fringes at the longest wavelength while ensuring that the fringe pairs at the shortest wavelength can be adequately sampled by the camera to meet or ideally exceed the Nyquist criterion. Calculations were performed for a number of birefringent materials including calcite, quartz and α-BBO, using equation (6.6), to find the ideal prism material and wedge angle.

The birefringence was calculated for a range of wavelength values (200 nm – 700 nm) using equations from the refractive index database [7]. Using these values and taking a set dimension of $15\,mm \times 15\,mm$ for the prism face, the number of fringes created for each wavelength could be calculated and this resulting data can be seen in Fig. 6.9B. A value for the wedge angle α could then be determined to provide a balance between the wavelength range capable of being recorded and the resulting spectral resolution for this region, taking into consideration the limitations of the lower resolution camera.

The final prism material chosen was α-BBO as it provided a large transmission wavelength range $(190\,nm - 3500\,nm)$ encompassing the desired UV-VIS region, which resulted in an optimum wedge angle of 4.3° for the $15\,mm \times 15\,mm$ prism. The Wollaston prism used in the prototype WPFT spectrometer was manufactured by United Crystals™

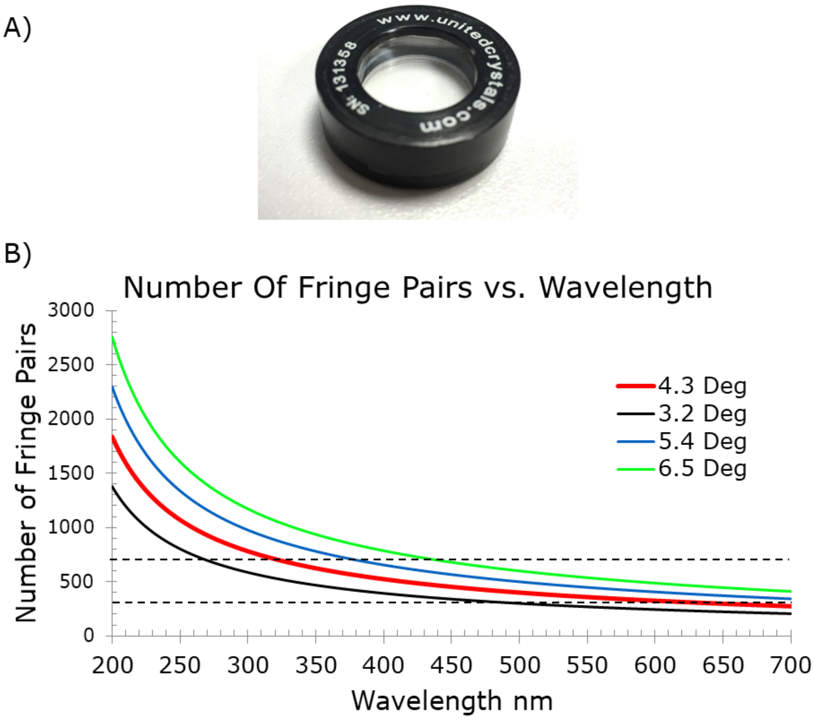

Fig. 6.9 A) The α-BBO Wollaston prism; the Wollaston prism was manufactured by United Crystals with a wedge angle of 4.3 degrees. It has dimensions of 15 mm × 15 mm and is housed in a one-inch optical mount. B) Theoretical number of fringe pairs created vs. wavelength for an α -BBO 15 mm × 15 mm prism. The region formed between the two lines is determined by the desired resolution and the limitations of the camera resolution. It determined a Wedge angle of ~4.3 degrees was the optimal wedge angle for the system.

to these specifications along with a broadband anti-reflection coating to reduce reflections in the $200\,nm - 450\,nm$ region and to provide the α-BBO optic with a protection layer as it is a hygroscopic material. The Wollaston prism can be seen in Fig. 6.9A.

Imaging optic

The prototype WPFT spectrometer design uses a focusing optic to image the interference plane of the Wollaston prism onto the detector. Initially a simple lens was used but it was observed that it exhibited severe chromatic aberration effects. In the prototype spectrometer this caused the interferograms at short wavelengths to be focused in a separate plane to those corresponding to the longer wavelengths. The solution was to replace the lens with an achromatic doublet lens or curved aluminium mirror. The former uses two lenses of different refractive indices to compensate for the chromatic aberration, while the latter, as a single plane reflective optic, does not introduce chromatic aberration. In practice the achromatic doublet allowed far more robust and quicker alignment while the curved aluminium mirror allowed a broader range of wavelengths to be recorded. However, the difference in performance between the two optical elements for the visible spectral region was negligible and so the achromat was selected for the final design.

Polarisers

When choosing polarisers for the prototype WPFT spectrometer, there were a few key parameters to consider. Firstly, maximum optical transmission over the operating wavelength range of the prototype WPFT spectrometer was essential to ensure high throughput. Secondly a large extinction ratio, which is the ratio of the transmission through parallel polarisers to the transmission through crossed polarisers, was required. If the extinction ratio is not high enough the second (analyser) polariser in the prototype spectrometer will produce an interferogram with poor contrast between the bright and dark fringes.

The polarisers in the prototype WPFT spectrometer (purchased from Edmund Optics™) are dichroic linear polarisers with a wide wavelength range of 300 nm – 2700 nm and high extinction ratio typically >1000:1 as seen in Fig. 6.10 [8].

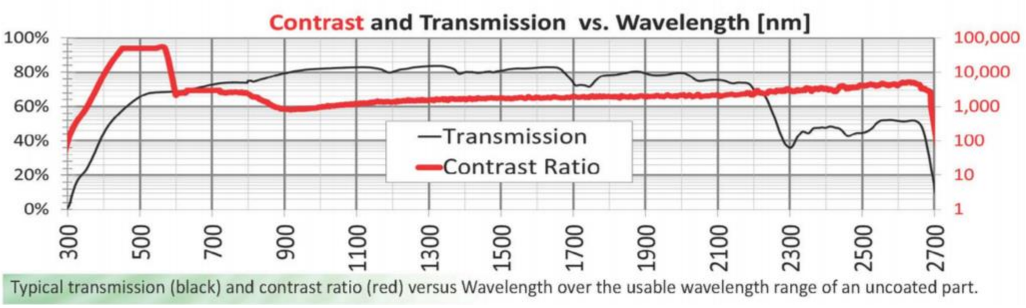

Typical transmission (black) and contrast ratio (red) versus Wavelength over the usable wavelength range of an uncoated part.

Fig. 6.10 Transmission vs. Wavelength & Contrast Ratio vs. Wavelength data for the Edmund Optics broadband polarisers, Part#89-602 Taken from [8]

6.4 Stellarnet® EPP2000

The prototype WPFT spectrometer was benchmarked in experiments against a commercial Stellarnet® EPP2000 spectrometer, which was a portable fibre-coupled grating-based spectrometer. It uses a Sony™ ILX511 CCD array of 2048 pixels each $14\,\mu m$ wide × $200\,\mu m$ tall, resulting in a FWHM resolution of c.a. $2\,nm$, which was determined experimentally using a Cd discharge lamp. The EPP2000 is capable of obtaining spectra in the $190\,nm$ – $850\,nm$ spectral range and utilised an optical trigger to capture the plasma signals. The fibre optic used in conjunction with the EPP2000 was a UV-VIS fibre with a $\phi 100\,\mu m$ core.

6.5 Comparison between the WPFT and Stellarnet® EPP2000 Spectrometers

6.5.1 Resolution

In order to compare resolution provided by the prototype WPFT spectrometer with that of the Stellarnet® spectra of different low-pressure, elemental discharge lamps were obtained. The narrow emission lines are ideal for determining the instrument function or 'impulse response' of each spectrometer in different wavelength ranges. The spectrometers were both set to similar acquisition parameters ($100\,ms$ acquisition with no focusing/collecting lens) and the full width at half maximum (FWHM) of each of the spectral lines was measured from the resulting spectra. The FWHM is often used as a standard when measuring signal widths as it does not depend on the signals function or shape; Gaussian, Lorentzian etc.

The Stellarnet® spectrometer had a near constant FWHM resolution of ca. $2\,nm$ across its operational wavelength range of $200 - 850\,nm$. In the case of a Fourier Transform spectrometer, for shorter wavelengths there are more fringe pairs formed than for longer wavelengths. Hence the instrument function varies with wavelength as the resolution of a FT spectrometer is dependent on the number of fringe pairs sampled. The

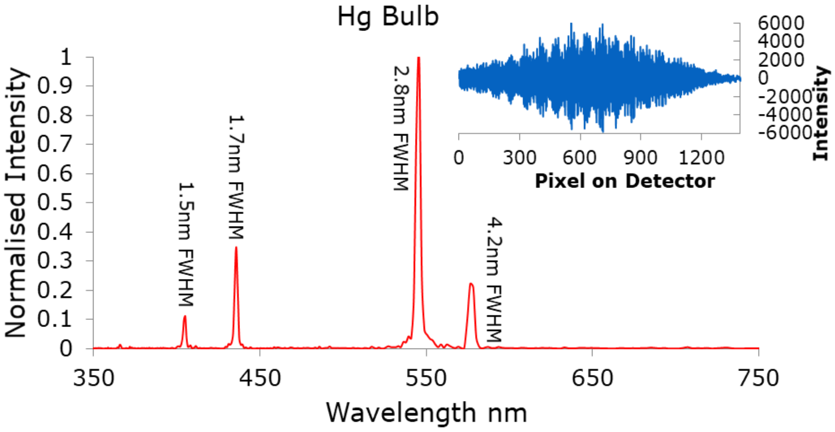

Fig. 6.11 Spectrum of a Mercury gas (Hg) bulb with its corresponding interferogram inset. The mercury spectrum is dominated by the $546.1\,nm$ *emission line. This line also dominates the interferogram, and the remaining emission lines contribute to the beating observed in the interferogram*

UV-visible spectrum of a mercury (Hg) discharge lamp is shown in Fig. 6.11. The FWHM resolution varies from $1.7\,nm$ at $435.8\,nm$ to $2.8\,nm$ at $546.1\,nm$.

The mean instrument function of the prototype WPFT spectrometer has a value of ca. $3\,nm$, which is not as sharp as the $2\,nm$ value for the Stellarnet®. However, if the detector had more horizontal pixels, and hence could sample more fringe pairs, such as the 2048-pixel sensor on the Stellarnet® sensor, the resolution would be improved with relative ease such that the FWHM resolution at all points would be comparable to the Stellarnet®.

In order to investigate this phenomenon, artificial monochromatic interferograms were created using sine waves with varying sampling rates ($4-8$ pixels per fringe pair). These artificial interferograms were analysed and the corresponding FWHM values of the peaks calculated. The results are shown in Fig. 6.12. It can be seen that as long as the Nyquist sampling criterion is met, that the sampling rate of the interferogram did not have a significant effect with all lines following the same trend, exhibiting a minimum deviation ($< 0.3\,nm$).

Scaling the number of fringe pairs recorded in the Hg spectrum in Fig. 6.11 proportionately, it is estimated that with a 2048-pixel sensor the resolution could be improved to a mean instrument function of close to $2\,nm$ FWHM at $546.1\,nm$. Looking at Fig. 6.12, once a figure of 500

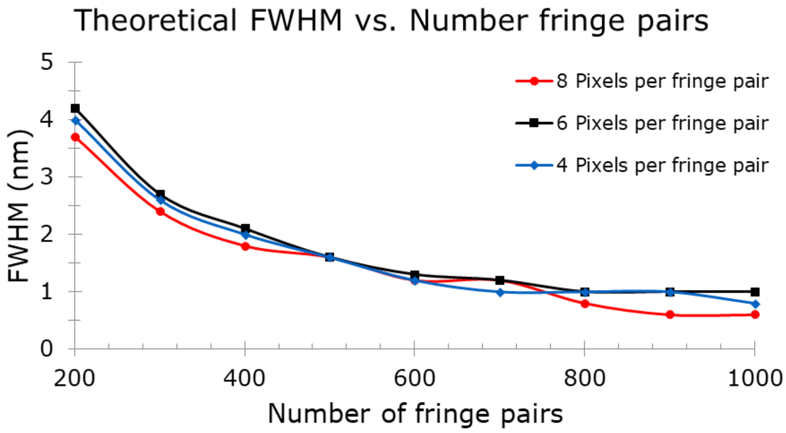

Fig. 6.12 Resolution test data; various interferograms were created using sets of sine waves while the number of fringe pairs was varied from 200-1000. For each interferogram the sampling frequency was varied from 4 to 8 pixels per fringe pair

fringe pairs is achieved, the FWHM of the instrument function lies close to this value. The main point is that a 2048 pixel sensor, similar to that used on the Stellarnet® spectrometer, would result in a resolution equal to that spectrometer platform (but with significantly greater throughput).

6.5.2 Signal to Noise Ratio

Along with resolution, another key parameter in spectroscopy is the signal to noise ratio (SNR). Noise on a photon detector can be represented by the Poisson distribution which scales as $\sqrt{N}$ where N is the number of photoelectrons stored in each well of a CCD pixel. Therefore, we can write that the SNR for a pixel containing N electrons is simply given by:

$$SNR = \frac{Signal}{Noise} \approx \frac{N}{\sqrt{N}} \approx \sqrt{N} \qquad (6.8)$$

An experiment was designed and set up to test the SNR performance of the prototype WPFT spectrometer in order to compare it with the Stellarnet® (Fig. 6.13). A sodium discharge bulb was located at one end of an optical table and the spectrometer placed at the other end, ca. $1.2\,m$ away. A pair of polarizers P_1 and P_2 were used as an attenuator; P_2 was kept at a fixed angle, aligned with the polariser at the entrance to the WPFT spectrometer, i.e., set at 45^o and P_1 could be rotated from

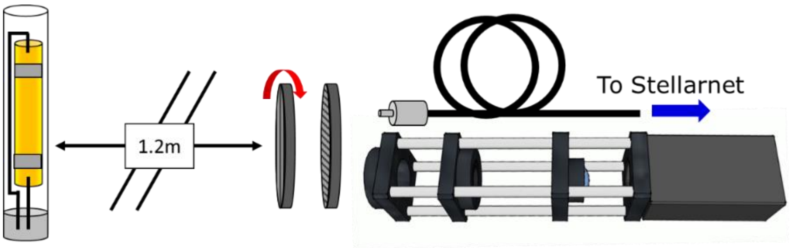

Fig. 6.13 Set up of the signal to noise comparison; a Na gas discharge bulb is placed $1.1\ m$ *from an attenuator and spectrometer the attenuator is used to lower the source intensity and the signal is recorded for comparison*

$0^o - 180^o$. The effective transmission T of the polariser pair is dependent on the angle between the polarisers and is given by Malus' Law:

$$T = \cos^2|\Theta_{P1} - \Theta_{P2}| \qquad (6.9)$$

The spectrometers were set to similar acquisition parameters ($30\ ms$ acquisition with no focusing/collecting lens) and both were located at a fixed distance from the source. The data was taken in steps of five degrees across the 180^o range, encompassing two full sweeps from zero to one-hundred percent transmission through the attenuator. Sample spectra of a Na discharge lamp from the SNR experiment can be seen in Fig. 6.14. The sample spectra were recorded with 1% transmission through the attenuator, and it can be seen that the signal observed in the prototype WPFT spectrometer is significantly cleaner than that from the Stellarnet®. This resulted in SNR values of ~ 10 and ~ 2 for the prototype WPFT spectrometer and Stellarnet® respectively. The SNR was obtained by integrating the total emission from the spectral line of interest and measuring it against three times the standard deviation of the background noise; this result in the basic formula given in (6.10):

$$SNR = \frac{I}{3\sigma} \qquad (6.10)$$

Fig. 6.15 shows a comparison of the full set of SNR values for the prototype WPFT spectrometer and the Stellarnet®. The prototype WPFT spectrometer was found to have on average five times greater SNR compared to the Stellarnet® grating spectrometer. This enhancement in SNR allows the signal to be distinguished from the noise at significantly lower light levels in the prototype WPFT spectrometer than the Stellarnet® spectrometer, a trait of great value for low light level applications.

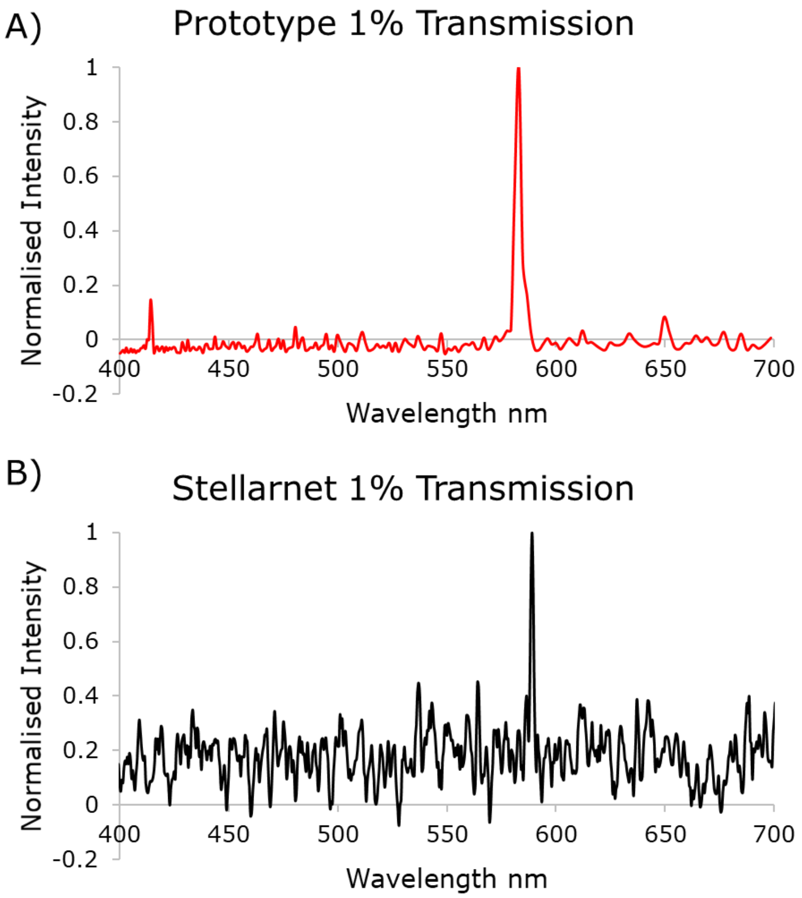

Fig. 6.14 Sample stand-off spectra of a Na discharge bulb $\sim 1.1\ m$ *from A) the prototype spectrometer and B) the Stellarnet® EPP2000. The prototype was seen to exhibit a far greater SNR.*

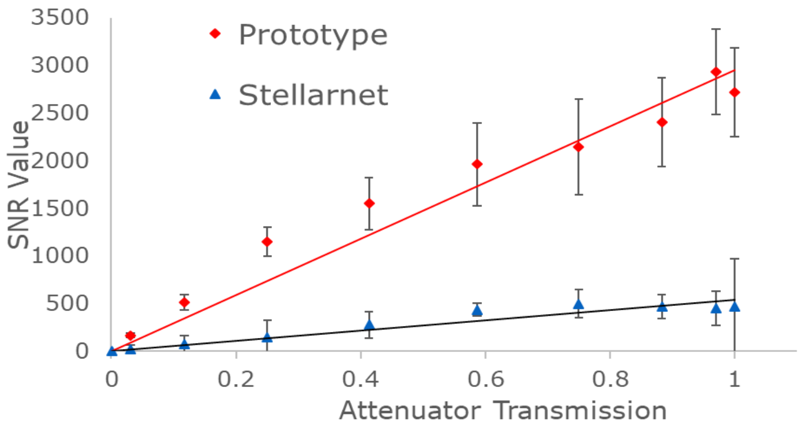

Fig. 6.15 SNR vs. Attenuator Transmission graph. The graph shows the linear response of the two spectrometers as the signal was attenuated. The prototype spectrometer averaged a five times improvement in SNR over the Stellarnet®.

6.6 LIBS Experiment: Mn in Steel

With the prototype WPFT spectrometer benchmarked against the Stellarnet® the improvement in SNR was sufficiently promising to attempt a LIBS experiment on targets of low concentrations of Mn in a steel matrix. Manganese is known to emit a weak line at $482.4\,nm$ which could be used to compare the spectral sensitivity of each spectrometer.

6.6.1 LIBS Set Up

Fig. 6.16 shows the experimental set up used in order to perform LIBS experiments with the WPFT spectrometer. An optical delivery system comprising a $1064\,nm$ steering mirror with a ½-wavelplate & cube polariser attenuator allowed control of the incident pulse energy, which was set to $20\,mJ$. The laser was focussed using a plano-convex lens of focal length $f = 250\,mm$ and resulted in an on-target spot size of c.a. $100\,\mu m$. Targets of different materials were used for initial tests including aluminium, carbon, steel, silicon, and copper. For the LIBS experiment, four steel samples, with varying trace concentrations of manganese (1.75%, 1.2%, 0.68%, and 0.04%) held in a six-sample target holder, were used. The target holder was attached to a XYZ target stage and could be rotated to swap between each sample. Experiments were performed within a small target chamber which was not evacuated. Collection of the light emitted from the plasma was via a bi-convex lens with focal length $f = 100\,mm$, along with a notch filter to block out the stray $1064\,nm$ laser light.

A fire-box, consisting of an Arduino™ Mega board and basic push-button circuit was used to send a TTL fire pulse signal to one input of the AND gate with the output pulse train from channel-B of the Quantum

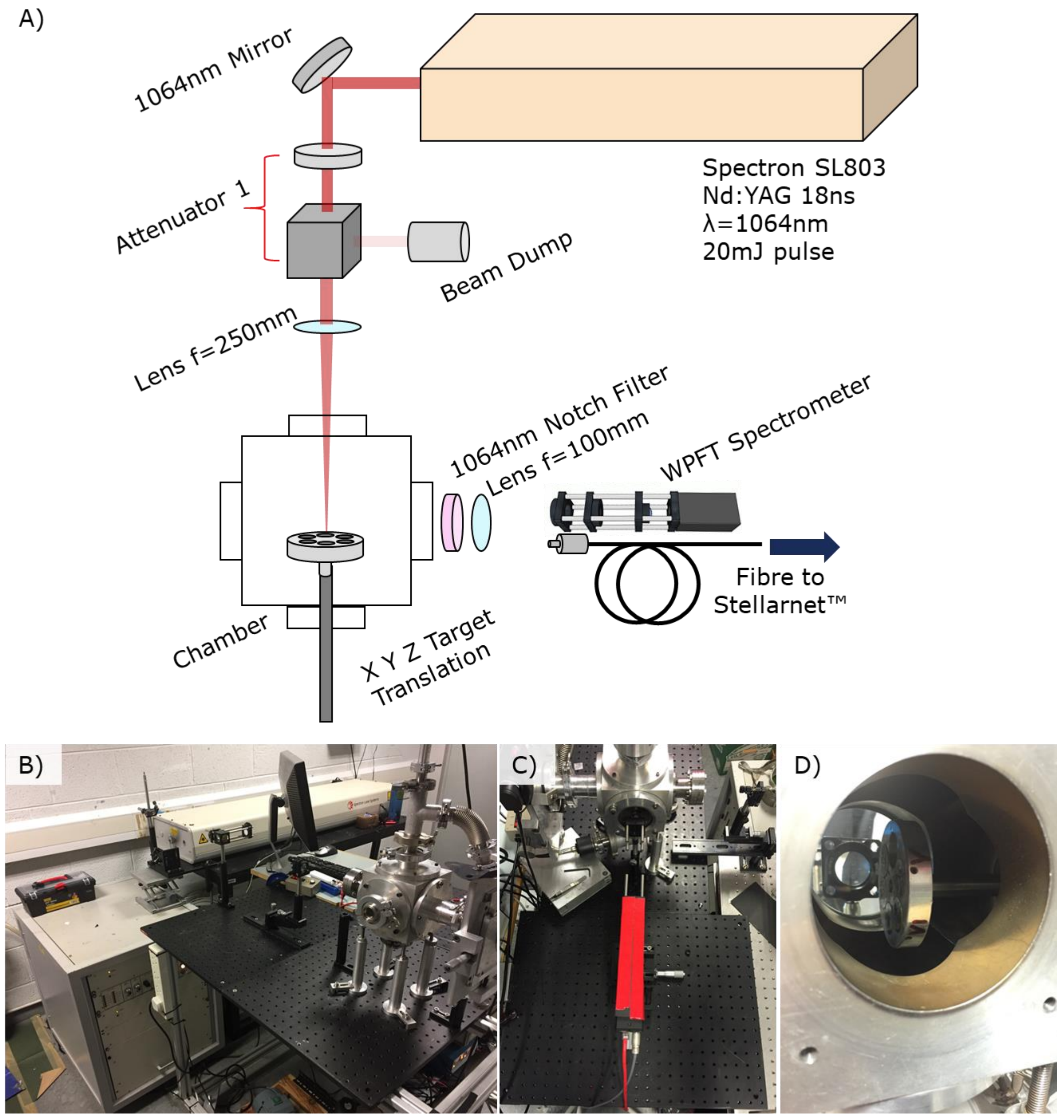

Fig. 6.16 Schematic of the experimental system used for the LIBS experiments along with images of the experimental set up from the lab.

Composer™ delay/gate generator fed to the other input of the AND gate. The output from the AND gate was then used to trigger the Q-switch on the Spectron™ SL803 Nd:YAG laser. In order to trigger the camera, the TTL pulse from the fire box was also fed to a second AND gate along with the pulse train from channel-A of the quantum composer, where channel-A was used to trigger the laser flashlamps continuously at a pulse repetition frequency of $1\,Hz$. This resulted in the camera being triggered $160\,\mu s$ before the Q-switch which was required as the JAI™ camera had a long internal delay (on the order of $120\,\mu s$). In order to ensure all of the emission was captured the acquisition time was set to $100\,ms$.

6.6.2 LIBS Results

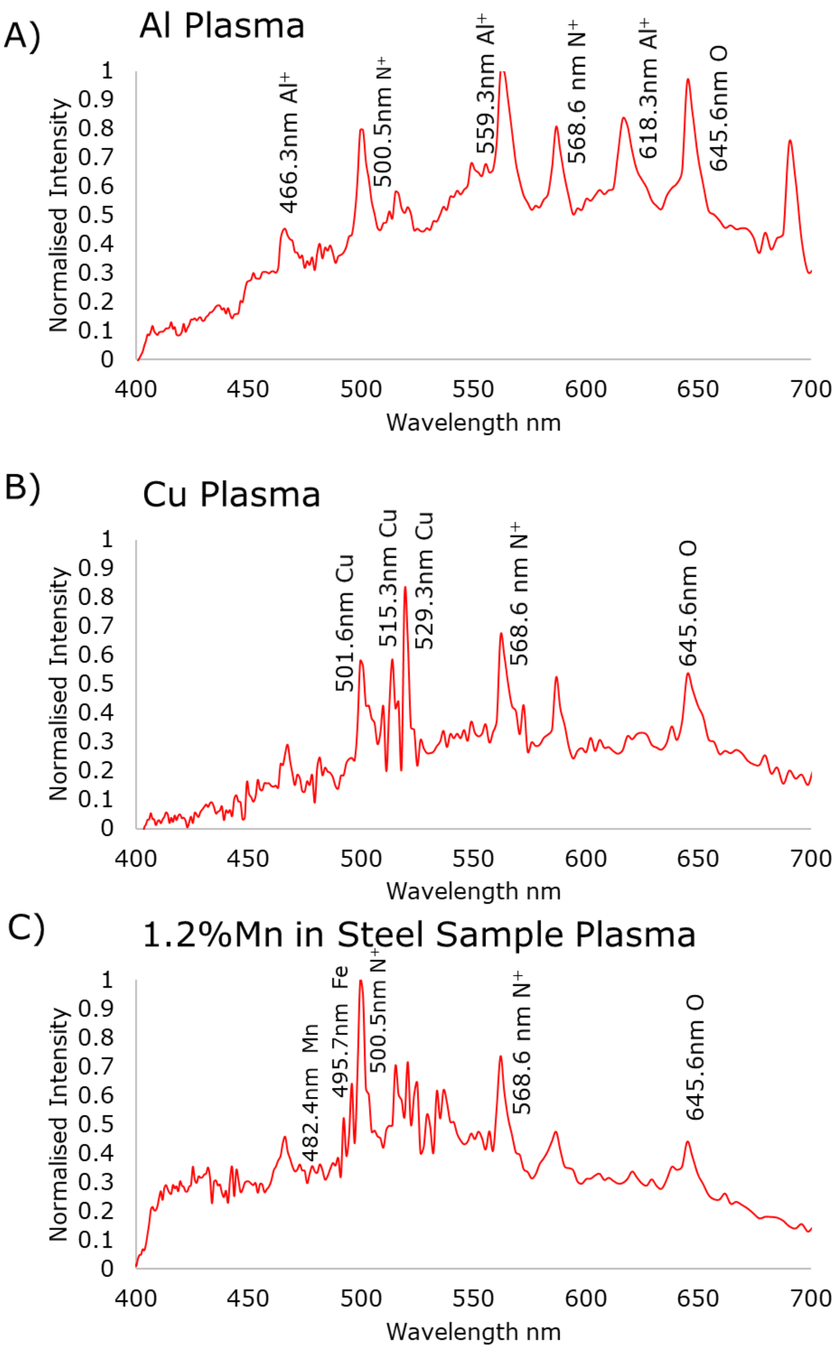

Fig. 6.17 Sample spectra of laser produced plasmas of A) Aluminium, B) Copper, C) 1.2% Manganese in Steel. Spectra were all recorded in air at atmospheric pressure.

Fig. 6.17 shows sample spectra of laser produced plasmas from various metal targets. The prototype WPFT spectrometer was capable of recording *single-shot spectra* which proved impossible with the Stellarnet® where single shots provided spectra which were dominated by noise. In that case an accumulation of typically 100 laser shots were required to obtain a clear spectrum. Hence there are no single shot

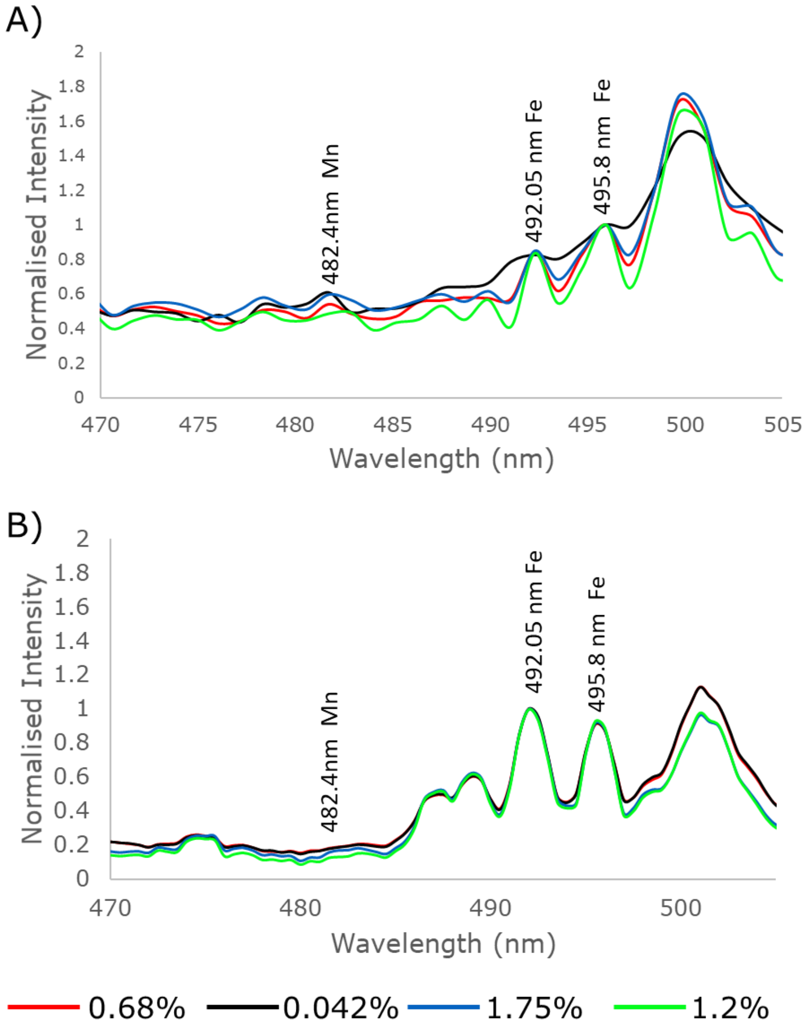

Fig. 6.18 Region of interest form the Manganese in Steel spectra part of the LIBS experiment for the A) prototype spectrometer and B) Stellarnet® EPP2000. Spectra were normalised to the Fe 495.8 nm line.

Stellarnet® spectra to compare with Fig. 6.17. As the spectra are all time-integrated, a large continuum pedestal is visible in emission spectra of plasmas formed on all targets. The various metal plasmas exhibit atomic emission lines from both the target materials and also from the background air at atmospheric pressure.

A typical single shot spectrum of Manganese (1.2%) in Steel is shown in Fig. 6.17C. The line at $482.4\ nm$ is present, although very weakly, in this singe shot spectrum. In addition to this weak emission from trace levels of Mn, the spectrum also comprises many strong lines from Fe, along with N and O from the background gas.

The acquired spectra were normalised to the Fe $495.6\ nm$ emission line in order to compare relative line intensities of the Fe $492.05\ nm$ and

$Mn\ 482.4\ nm$ lines. For direct comparison with the Stellarnet®, 100 single shot spectra were accumulated, and the results are shown in Fig. 6.18.

As can be seen from these spectra the $Mn\ 482.4\ nm$ line appeared as a weak feature in the case of the prototype WPFT spectrometer (Fig. 6.18A). On the other hand, the Stellarnet® spectrometer was not able to detect the line at all for any of the concentrations used (Fig. 6.18B).

Although the prototype WPFT spectrometer was able to see the Mn lines, it is clear that without the ability to delay the camera exposure by $150 - 200\ ns$, thereby allowing the background continuum to die away, that it is extremely difficult to make concentration calibrations and determine the limit-of-detection in a reliable fashion. Hence in a future upgrade, the prototype WPFT spectrometer will be fitted with a controllable delay to trigger. This should allow the spectrometer to be usefully used in LIBS for both classification and potentially quantification of trace elements in a matrix.

6.7 WPFT Spectrometer: Conclusions and Future Work

Overall the prototype WPFT spectrometer showed strong promise as a compact spectrometer for low light level applications. The prototype WPFT spectrometer was shown to have greater throughput than the Stellarnet® EPP2000, a comparable commercial grating-based spectrometer with a current improvement in SNR of a factor of ca. $5\times$. However, the ability to delay the exposure with respect to the laser pulse could lead to significantly better performance in signal to background ratio for LIBS.

In addition, the current detector could be substituted by a sensor with the ≥ 2048 horizontal pixels, predicted bring the prototype WPFT spectrometer resolution in line with that of the Stellarnet®. Finally, the JAI™ CM-140GE-UV used in the prototype WPFT spectrometer is a machine vision camera, designed for well-lit applications. This contrasts with the sensor in the Stellarnet® spectrometer (ILX511) which has large pixels ($13\ \mu m\ x\ 200\ \mu m$) and far superior sensitivity. By changing to a detector designed for low light applications the prototype WPFT spectrometer could become much more sensitive and correspondingly yield a significantly higher SNR.

References

1. Harvey a. R. Stationary Fourier transform spectrometer for use as a teaching tool. Am J Phys [Internet]. 1994;62(11):1033. Available from: http://link.aip.org/link/?AJP/62/1033/1&Agg=doi

2. Padgett MJ, Harvey a R, Duncan a J, Sibbett W. Single-pulse, Fourier-transform spectrometer having no moving parts. Appl Opt. 1994;33(25):6035–40.

3. Fellgett P. I. — les principes généraux des méthodes nouvelles en spectroscopie interférentielle - A propos de la théorie du spectromètre interférentiel multiplex. J Phys le Radium [Internet]. 1958;19(3):187–91. Available from: http://www.edpsciences.org/10.1051/jphysrad:01958001903018700

4. Jacquinot P. The Luminosity of Spectrometers with Prisms, Gratings, or Fabry-Perot Etalons. 1954;44(10):761–5.

5. MATLAB. Massachusetts: MathWorks Inc; 2015.

6. CM140-GE-UV Datasheet . [Internet]. Jai Cameras; 2012. Available from: http://www.jai.com/ProtectedDocuments/datasheets/Datasheet_CM-140GE-UV.pdfhttp://www.jai.com/ProtectedDocuments/datasheets/Datasheet_CM-140GE-UV.pdf

7. Polyanskly M. Refractive Index Database [Internet]. 2014. Available from: http://refractiveindex.info/

8. Broadband Polarisers Data Sheet. Part#89-602 [Internet]. Edmund Optics; Available from: https://www.edmundoptics.eu/optics/polarizers/linear-polarizers/25.4mm-dia.-300-2700nm-broadband-polarizer/#specs

9. Hecht E. Optics. Fourth Edi. San Fransisco: Addison Wesley; 2002.

7 Conclusions

7.1 Summary and Conclusions

A study of plasmas formed on V-channel targets with vertex angles ranging from 90° to 30° was undertaken with a view to creating plasmas in atmospheric pressure air with properties similar to those encountered in stagnation layers formed at the collision plane between two (or more) plasmas formed *in vacuo*. Time-resolved fast imaging and spectroscopy were used to characterise and diagnose these colliding plasmas.

Experiments utilising time resolved imaging to explore the formation and evolution of plasmas formed on V-channel targets were presented in Chapter 4. It was seen that both the V-channel targets and the flat target exhibited plume splitting at the early time delays ($< 100\, ns$) into a primary plasma region close to the target vertex separated from a rapidly expanding plasma front. The V-channel targets were seen to exhibit greater plasma confinement than the flat targets and confinement was seen to increase with decreasing V-channel vertex angle.

As the plasmas evolved, further differences between the flat and V-channel targets became noticeable, most notably with the formation of a 'stationary' or 'stagnated' plasma near the target vertex and a 'plasma lobe' further away from the vertex. The plasma lobe formed a distinct region in the 90° and 60° V-channel target cases. The 30° V-channel target did not show evidence of a discrete and distinct plasma lobe in the imaging experiments. The expansion velocities of plasma components were higher in this case and so it is possible that they were more extended and hence overlapped than in the other two cases, creating the appearance of a single, albeit structured, plasma column.

It was the 'stationary' or 'stagnated' plasma plumes or regions however which attracted most focus as they were located at what would be the region where the plasmas from the target walls would collide along with exhibiting characteristics one would expect from a stagnation layer. Those properties include showing little or no expansion and quite uniform light intensity distributions which are sustained for longer periods than for other plasma plume components.

Optical Emission Spectroscopy (OES) was used to diagnose the laser plasmas and results from this study were presented in chapter 0. From the recorded spectra it was seen that the V-channel target plasmas exhibited an enhancement in emission for the 90° and 60° V-channel targets with the 90° V-channel target performing the best of the V-channel targets. As there was an increase in intensity for both Al^0 and Al^+ emission lines which was also accompanied by an increase in signal-to-background ratio (SBR), it was clear that the increase in line emission signal was indeed real and not just an increase in total flux from the target. A correlation between the rate at which the emission line intensities dropped below those of the flat target and later dropped below the background was observed and may be attributed to the higher rates of recombination for confined target plasmas.

Electron densities and temperatures were also extracted from the OES data. The electron density measurements for the confined V-channel targets showed an overall increase in electron density over the flat target. The stationary plasma region exhibited a rather gentle gradient for long time delays, right out to more than $1000\,ns$. This contrasts with stagnation layers formed in vacuo where the line emission is rather weak and the electron densities also rather low at these time delays. Electron temperatures were seen to also exhibit quite spatially uniform profiles, and decay in time at a slower rate, within the stationary plasma. Overall the V-channel targets were seen to exhibit faster cooling than seen from the flat target and this was particularly evident in the more confined 60° and 30° V-channel target cases.

A collisional radiative model was used to extract rates of collisional ionisation, radiative recombination, and three-body recombination. The V-channel target plasma rates were about an order of magnitude greater the rates obtained from the flat target. Similar to the electron densities and electron temperatures, rates from the stationary plasmas were also seen to decay at slower rates than at the other regions within the plasma plumes.

Due to their shape alone, it is clear that these stationary plasmas are not exactly the same as stagnation layers formed *in vacuo*. However, they exhibit many characteristics one would expect from a stagnation layer, such as uniformity of density, temperature, and light intensity along with slower rates of decay for these parameters. For a more concrete answer as to whether they are fully stagnating plasmas more work will need to be carried out, some of which is proposed in the future work.

Finally, the WPFT spectrometer shows strong promise as an optical spectroscopic platform with a clear increase in throughput and SNR demonstrated. It could be much improved and a main focus of the future work for the WPFT spectrometer is related to the detector which limited the sensitivity of the system, albeit it already is a factor of $5\times$ higher in signal level than commercial variants.

7.2 Future Work

OES of Dissimilar targets

By introducing dissimilar metal targets it should be possible to track the degree of stagnation/interpenetration at the centre plane extending from each V-channel target vertex. Fig. 7.1 [1] shows a stagnation layer formed by Al and Ti plasmas. The different spectral lines corresponding to each of the target walls can be used to investigate the level of interpenetration or stagnation. If the two sets of lines stop at the collision plane, as seen in this image, hard stagnation has occurred. However, if the lines were seen to continue past the collision plane, interpenetration is occurring, and its degree could be measured. This

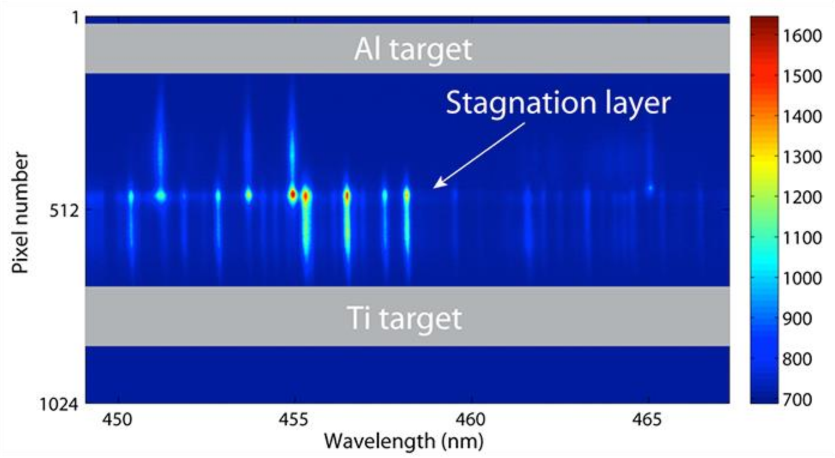

Fig. 7.1 Example spectrum from a stagnation layer formed from dissimilar targets. By colliding plasma formed form dissimilar targets spectroscopy can be used to verify that the different species indeed stop at the collision plane of the stagnation layer

could potentially be one of the simplest of methods for absolute determination whether hard stagnation is occurring within the stationary plasmas.

Shadowgraphy

In plasma diagnostics Shadowgraphy [2] is used to study the shock front produced by the laser plasma formation in a background gas. Tracking the shock front can provide further information to how the plasmas formed within the V-channel targets interact with the background gas.

Interferometry

Interferometry can be used to investigate the plasma at very early lifetimes $(0 - 100\,ns)$ to obtain electron densities. The method of electron density determination via Stark broadening used in this work was not able to obtain results before c.a. $150\,ns$ due to the strong continuum emission. Therefore interferometry could shed some light on these early time delays when the initial plasma collisions occur [3].

Broaden parameter space

The systematic formation and study of confined plasmas in air is new and due to time restraints, this study was carried out within a limited experimental parameter space. Work is required to expand this parameter space in order to obtain a more complete understanding of the requirements and conditions for the formation of stagnated or stationary plasmas in such conditions. There are many parameters to consider including laser pulse energy, laser wavelength, spectral range, wedge angle, and spot size to name but a few.

LIBS limit of detection experiment

As seen in section 5.4, the 90° and 60° V-channel targets exhibit an increase in signal to background ration (SBR) over that of the flat target. The limit of detection (LOD) in LIBS is given by $LOD = 3\sigma/m$ where σ is the standard deviation of the background signal and m is the slope of the elemental concentration calibration curve. Therefore by increasing the SBR the background is effectively reduced, and a lower limit of detection should be obtained. It is proposed that such a LIBS LOD experiment would be carried out for standard stationary plasmas in air.

For LIBS, it is desirable to optimize both the laser ablation and plasma excitation processes. However, as Noll states [4], this cannot fully be realised using a single laser pulse for both steps. Therefore many multi-pulse techniques have been explored in some detail with methods involving pre-ablation, crossed beams and the re-heating, it is the latter that would be of the most interest for future work. In the first (ablation) step the confined plasma is formed on a V-channel target. In the second step it is irradiated (further excited) by a time delayed laser pulse. By delaying the reheating laser pulse appropriately, a significant enhancement in the line emission can be obtained [5]. This is double pulse LIBS and the process is, in effect, one of tuning the plasma electron temperature and density values to find a region of the plasma plume where energy from the second laser pulse can be most efficiently absorbed. Work undertaken within the DCU research group [6] and the broader literature [7] have already shown that reheating of stagnation layers can yield further increases in emission and in the limit-of-detection (LOD) over that of standard single-pulse experiments.

Laser Induced Fluorescence

As mentioned in chapter 1.2, laser plasmas and stagnation layers can yield measurable fluxes of nanoparticles that can be used for PLD, LA-ICP-MS and other applications. Therefore, it would make sense to investigate the formation of nanoparticles within the stationary plasmas. One common technique used to detect nanoparticles in plasma plumes is Laser induced Fluorescence or 'LIF'. After the initial laser plasma is formed a second laser or 'probe beam' irradiates the laser plasma with light at a wavelength that will induce a fluorescence signal of the nanoparticles formed from within the plasma [8]. Spectroscopic signals from nanoparticles are typically detected at long delays ($> 5\,\mu s$) using bandpass filters or spectrometers.

References

1. Fallon C. Colliding Plasmas and Stagnation Layers - A Potential Platform for Analytical Techniques [Internet]. [cited 2007 Aug 20]. Available from: https://www.oxinst.com/learning/view/article/colliding-plasmas-and-stagnation-layers-a-potential-platform-for-analytical-techniques

2. Villagrán-Muniz M, Sobral H, Camps E. Shadowgraphy and interferometry using a CW laser and a CCD of a laser-induced plasma in atmospheric air. IEEE Trans Plasma Sci. 2001;29(4):613–6.

3. Ruiz-Camacho J, Beg FN, Lee P. Comparison of sensitivities of Moiré deflectometry and interferometry to measure electron densities in z-pinch plasmas. J Phys D Appl Phys. 2007;40(7):2026–32.

4. Noll R. Laser-Induced Breakdown Spectroscopy: Fundamentals and Applications. Heidelberg, Dordrecht, London, New York: Springer; 2012. 7-16 p.

5. Gautier C, Fichet P, Menut D, Lacour JL, L'Hermite D, Dubessy J. Quantification of the intensity enhancements for the double-pulse laser-induced breakdown spectroscopy in the orthogonal beam geometry. Spectrochim Acta - Part B At Spectrosc. 2005;60(2):265–76.

6. Fallon C. Optical Diagnostics of Colliding Laser Produced Plasmas : Towards Next Generation Plasma Light Sources. Dublin City University; 2013.

7. Cummins T, O'Gorman C, Dunne P, Sokell E, O'Sullivan G, Hayden P. Colliding laser-produced plasmas as targets for laser-generated extreme ultraviolet sources. Appl Phys Lett. 2014;105(4):1–5.

8. Nakata Y, Kaibara H, Okada T, Maeda M. Two-dimensional laser-

induced fluorescence imaging of a pulsed-laser deposition process of YBa2Cu3O7-x. J Appl Phys. 1996;80(4):2458–66.

Appendices

A. Courses, Conferences, & Publications

Courses Taken

ECTS Courses Taken:

- FSH502 EXTATIC Foundation Module
- FSH509 EXTATIC Special Topics
- FSH508 EXTATIC Metrology
- FSH505 EXTATIC EUV Optics
- CS507 Advanced Statistics & Chemometrics
- GS601 Intellectual Property & Commercialization
- GS602 Postgraduate Tutor/Demonstrator Module
- GS607PS Laboratory Tutoring

Workshops Attended:

- EXTATIC welcome week Aachen 2013
- COST Action MP1203 Dublin 2013
- VUV/EUV Workshop UCD Dublin November 2nd, 2013
- Safelab 1&2 Postgraduate Modules 2013/14
- NCPST Plasma/NanoScience Conference DCU Dublin March 2014
- PLAS@PAR International Plasma Summer School 2014
- EXTATIC welcome week Warsaw 2014
- Laser World of Photonics ICM Munich Germany June 2015
- Perdue PIRE Annual Meeting DCU Dublin July 2015
- EXTATIC welcome week Southampton 2016
- Erasmus+: Laser, XUV and Charged Particle Optics seminar series 2016
- VUV/EUV Workshop UCD Dublin November 2nd, 2016

Publications

- Kelly T.J., Davitt S.J., Costello J.T., Simple, low cost interferometric autocorrelator with no moving parts. Meas. Sci. Technol. 27 117003 (2016)

- Davitt S.J., Costello J.T., Kelly T.J., A Compact Fourier Transform Spectrometer with No Moving Parts for Laser Induced Breakdown Spectroscopy. ***(Submitted)***

- Davitt S.J., Walsh N., Kelly T. J., Costello J.T., Colliding laser plasmas formed under atmospheric conditions. ***(Submitted)***

Oral Presentations

- The Slit-less Spectrometer: A Compact Fourier Transform Spectrometer with No Moving Parts. Davitt S.J., Costello J. T., Kelly T. J., EXTATIC Welcome week Warsaw, Poland, October 2014.
- Single-shot Fourier Transform Spectroscopy for Laser Induced Breakdown Spectroscopy, Davitt S.J., Costello J. T., Kelly T. J., EXTATIC Welcome week Southampton, England, January 2016.

Poster Presentations

- Compact Fourier Transform Spectrometer with No Moving Parts for The Application of a Portable Laser Induced Breakdown Spectroscopy System. Davitt S.J., Costello J. T., Kelly T. J., 5th NCPST Postgraduate Poster competition, DCU, December 2013.
- Single-shot Fourier Transform Spectroscopy for Laser Induced Breakdown Spectroscopy (LIBS): Davitt S.J., Costello J.T., Fallon C., Kelly T.J., DCU BOC Poster competition, Dublin, February 2015.
- Single-shot Fourier Transform Spectroscopy for Laser Induced Breakdown Spectroscopy (LIBS): Davitt S.J., Costello J.T., Fallon C., Kelly T.J., 42nd IOP Plasma conference, Milton Keynes England, March 2015.
- Single-shot Fourier Transform Spectroscopy for Laser Induced Breakdown Spectroscopy (Ver2), Davitt S.J., Costello J.T., Fallon C., Kelly T.J., Photonics Ireland, Cork, September 2015. *(Awarded first place student poster)*
- Single-shot Fourier Transform Spectroscopy for Laser Induced Breakdown Spectroscopy (Ver3), Davitt S.J., Costello J.T., Fallon C., Kelly T.J., IOP Spring Weekend '16, Belfast, February 2016.
- LIBS with a compact Fourier Transform Spectrometer, Davitt S.J., Costello J.T., Kelly T.J., 9th international conference on LIBS, Chamonix France, September 2016. *(Awarded overall best student poster)*
- Investigating the Formation of Stagnation Layers Under Atmospheric Conditions by Laser Produced Plasma (LPP), Davitt S.J., Walsh N., Costello J.T, IOP Spring Weekend '17, Dublin, March 2017.
- Towards The formation of Stagnation Layers in Air, Davitt S.J., Walsh N., Kelly T. J., Costello J.T, Photonics Ireland, Galway, September 2017.

- Towards The formation of Stagnation Layers in Air, Davitt S.J., Walsh N., Kelly T. J., Costello J.T, DCU BOC Poster competition, Dublin, September 2017.

- Towards The formation of Stagnation Layers in Air, Davitt S.J., Walsh N., Kelly T. J., Costello J.T, 24th International Conferenc3e on Spectral Line Shapes, Dublin, June 2018.

- LIBS with a compact Fourier Transform Spectrometer, Davitt S.J., Costello J.T., Kelly T.J., 24th International Conference on Spectral Line Shapes, Dublin, June 2018.

B. Supplementary Fast Imaging Data

Broadband time resolved image series

The broadband images have been normalised across the targets for each time point to aid in comparison, as such some images required their intensity to be increased.

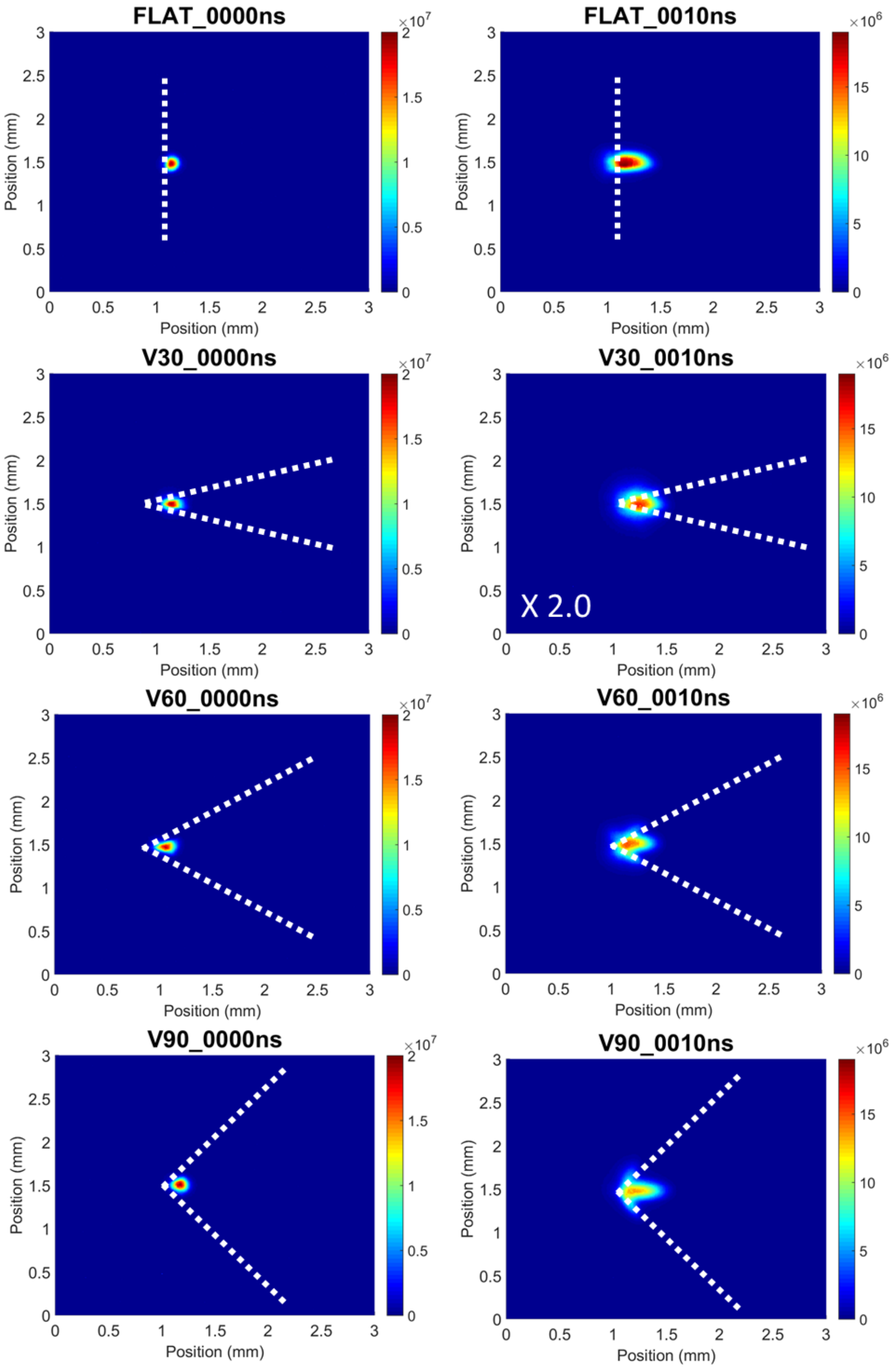

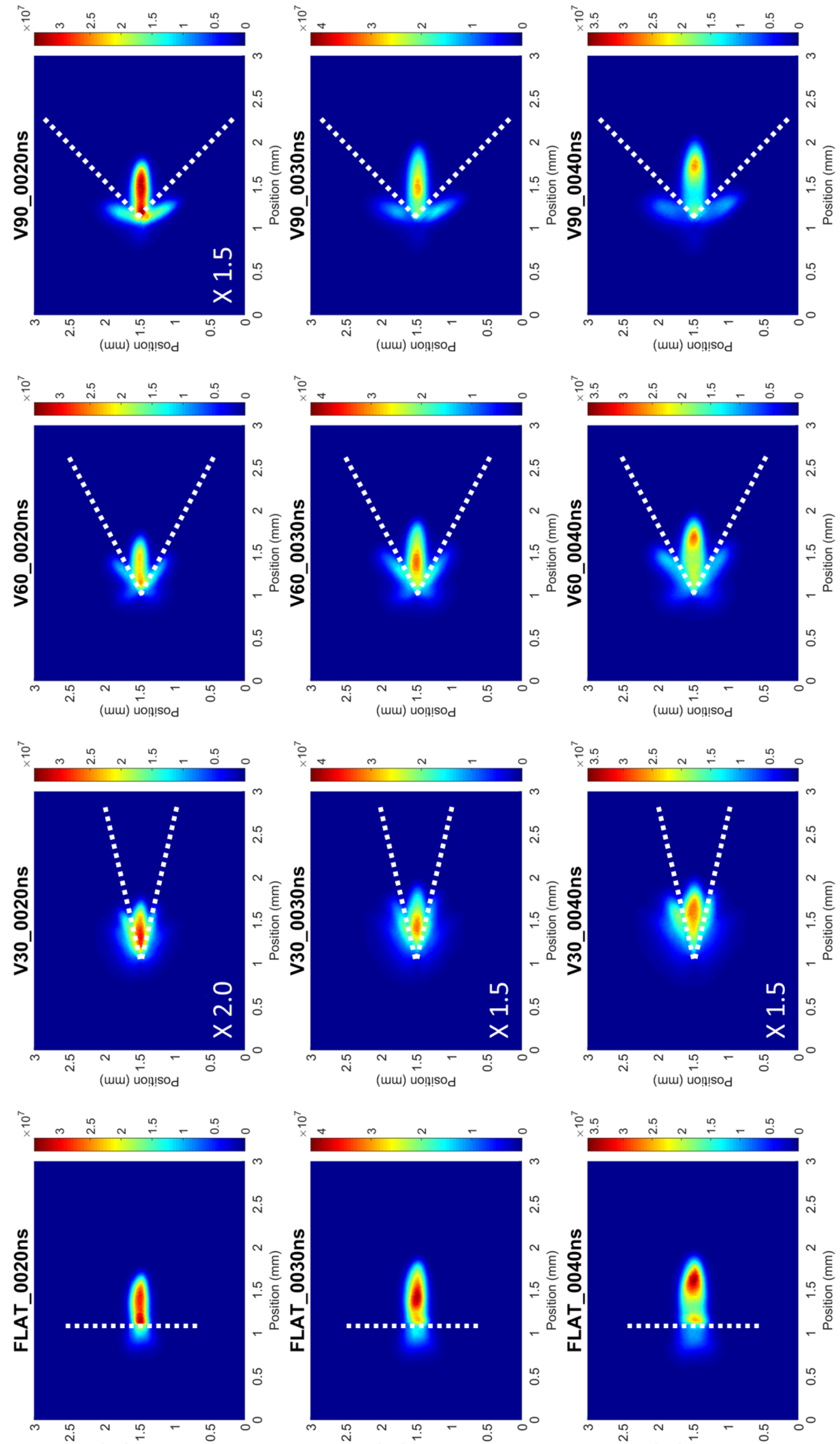
FLAT_0020ns
V30_0020ns
V60_0020ns
V90_0020ns
FLAT_0030ns
V30_0030ns
V60_0030ns
V90_0030ns
FLAT_0040ns
V30_0040ns
V60_0040ns
V90_0040ns
X 2.0
X 1.5
X 1.5
X 1.5
Position (mm)
Position (mm)
0
0.5
1
1.5
2
2.5
3
3.5
4
×10^7

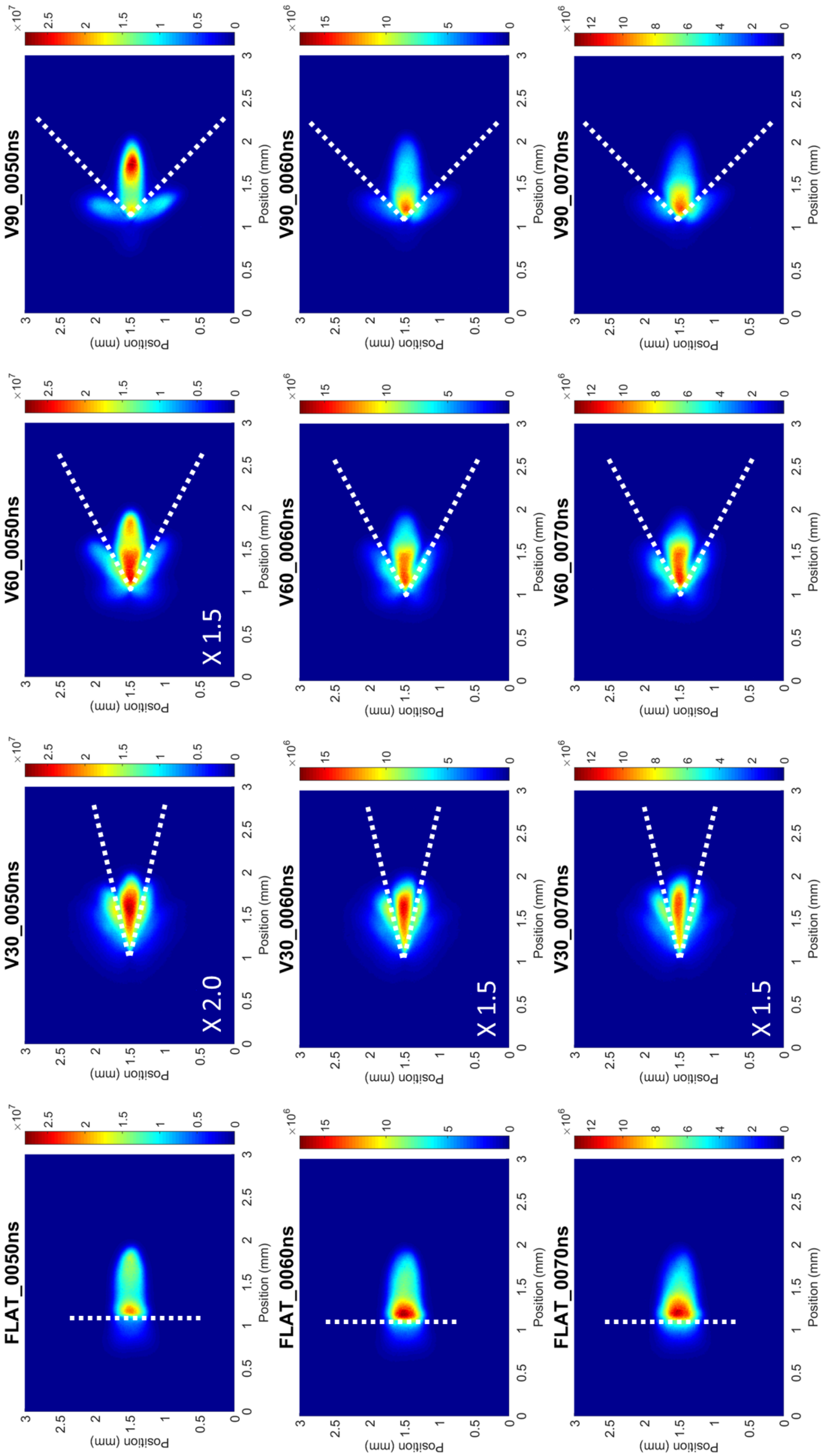
FLAT_0050ns
V30_0050ns
V60_0050ns
V90_0050ns
FLAT_0060ns
V30_0060ns
V60_0060ns
V90_0060ns
FLAT_0070ns
V30_0070ns
V60_0070ns
V90_0070ns
X 2.0
X 1.5
X 1.5
X 1.5
Position (mm)
0
0.5
1
1.5
2
2.5
3
$\times10^7$
$\times10^6$
0
0.5
1
1.5
2
2.5
0
5
10
15
0
2
4
6
8
10
12

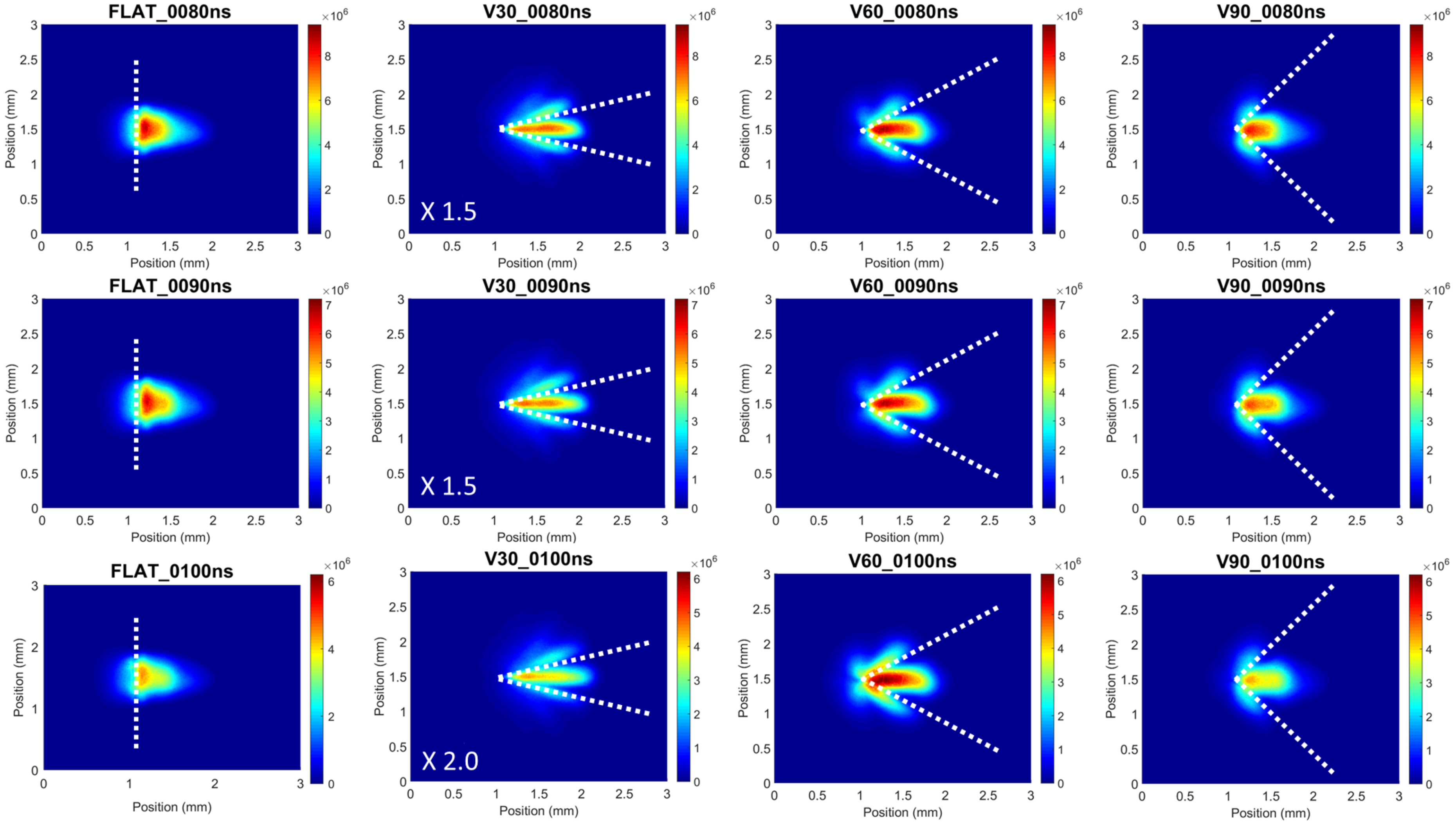
FLAT_0080ns
V30_0080ns
V60_0080ns
V90_0080ns
FLAT_0090ns
V30_0090ns
V60_0090ns
V90_0090ns
FLAT_0100ns
V30_0100ns
V60_0100ns
V90_0100ns
X 1.5
X 1.5
X 2.0
Position (mm)
Position (mm)
$\times 10^6$
0
0.5
1
1.5
2
2.5
3

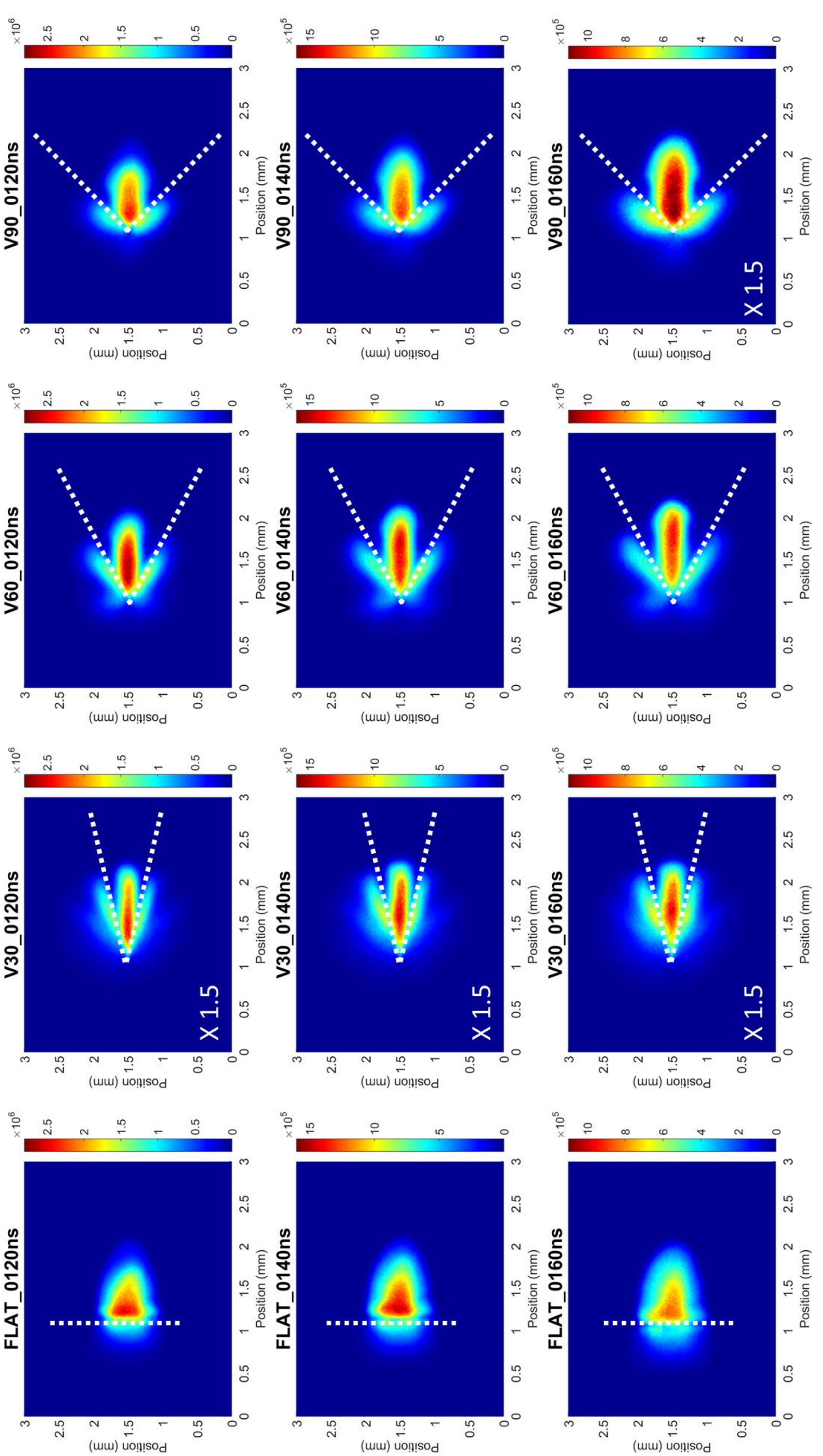
FLAT_0120ns
FLAT_0140ns
FLAT_0160ns
V30_0120ns
V30_0140ns
V30_0160ns
V60_0120ns
V60_0140ns
V60_0160ns
V90_0120ns
V90_0140ns
V90_0160ns
X 1.5
Position (mm)
$\times10^6$
$\times10^5$

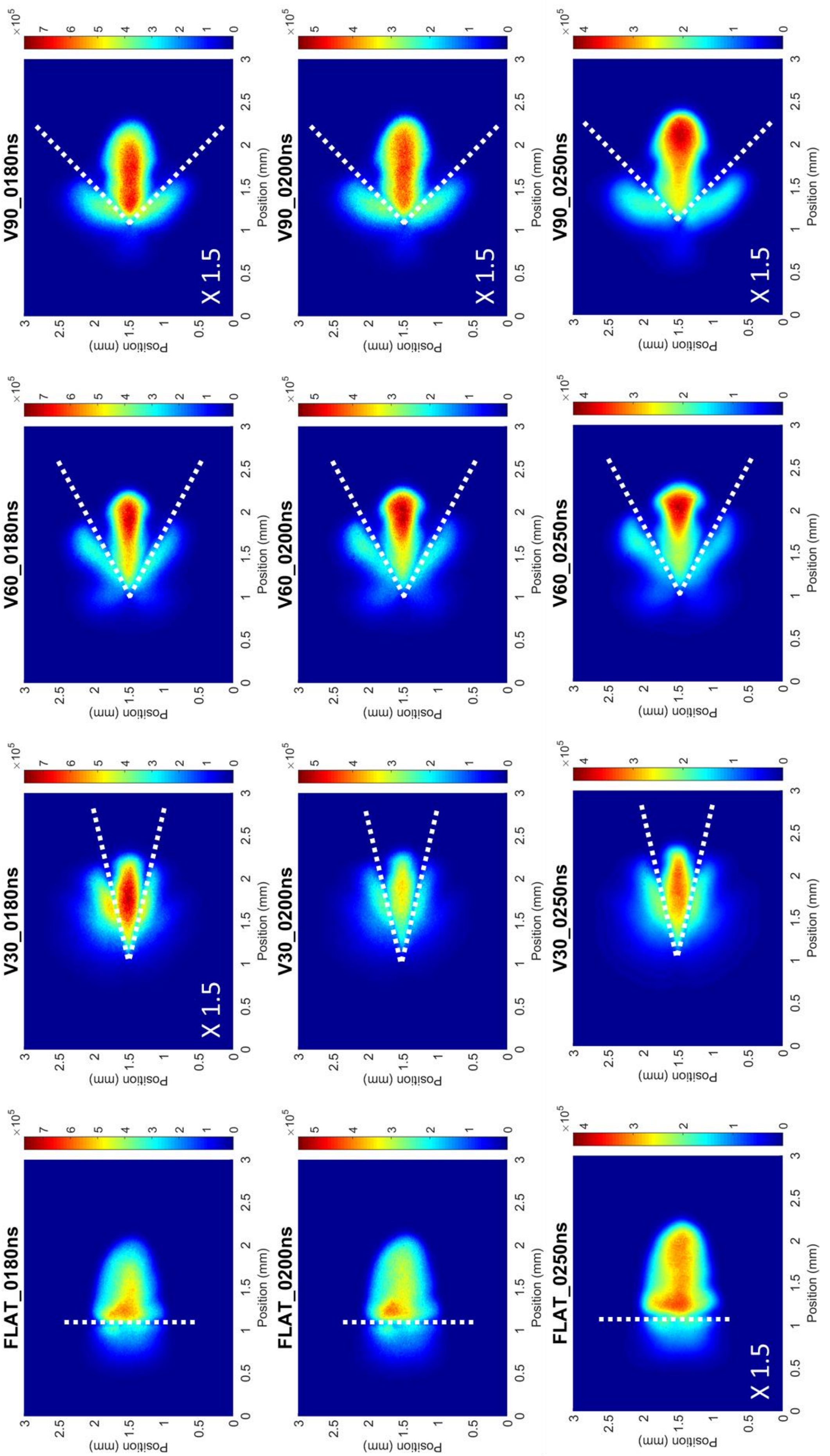
FLAT_0180ns
FLAT_0200ns
FLAT_0250ns
V30_0180ns
V30_0200ns
V30_0250ns
V60_0180ns
V60_0200ns
V60_0250ns
V90_0180ns
V90_0200ns
V90_0250ns
X 1.5
X 1.5
X 1.5
X 1.5
X 1.5
Position (mm)
Position (mm)
0
0.5
1
1.5
2
2.5
3
×10^5
0
1
2
3
4
5
6
7

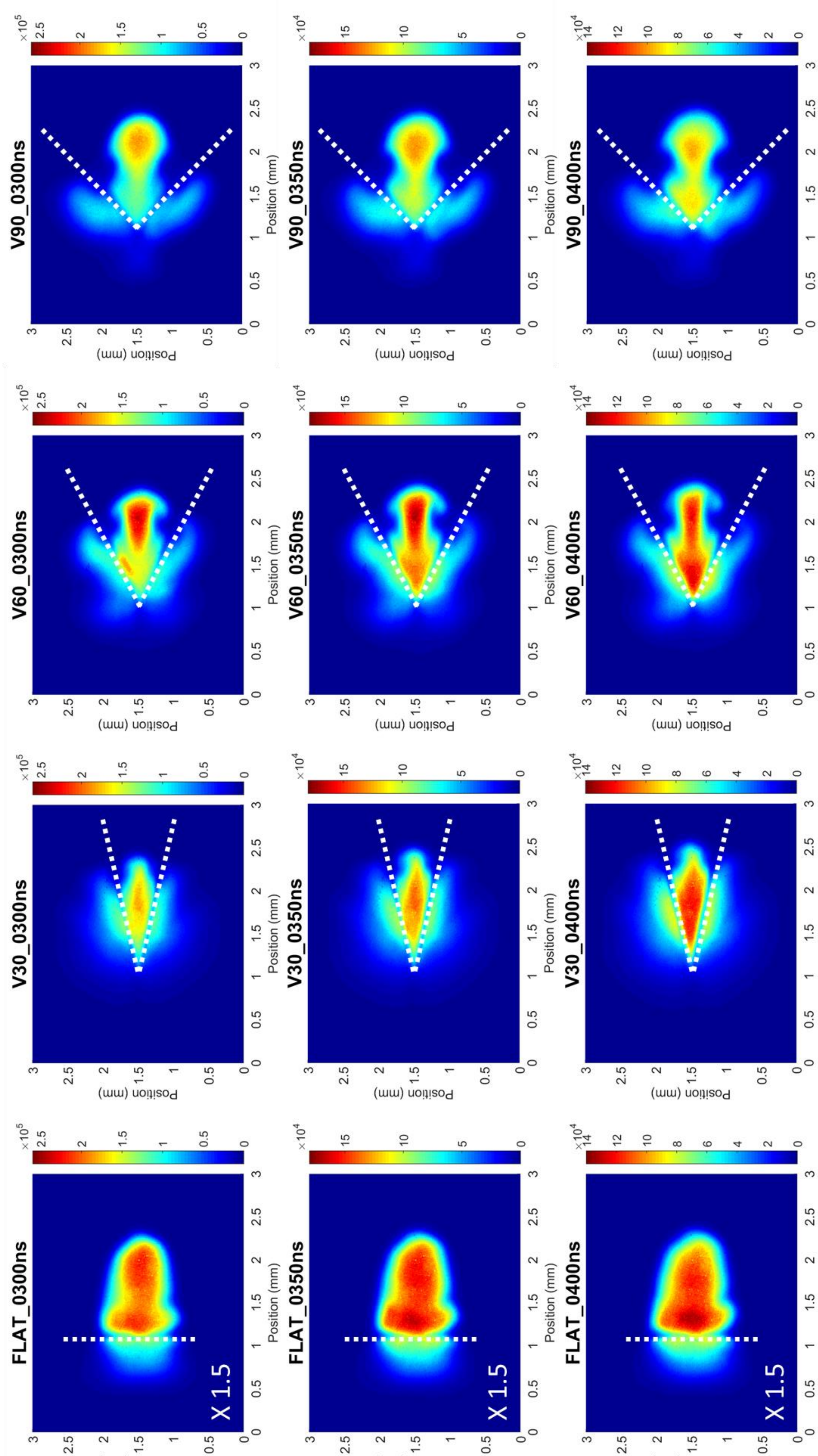
FLAT_0300ns
FLAT_0350ns
FLAT_0400ns
V30_0300ns
V30_0350ns
V30_0400ns
V60_0300ns
V60_0350ns
V60_0400ns
V90_0300ns
V90_0350ns
V90_0400ns
X 1.5
X 1.5
X 1.5
Position (mm)
Position (mm)
0
0.5
1
1.5
2
2.5
3
$\times 10^5$
0
0.5
1
1.5
2
2.5
$\times 10^4$
0
5
10
15
$\times 10^4$
0
2
4
6
8
10
12
14

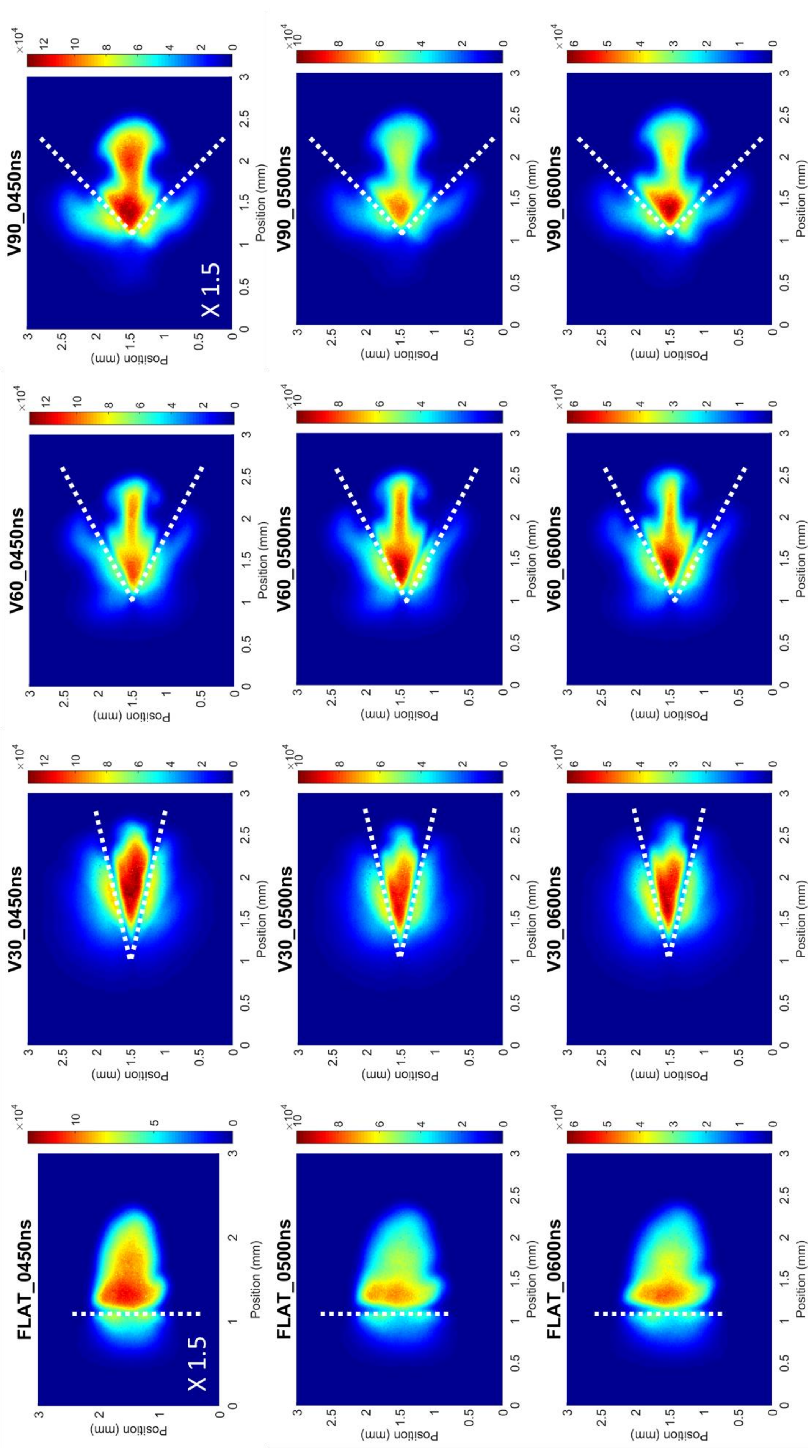
FLAT_0450ns
V30_0450ns
V60_0450ns
V90_0450ns
FLAT_0500ns
V30_0500ns
V60_0500ns
V90_0500ns
FLAT_0600ns
V30_0600ns
V60_0600ns
V90_0600ns
X 1.5
X 1.5
Position (mm)
Position (mm)
×10^4

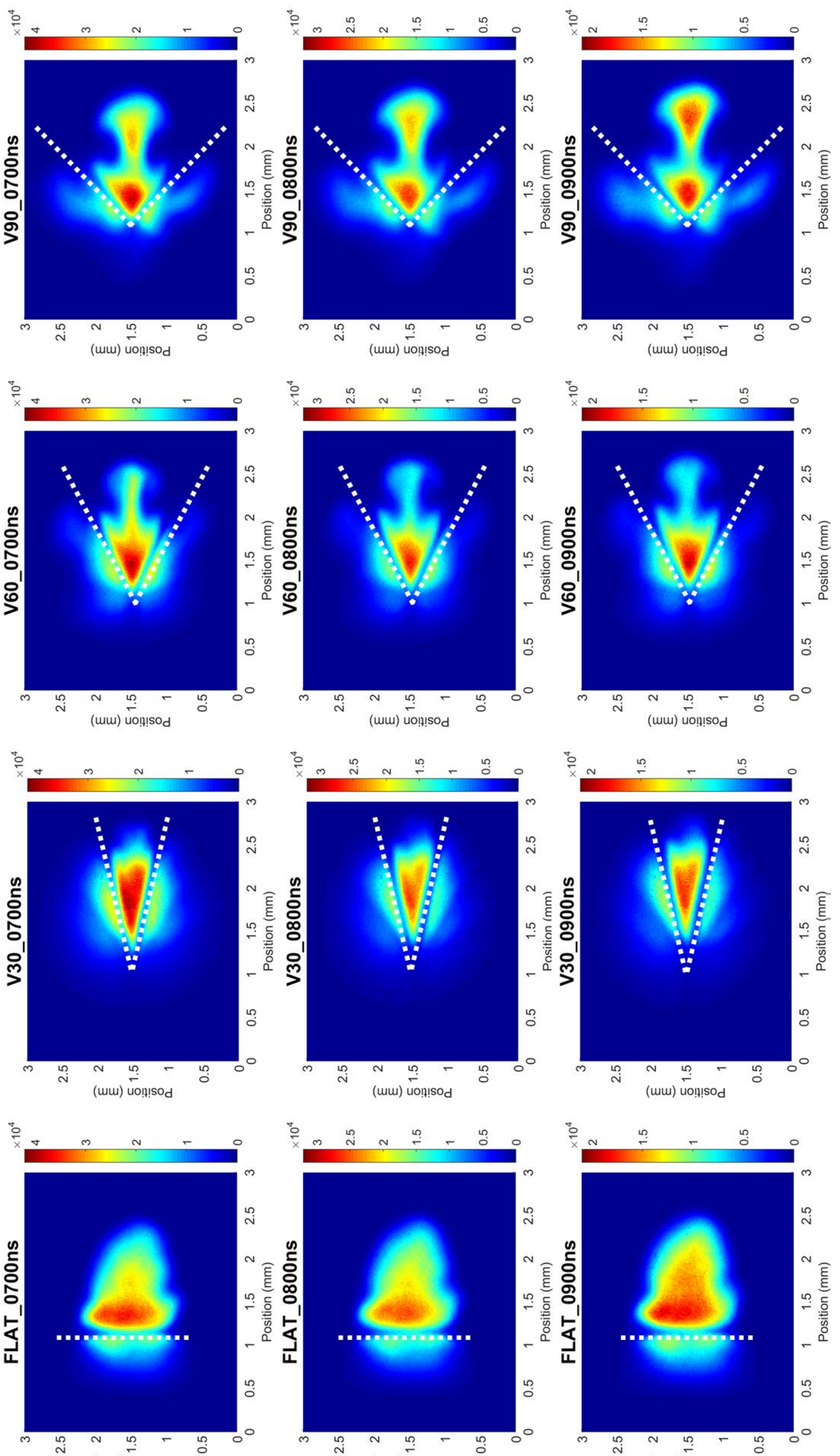
FLAT_0700ns
FLAT_0800ns
FLAT_0900ns
V30_0700ns
V30_0800ns
V30_0900ns
V60_0700ns
V60_0800ns
V60_0900ns
V90_0700ns
V90_0800ns
V90_0900ns
Position (mm)
Position (mm)
0
0.5
1
1.5
2
2.5
3
×10^4
0
1
2
3
4
0
0.5
1
1.5
2
2.5
3
0
0.5
1
1.5
2

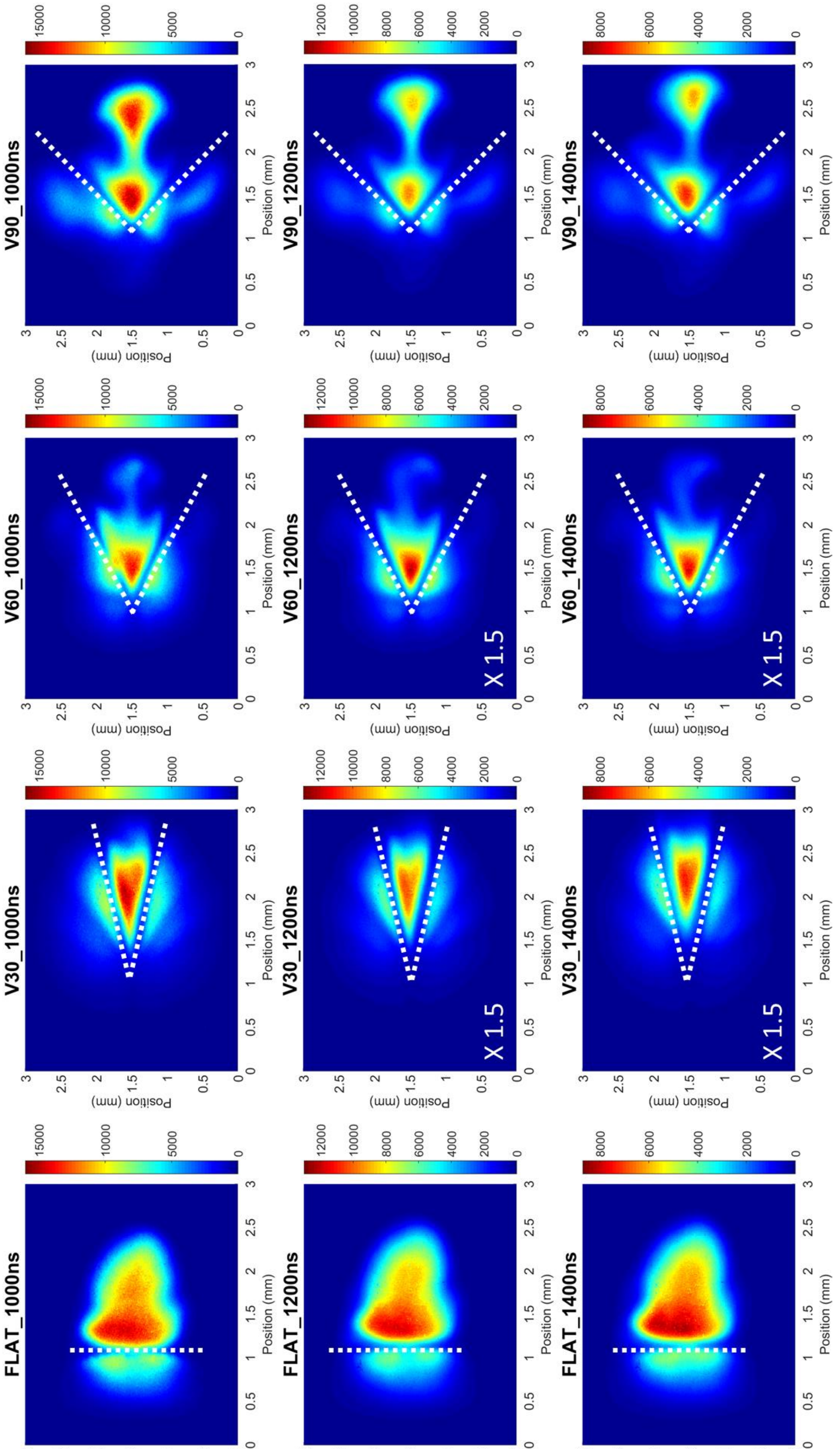
FLAT_1000ns
FLAT_1200ns
FLAT_1400ns
V30_1000ns
V30_1200ns
V30_1400ns
V60_1000ns
V60_1200ns
V60_1400ns
V90_1000ns
V90_1200ns
V90_1400ns
X 1.5
X 1.5
X 1.5
X 1.5
Position (mm)
Position (mm)
0
0.5
1
1.5
2
2.5
3
15000
10000
5000
12000
10000
8000
6000
4000
2000
8000
6000
4000
2000

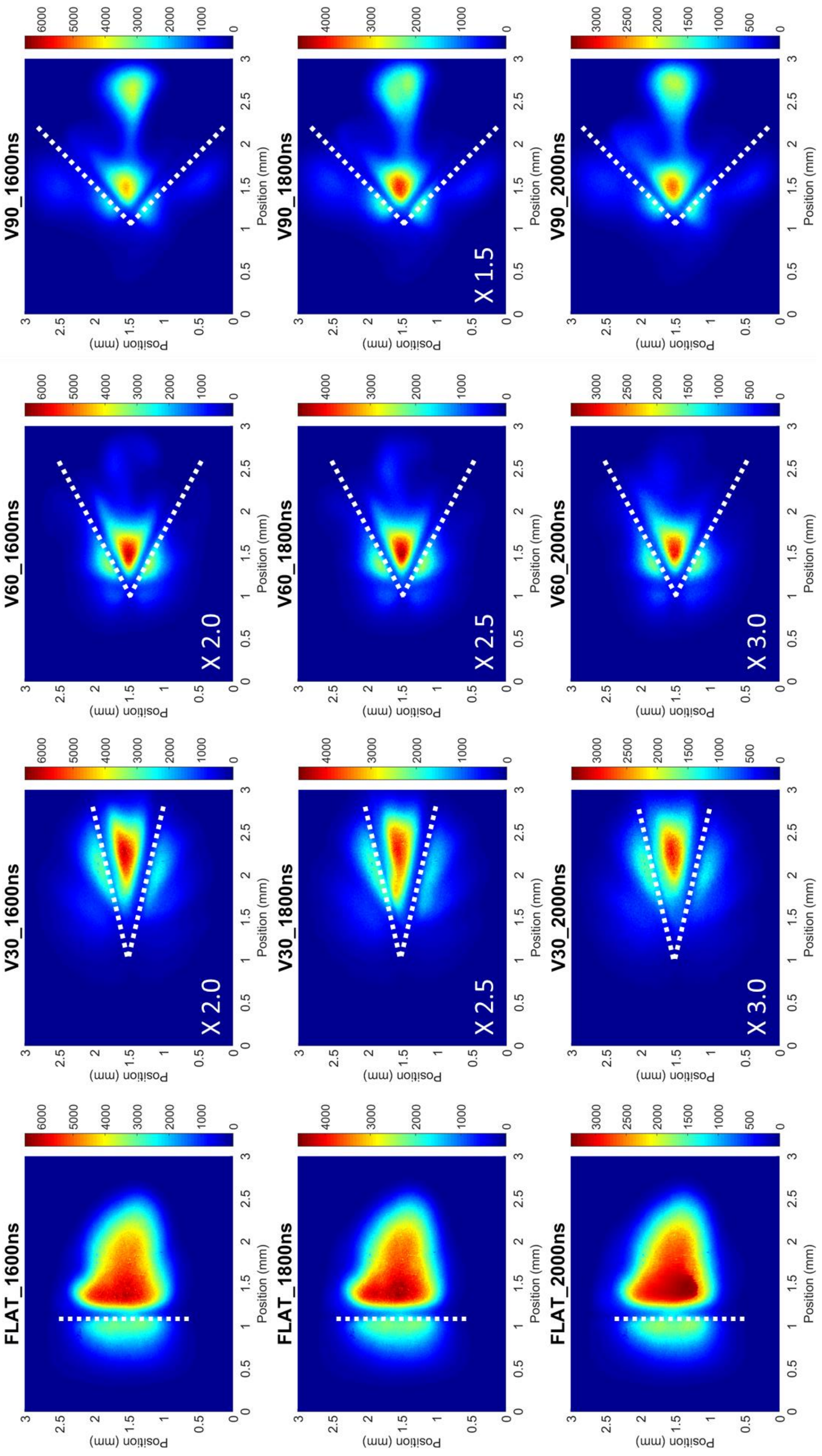
FLAT_1600ns
FLAT_1800ns
FLAT_2000ns
V30_1600ns
X 2.0
V30_1800ns
X 2.5
V30_2000ns
X 3.0
V60_1600ns
X 2.0
V60_1800ns
X 2.5
V60_2000ns
X 3.0
V90_1600ns
V90_1800ns
X 1.5
V90_2000ns
Position (mm)
Position (mm)
0
0.5
1
1.5
2
2.5
3
0
1000
2000
3000
4000
5000
6000
0
1000
2000
3000
4000
0
500
1000
1500
2000
2500
3000

Filtered time resolved image series

Below are the filtered imaging images of the different targets. Images were recorded with filters corresponding to the Al, Al^{+}, and Al^{2+} lines of wavelength $396.15\,nm$, $466.3\,nm$, and $569.6\,nm$ respectively.

Flat Target Images

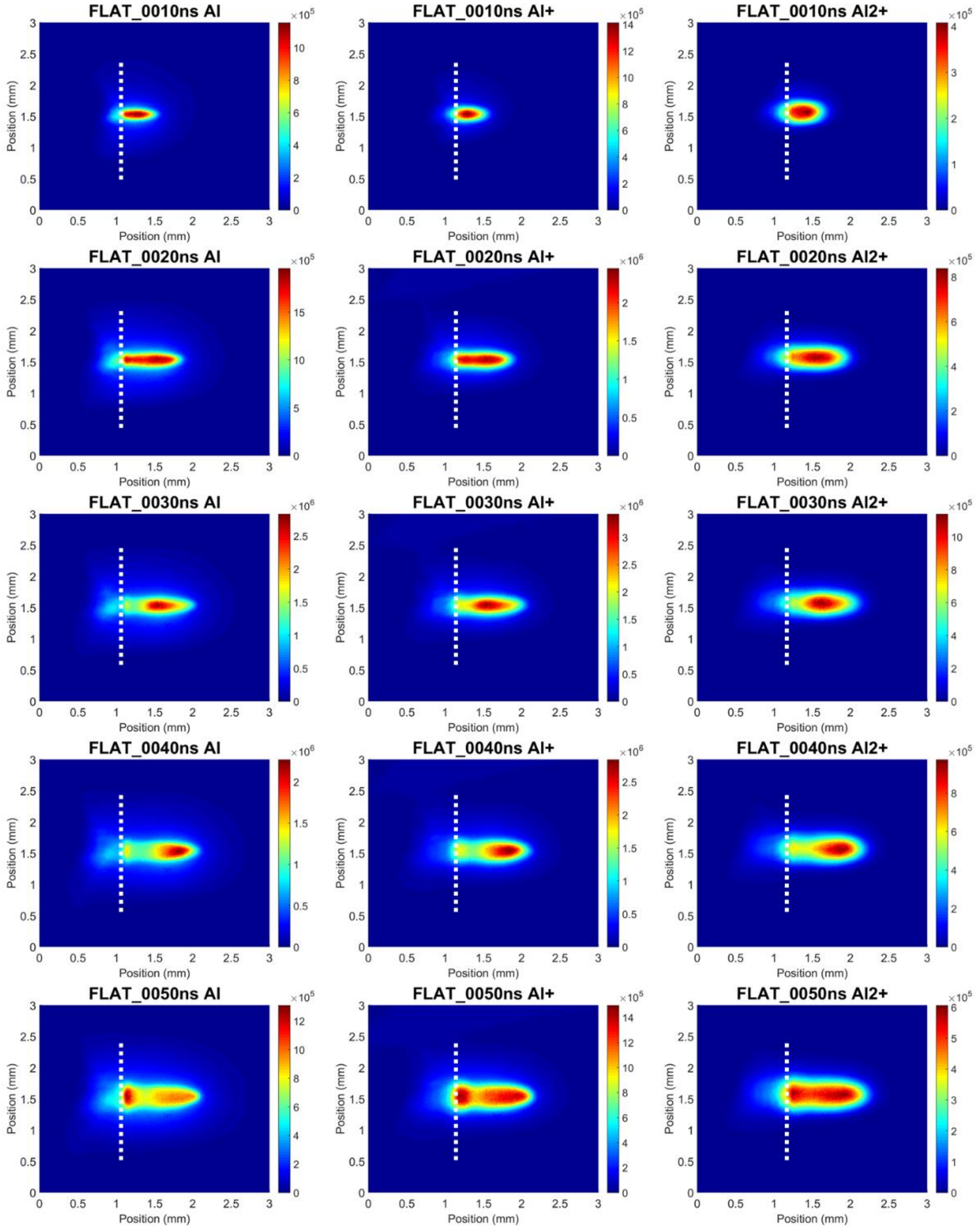

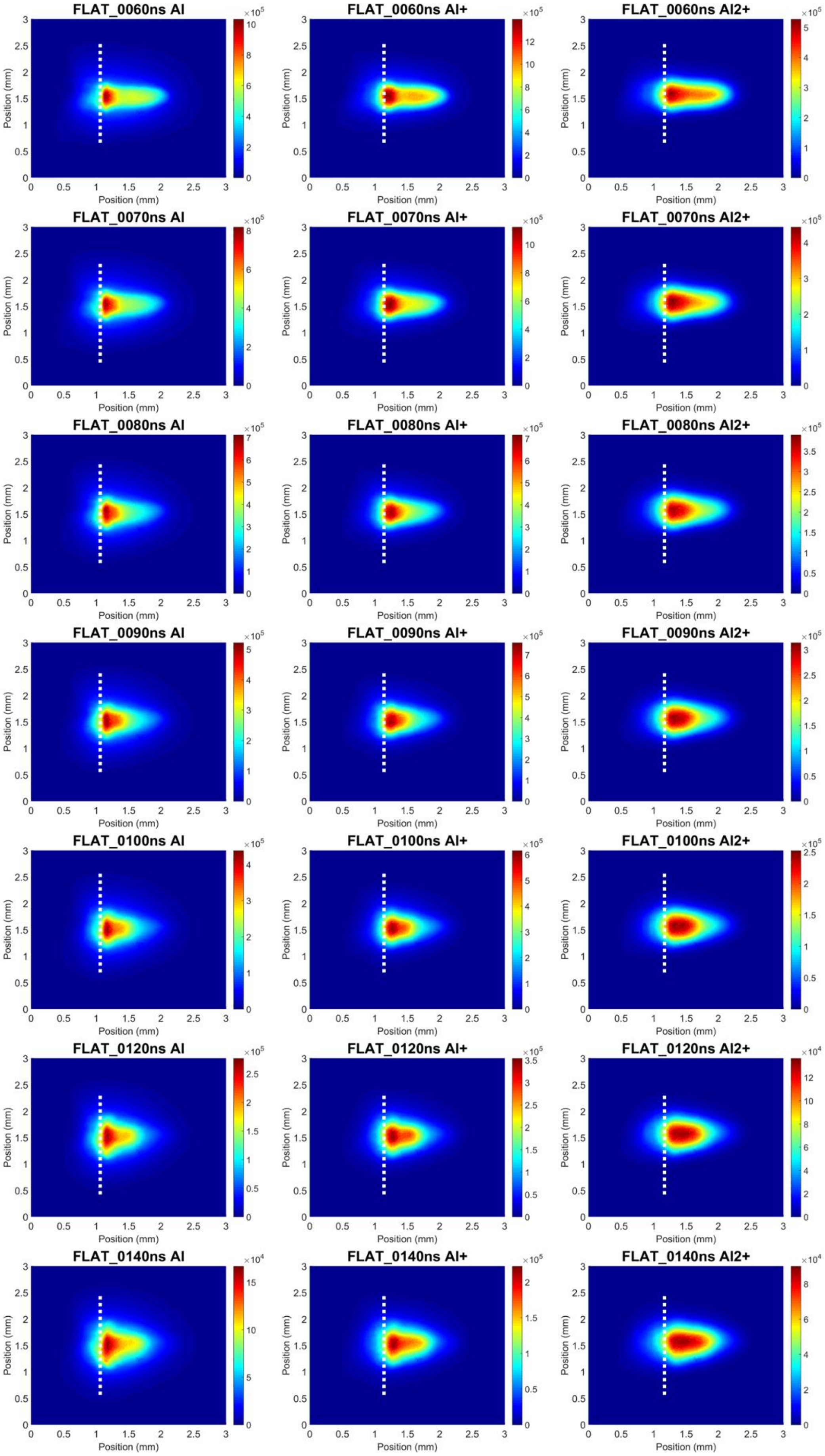
FLAT_0060ns Al
FLAT_0060ns Al+
FLAT_0060ns Al2+
FLAT_0070ns Al
FLAT_0070ns Al+
FLAT_0070ns Al2+
FLAT_0080ns Al
FLAT_0080ns Al+
FLAT_0080ns Al2+
FLAT_0090ns Al
FLAT_0090ns Al+
FLAT_0090ns Al2+
FLAT_0100ns Al
FLAT_0100ns Al+
FLAT_0100ns Al2+
FLAT_0120ns Al
FLAT_0120ns Al+
FLAT_0120ns Al2+
FLAT_0140ns Al
FLAT_0140ns Al+
FLAT_0140ns Al2+
Position (mm)
Position (mm)
×10^5
×10^4

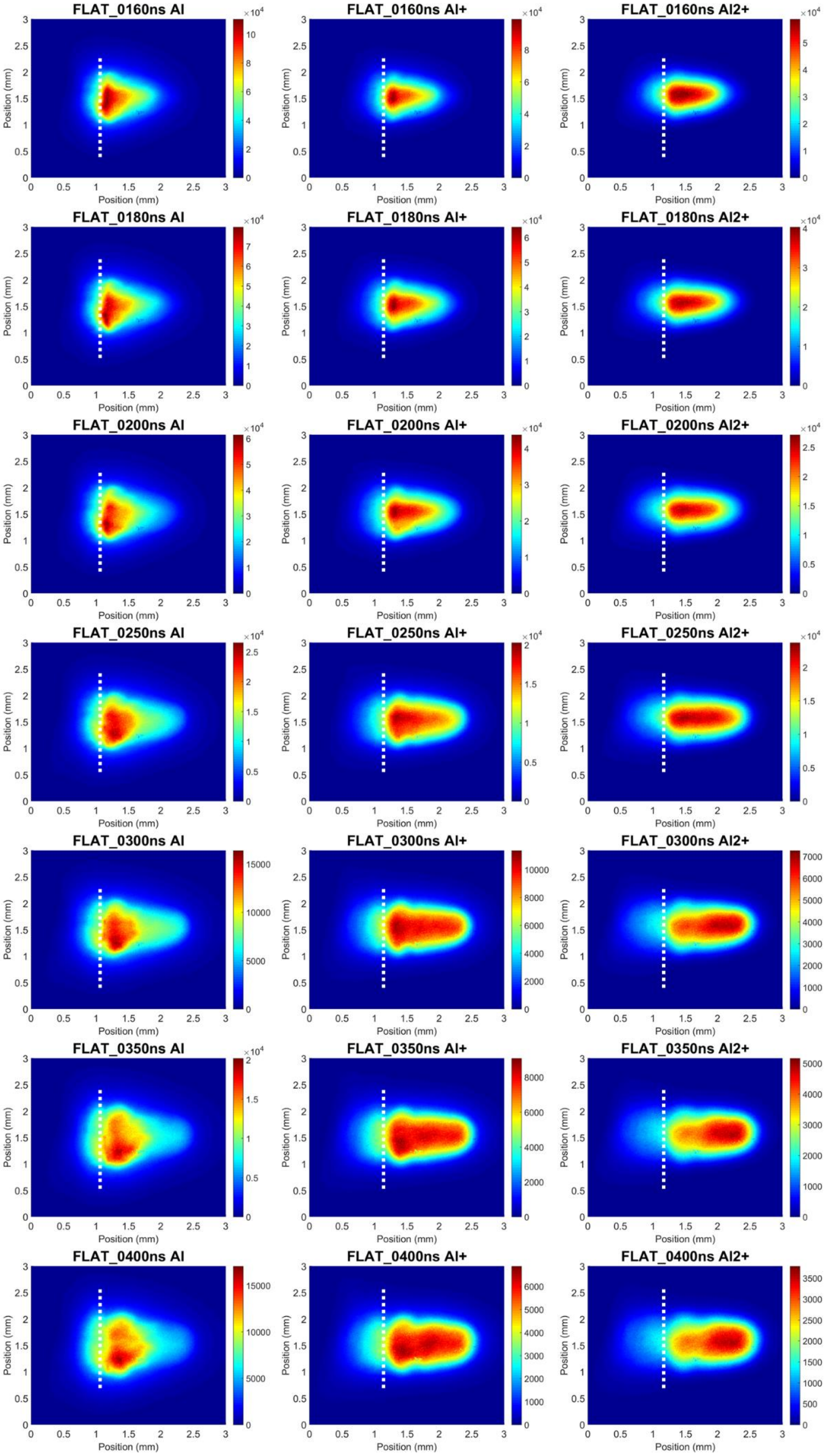
FLAT_0160ns Al
FLAT_0160ns Al+
FLAT_0160ns Al2+
FLAT_0180ns Al
FLAT_0180ns Al+
FLAT_0180ns Al2+
FLAT_0200ns Al
FLAT_0200ns Al+
FLAT_0200ns Al2+
FLAT_0250ns Al
FLAT_0250ns Al+
FLAT_0250ns Al2+
FLAT_0300ns Al
FLAT_0300ns Al+
FLAT_0300ns Al2+
FLAT_0350ns Al
FLAT_0350ns Al+
FLAT_0350ns Al2+
FLAT_0400ns Al
FLAT_0400ns Al+
FLAT_0400ns Al2+
Position (mm)
Position (mm)
0
0.5
1
1.5
2
2.5
3
×10^4
10
8
6
4
2
0
5
16000
10000
5000
7000
6000
4000
3000
2000
1000
9000
15000
3500
2500
1500
500

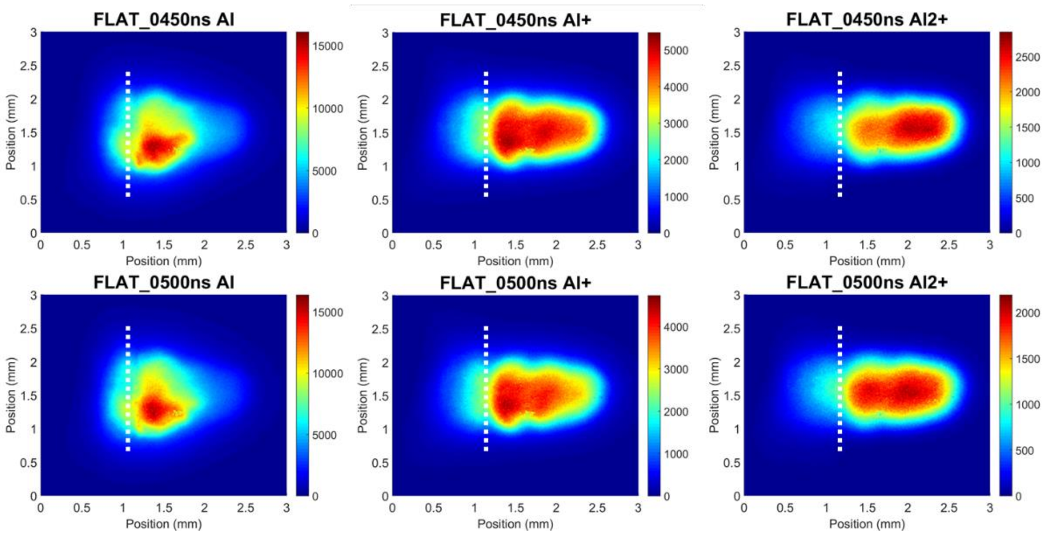
FLAT_0450ns Al

FLAT_0450ns Al+

FLAT_0450ns Al2+

FLAT_0500ns Al

FLAT_0500ns Al+

FLAT_0500ns Al2+

90^{o} V-channel Target Images

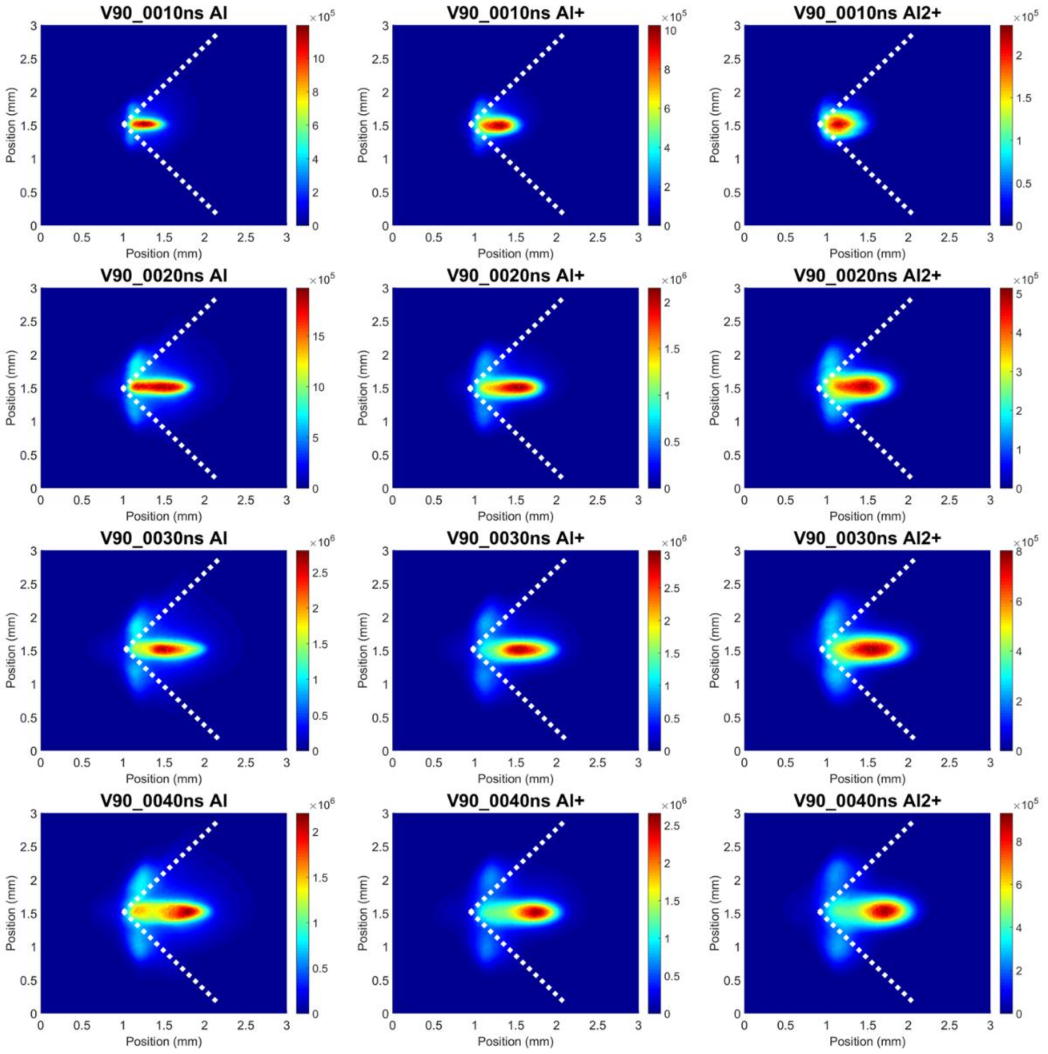
V90_0010ns Al

V90_0010ns Al+

V90_0010ns Al2+

V90_0020ns Al

V90_0020ns Al+

V90_0020ns Al2+

V90_0030ns Al

V90_0030ns Al+

V90_0030ns Al2+

V90_0040ns Al

V90_0040ns Al+

V90_0040ns Al2+

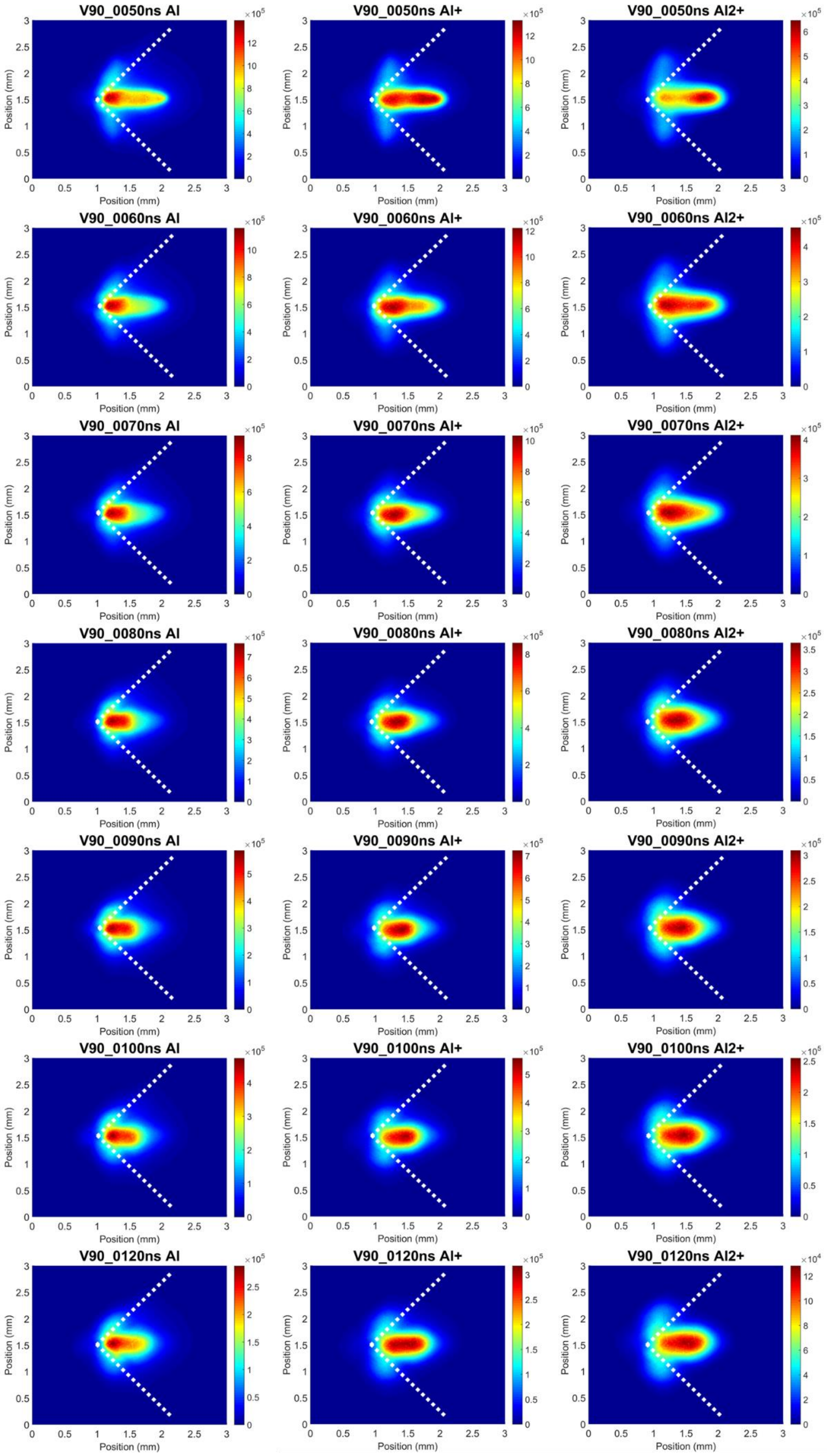
V90_0050ns Al
V90_0050ns Al+
V90_0050ns Al2+
V90_0060ns Al
V90_0060ns Al+
V90_0060ns Al2+
V90_0070ns Al
V90_0070ns Al+
V90_0070ns Al2+
V90_0080ns Al
V90_0080ns Al+
V90_0080ns Al2+
V90_0090ns Al
V90_0090ns Al+
V90_0090ns Al2+
V90_0100ns Al
V90_0100ns Al+
V90_0100ns Al2+
V90_0120ns Al
V90_0120ns Al+
V90_0120ns Al2+
Position (mm)
Position (mm)
$\times 10^5$
$\times 10^4$

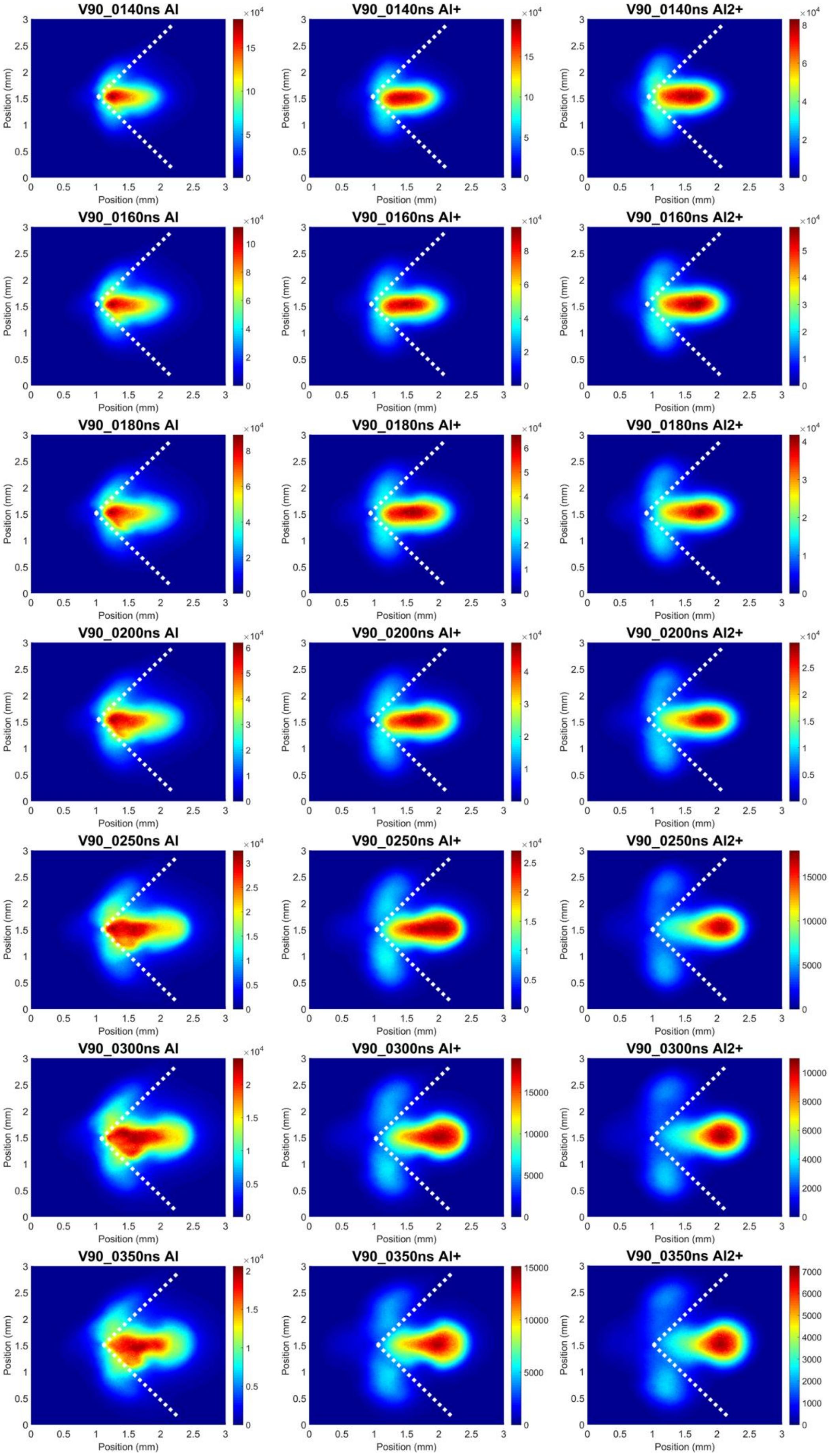
V90_0140ns Al
V90_0140ns Al+
V90_0140ns Al2+
V90_0160ns Al
V90_0160ns Al+
V90_0160ns Al2+
V90_0180ns Al
V90_0180ns Al+
V90_0180ns Al2+
V90_0200ns Al
V90_0200ns Al+
V90_0200ns Al2+
V90_0250ns Al
V90_0250ns Al+
V90_0250ns Al2+
V90_0300ns Al
V90_0300ns Al+
V90_0300ns Al2+
V90_0350ns Al
V90_0350ns Al+
V90_0350ns Al2+
Position (mm)
Position (mm)
×10⁴

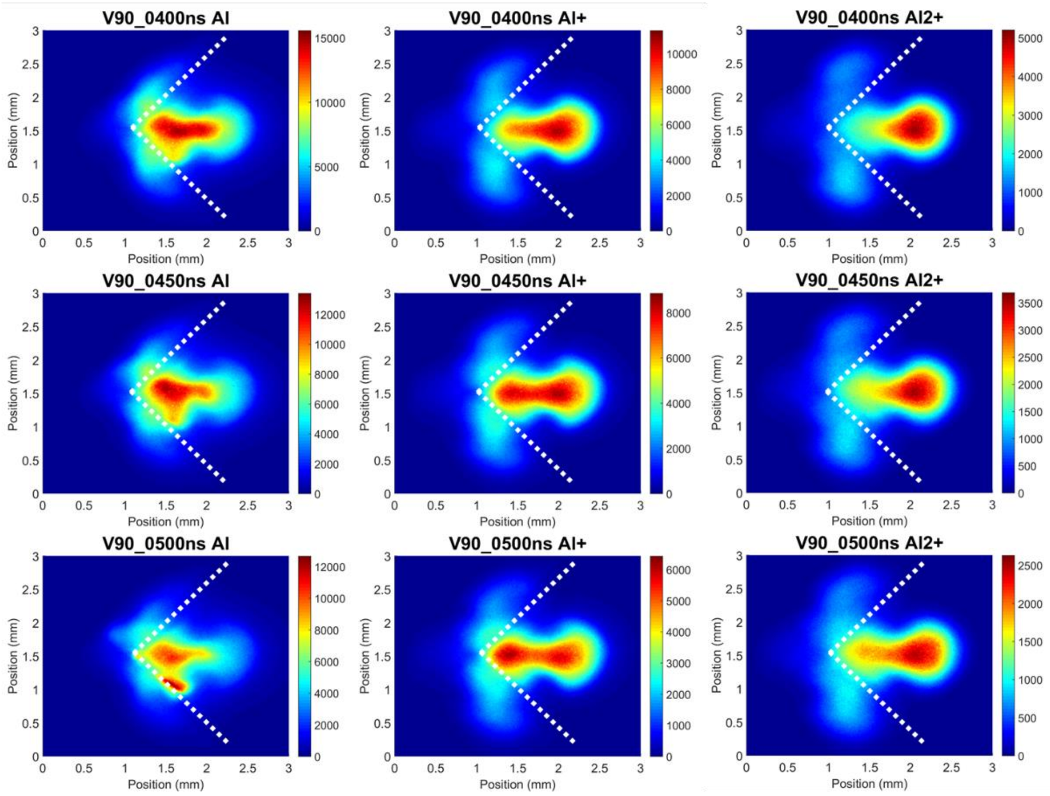

60° V-channel Target Images

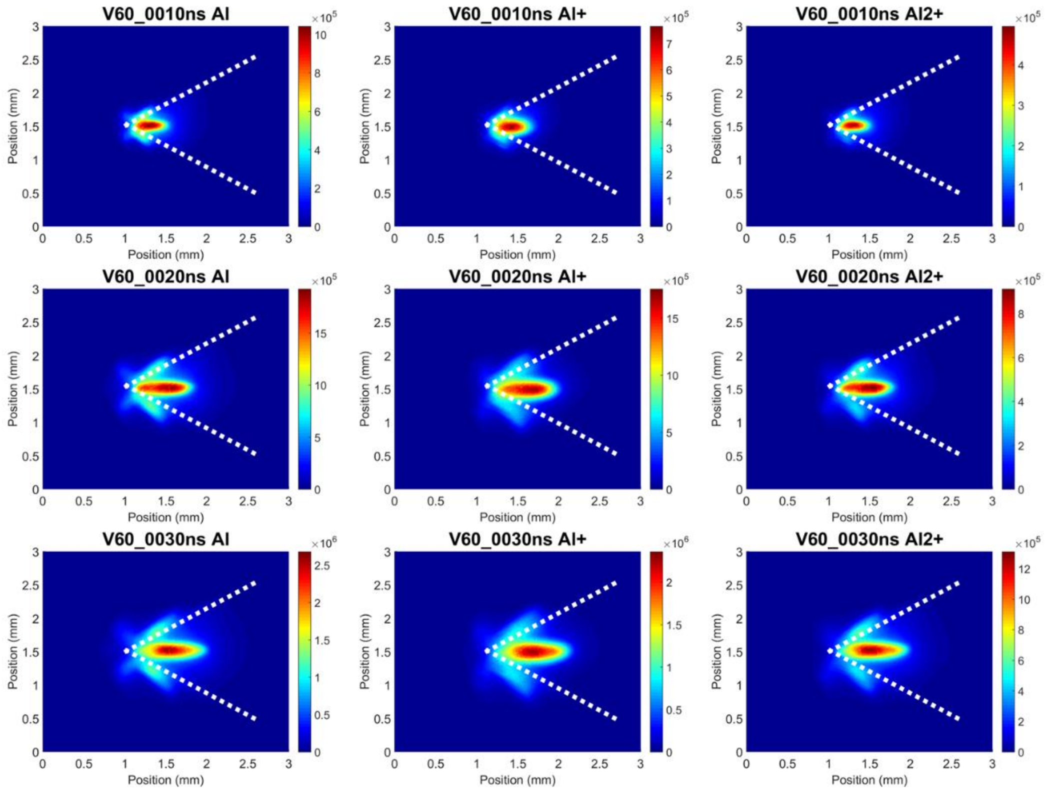

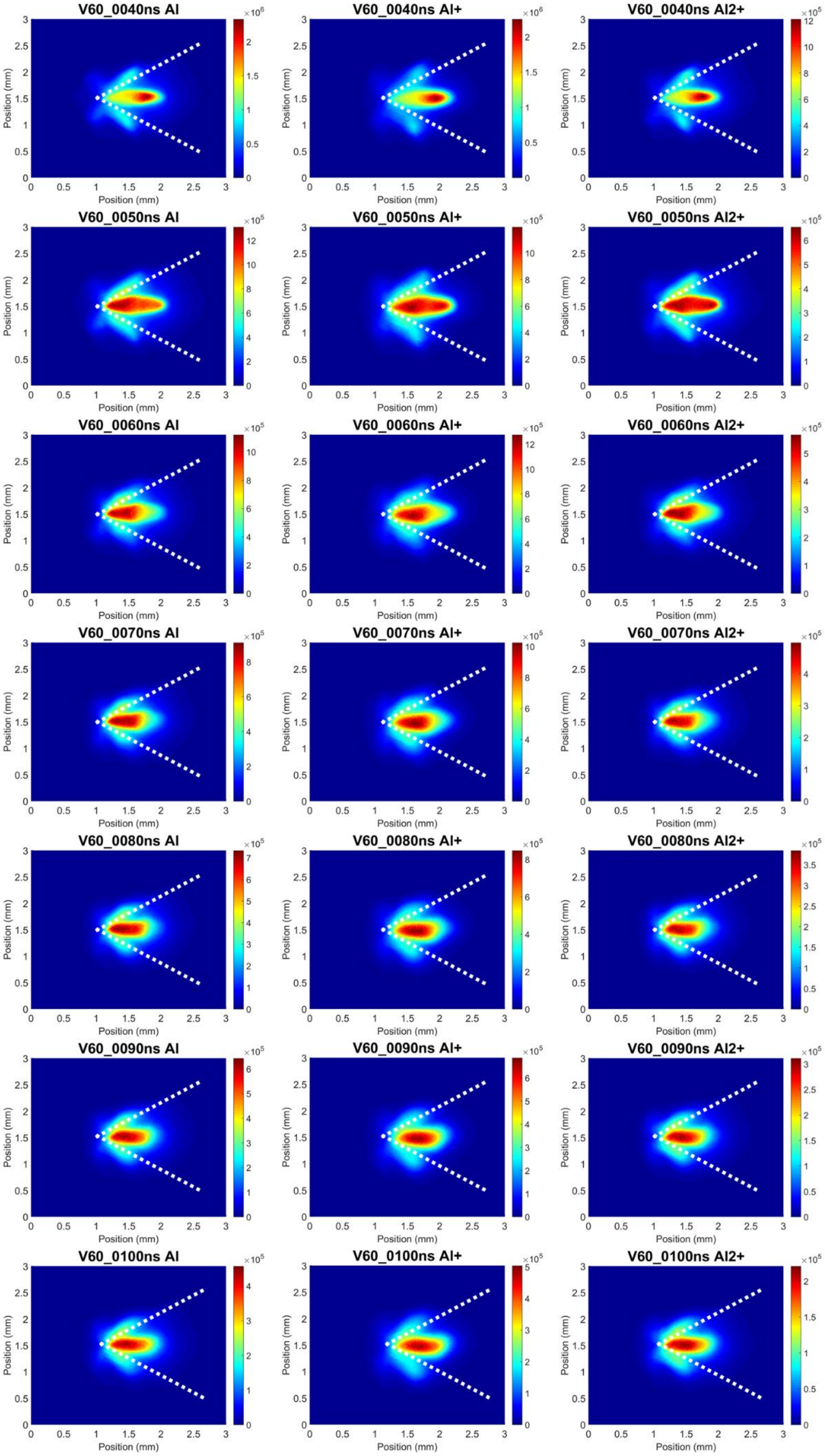
V60_0040ns Al
V60_0040ns Al+
V60_0040ns Al2+
×10^6
×10^6
×10^5
V60_0050ns Al
V60_0050ns Al+
V60_0050ns Al2+
V60_0060ns Al
V60_0060ns Al+
V60_0060ns Al2+
V60_0070ns Al
V60_0070ns Al+
V60_0070ns Al2+
V60_0080ns Al
V60_0080ns Al+
V60_0080ns Al2+
V60_0090ns Al
V60_0090ns Al+
V60_0090ns Al2+
V60_0100ns Al
V60_0100ns Al+
V60_0100ns Al2+
×10^5
Position (mm)
Position (mm)

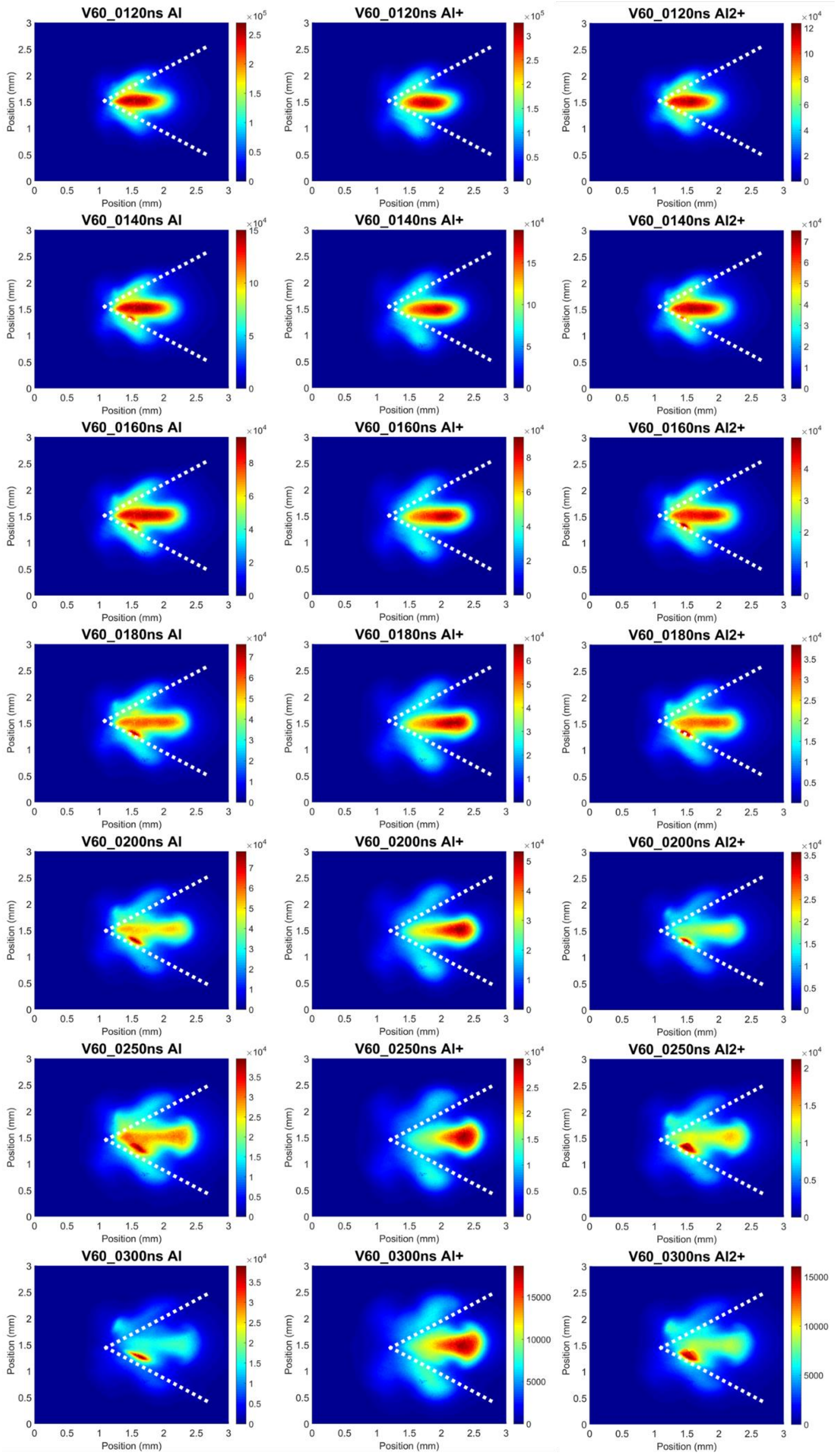
V60_0120ns Al
V60_0120ns Al+
V60_0120ns Al2+
V60_0140ns Al
V60_0140ns Al+
V60_0140ns Al2+
V60_0160ns Al
V60_0160ns Al+
V60_0160ns Al2+
V60_0180ns Al
V60_0180ns Al+
V60_0180ns Al2+
V60_0200ns Al
V60_0200ns Al+
V60_0200ns Al2+
V60_0250ns Al
V60_0250ns Al+
V60_0250ns Al2+
V60_0300ns Al
V60_0300ns Al+
V60_0300ns Al2+
Position (mm)
Position (mm)
×10^5
×10^4

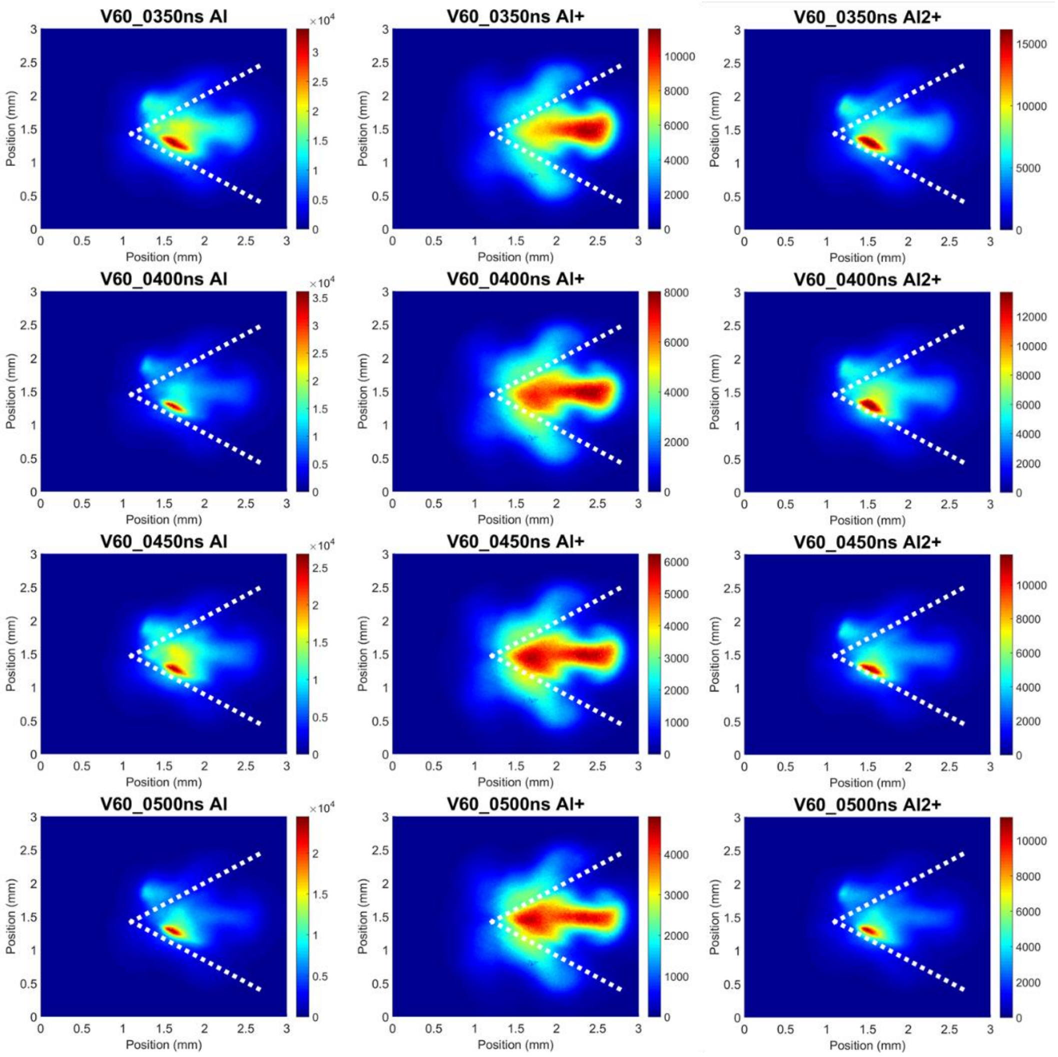

30^o V-channel Target Images

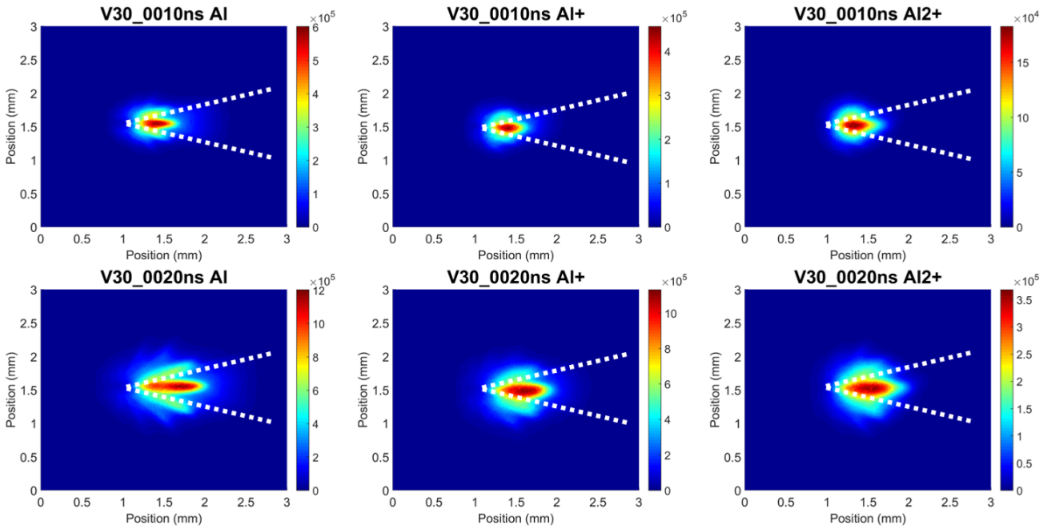

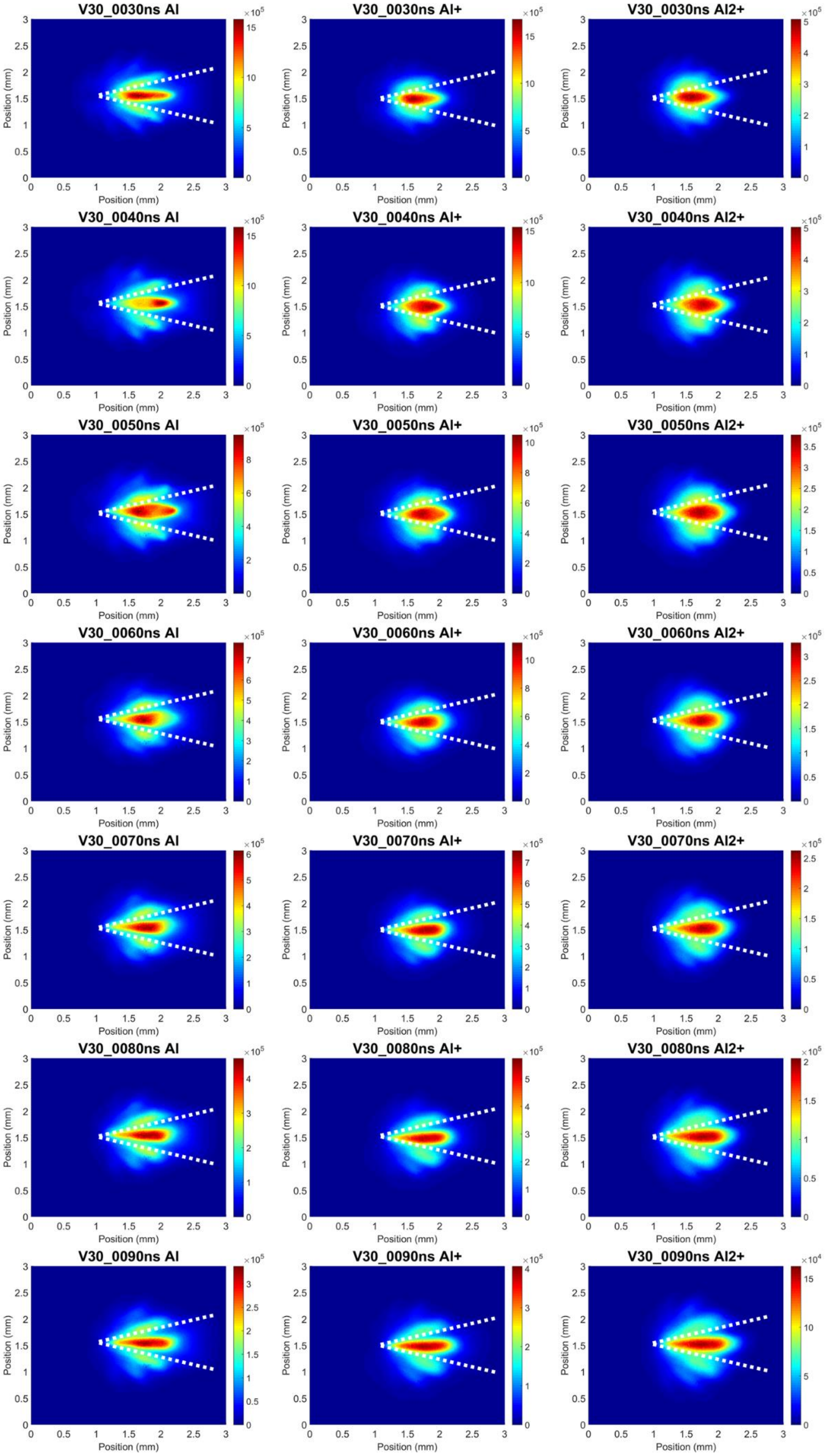
V30_0030ns Al
V30_0030ns Al+
V30_0030ns Al2+
V30_0040ns Al
V30_0040ns Al+
V30_0040ns Al2+
V30_0050ns Al
V30_0050ns Al+
V30_0050ns Al2+
V30_0060ns Al
V30_0060ns Al+
V30_0060ns Al2+
V30_0070ns Al
V30_0070ns Al+
V30_0070ns Al2+
V30_0080ns Al
V30_0080ns Al+
V30_0080ns Al2+
V30_0090ns Al
V30_0090ns Al+
V30_0090ns Al2+
Position (mm)
Position (mm)
0
0.5
1
1.5
2
2.5
3
×10⁵
×10⁴

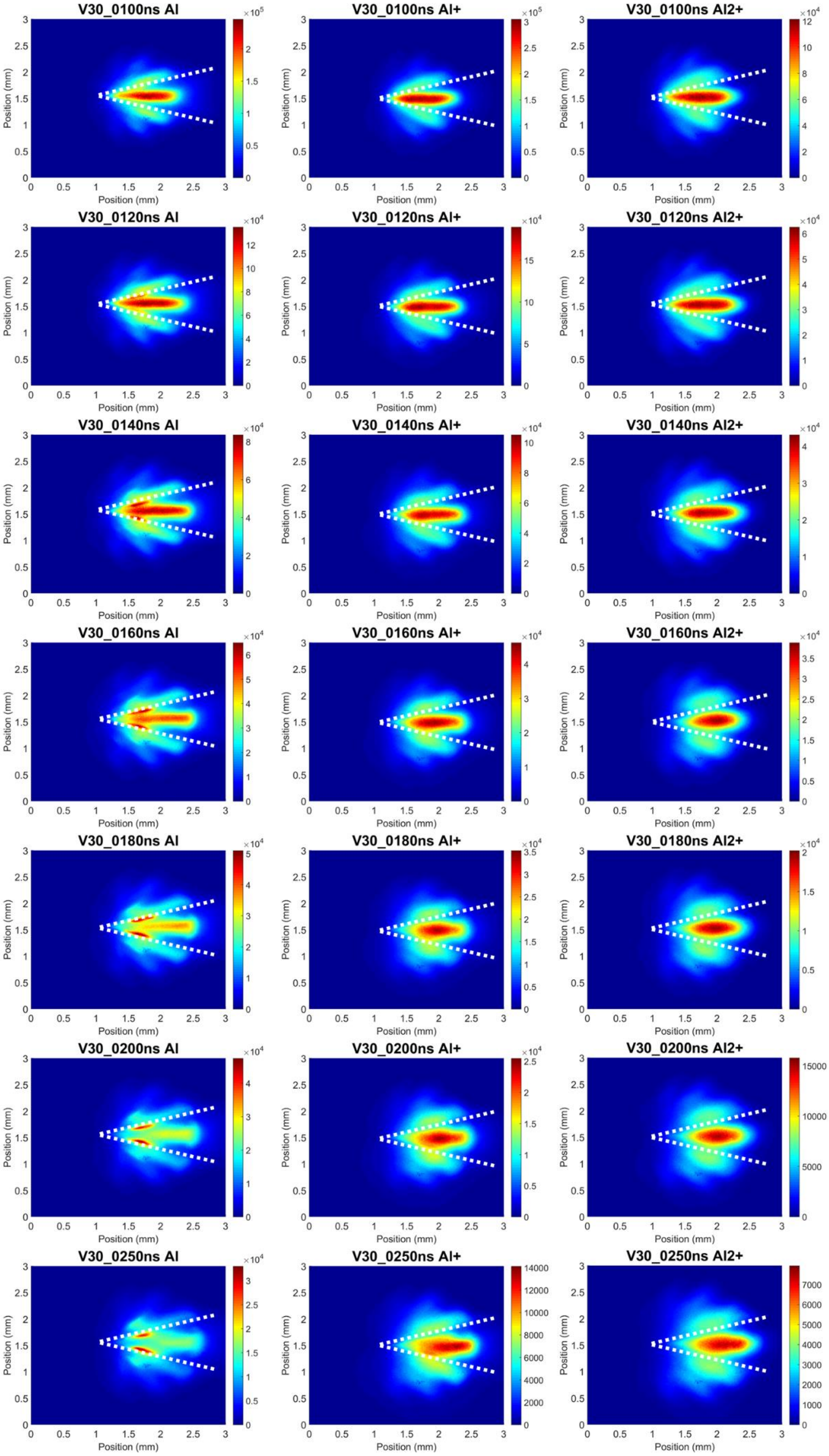
V30_0100ns Al
V30_0100ns Al+
V30_0100ns Al2+
V30_0120ns Al
V30_0120ns Al+
V30_0120ns Al2+
V30_0140ns Al
V30_0140ns Al+
V30_0140ns Al2+
V30_0160ns Al
V30_0160ns Al+
V30_0160ns Al2+
V30_0180ns Al
V30_0180ns Al+
V30_0180ns Al2+
V30_0200ns Al
V30_0200ns Al+
V30_0200ns Al2+
V30_0250ns Al
V30_0250ns Al+
V30_0250ns Al2+
Position (mm)
Position (mm)
0
0.5
1
1.5
2
2.5
3

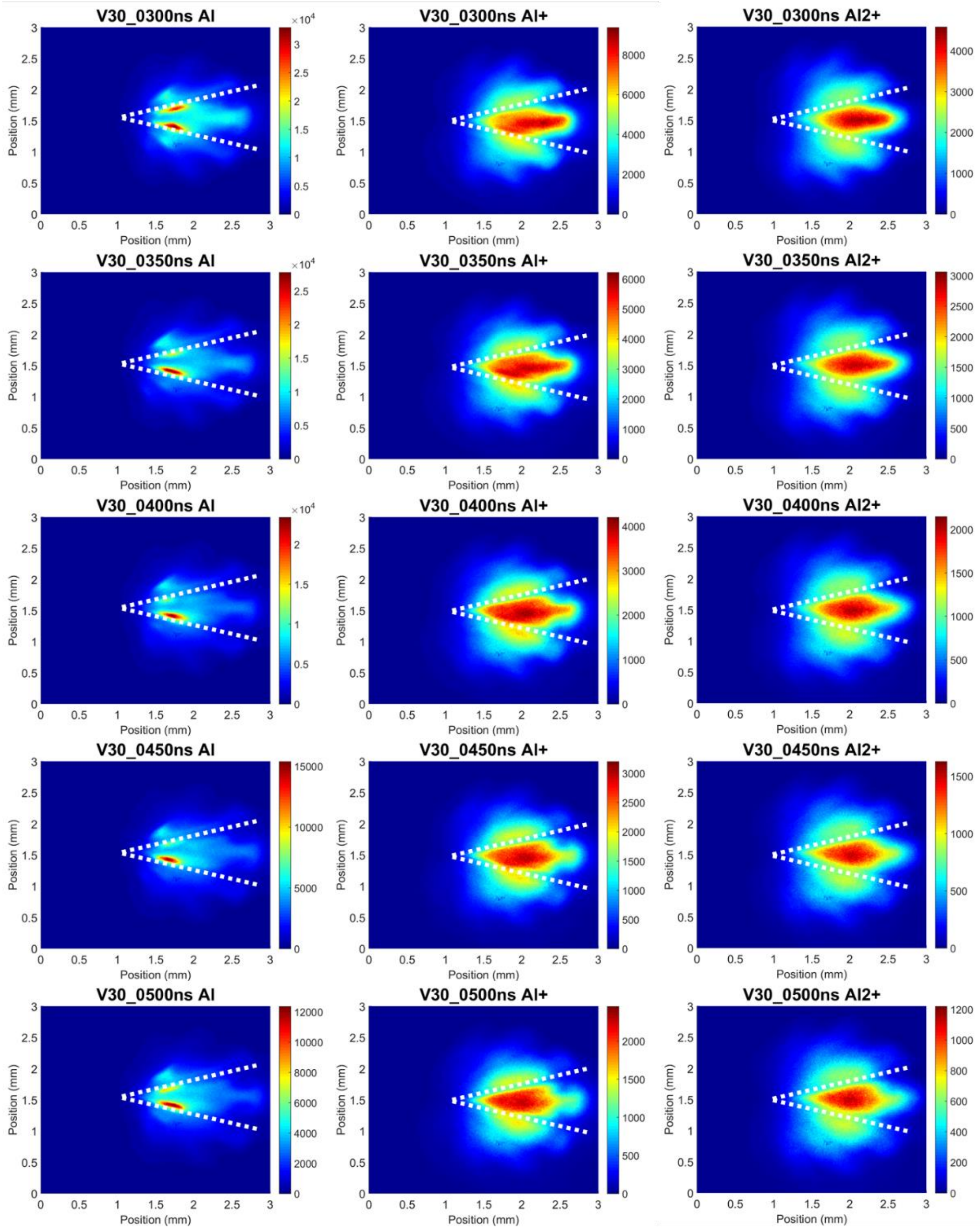

V30_0300ns Al
V30_0300ns Al+
V30_0300ns Al2+
V30_0350ns Al
V30_0350ns Al+
V30_0350ns Al2+
V30_0400ns Al
V30_0400ns Al+
V30_0400ns Al2+
V30_0450ns Al
V30_0450ns Al+
V30_0450ns Al2+
V30_0500ns Al
V30_0500ns Al+
V30_0500ns Al2+
Position (mm)
Position (mm)
0
0.5
1
1.5
2
2.5
3
$\times 10^4$

C. Supplementary Optical Emission Spectroscopy Data

Space integrated OES spectra in Y-direction for A) Flat, B) 60° V-channel, and C) 30° V-channel targets. 90° V-channel target data can be seen in Fig. 5.2

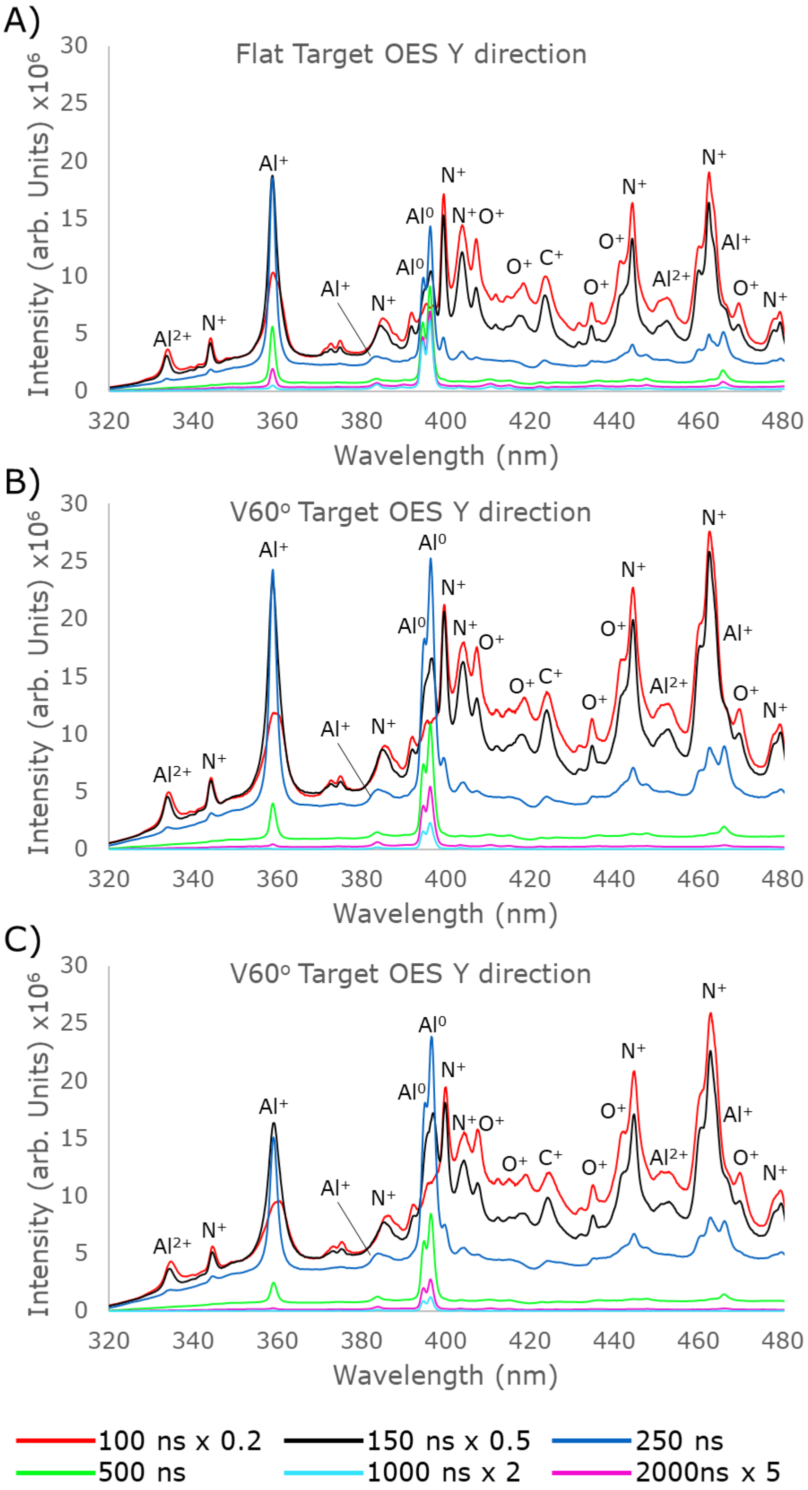

Spatially integrated OES spectra recorded at Y direction and different positions in the X direction: $0.4\,mm$, $0.7\,mm$ (used in thesis as X-direction), and $1.4\,mm$ for the various targets.

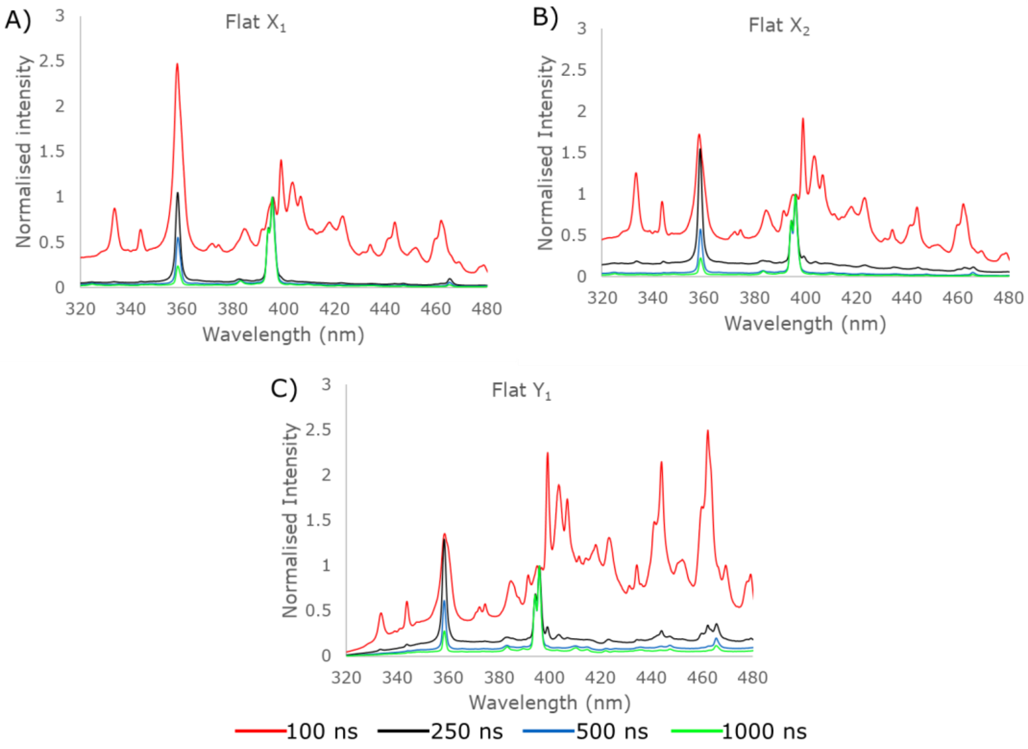

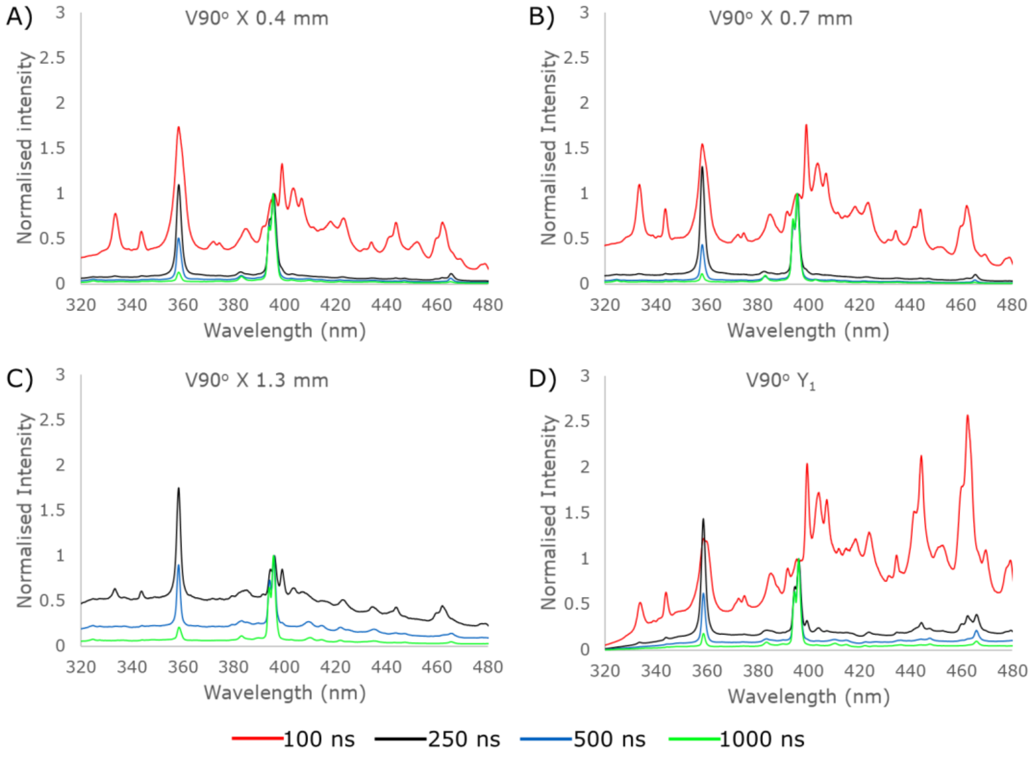

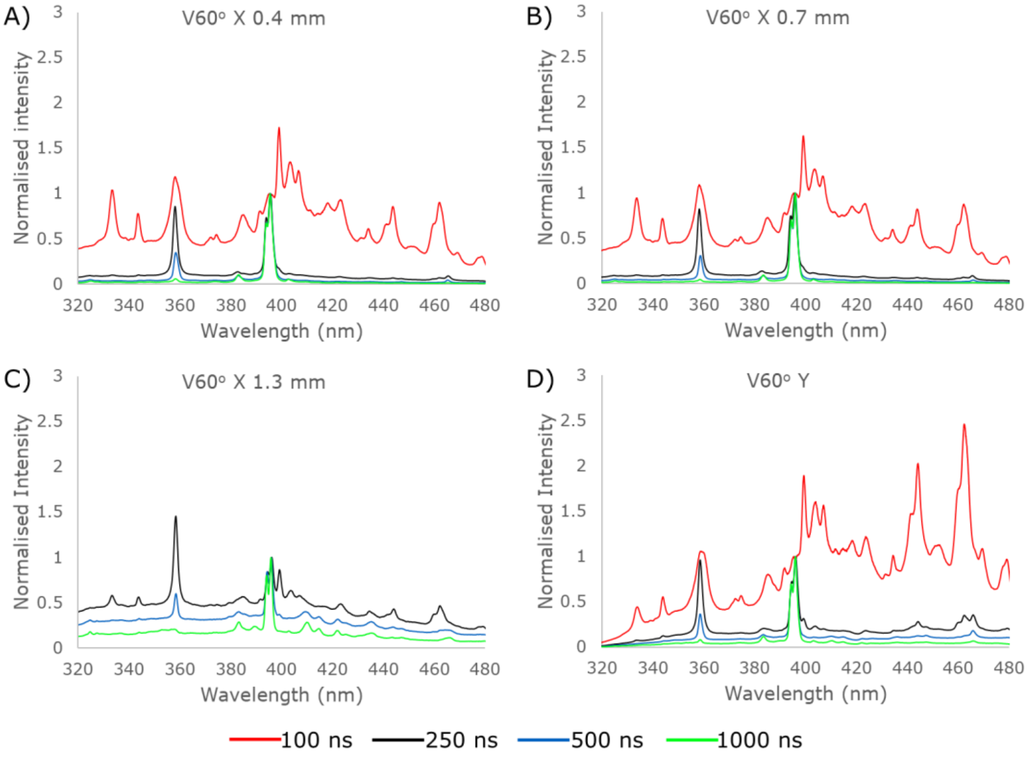
A)
V60° X 0.4 mm
B)
V60° X 0.7 mm
C)
V60° X 1.3 mm
D)
V60° Y
Normalised intensity
Normalised Intensity
0
0.5
1
1.5
2
2.5
3
320
340
360
380
400
420
440
460
480
Wavelength (nm)
100 ns
250 ns
500 ns
1000 ns

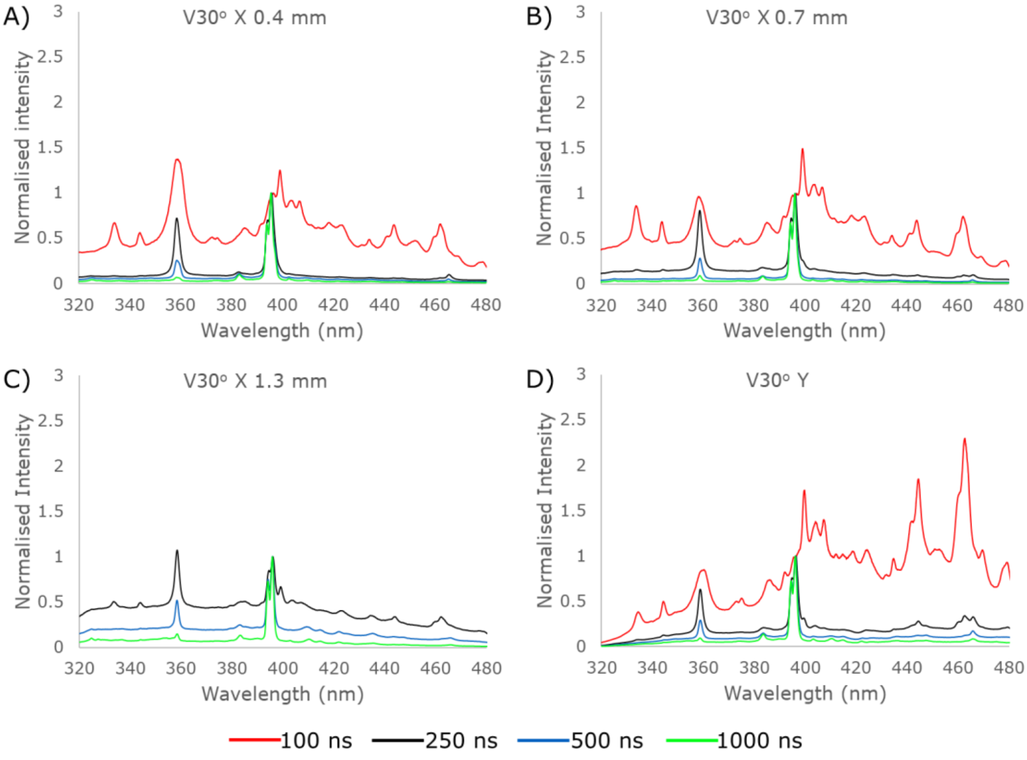
A)
V30° X 0.4 mm
B)
V30° X 0.7 mm
C)
V30° X 1.3 mm
D)
V30° Y
Normalised intensity
Normalised Intensity
0
0.5
1
1.5
2
2.5
3
320
340
360
380
400
420
440
460
480
Wavelength (nm)
100 ns
250 ns
500 ns
1000 ns

Comparison of the spatially integrated OES spectra in the Y-direction of the various targets at various time delays. Line emission from the $Al^{+}\ 358.7\ nm$ and $Al^{0}\ 396.15\ nm$ lines were integrated for the intensity comparison in section 5.4.

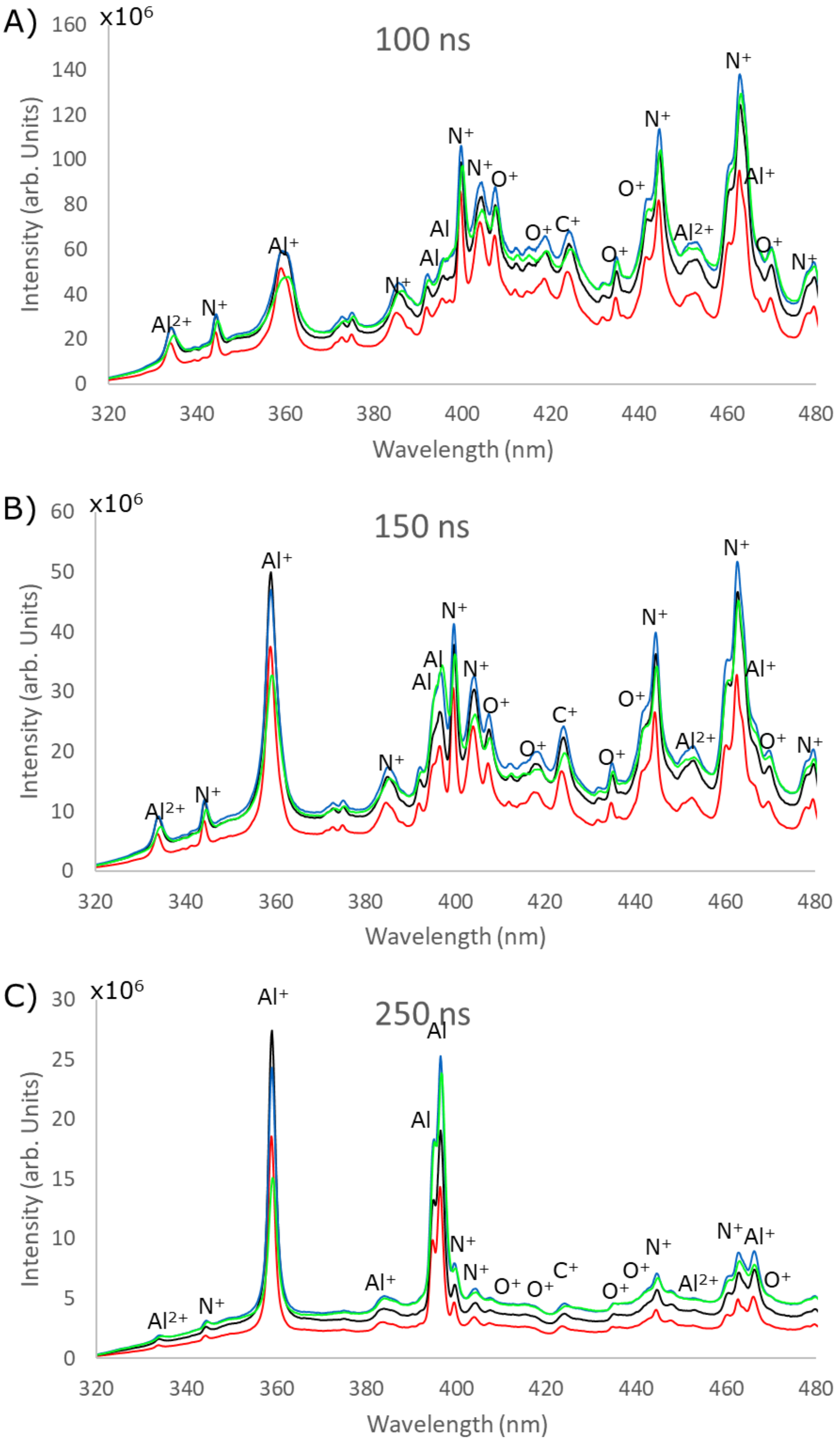

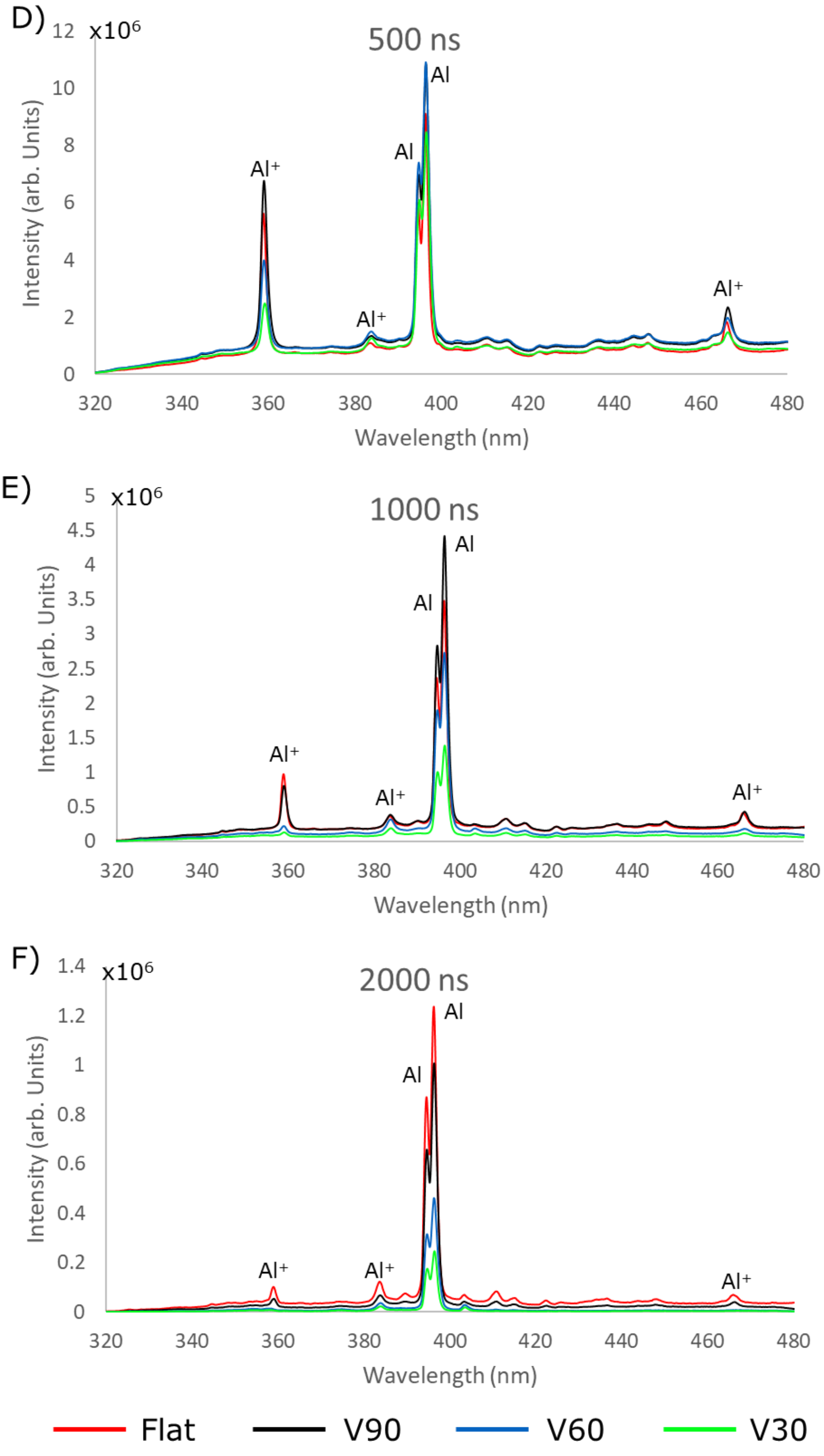
D)
x10^6
500 ns
Intensity (arb. Units)
0
2
4
6
8
10
12
Al
Al
Al+
Al+
Al+
320
340
360
380
400
420
440
460
480
Wavelength (nm)
E)
x10^6
1000 ns
Intensity (arb. Units)
0
0.5
1
1.5
2
2.5
3
3.5
4
4.5
5
Al
Al
Al+
Al+
Al+
320
340
360
380
400
420
440
460
480
Wavelength (nm)
F)
x10^6
2000 ns
Intensity (arb. Units)
0
0.2
0.4
0.6
0.8
1
1.2
1.4
Al
Al
Al+
Al+
Al+
320
340
360
380
400
420
440
460
480
Wavelength (nm)
Flat
V90
V60
V30

Space resolved spectra of the different targets at a time delay of $500\,ns$ with corresponding spatial profiles of the $Al^0 394.4\,nm$ and $396.15\,nm$ emission lines. The presence of bright spots of Al^0 predicted to be forced recombination is evident in the V-channel targets.